Using galaxy surveys to understand the cosmological evolution

By

ROSSANA RUGGERI

Institute of cosmology and gravitation
UNIVERSITY OF PORTSMOUTH

This thesis is submitted in partial fulfilment of the requirements for the award of the degree of DOCTOR OF PHILOSOPHY of the University of Portsmouth.

APRIL 2018

ABSTRACT

Forthcoming galaxy redshift surveys are to a large extent motivated by the desire to obtain data on galaxy clustering so as to more accurately quantify the accelerating expansion of the Universe and thereby provide insight into the mechanism responsible for acceleration. Currently suggested mechanisms are: a cosmological constant, a new scalar field that contributes to the energy budget of the Universe as dark energy, and modification on the cosmological scale of the law of gravitation. It is also possible that the accelerating expansion of the Universe may only be properly understood by an as yet undeveloped alternative to the standard cosmological model.

Because the large-scale distribution of galaxies is expected to follow a gaussian random field - for which statistical information is fully encoded in 2-point statistics, the key quantities provided by redshift surveys are the correlation function and its Fourier space analogue, the power spectrum. The detection of features due to baryonic acoustic oscillations (BAO) in these data will allow them to be used as standard rulers to reconstruct the expansion history of the Universe. In addition, the anisotropies (redshift-space distortions) induced by the velocities of galaxies on these correlators will provide a measurement of the growth rate of cosmic structures, and hence an independent probe of possible departures from the standard model. The power and scope of the forthcoming surveys (DESI and Euclid) will push measurements at least an order of magnitude beyond what is currently available, to provide unprecedented constraints on cosmological models.

It is important therefore to refine the methods used to analyze the large data-sets being produced by these surveys. The investigations reported in this thesis contribute to this goal in several ways. The first part of this thesis describes the development of a faster method to measure the anisotropic clustering signal so as reduce computational load. In particular the measurement of line-of-sight-dependent clustering using fast Fourier transform routines is described, that results in an impressive increase in efficiency compared to standard pair-counting approaches.

The second part is concerned with how best to combine data from different volumes within the surveys. Current analyses split the redshift range into separate bins and repeat the traditional analysis within each bin. However, this method is not only computationally expensive but also results in loss of information (ignoring galaxy pairs across different bins), and increased edge effects on large scales. An alternative approach is presented that applies weighting schemes to account for the redshift evolution of clustering. It is shown that the weightings act as a smooth window on the data, compressing the signal in the redshift direction with no theoretical loss of information. Subsequent development derived and

optimum set of weightings to constrain the growth of structure from the redshift space distortions signal. The weighting technique was also applied to improve constraints on primordial non-gaussianity at large scales.

The third part of this work describes the development and testing of an efficient algorithmic pipeline, developed to perform the analyses, including the development of faster new algorithms (incorporating the new weighting schemes) to measure the anisotropic signal. This part also discusses how to deal with survey geometry when considering redshift evolution in clustering.

The final part describes the application of the pipeline to analyze eBOSS data. In particular the first constraint on growth rate evolution over an unprecedented volume ($1 < z < 2$), as covered by the DR14 quasars, is presented.

Magna pars est profectus velle proficere.

(Lucius Annaeus Seneca)

DEDICATION

This thesis is dedicated to my mom and my dad, the brightest stars in my life.

ACKNOWLEDGMENTS

Here I would like to thank my supervisor Prof. Will Percival, with all my heart, for the support and inspiration he gave me throughout my PhD.

Sempre con tutto il mio cuore vorrei ringraziare le persone vicine a me in questi lunghi tre anni. Mi avete riempito di affetto e di supporto, (da Milano a Portsmouth/Londra fino a Melbourne). Senza di voi non so davvero come sarei arrivata a finire questo percorso.[1]

---

[1]I promise I will thank everyone else personally as there are so many important people to list that one page would never be enough.

AUTHOR'S DECLARATION

Whilst registered as a candidate for the above degree, I have not been registered for any other research award. The results and conclusions embodied in this thesis are the work of the named candidate and have not been submitted for any other academic award. Except where indicated by specific reference in the text, the work is the candidate's own work. Work done in collaboration with, or with the assistance of, others, is indicated as such. Any views expressed in the dissertation are those of the author. This thesis is based on the published works:

1. Rossana Ruggeri et al.. The clustering of the SDSS-IV extended Baryon Oscillation Spectroscopic Survey DR14 quasar sample: measuring the evolution of the growth rate using redshift space distortions between redshift 0.8 and 2.2. Jan 9, 2018. 11 pp. e-Print: arXiv:1801.02891

2. Rossana Ruggeri, Will J. Percival, Eva-Maria Mueller, Hector Gil-Marin, Fangzhou Zhu, Nikhil Padmanabhan, Gong-Bo Zhao. The extended Baryon Oscillation Spectroscopic Survey (eBOSS): testing a new approach to measure the evolution of the structure growth. Dec 11, 2017. 11 pp. e-Print: arXiv:1712.03997

3. Eva-Maria Mueller, Will J. Percival, Rossana Ruggeri. Optimising primordial non-Gaussianity measurements from galaxy surveys. Feb 16, 2017. 8 pp. e-Print: arXiv:1702.05088

4. Rossana Ruggeri, Will Percival (Portsmouth U., ICG), Héctor Gil-Marín, Fangzhou Zhu, Gong-bo Zhao, Yuting Wang. Optimal redshift weighting for redshift-space distortions Published in Mon.Not.Roy.Astron.Soc. 464 (2017) no.3, 2698-2707

5. Davide Bianchi, Héctor Gil-Marín, Rossana Ruggeri, Will J. Percival. Measuring line-of-sight dependent Fourier-space clustering using FFTs. Published in Mon.Not.Roy.Astron.Soc. 453 (2015) no.1, L11-L15

SIGNED: .... DATE: ....20/11/2018...................

TABLE OF CONTENTS

THE HOMOGENEOUS UNIVERSE

1.1 Introduction

Despite major discoveries in high precision observational astronomy over the last few decades, current theoretical models of the Universe still present a number of unsolved problems. The standard cosmological model, usually referred to as the Lambda-CDM model (ΛCDM), is notable for positing that around 90% of the matter in the Universe consists of non-baryonic weakly-interacting particles called cold dark matter (CDM). It also posits a cosmological constant (Lambda) associated with an unknown form of energy whose density is constant in space and time, which would explain the accelerating expansion of the Universe [27]. In addition to accounting for the expansion of the Universe, ΛCDM satisfactorily explains light element abundances, the large-scale structure of the Universe, and the cosmic microwave background (CMB). However it includes dark matter and dark energy about which very little is known but which together make up at least 95% of the contents of the Universe.

Modern observational cosmology is a powerful data-driven discipline that may be expected to shed light on the nature of dark matter and dark energy. It is already providing constraints on attempts to develop a solid theory of gravity, is informing research to detect dark matter, and is improving understanding of space-time by quantifying factors that have determined its expansion from the Big Bang to today. Next generation observations are expected to more accurately constrain energy budgets, allowing better understanding of their properties and thus providing insights into the mechanism of acceleration. Current

ideas that may explain the accelerating expansion of the Universe include a new scalar field (dark energy) or a cosmological constant that contributes to the energy budget of the Universe; a modification of the law of gravitation on the cosmic scale; or even an as yet unknown alternative to the current model.

Detailed observation of the CMB has provided a picture of the early Universe that is remarkably isotropic: the observed black body radiation is characterized by a constant temperature of $T \sim 2.7K$ in every direction, with only small fluctuations ($\partial T / T$, of the order of 1 part in 100,000). By contrast, maps of the Universe produced by large surveys, show that, although on a large scales ($\sim$ 150Mpc) the Universe is isotropic, on smaller scales, galaxies are not uniformly distributed but are organized into over-dense regions (clusters) themselves forming filamentary structures. Outside these filaments are under-dense regions known as voids.

Current models indicate that the tiny fluctuations in early Universe revealed by the CMB gave rise to these inhomogeneities by the action of gravity, which caused structure to develop by dragging matter into regions that were slightly over-dense and out of regions that were slightly under-dense.

In broad terms, the investigations presented is this thesis are concerned with the statistical properties of galaxies derived from observations and their use to measure the recent expansion history of the universe and estimate how gravity caused the growth of the observed inhomogeneities. As described in chapter 2, a requirement for performing these investigations is to be able obtain accurate values for key observables, particularly the statistical distribution of galaxies in space – dominated by the so-called correlation functions.

Given the complexity of the Universe, it is appropriate to study it "piecemeal" – at the different scales on which it is observed. The rest of this chapter reviews the properties of the Universe as it appears in the large-scale limit (where it appears smooth, isotropic and homogeneous) and goes on to briefly go over the key observational evidence for the current view of the Universe at this scale. Chapters 2 and 3 are concerned with modeling cosmic inhomogeneities and their evolution during expansion to form the large-scale structures (LSS) observed today. This chapter provides a context for the research reported in chapters 4 - 8. Chapter 4 presents the new estimators developed to measure correlation functions in Fourier space. Chapters 5 and 6 present a new approach to account for the evolution of the observed distribution of galaxies. To improve constraints on the growth of the structures (chapter 5) and understanding of the primordial inhomogeneities observed in the CMB (chapter 6), a set of optimal weightings is derived to compress the data from different epochs without loss of information. Chapter 7 presents the tests performed on the simulated (com-

pressed) data to validate the new weighting technique introduced in chapter 5, and chapter 8 presents results obtained by applying the weightings to the latest data from the extended Baryon Oscillation Spectroscopic Survey (eBOSS) [28]. Chapter 9 briefly summarizes the main findings of the thesis and suggests future research directions.

1.2 The Friedmann-Lemaître-Robertson-Walker (FLRW) metric

One fundamental question following Einstein's theory of general relativity (GR) [29], is that of finding solutions to the field equations able to describe the Universe. One approach to finding solutions is to use inputs derived from observations. However it is not possible to develop a complete theory based on observations only. Firstly because the short span of human civilization compared to the cosmological time-scale implies severe knowledge limitations. More specifically, and as discussed in the next section, we can only access a limited portion of the past light-cone implying that much of the universe is inaccessible to observations. A better approach is to develop theoretical models of the universe and its evolution based on various assumptions driven by observations. Such models can then be tested for their ability to predict or account for observed phenomena.

One of the most important assumptions is the **cosmological principle** that at every point in space any observer will observe the same physics. Observations on a sufficiently large scale – CMB measurements [30] and the distribution of galaxies [23] – indicate that this is the case: that the universe is homogeneous (no preferred origin) and isotropic (no preferred direction). The cosmological principle is the assumption that the universe is isotropic and homogeneous.

According to GR, the metric defined on space-time is related to the matter/energy content of the universe through Einstein's equations. The predicted functional form of the metric is – applying the cosmological principle – derived from the homogeneous and isotropic solution to Einstein's equations. This solution is the Friedmann-Lemaître-Robertson-Walker (FRLW) metric. In detail, the symmetry due to (spatial) homogeneity requires space-time to be foliable into space-like surfaces, say Σ_t, where time t parametrizes each surface and where a space-like surface is defined as a one in which, given generic points, p and $q \in \Sigma_t$, the metric that maps p to q is isometric.

As noted, isotropy implies there cannot be a privileged direction from which to observe the Universe: in other words, no vector or direction differs from any other. To ensure this,

isotropic observers are defined as a family of time-like curves perpendicular to the space-like surfaces.

The metric under this assumption is defined as,

$$(1.1) \qquad ds^2 = -c^2 dt + a^2(t)\left[\frac{dr^2}{1 - kr^2} + r^2\left(d\theta^2 + \sin^2\theta \, d\phi^2\right)\right]$$

where $c^2 dt^2$ corresponds to the *cosmic time*, or proper time as measured by a co-moving observer with constant spatial coordinates, r, θ, ϕ. It is sometimes useful to work with the conformal time τ, defined as, $dt^2 \equiv a^2(\tau)d\tau^2$ where $a(t)$ is the scale factor describing the expansion of the Universe, whose evolution is described by Einstein's equations. Assuming isotropy the terms in the brackets will depend only on r. The k term defines the curvature space-time which takes values $0, +1, -1$ for flat, closed, and open universes, respectively.

Comoving and physical distances   It is clear from Eq.1.1 that the metric is dynamic: the distance between 2 points in space-time will increase if the Universe is expanding and decrease if the Universe is contracting. Therefore, to probe cosmological evolution, the evolution of the scale factor with time must be investigated. To deal with the dynamic of space-time, it is often useful to work with a system of co-moving coordinates $\mathbf{x}(t)$, related to the physical coordinates, $\mathbf{r}(t)$:

$$(1.2) \qquad \mathbf{r} = a(t)\mathbf{x}.$$

1.2.1   Gravitational redshift

Gravitational redshift is a major consequence of the dynamic of the metric. For light propagation between two points ($ds^2 = 0$), a radial trajectory ($d\phi, d\theta = 0$) is selected such that $dt^2 = a^2(t)dr^2/(1 - kr^2)$; an observer is supposed to be at $r = 0$ and a light source at r_s, in co-moving coordinates. If the source emits a signal at $t = t_e$, which is received by the observer at $t = t_o$ we have,

$$(1.3) \qquad \int_{t_e}^{t_o} \frac{dt}{a(t)} = \int_0^{r_s} \frac{dr}{\sqrt{1 - kr^2}}.$$

For a second emission at $t = t_e + \delta t_e$, from Eq. 1.3 we have,

$$(1.4) \qquad \int_{t_e+\delta t_e}^{t_o+\delta t_o} \frac{dt}{a(t)} = \int_0^{r_s} \frac{dr}{\sqrt{1 - kr^2}} \rightarrow \int_{t_e+\delta t_e}^{t_o+\delta t_o} \frac{dt}{a(t)} = \int_{t_e}^{t_o} \frac{dt}{a(t)}.$$

Subtracting the quantity $\int_{t_e + \delta t_e}^{t_o} dt / a(t)$ from both sides, we have,

$$(1.5) \qquad \frac{\delta t_e}{a(t_e)} = \frac{\delta t_o}{a(t_o)}.$$

If the two emissions are interpreted as different peaks of a wave-train, the wavelength at emission λ_e is proportional to the time δt_e, whereas, according to the observer, λ_o is proportional to δt_o. This leads to

$$(1.6) \qquad \frac{\lambda_{\text{observed}}}{\lambda_{\text{emitted}}} = \frac{\delta t_o}{\delta t_e} = \frac{a(t_o)}{a(t_e)} \equiv 1 + z,$$

where z is the redshift, defined as $\equiv \lambda_0 / \lambda_e - 1$.

From Eq 1.6 it follows that if the Universe is expanding i.e. $a(t_o) > a(t_e)$ when $t_o > t_e$, the wavelength of the light is stretched by the expansion of space (redshift) or, if the Universe is contracting, the wavelength is shortened (blueshift).

1.2.2 Distance measures

Astronomical observations allow us to measure the redshift of each galaxy. However it is not obvious how to relate the measured redshifts to the distances between us and the galaxies as, in an expanding universe, there are multiple ways to define a distance; the most straightforward definition is given by the *proper distance*, defined as the length of the spatial geodesic between two points, for a fixed value of $a(t)$. However in an expanding universe this proper distance is not a measurable property as the scale factor relative to the time in which a source emits the signal is different from the scale factor relative to the time in which we make the observations. Measurable distances are instead the *luminosity distance*, which depends on the flux of the light emitted by the source and the *angular distance* which depends on an objects size and the angle it subtends on the sky.

Luminosity distance Consider a luminous object (source) at $r = r_1$, a_1, with intrinsic luminosity L. An observer at $r = 0$, a_0 detects the light with a detector of area A. The power, as seen by an observer, is

$$(1.7) \qquad P = L \left(\frac{a_1}{a_0} \right)^2 \frac{A}{4\pi a_0^2 r_1^2};$$

where $4\pi a_0^2 r_1^2$ corresponds to the physical area over which L is distributed at the time of detection. The power in equation 1.7, is suppressed by a factor of two through $(a_1 / a_0)^2$ compared to the power emitted at r_1, where the first factor is due to the fact that the energy

of the photons is red-shifted through expansion; the second is due to the stretching of time between photon arrivals.

Rescaling the flux at the observer:

$$(1.8) \qquad F = \frac{P}{A} = \frac{L}{4\pi a_0^2 r_1^2 (1+z)^2},$$

the Luminosity distance d_L can be defined as,

$$(1.9) \qquad F = \frac{L}{4\pi d_L^2}.$$

In absence of expansion, this luminosity distance corresponds to the proper distance of the source, $d_L = r_1$. In general, considering the different scalings, the relation between these two quantities is given by

$$(1.10) \qquad d_L = r_1 a_0 (1+z).$$

where,

$$(1.11) \qquad r_1 = \int_{t_e}^{t_o} \frac{c\,dt}{a(t)},$$

according to the definition of the proper distance.

From equations 1.10 and 1.11, it is clear that the distance depends strictly on the assumed cosmology.

This is relevant as it constitutes one of the main lines of evidence that the Universe is currently undergoing rapid accelerating expansion [27]. If for a given source the intrinsic luminosity is known and flux can be measured, by measuring the luminosity distance d_L, at different redshifts, $a(t)$ and $\dot{a}$ can be reconstructed. For a flat Universe and from equation 1.10 the luminosity distance can be written as

$$(1.12) \qquad d_L(z) = c(1+z) \int_0^z \frac{dz'}{H(z')},$$

where,

$$(1.13) \qquad r_1 = \int_0^z \frac{dz'}{H(z')}.$$

Note that Eq. 1.12 introduces the Hubble parameter H defined as the derivative of the scale factor with respect to time over the scale factor,

$$(1.14) \qquad H(a) = \frac{\dot{a}}{a}.$$

To test the acceleration of the expansion the scale factor at the present time (t_0) is expanded to give

$$a(t) \simeq a_0 + \dot{a}_0(t - t_0) + \frac{\ddot{a}_0}{2}(t - t_0)^2, \tag{1.15}$$

which can be reformulated as,

$$\frac{a(t)}{a_0} = 1 + H_0(t - t_0) - \frac{1}{2}q_0 H_0^2 (t - t_0)^2 + \cdots \tag{1.16}$$

where H_0 is the present value of the Hubble factor (assuming $H_0(t - t_0) \ll 1$ in the expansion) and q_0 is the so-called[1] deceleration parameter, defined as,

$$q_0 = -\frac{\ddot{a}}{a_0 H_0^2}. \tag{1.17}$$

Using Eq. 1.16 d_L, can be expressed in terms of q_0, e.g. at second order in z,

$$H_0 d_L(z) = z + \frac{1}{2}(1 - q_0)z^2 + \cdots. \tag{1.18}$$

Note that the acceleration gives a quadratic correction to the Hubble law so by measuring the luminosity distance as a function of redshift, q_0 is constrained.

Objects whose intrinsic luminosity is known (or can be standardized) are called standard candles. Important standardizable candles are type 1a supernovae. Supernova events are very bright (typically comparable in brightness to the host galaxy) and can therefore be observed at high redshifts ($z \sim 1 - 2$). Furthermore the mechanism of supernova formation (white-dwarf accretion from a companion star) is known, from which the intrinsic luminosity ($\sim M_{ch}c^2$) can be predicted using the Chandrasekhar limit ($M_{ch} \sim 1.4 M_\odot$).

Angular diameter distance   The angular diameter distance D_A is defined as the ratio of an object's *true* transverse size to its angular size in the sky (in radians). Similarly to the luminosity distance, the D_A can be measured from the observational properties of cosmological objects. Instead of using standard candles we select *standard rulers* i.e. objects whose physical size is known. If the universe is static and Euclidean, D_A is equal to the proper distance; more in general if the universe it is flat but expanding , the relation between the distances is given by

$$D_A(1 + z) = r_1 = \frac{d_L}{1 + z}. \tag{1.19}$$

An important cosmological standard ruler is given by the baryon acoustic oscillation (BAO) peak; we revise this in details in 2.3.4.

---

[1]for historical reasons

1.2.3 Einstein Equations

The metric in Eq. 1.1 comes from the homogeneous solution of Einstein equations

$$G_{ab} \equiv R_{ab} - \frac{1}{2} g_{ab} R = 8\pi T_{ab},$$

(1.20)

where $R_{a,b}$ and R are the Ricci tensor and scalar arising from the second derivatives of the metric and T_{ab} stress-energy momentum tensor respectively.

On large cosmological scales ($\gtrsim 300 \ h^{-1}$ Mpc) galaxies can be considered as point-like objects moving in a fluid, so that the stress-energy momentum tensor for all matter, describing the dynamic, has the form,

$$T_{ab} = \rho u_a u_b + P(g_{ab} + u_a u_b),$$

(1.21)

with ρ is the mass density and P the pressure. For radiation $P = \rho/3$ while for matter $P \sim 0$.

Inserting Eq. 1.21 into the Einstein equation, affords two non-trivial equations (out of the initial 10); one for the time component, the other for the space component,

$$G_{\tau\tau} = 8\pi T_{\tau\tau},$$

(1.22)

$$G_{xx} = 8\pi T_{xx}.$$

(1.23)

Assuming isotropy and geometry, all off-diagonal terms can be set to zero.[2]

This leaves two equations,

$$G_{tt} = 8\pi T_{tt} = 8\pi[\rho u_t u_t + P(\rho_{tt})] = 8\pi\rho$$

(1.24)

$$G_{ii} = 8\pi T_{ii} = 8\pi[\rho u_i u_i + P[\rho_{ii} + u_i u_i] = 8\pi a^2(t) P$$

(1.25)

Briefly, by deriving R_{ab}, (R from $R = g^{ab} R_{ab}$) and substituting the diagonal stress-energy tensor for a perfect fluid, the following is obtained,

(1.26)
$$3\frac{\dot{a}^2}{a^2} = 8\pi\rho - \frac{3}{a^2} K,$$
$$3\frac{\ddot{a}}{a} = -4\pi(\rho + 3P).$$

From Eq.1.26 it follows that once the components of the geometry of the Universe, and the equation of state, are known, the geometry of the Universe can be deduced. The first

---

[2]From isotropy: suppose we select an isotropic observer such as $u^b = (1,0,0,0)$ we would have $G_{ab} u^b = G_{a0} u^0$, where $G_{a0} u$ is a vector pointing to privileged observing direction, it follows, (for all spatial components) $G_{i0} = 0$. From isotropy + homogeneity, considering the projection on a space-like surface of $G_{ab} h^{ab} \equiv G_a^c = A\delta_a^c$. If $G_{1b} \neq 0$ for $b \neq 1$, it would be exist a a mixed time-space component vector not rotationally invariance.

part of Eq. 1.26 known as the Friedmann equation, gives the expansion rate, measured by the Hubble parameter. This equation implies that the Universe is not static. However only observations can indicate whether the Universe is expanding ($\dot{a} > 0$) or contracting($\dot{a} < 0$), since both $\dot{a} \gtrless 0$ are solutions to the first part of Eq. 1.26. The second part of Eq. 1.26 is important as it defines how the Universe accelerates; in particular the combination of $\rho + 3P$ determines the sign of $\ddot{a}$.

1.2.3.1 Single component solutions

An important set of solutions of Eq. 1.26 considers the evolution of an isotropic universe filled with a (single) perfect fluid with equation of state,

$$(1.27) \qquad P(t) = w\rho(t)$$

where w is a dimensionless number, constant with time.

Inserting Eq 1.27 in Eq. 1.26, affords solution of the kind

$$(1.28) \qquad \rho(t) \propto a^{-3(1+w)}.$$

matter only Considering a matter component, where $\rho \neq 0$, $P = 0$; from the Friedmann equation in 1.26, it follows that the density evolves as $\rho \sim a^{-3}$, which, combined with the second part of Eq. in 1.26, leads to $a(t) \sim t^{2/3}$.

radiation only For the radiation component where $P = \rho/3$ we obtain $\rho \sim a^{-4}$ with $a(t) = t^{1/2}$. Note that the additional a^{-1} factor (compared to the matter case) is due to photons redshift as the universe expands.

cosmological constant When $P = -\rho$, $w = -1$, it follows that $\rho_\Lambda = $ const, $a(t) \propto e^{\Lambda t}$.

As a consequence of the different scalings of $\rho(t)$, if the Universe contains e.g. matter, radiation and Λ, its evolution is ruled by a different component in different epochs. The transition time between the different epochs is defined by the ratio between the energy densities.

1.2.3.2 Critical density

Dividing for $\dot{a}/a$ on both sides of the Friedman equation, Eq. 1.26 affords

$$(1.29) \qquad 1 = \frac{k}{a^2 H^2} + \frac{8\pi}{3H^2}\rho.$$

The critical density of the Universe is defined as the total density of the Universe when the curvature is zero ($k = 0$, flat universe),

$$(1.30) \qquad\qquad \rho_{\text{crit}} \equiv \frac{3H^2}{8\pi}.$$

It is often convenient to use an alternative formulation of the Friedman equation – the one obtained by rescaling each energy contribution to the critical energy density: $\Omega_i = \rho_i(t)/\rho_{\text{crit}}(t)$. To obtain this, both sides of Eq. 1.26 are divided by the Hubble parameter H_0 as measured at $a = 1$; since $H_0 = \rho_{c,0} 8\pi/3$ by definition, we obtain

$$(1.31) \qquad\qquad \frac{H^2}{H_0^2} = \frac{\Omega_{r,0}}{a^4} + \frac{\Omega_{m,0}}{a^3} + \Omega_\Lambda + \frac{(1-\Omega_0)}{a^2}.$$

Note that curvature component of Eq. 1.31 is interpreted as an energy density contribution, $1 - \Omega_0$, where $\Omega_0 = \Omega_{r,0} + \Omega_{m,0} + \Omega_{\Lambda,0}$ and the scalings with a of each energy density fraction are substituted, $\rho_i = \rho_{i,0} a^{-p}$, where $p = 4, 3, 0, 2$ for radiation, matter, Λ and curvature, respectively.

Note that in Eq. 1.31 we interpret the curvature component as an energy density contribution, $1 - \Omega_0$, with $\Omega_0 = \Omega_{r,0} + \Omega_{m,0} + \Omega_{\Lambda,0}$ and we substitute the scalings with a of each energy density fraction: $\rho_i = \rho_{i,0} a^{-p}$ with $p = 4, 3, 0, 2$ for radiation, matter, Λ and curvature respectively.

1.2.4 Early-time problems with the standard model

The standard cosmological model ΛCDM satisfactorily accounts for the observed cosmic abundances of the isotopes of hydrogen, helium and lithium, and the existence and structure of the CMB. Nevertheless there are open questions related to the late-time acceleration phase; while solution of the FRLW metric indicates that also the early Universe has unexplained properties that seem to require a framework larger than that provided by the standard ΛCDM model. The main problems with the standard model are

. *The flatness problem;* Ω_k, the term that accounts for the curvature in Eq. 1.26, scales with

$$(1.32) \qquad\qquad \Omega_k \equiv \frac{8\pi G\rho}{3H^2} - 1 = \frac{k}{a^2 H^2}.$$

For standard cosmology (not including the dark component Λ that pertains only to the more recent past), the scale factor a goes as t^p (where $p = 1/2$ for radiation and

$p = 2/3$ for non relativistic matter). From equation 1.32, ot follows that $|\Omega_k|$ increases with time. Today the curvature term is considered to be < 0.2, so rescaling it to the Planck time affords $\Omega_k \lesssim 10^{-60}$. This is a highly contrived and unsatisfactory initial condition. A more satisfactory approach would be to find a physical mechanism that flattened space in the early Universe.

. *Horizon problem;* In special relativity, space is flat and static so that every event at the infinite is connected to the origin by a light-trajectory. In GR, since the Universe is expanding and is finite in time, not all regions are in "casual" contact with each other. This becomes clear when computing the particle horizon (or the co-moving horizon) which is the maximum distance covered by photons. In standard cosmology, where $a(t) \sim t^p$ with $p < 1$, for a light-like radial trajectory $dr = a(t)dt$, the horizon at time t with initial time $t_i = 0$, is given by

$$(1.33) \qquad\qquad d_H(t) = \frac{p}{1-p} H^{-1};$$

thus for standard components (matter and radiation) the horizon is of finite size. However the CMB shows that the temperature of the Universe is markedly uniform (on the large scale), implying the need for a horizon of infinite size that would enable the entire Universe to have initially been in thermal equilibrium.

A possible solution to complete the puzzle is obtained by inverting the behavior of the co-moving Hubble radius $(aH)^{-1}$ - which represents the fraction of the universe in causal contact. This requires inserting an additional component in the Hubble-Friedman equation such that the early universe undergoes positive acceleration (inflation),

$$(1.34) \qquad\qquad\qquad\qquad \ddot{a} > 0$$

Thus we have the hypothesis that the early universe underwent an inflationary phase. One *cause* of this inflation could be a cosmological constant Λ_i as discussed for the late-time acceleration. However, as shown in section 1.2.3.1 this would imply exponential inflation which would dominate all power expansions, so that there would be no subsequent radiation or matter epochs – predictions not borne out by observations, e.g. [30]. A better idea would be to introduce a gravity-coupled scalar field that decays after a finite time. Section 1.2.5 reviews one of the main theories of such a field.

1.2.5 Inflation

The inflationary model was first introduced ad hoc to deal with problems related to the solution of an FRLW Universe. However it later became apparent that inflation could also overcome difficulties in accounting for the birth of the primordial fluctuations supposed to give rise to the observed fluctuations in the CMB and the distribution of galaxies. This section reviews a basic inflationary model and its implications. Ref [31] provides a more complete treatment.

Inflation scalar field dynamics are given by the action,

$$(1.35) \qquad S = \int d^4 x \sqrt{-g} \left[-\frac{1}{2} \partial_a \varphi \partial^a \varphi - V(\varphi) \right]$$

where $V(\varphi)$ is a generic potential for a scalar field φ. By variation of the action the energy-momentum components are derived,

$$(1.36) \qquad T_{ab} = \frac{-2}{\sqrt{-g}} \frac{\delta S}{\delta g^{ab}} = \partial_a \varphi_b \partial_b \varphi - g_{ab} \left(\frac{1}{2} \partial_c \varphi \partial^c \varphi + V(\varphi) \right),$$

where only the diagonal components are $\neq 0$, as required for isotropy and homogeneity are

$$(1.37) \qquad \begin{aligned} \rho &= \frac{1}{2} \dot{\varphi}^2 + V(\varphi) \\ a^2 \mathbf{P} &= a^2 \left(\frac{1}{2} \dot{\varphi}^2 - V(\varphi) \right). \end{aligned}$$

Combining ρ and P from Eq. 1.37 affords,

$$(1.38) \qquad (\rho + 3P) = 2\dot{\varphi}^2 - 2V.$$

The equation of motion for φ is derived by requiring the minimum action variation ($\delta S = 0$),

$$(1.39) \qquad \nabla_a \partial^a \varphi = V',$$

where $V' = \frac{\partial V}{\partial \varphi}$ and ∇_a is the covariant derivative. Thus,

$$(1.40) \qquad \partial_a \partial^a \varphi + \Gamma^a_{ab} \partial^b \varphi = V'.$$

Next, φ is set so that it depends only on time (homogeneity),

$$(1.41) \qquad -\ddot{\varphi} - 3H\dot{\varphi} - V' = 0$$

and combined with Eq. 1.26 to affords,

$$(1.42) \qquad H^2 = \frac{8}{3}\pi \left(\frac{1}{2}\dot{\varphi}^2 + V \right).$$

Combining Eq. 1.26 and 1.31 with the expression of ρ and P in Eq. 1.37, we arrive at

$$(1.43) \qquad\qquad \dot{H} = -4\pi\dot{\varphi}^2.$$

By considering (1.42) and (1.43) it is possible to explore the dynamic of the inflaton field. From equation (1.38) we can obtain

$$(1.44) \qquad\qquad \rho + 3P = 2(\dot{\varphi}^2 - V).$$

We can then ensure that $\rho + 3P < 0$ (i.e. $\ddot{a}$ to be positive), by requiring that the kinetic energy of the particle is negligible respect to this potential (slow-roll regime),

$$(1.45) \qquad\qquad \frac{1}{2}\dot{\varphi}^2 \ll V.$$

Note that from equation 1.45 it is possible to determine different conditions on the potential required for the inflation in the slow roll regime without introducing an explicit form for it.

Inflation implies that the particle horizon undergoes explosive growth in the early Universe, to therefore resolve the problem arising in standard FLRW cosmology. Furthermore inflation provides a natural mechanism (quantum fluctuations) for generating primordial perturbations,

$$\varphi = \varphi_0 + \delta\varphi.$$

In fact, as reviewed in Chapter 2, the current model for the evolution of the matter density field assumes that field to be random. For the simplest inflation model, and using the operators of annihilation and construction, the quantum fluctuations (QF) of the inflation field can be decomposed in Fourier space as,

$$(1.46) \qquad\qquad \delta\varphi = \int d^3\mathbf{k}[a_{\mathbf{k}}\psi_k(t)\exp(i\mathbf{k}\,\mathbf{x}) + a_{\mathbf{k}}^+\psi_k^*(t)\exp(-i\,k\,x)].$$

The mode functions ψ_k in Eq. 1.46 come from the Klein Gordon Equation applied to an expanding Universe: if $\Omega_m = 1$ and taking a and H from the Friedmann Equations, we obtain,

$$(1.47) \qquad\qquad \psi_k(t) = \frac{H}{(2k)^{1/2}k}\left(i + \frac{k}{aH}\right)\exp\left[\frac{ik}{aH}\right].$$

Note that as $k/(aH) \ll 1$, the dominant mode in Eq. 1.47 reads

$$(1.48) \qquad\qquad \varphi_k \sim \frac{iH}{\sqrt{2}k^{3/2}}(a_k + a_{-k}^+),$$

$$(1.49) \qquad\qquad \delta\varphi = \int d^3\mathbf{k}\varphi_k e^{i\mathbf{k}\mathbf{x}};$$

so that now, any combination of φ commutes with the others and φ is transformed in a classic stochastic field.

Thus the idea is that, at the end of the inflationary phase, within the Hubble radius the gravitational potential maintains the imprint of the energy fluctuations due to the QFs. The QFs are stretched out over cosmological scales by the accelerated expansion and form the sources of the initial density perturbations. According to this scenario, the stochasticity in the cosmic field can be described in terms of φ_k.

1.2.6 Late-time acceleration of the Universe

As noted (section 1.2.2) type 1A supernovae are useful standard candles and observations on the relation of supernova-distance luminosity to redshift [27] indicate that the Universe is undergoing (late) accelerated expansion. However in section 1.2.3.1 it was shown that the standard components matter ($w = 0$) and radiation ($w = 1/3$), are characterized by decelerated expansion $\ddot{a} \sim (-) t^{-3/2}$ and $\ddot{a} \sim (-) t^{-4/3}$ respectively. For this reason a third component, Λ, for which $\ddot{a} > 0$ has been added to the Friedmann equation to account for "late" inflation implied by these data.

One of the major challenges of theoretical and observational cosmology is to understand the nature of Λ. Is it a cosmological constant? Is it an additional scalar field? Or does it imply that the law of gravitation requires modification? [32][33] [34] [35]. Various probes [30] indicate that the acceleration phase started only about 5 billion years ago, which complicates the interpretation of observational data. In the light of this, current observational astronomy is aiming to determine cosmological variables with accuracy at 1% level in the hope that this may allow us to decide which of the possible theories best fits the data. As noted in section 1.2.2, improved determinations of the distance-redshift relation, together with quantification of the factors determining the evolution of space-time are required in order to test different cosmological models. Various methods are available to obtain improved data including enhanced CMB measurements combined with other data at lower redshifts to provide constraints on cosmological parameters. Chapters 2 and 3 examine how large-scale structure analysis can be used to probe Λ and gravity. In the rest of this section we present individually other important probes based on observational data that support the ΛCDM Universe.

CMB The CMB has an almost perfect black-body spectrum at the temperature of $T = 2.7255 \pm 0.00057$ [36], however, it presents tiny anisotropies of around 1 part in 100,000, at

different angles in the sky. According to the inflationary paradigm, as described in 1.2.5, those thermal variations are generated from scalar-field quantum fluctuations during inflation.

As we will review in the next chapter, we are not interested in the particular pattern of hotter and colder regions observed but rather on the statistical properties of the anisotropies. Briefly: if the statistical properties of the tempererature fluctuations present at the time of decoupling, and the energy content of the universe ($\Omega_r, \Omega_m, \Omega_\Lambda H_0$, etc.), is specified, this will enable prediction of the full range of CMB anisotropies and hence testing against observation.

As noted, variations in CMB are small, therefore high sensitivity and good control of systematic errors (such as those arising from signal contamination) are essential. The temperature fluctuations of the CMB have been measured by different surveys, including measurements by COBE, [37], SPT [38], ACT [39], WMAP [40]. Improved measurements were obtained by Planck (see [3] and references within) at small angular resolution which give the tightest constraints on the cosmological parameters: $\Omega_b h^2 = 0.02225 \pm 0.00016$, $\Omega_c h^2 = 0.1198 \pm 0.00015$. Assuming ΛCDM, the inferred Hubble parameter and the power spectrum variance are constrained as $H_0 = (67.4 \pm 0.5)$, $\sigma_8 = 0.811 \pm 0.006$. Further, constraints on the scalar index of the primordial power spectrum $n_s = 0.9645 \pm 0.0049$ and on the amount of non-Gaussianity (details provided in chapters 3 and 6) improve our understanding about inflation putting a severe limit on the class of models allowed.

Figure 1.2.6 shows the Planck temperature power spectrum $\mathscr{D}_\ell^{TT}$ (red dots), squared into spherical harmonics ($Y_{\ell,m}(\theta, \phi)$), from [3]; error bars (at 1σ confidence level) include cosmic variance and foreground systematic errors. The best-fit power spectrum (light blue) is also plotted, showing no evidence for deviations from the ΛCDM model.

Supernovae Type IA   In 1.2.2 we discussed how Supernovae Type Ia can be used as standard candles to measure the distance luminosity without making assumptions on the cosmological model.Using the properties of the Type 1A supernovae, the accelerated expansion was measured for the first time by [27] and [4].

Figure 1.2 shows the first significant detection of cosmic acceleration, obtained using the Supernovae type Ia sample from the Supernova Cosmology project and the High-z Supernova Search Team [4] [27]. In particular bottom panel shows the difference between the distance modulus measured (in magnitude units) using the SNe type Ia and the predictions of models $\Omega_\Lambda = 0.7\, \Omega_m = 0.3$ (continuous line), $\Omega_\Lambda = 0.0\, \Omega_m = 0.3$ (dotted line) and $\Omega_\Lambda = 0.0\, \Omega_m = 1.0$ (dashed line). The proof of the decelerating Universe is given by supernovae at $z \sim 0.5$ which are about 0.25 magnitude fainter than they would be in the scenario of $\Omega_\Lambda = 0.0\, \Omega_m = 0.3$
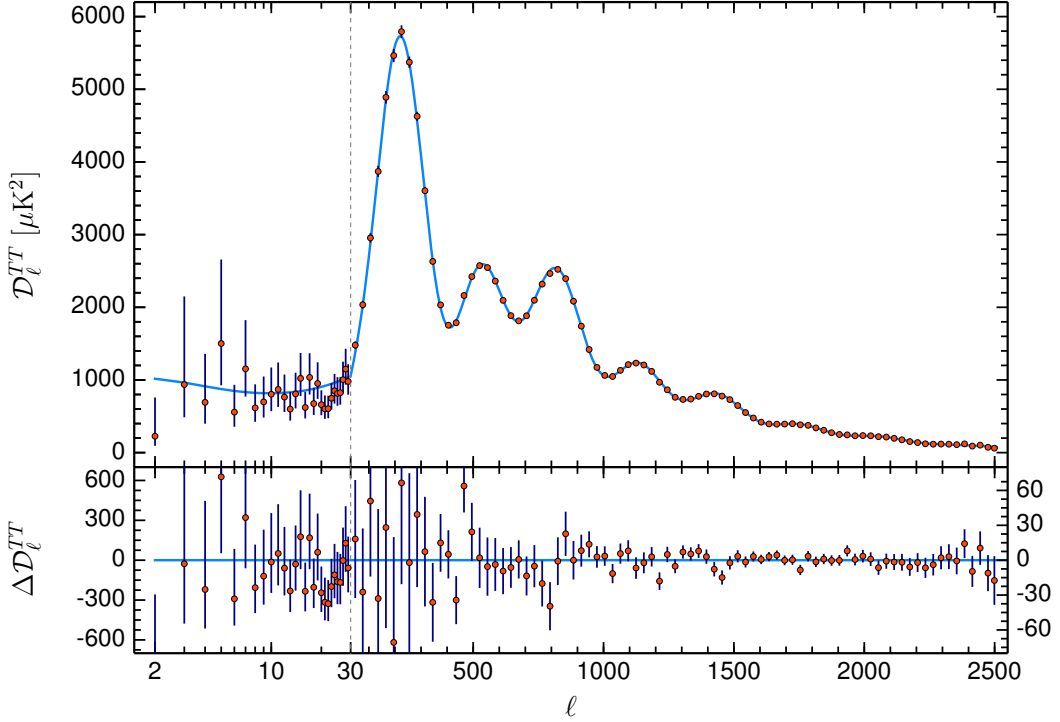
Figure 1.1: The Planck CMB temperature power spectrum (Figure from [3])

(decelerating universe).

Nowadays supernovae Type 1A provide independent constraints of Ω_m and H_0. $\Omega_m = 0.295 \pm 0.024$ [41] is consistent with the Planck measurements presented above, while the Hubble parameter, $H_0 = 73.8 \pm 2.4 km s^{-1} Mpc^{-1}$ [42] is in contrast with the inferred $H(z)$ from Planck by $\sim 2.5\sigma$. Planned future investigations include more extensive supernova surveys which will help to understand whether this discrepancy is caused by systematic errors not accounted for in the different analyses or it may invoke new physics and extensions for the standard concordance model.

In particular, the 10-years-program using the Large Synoptic Survey Telescope (LSST) [43] is expected to discover three to four million of supernovae, of which 50,000 are of type Ia, pushing photometry to allow observations at redshifts beyond $z \simeq 1$. The SNe Ia at $z \sim 0.45$, up to $z \sim 0.8$. are expected to constrain the dark energy equation of state at 5% accuracy or better [43].

Weak gravitational lensing Distant galaxies observed in the sky appear distorted as their emitted light can be deflected by the foreground structures while propagating towards
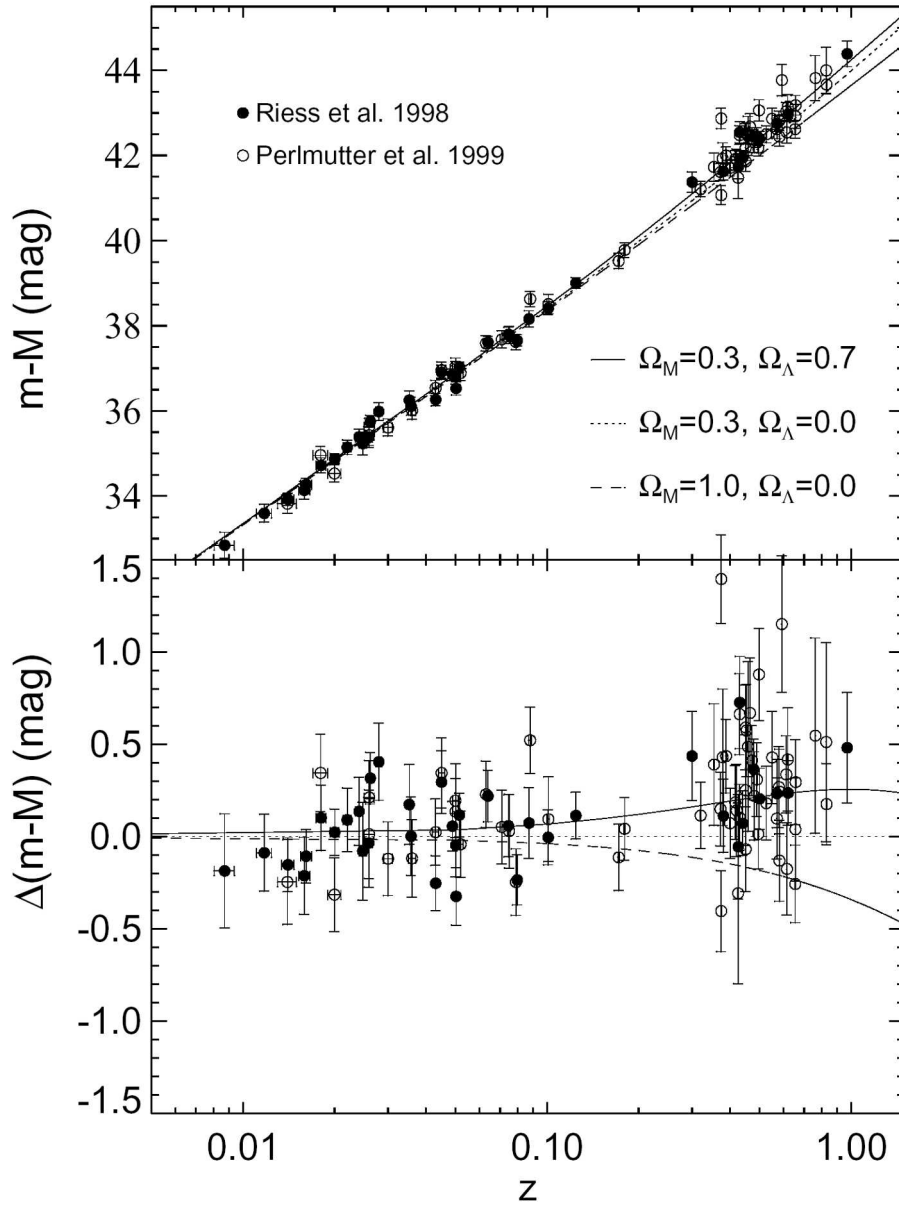
Figure 1.2: Distance modulus measurements using the Supernovae type Ia sample from the Supernova Cosmology project and the High-z Supernova Search Team (from [4])
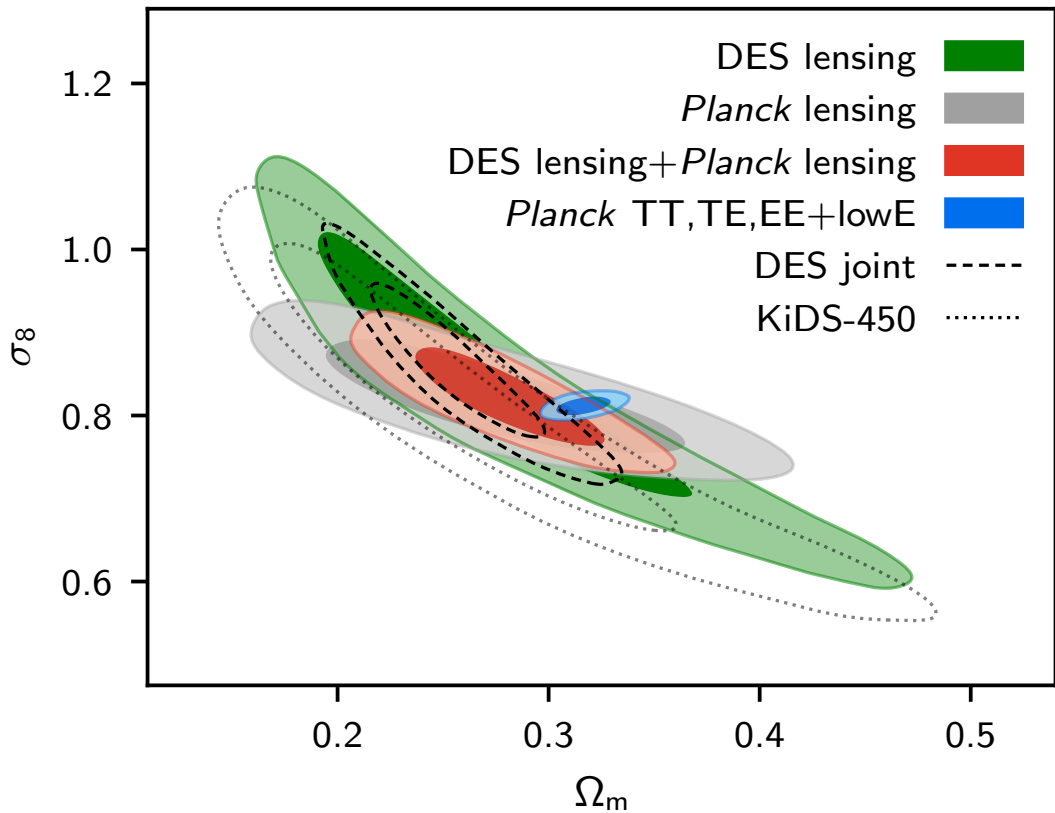
Figure 1.3: A comparison between WL constraints on Ω_m and σ_8 from [5] [6] and the Planck experiment results [3]. (Figure taken from [3])

the observer. This phenomenon is referred to as *strong* gravitational lensing if the light originated by distant galaxies, is deflected by massive structures (e.g. clusters) and the distortion can results in multiple images of the same source. However in most cases, where no massive object is involved, we have a distortion in the size and shape of the galaxies of order of 1%, depending on the distribution of matter crossed by the emitted light. This phenomenon is referred to as *weak* lensing (WL).

A number of applications of weak gravitational lensing have proven its potential to improve our understanding of the properties of dark energy and dark matter on cosmological scales [44] [45] [46]. In fact, lensing measurements are sensitive to the geometry similarly to type Ia supernovae but also to the growth of the large scale structures, providing a direct measurement of the matter field distribution. Important results have been achieved from the CFHTLens survey [47], the ongoing Kilo-Degree Survey and Dark Energy Survey (DES) [48], [49],

Figure 1.3 shows a comparison between KiDS and DES WL data [5] [6] and Planck experiment (temperature power spectra and CMB lensing) [3], in constraining the matter-density Ω_m and the fluctuation amplitude σ_8. It is out of the scope of this work to review these experiments, however it is interesting to see e.g. from Figure 1.3 that there is some discrepancy between KiDS results and those obtained from Planck. Similarly, results from the CFHTLens experiment [47], $\sigma_8(\Omega_m/0.27)^{\alpha} = 0.79 \pm 0.03$, with $\alpha = 0.61 \pm 0.02$ seem to also prefer lower values of Ω_m or σ_8.

Future experiments, e.g. [50], [43] will involve large area imaging surveys to improve measurements of weak gravitational lensing by reducing systematic errors such as intrinsic alignment of galaxies. This will allow to investigate whether or not there is an actual tension in the concordance model.

Combined probes   As we have reviewed in this section, different probes such as lensing or CMB data are able to provide constraints only on combinations of cosmological parameters, rather than on individual values. On the other hand, if different probes are combined, it is possible to break part of this degeneracy and obtain a consensus model. The current concordance cosmological model is given by the combination between CMB, Supernovae data and BAO measurements and it is consistent with a 6-parameters flat ΛCDM universe.

Figure 1.4 shows the constraints on the dark energy equation of state, as obtained from CMB meaurements [3], weak lensing data from DES [8], redshift space distortions and BAO from BOSS [7] and supernovae from [9]. The dark-energy equation of state parameter obtained is consistent with a cosmological constant: $w = -1.03 \pm 0.03$.
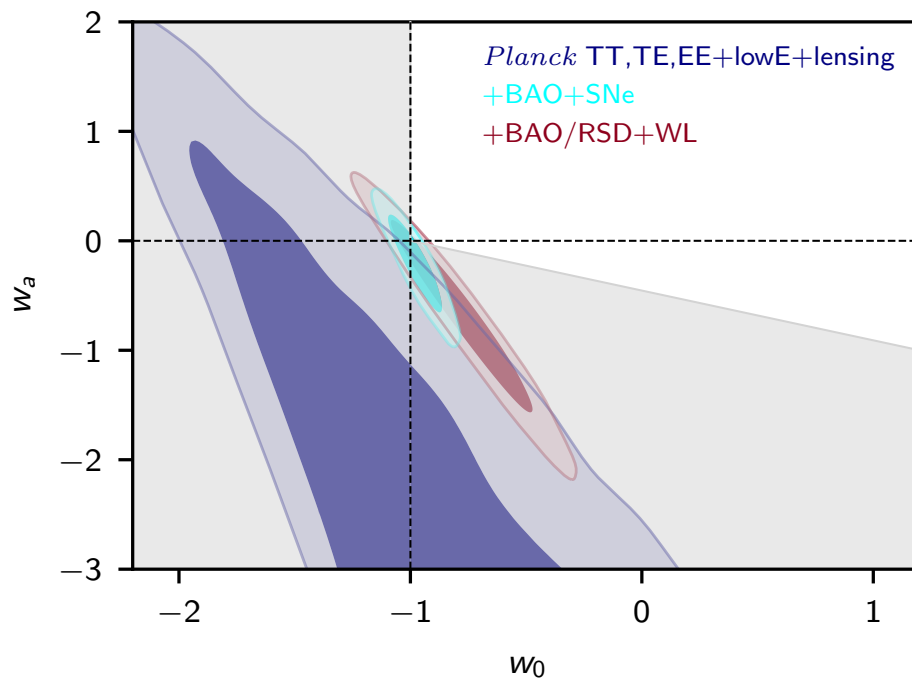
Figure 1.4: Constraints on the time-varying dark energy equation of state using a combination of CMB [3], BAO and RSD [7], WL [8] and Type 1A supernovae data [9]. (Figure from [3])

THE LARGE SCALE STRUCTURE OF THE UNIVERSE

2.1   A statistical approach

The current explanation for the large-scale distribution of matter in the universe is that this distribution arose from small fluctuations in the primordial universe which were amplified by gravitational attraction during subsequent evolution. Tests of theories relating to these primordial fluctuations cannot be deterministic but must be statistical in nature. This is because, firstly, we cannot directly observe these initial conditions. And secondly because the time-scale of cosmological evolution (time since Big Bang 14 billion years) is much longer than the observation period available to humans, so it is impossible to follow the evolution of individual systems. However cosmologists do observe (through the past light cone) different systems at different epochs, and from such observations theories of structure evolution are developed which can be tested statistically. For the large-scale structures of the Universe, the set of systems corresponds to perturbations in density and velocity. We cannot predict, for example, whether a particular point in the Universe is over-dense or under-dense, but we can estimate the probability that a point will be over-dense or under-dense, and the probability that a point x_1 will be over-dense, given that point x_2 is under-dense.

2.1.1 Random field

The statistical approach usually adopted is to model the observable Universe as a particular stochastic state arising from a statistical ensemble of possibilities. The inflationary paradigm predicts that the initial fluctuations will be adiabatic and Gaussian. Therefore a Gaussian random field is assumed, and its statistical properties investigated. The field can be any field of interest, for example cosmic density perturbations $\delta(x)$, the velocity divergence field, or a potential.

To define a random field we start with the concept of a random variable, say x, to which is associated a probability distribution function (PDF), $\mathscr{P}(x)$. By definition, the statistical properties of x, e.g. the average $\langle x \rangle$, the second moment $\langle x_2 \rangle$, and the variance σ_x are determined by P. If all the moments are known, it is, in principle, possible to reconstruct the PDF. A random field is the natural generalization of the random variable x: if $\phi(x)$ is a random field, it follows that there is a random variable x at each point in space. Each quantity that fluctuates is defined in terms of its mean and its fluctuation about the mean:

$$(2.1) \qquad \phi(\mathbf{x}, t) = \langle \phi(\mathbf{x}, t) \rangle + \delta\phi(\mathbf{x}, t) \equiv \overline{\phi}(t)\delta + \phi(\mathbf{x}, t),$$

where it is assumed that the mean depends on time only (for reasons discussed in section 2.1.2). It is convenient to study the statistical properties of the dimensionless fluctuation amplitude, defined by

$$(2.2) \qquad \delta_\phi = \frac{\phi - \overline{\phi}}{\overline{\phi}},$$

where the mean is zero as shown,

$$\langle \delta_\phi \rangle = \left\langle \frac{\phi - \overline{\phi}}{\overline{\phi}} \right\rangle = \frac{1}{\phi}\left(\overline{\phi} - \overline{\phi} \right) = 0.$$

2.1.2 Ergodic hypothesis

Since observations are limited to a single universe, there is no access to different realizations of the statistical ensemble which can be averaged to obtain expected values. To get round this cosmic random fields are assumed to be ergodic, i.e. that the averages of the ensemble are assumed equal to the spatial averages:

$$(2.3) \qquad \int \mathrm{d}\phi \, \phi \mathscr{P}(\phi) = \langle \phi(\mathbf{x}, t) \rangle = \frac{1}{V} \int_V \mathrm{d}^3\mathbf{x} \, \phi(\mathbf{x}, t) \equiv \phi(t)$$

Note that by definition, $\overline{\phi}$ is a function of time t only.

2.1.3 Correlation functions

A random field is described by an infinite set of random variables, correlation functions are defined as the averages of different random variables, or as the product of the field at different points. For example, a two-point correlation function is given by:

$$(2.4) \qquad \left\langle \delta_\phi(\mathbf{x}_1)\delta_\phi(\mathbf{x}_2) \right\rangle;$$

and if $\mathbf{x}_1 \equiv \mathbf{x}_2$, Eq. 2.4 reduces to the first moment.

Correlation functions are expected to vanish if the fluctuations at one point are independent from those at another (Poisson fluctuations). For physical reasons, they are also expected to vanish as some inverse of the distance between points, as there is no influence of one point on another at infinite distances. These properties are further discussed in section 2.1.6.

2.1.4 Homogeneity, isotropy and cosmic fields

In line with the cosmological theories discussed in chapter 1 and observations, the cosmic field is assumed to be statistically homogeneous and isotropic. These assumptions are applied to the field correlation functions which are thus expected to be invariant under translation (statistical homogeneity) and rotation (statistical isotropy).

Note that although the field varies from one point to another because it is fluctuating, the correlation functions and all the other averaged quantities are assumed to be invariant. This condition can be reformulated as: the physics that created the fluctuations and allowed them to evolve cannot distinguish one point from another (statistical homogeneity) or a particular direction (statistical isotropy).

2.1.5 Fourier Space

Fourier space is the natural choice for working with fluctuations. In part because at large scales, when fluctuations are small, the equation of motion describing the cosmological fields can be linearized, and also because as we show in this section, each Fourier mode evolves independently of the others. The Fourier transform is defined as

$$(2.5) \qquad A(\mathbf{k}) = \frac{1}{(2\pi)^3} \int d^3\mathbf{x} \exp(-i\mathbf{k}\cdot\mathbf{x})\, A(\mathbf{x}).$$

A generic random field $\phi(\mathbf{x})$ can be decomposed in Fourier space into

$$\phi(\mathbf{x}) = \int d^3\mathbf{k} \exp(i\mathbf{k}\cdot\mathbf{x})\phi(\mathbf{k})$$

where $\phi(\mathbf{k})$ are the Fourier coefficients and each $\exp(i\mathbf{k}\cdot\mathbf{x})$ corresponds to a different Fourier mode (wave). The Fourier coefficients $\phi(\mathbf{k})$ are also interpreted as a random field: they represent a collection of infinite random variables (2 for each k, since ϕ is complex).

Note that if the average $\langle\delta\delta\rangle$ vanishes in configuration space, this is also the case in Fourier space,

$$\langle\delta_\phi(\mathbf{k})\rangle = \left\langle \frac{1}{(2\pi)^3}\int \mathrm{d}^3\mathbf{x}\exp(-i\mathbf{k}\cdot\mathbf{x})\delta_\phi(\mathbf{x})\right\rangle = \frac{1}{(2\pi)^3}\int \mathrm{d}^3\mathbf{x}\exp(-i\mathbf{k}\cdot\mathbf{x})\langle\delta_\phi(\mathbf{x})\rangle = 0$$

as $\langle\delta_\phi(\mathbf{x})\rangle = 0$, for construction.

Note that we took $\int \mathrm{d}^3\mathbf{x}\exp(-i\mathbf{k}\cdot\mathbf{x})$ outside of the average over the PDF as the Fourier modes are not random variables. Consider the 2-point correlation function:

$$(2.6) \qquad \langle\delta_\phi(\mathbf{k}_1)\delta_\phi(\mathbf{k}_2)\rangle = \frac{1}{(2\pi)^6}\int \mathrm{d}^3\mathbf{x}_1\,\mathrm{d}^3\mathbf{x}_2\,\exp(-i\mathbf{k}_1\cdot\mathbf{x}_1)\exp(i\mathbf{k}_2\cdot\mathbf{x}_2)\langle\delta_\phi(\mathbf{x}_1)\delta_\phi(\mathbf{x}_2)\rangle,$$

introducing $\mathbf{x}_{12} = \mathbf{x}_1 + \mathbf{x}_2$ and $r = |\mathbf{x}_1 + \mathbf{x}_2|$, recalling the expression in Fourier space for delta Dirac δ_D,

$$(2\pi)^3\delta_D = \int \mathrm{d}^3\mathbf{k}\exp(-i\mathbf{k}\mathbf{x}),$$

and the real space two-point correlation function ξ, Eq. 2.6 can be transformed into

$$(2.7) \qquad \langle\delta_\phi(\mathbf{k}_1)\delta_\phi(\mathbf{k}_2)\rangle = \delta_D(\mathbf{k}_1+\mathbf{k}_2)\frac{1}{(2\pi)^3}\int \mathrm{d}^3 r\exp(-i\mathbf{k}\mathbf{r})\xi_\phi(r).$$

Unlike in real space, the left side of Eq. 2.7 does not vanish only for modes $\mathbf{k} = -\mathbf{k}$; therefore the Fourier modes are uncorrelated.

The same conclusion is reached if translation invariance is assumed directly. For the translation $\mathbf{r}\to\mathbf{r}+\mathbf{s}$, it follows that:

$$(2.8) \qquad \delta_\phi(\mathbf{k}) \to \frac{1}{(2\pi)^3}\int \mathrm{d}^3\mathbf{r}\exp(-i\mathbf{k}\cdot\mathbf{r}) = \exp(i\mathbf{k}\cdot\mathbf{s})\delta_\phi(\mathbf{k}),$$

Including the transformation of Eq. 2.8 in the definition of the 2-point correlation function affords the expression:

$$(2.9) \qquad \langle\delta_\phi(\mathbf{k}_1)\delta_\phi(\mathbf{k}_2)\rangle = \exp(i\mathbf{s}\cdot(\mathbf{k}_1+\mathbf{k}_2)\langle\delta_\phi(\mathbf{k}_1)\delta_\phi(\mathbf{k}_2)\rangle,$$

which is invariant under translation only if $\mathbf{k}_1 + \mathbf{k}_2 = 0$, hence the $\delta_D(\mathbf{k}_1+\mathbf{k}_2)$ term.

Considering the left side of Eq. 2.7, the power spectrum of the field P_ϕ, can be defined as the Fourier transform of the correlation function:

$$(2.10) \qquad P_\phi \equiv \frac{1}{(2\pi)^3}\int \mathrm{d}^3\mathbf{r}\exp(-i\mathbf{k}\cdot\mathbf{r})\xi_\phi(r).$$

Inserting the definition of Eq. 2.10 into Eq. 2.7, affords

$$(2.11) \qquad \left\langle \delta_\phi(\mathbf{k}_1)\delta_\phi(\mathbf{k}_2) \right\rangle = \delta_D(\mathbf{k}_1 + \mathbf{k}_2)P_\phi(\mathbf{k}_1).$$

The three-point correlation function in Fourier space, called the Bispectrum can be defined analogously:

$$(2.12) \qquad \left\langle \delta_\phi(\mathbf{k}_1)\delta_\phi(\mathbf{k}_2)\delta_\phi(\mathbf{k}_3) \right\rangle = \delta_D(\mathbf{k}_1 + \mathbf{k}_2 + \mathbf{k}_3)B(k_1, k_2, k_3).$$

Once again the term δ_D is required for translation invariance. Note that B depends only on 3 variables for isotropy.

2.1.6 Connected correlation function

It is useful to work with connected correlation functions when dealing with theories of the large-scale structure of the Universe. The connected part of the correlation function expresses the physical correlation between different points in space. To explore this, a field with non-zero mean, $\langle \phi \rangle = \overline{\phi}(t)$, is selected and, for example, the two-point statistic of the field is derived:

$$(2.13) \qquad \langle \phi(x_1)\phi(x_2) \rangle = \langle \phi(x_1) \rangle \langle \phi(x_2) \rangle + \langle \phi(x_1)\phi(x_2) \rangle_c.$$

In Eq. 2.13 the term corresponding to the connected part of the correlation function is denoted with a c subscript. This is non-zero when $\mathscr{P}(x_1, x_2) \neq \mathscr{P}(x_1)\mathscr{P}(x_2)$. If the point x_2 is moved to a great distance from $\phi(x_1)$, the term $\langle \phi(x_1)\phi(x_2) \rangle_c$ typically goes to zero since points at a great distance are not expected to influence each other. However the full two-point correlation function does not vanish because $\langle \phi(x_1)\phi(x_2) \rangle \sim \overline{\phi}^2(t)$, even if there is no true correlation. To deal with this, it is common, with the two-point correlation function, to work with δ_ϕ instead of ϕ, since the mean of δ_ϕ is zero. However even when working with δ_ϕ, higher order statistics still contain a non-connected contribution to the correlation function.

2.1.7 Gaussian random field

With regard to the inflationary scenario discussed in section 1.2.5, it is common to assume that the initial energy fluctuation is that of a Gaussian random field [51]; If the field is Gaussian, then according to the Wick theorem, any ensemble average of products of variables can be written in terms of the product of the ensemble average of pairs; so that all the connected correlation functions of order greater than two vanish. In such a situation a

Gaussian field is fully characterized by its power spectrum and its mean (typically the interest is in fields for which the mean is zero). Considering the $\delta(r)$ field at a single point, the Gaussian PDF is

$$(2.14) \qquad \mathscr{P}_G(\delta) = \frac{1}{\sqrt{2\pi\sigma^2}} \exp\left(-\frac{1}{2}\frac{\delta^2}{\sigma_2}\right)$$

where $\sigma^2 = \langle\delta^2(x)\rangle$ is the only non-zero moment that characterizes the Gaussian. The equation analogous to Eq. 2.14 for N-point is a multivariate Gaussian,

$$(2.15) \qquad \mathscr{P}_G(\delta_1\cdots\delta_N) = \frac{1}{\sqrt{2\pi\det C}} \exp\left(-\frac{1}{2}\delta_i C_{ij}^{-1} \delta_j\right).$$

where $C_{ij} \equiv \langle\delta_i\delta_j\rangle$.

The equivalent in Fourier space, where the different modes are not correlated, corresponds to the product of independent Gaussian distributions,

$$(2.16) \qquad \mathscr{P}_G\left[\delta(\mathbf{k})\right] = \Pi_{\mathbf{k}} \frac{1}{\sqrt{2\pi P(k)}} \exp\left(-\frac{|\delta(\mathbf{k})|^2}{2P(k)}\right).$$

2.2 Linear evolution of the fluctuations

In section 1.2.5 we discussed how inflation generates a spectrum of curvature perturbations that is nearly scale invariant. During inflation, modes become larger than the Hubble radius, and GR is required to describe the evolution. Without entering into detail, calculations indicate that curvature perturbations are conserved for $\frac{k}{aH} < 1$, until they re-enter the Hubble radius, as occurs during the radiation and matter era, as discussed in detail elsewhere [32]. After perturbations re-enter the Hubble radius (after primordial inflation has finished) their evolution can be accounted for by a Newtonian analysis. The contents of the Universe we will consider are

- Baryons ρ_B. These are non-relativistic particles, so their equation of state, $P_B = \frac{\rho_B T_B}{m_B} \ll \rho_B$ is given by the collisional pressure. Thus, for the background (homogeneous component) it can be assumed that $P_B \approx 0$. To describe their perturbations, sound speed, defined $c_s = \left(\delta P_B/\delta\rho_B\right)^{1/2}$, is required.

- Dark matter ρ_M. Dark matter is assumed to be cold (non-relativistic); it has negligible pressure $P_M \propto \delta P_m \sim 0$.

- Radiation. The equation of state for photons $P_R = 1/3\rho_M$.

- Cosmological constant ρ_Λ. In ΛCDM, ρ_Λ is introduced as an additional homogeneous source term, whose equation of state is $P_\Lambda = -\rho_\Lambda$.

2.2.1   Comoving and physical velocities

The cosmological dynamics has to deal with the characteristic feature of the Universe expansion. Therefore it is convenient to work with comoving units, and to consider primarily peculiar velocities - i.e. deviations from the Hubble flow. Comoving distances were introduced in section 1.2. Physical velocities, $\mathbf{V}(t)$, are related to comoving (peculiar) velocities as follows:

$$(2.17) \qquad \mathbf{V}(t) = \frac{dr}{dt} = \dot{a}\mathbf{x}(t) + a\frac{d\mathbf{x}(t)}{dt} = H\mathbf{r}(t) + \mathbf{v}(t)$$

where $H\mathbf{r}(t)$ is the contribution to the physical velocity given by the Hubble expansion, and $\mathbf{v}$ is the comoving (peculiar) velocity of every object.

The conformal expansion rate (or comoving Hubble radius) is given by $\mathcal{H} \equiv aH = \dot{a}$, so Eq. 2.17 can be expressed as:

$$\mathbf{V}(t) = \mathcal{H}\mathbf{x}(t) + \mathbf{v}(t).$$

By applying the transformation of Eq. 1.2, the relation between the partial derivatives in $(\mathbf{r}, t)$ and the partial derivatives in $(\mathbf{x}, \tau)$ is derived,

$$(2.18) \qquad \frac{\partial}{\partial t} = \frac{1}{a}\frac{\partial}{\partial \tau} - \frac{\mathcal{H}}{a}\mathbf{x} \cdot \nabla,$$

$$(2.19) \qquad \frac{\partial}{\partial r} = \frac{1}{a}\nabla.$$

2.2.2   Newtonian equations of motion

Newtonian dynamics are captured by the equations of continuity, of Euler (that respectively assume conservation of mass and momentum), and the Poisson equation. In physical coordinates these are, respectively:

$$(2.20) \qquad \frac{\partial \rho}{\partial t} + \nabla_r \cdot (\rho \mathbf{V}) = 0,$$

$$(2.21) \qquad \frac{\partial \mathbf{V}}{\partial t} + (\mathbf{V} \cdot \nabla_r)\mathbf{V} = -\frac{\nabla P}{\rho} - \nabla_r \Phi_{\text{tot}},$$

$$(2.22) \qquad \nabla^2 \Phi_{\text{tot}} = 4\pi G\rho,$$

where Φ_{tot} is the total gravitational potential (background + fluctuation). Equations 2.20,2.21,2.22, combined together, afford the usual acceleration equations in the absence of pressure (GR is required in order to include pressure);

To study the evolution of perturbations, these equations of motion are separated into background and fluctuation components:

(2.23)
$$\rho(\mathbf{x}, t) = \overline{\rho}(t) + \delta\rho(\mathbf{x}, t) = \overline{\rho}(t)\left[1 + \delta(\mathbf{x}t)\right]$$

(2.24)
$$P(\mathbf{x}, t) = \overline{P}(t) + \delta P(\mathbf{x}, t)$$

and

(2.25)
$$H(\mathbf{x}, t) \equiv \frac{1}{3}\nabla_r \mathbf{V} = \overline{H}(t) + \delta H(\mathbf{x}, t)$$

(2.26)
$$\Phi_{\text{t}ot} = \phi_b + \Phi(\mathbf{x}, t)$$

where $\delta H(\mathbf{x}, t) \equiv 1/3\nabla_r \cdot \mathbf{v}$. From the solutions for the homogeneous background it follows that $\phi_b = 2\pi G/3$. By inserting Eq. 2.23 into Eq. 2.20, and assuming that $\overline{\rho} \sim a^{-3}$, as when in the matter era[1], the continuity equation reduces to,

(2.27)
$$\frac{\partial\delta}{\partial\tau} = \nabla \cdot \left[(1+\delta)\mathbf{v}\right];$$

Analogously, the Euler and Poisson equations for perturbations are,

(2.28)
$$\frac{\partial\mathbf{v}}{\partial\tau} + \mathcal{H}\mathbf{v} + (\mathbf{v}\cdot\nabla)\,\mathbf{v} = -\nabla\Phi - \frac{\nabla P}{\rho},$$

(2.29)
$$\nabla^2\Phi = \frac{3}{2}\mathcal{H}^2\Omega_m\delta.$$

Note that Eqs. 2.27, 2.28 are also valid in the presence of Λ. If ρ_Λ is homogeneous, it only impacts the background evolution.

Letting divergence of the velocity be θ, the two equations of motion can be re-written as:

(2.30)
$$\frac{\partial\delta}{\partial\tau} + \theta = -\nabla(\delta\overline{v})$$

(2.31)
$$\frac{\partial\theta}{\partial\tau} + \mathcal{H}\theta + \frac{3}{2}\mathcal{H}^2\Omega_m\delta = -\nabla\cdot\left[(\mathbf{v}\cdot\nabla)\mathbf{v}\right]$$

To solve Eqs. 2.27, 2.28 in linear perturbation theory, it is assumed that $\delta \ll 1$ and $\nabla\mathbf{v}/\mathcal{H} \ll 1$. The linearized continuity and Euler equations are:

(2.32)
$$\frac{\partial\delta}{\partial\tau} + \theta = 0,$$

(2.33)
$$\frac{\partial\mathbf{v}}{\partial\tau} + \mathcal{H}\mathbf{v} = -\nabla\Phi - \frac{\nabla^2 P}{\overline{\rho}}.$$

---

[1]We are considering the evolution of the fluctuations in absence of pressure (non-relativistic condition) and this implies being in the matter era.

[2] Taking the divergence of Eq. 2.33 and combining it with the Poisson equation affords:

$$(2.34) \qquad \frac{\partial \theta}{\partial \tau} + \mathcal{H}\theta = -\nabla^2\Phi - \frac{\nabla^2 P}{\overline{\rho}} = -\frac{3}{2}\mathcal{H}^2\Omega_m\delta - \frac{\nabla^2 P}{\overline{\rho}}$$

Or, in Fourier space,

$$(2.35) \qquad \frac{\partial \delta_k}{\partial \tau} + \theta_k = 0,$$

$$(2.36) \qquad \frac{\partial \theta}{\partial \tau} + \mathcal{H}\theta = -\frac{3}{2}\mathcal{H}^2\Omega_m\delta_k - k^2\frac{P}{\overline{\rho}}$$

Taking the time derivative of equation 2.36 and combining it with equation 2.37 affords a second order differential equation describing the evolution of the perturbations:

$$(2.37) \qquad \frac{\partial^2 \delta_k}{\partial \tau^2} = -\mathcal{H}\frac{\partial \delta_k}{\partial \tau} + \frac{3}{2}\mathcal{H}^2\Omega_m\delta_k - k^2\frac{P}{\rho}.$$

where $\mathcal{H}\frac{\partial \delta_k}{\partial \tau}$ is the friction term due to the expansion of the Universe: both this and the pressure term have a negative sign ($\dot{a} > 0$ for expansion) indicating that the growth of perturbations is slowed by pressure and expansion. The $\frac{3}{2}\mathcal{H}^2\Omega_m\delta_k$ term corresponds to the source of gravity which determines the growth.

Pressureless case, $P_k = 0$, Dark matter evolution   Consider solving Eq. 2.37 when pressure is negligible: this amounts to modelling the linear evolution of dark matter fluctuations as a non-collisional fluid interacting with the other components by gravitation only:

$$(2.38) \qquad \frac{\partial^2 \delta_k}{\partial \tau^2} = -\mathcal{H}\frac{\partial \delta_k}{\partial \tau} + \frac{3}{2}\mathcal{H}^2\Omega_m\delta_k.$$

Since there is no explicit dependence on k, Eq. 2.36 is amenable to factorizable solutions of the type $\delta_k(\tau) = D(\tau)A_k$, where the coefficients A_k depend only on k.

$$(2.39) \qquad \frac{d^2 D}{d\tau} + \mathcal{H}\frac{dD}{d\tau} = \frac{3}{2}\Omega_m(\tau)\mathcal{H}^2(\tau)D(\tau).$$

The resulting Eq. 2.39 is a homogeneous differential equation that describes the evolution of the growth factor $D(\tau)$. The evolution of $H(\tau)$ and $\Omega_m(\tau)$ is described by the Friedman equations:

$$(2.40) \qquad \mathcal{H}^2[1 - \Omega_m(\tau)] = k$$

$$(2.41) \qquad \mathcal{H}' = -\frac{\mathcal{H}^2}{2}\Omega_m(\tau)$$

---

[2] $\frac{\nabla P}{\overline{\rho}(1+\delta)} \simeq \frac{\nabla P}{\overline{\rho}}(1-\delta)$ which at first order is $\simeq \frac{\nabla P}{\overline{\rho}}$.

Case where $\Omega_m = 1$. If we let $\Omega_m = 1$ and the curvature $k = 0$, then $\mathcal{H}' = -\mathcal{H}^2/2$ and Eq. 2.39 reduces to,

$$(2.42) \qquad \frac{d^2 D}{d\tau^2} + \frac{2}{\tau}\frac{dD}{d\tau} = \frac{3}{2}\frac{4}{\tau^2}D(\tau).$$

which has a solution of the kind:

$$(2.43) \qquad \delta_k(\tau) = A_k a + B_k a^{-3/2}.$$

Note that A_k, B_k are determined by the initial condition, which in turn determine what combinations of growing and decaying modes are excited. The evolution of velocity perturbations is obtained from Eq. 2.36, by taking the derivative of $\theta_k = -\frac{\partial \delta}{\partial \tau}$, which leads to:

$$(2.44) \qquad \theta_k(\tau) = \mathcal{H}(A_k a + -\frac{3}{2}B_k a^{-3/2})$$

Since the evolution of θ_k (Eq 2.44) is proportional to $\mathcal{H}$, it is convenient to define $\Theta_k \equiv \frac{\theta_k}{\mathcal{H}}$.

Note that as the velocity $\mathbf{v}$ is a vector field, it can be decomposed into divergence (scalar mode) and vorticity (vector mode) components. So far only the divergence component has been considered. The vorticity component can be obtained from Eq. 2.33 as $\omega \equiv \nabla \times \mathbf{v}$ affording:

$$(2.45) \qquad \frac{\partial \omega}{\partial \tau} + \mathcal{H}\omega = 0.$$

In Eq. 2.45 the source terms are all zero. Thus it is a good approximation (on scales large enough for linear equations to hold) to assume that the velocity is irrotational and so that the component $\omega = 0$.

Case where $\Omega_m \neq 1$ For $\Omega_m \neq 1$, a solution to equation 2.39 can be obtained by introducing a change of variable:

$$(2.46) \qquad \chi = \frac{1}{\Omega_m} - 1 \geq 0,$$

and assuming that at early times the Universe is matter-dominated with $\Omega_m \to 1$ and thus $\chi \to 0$, while at a late stage the Universe is expected to be dark energy-dominated, so that $\Omega_m \to 0$ and $\chi \to \infty$. Solving Eq. 2.39 under these conditions affords:

$$(2.47) \qquad D_+ = 1 + \frac{3}{\chi} + 3\sqrt{\frac{1+\chi}{\chi^3}}\log\left(\sqrt{1+\chi} - \sqrt{\chi}\right),$$

$$(2.48) \qquad D_- = \sqrt{\frac{1+\chi}{\chi^3}}.$$

For small χ, ($\Omega_m \approx 1$), the solutions of Eqs. 2.47 and 2.48 tend towards the solution of Eq. 2.43. For large $\chi \gg 1$ ($\Omega_m \approx 0$) the solutions to Eqs. 2.47 and Eq. 2.48 reduce to $D_+ \simeq 1$, $D_- \simeq \frac{1}{\chi}$, which means that fluctuations stop growing as Ω_m tends to zero, as expected because there is no source of gravity. Similarly, as the Universe transits from the matter era to an era dominated by dark energy ρ_Λ, fluctuations stop growing because the expansion of the universe accelerates. The combined solutions of Eqs. 2.47 2.48 afford:

$$(2.49) \qquad \delta_k = A_k D_+(a) + B_k D_-(a) \approx {}^3 A_k D_+(a).$$

Since $\mathbf{v} = \frac{-i\mathbf{k}}{k^2}\theta_k$ and $\theta_k = -\frac{\partial \delta}{\partial \tau} = -\mathcal{H}\frac{\partial \delta}{\partial \log a}$, and introducing the logarithmic growth rate $f \equiv \frac{d \log D_+}{d \log a}$, in linear theory the velocities and densities are related through:

$$(2.50) \qquad \theta_k = -\mathcal{H} f \delta_k,$$

$$(2.51) \qquad \mathbf{v}_k = \frac{i\mathbf{k}}{k^2}\mathcal{H} f \delta_k.$$

Using Eq. 2.50 it is possible to rewrite a differential equation equivalent to Eq.2.39 in terms of f as a function of Ω_m for which approximate solutions are $f(\Omega_m) \sim \Omega_m^{0.6}$ for an open universe and $f(\Omega_m) \sim \Omega_m^{5/9}$ for a flat universe with a cosmological constant [52].

Solution with pressure, baryon evolution   Consider the equation of motion for δ_k adding the pressure term

$$(2.52) \qquad \frac{\partial^2 \delta_k}{\partial \tau} + \mathcal{H}\frac{\partial \delta_k}{\partial \tau} = \frac{3}{2}\Omega_B \mathcal{H}^2 \delta_k - k^2 \frac{P_k}{\rho}.$$

To solve Eq. 2.52 the equation of state for the pressure perturbation is required. In configuration space and assuming that pressure is a function of density alone:

$$(2.53) \qquad \nabla^2 \frac{\delta P}{\rho} = c_s^2 \nabla^2 \frac{\delta \rho}{\rho} = -k^2 c_s^2 \delta_k,$$

where $c_s^2 = \delta P / \delta \rho$ is the adiabatic sound speed. For radiation, $c_s^2 = 1/3$. For baryons we consider the equation of state for a monoatomic ideal gas, (hydrogen), where $\gamma = 5/3$, thus,

$$(2.54) \qquad c_s^2 = \frac{5}{3}\frac{k_b T}{m_B},$$

where T is the temperature and k_b Boltzmann constant. Note that c_s is a function of time since the temperature scales with a; The term c_s is introduced into the equation of motion

$$(2.55) \qquad \frac{\partial^2 \delta_k}{\partial \tau^2} + \mathcal{H}\frac{\partial \delta_k}{\partial \tau} = \left(\frac{3}{2}\Omega_B \mathcal{H}^2 - k^2 c_s^2\right)\delta_k;$$

Then Eq. 2.55 can be rewritten as

$$(2.56) \qquad \frac{\partial^2 \delta_k}{\partial \tau^2} + \mathcal{H} \frac{\partial \delta_k}{\partial \tau} = c_s^2 (k_j^2 - k^2) \delta_k,$$

which contains the comoving Jeans wavenumber k_j defined as,

$$(2.57) \qquad k_j^2 c_s^2 = \frac{3}{2} \Omega_B \mathcal{H}^\epsilon = 4\pi G \overline{\rho}_B a^2.$$

On the large scales, for $k \ll k_j$, perturbations evolve as in the pressure-less case, while on the small scale, $k > k_j$, pressure predominates over gravity preventing growth. For the situation without expansion ($\tau = t$), c_s becomes independent of time and the solution to Eq. 2.55 takes the form of a plane wave (as is usual with sound waves, $\delta_k = exp(\pm i k c_s t)$.

To obtain a qualitative idea of the implications of Eq. 2.55 at different epochs, it is convenient to consider the Jeans mass M_J, or the mass contained in a radius equal of $\lambda_j/2$. It is the minimum mass an object (gas cloud) can have and still undergo gravitational collapse. During the radiation era, baryons and photons are coupled, the pressure is provided by photons, $c_s^2 = 1/3$ and the resulting Jeans mass is huge:

$$M_J^B = 4\pi/3 \overline{\rho_B} (\lambda_j/2)^3 \approx 5.4 \times 10^{18} \Omega_B h^2 (T/1eV)^{-3/2} M_\odot.$$

Thus, perturbations are unable to grow at (at least) all sub-Hubble scales. Later the universe enters the matter-dominated era and the baryon pressure is provided by thermal motion of the gas particles as shown in Eq. 2.54. The temperature T decreases as the scale factor a increases since they are related by an inverse square law ($T \propto \sim a^{-2}$). Thus, as photons decouple there is a substantial drop in pressure and consequently in the Jean mass, which reduces to:

$$M_J \approx 10^5 \Omega_B h^2 \left(\frac{z}{1100}\right)^{3/2} M_\odot.$$

at which point perturbations on scales smaller than the Hubble radius can grow.

2.3 The processed power spectrum

To model how the large-scale structure of the observable Universe evolves, it is necessary to determine how primordial fluctuations are "processed" during different epochs. Super-Hubble modes are not discussed here in detail, but from GR calculations recall that, at super-Hubble scales, curvature perturbations are conserved and proportional to the Newtonian potential [32]. As regards sub-Hubble evolution (when ($k > H^{-1}$)) it is important to distinguish two categories of perturbations: those that become sub-Hubble during the radiation-era, and those that become sub-Hubble during the matter era.

2.3.1 Cold dark matter and radiation during the radiation era

Consider a two-fluid system consisting of non-relativistic CDM and photons. For CDM the variation pressure is assumed negligible c_s^2. The Poisson equation at sub-Hubble scales is:

$$(2.58) \qquad -k^2\phi = 4\pi G a^2(\rho_m \delta_m + \rho_r \delta_r) = \frac{3}{2}\mathcal{H}(\Omega_m \delta_m + \Omega_r \delta_r)$$

Therefore the evolution of fluctuations in the matter component, well within the Hubble radius is given by:

$$(2.59) \qquad \frac{\partial^2 \delta_m}{\partial \tau^2} + \mathcal{H}\frac{\partial \delta_m}{\partial \tau} = \frac{3}{2}\mathcal{H}(\Omega_m \delta_m + \Omega_r \delta_r) \simeq \frac{3}{2}\mathcal{H}\Omega_r \delta_r$$

where Ω_m has been approximated to 0, and Ω_r has been approximated to 1. From GR, [32] the evolution of δ_r during the radiation era can be shown to be governed by:

$$(2.60) \qquad \frac{\partial^2 \delta_r}{\partial \tau^2} + \frac{k^2}{3}\delta_r.$$

As δ_r undergoes acoustic oscillation (see 2.3.4), then $\langle \delta_r \rangle \simeq 0$ (Eq. 2.59) and:

$$(2.61) \qquad \frac{\partial^2 \delta_m}{\partial \tau^2} + \mathcal{H}\frac{\partial \delta_m}{\partial \tau} \simeq 0;$$

which affords solutions of the kind,

$$(2.62) \qquad \delta_m = c_1 + c_2 \int \frac{d\tau}{a}$$

where c_1 and c_2 are constants. By substituting $a \sim t^{1/2}$ into Eq. 2.62 it emerges that matter perturbations have logarithmic growth during the radiation era,

$$(2.63) \qquad \delta_m c_1 + c_2 \log a.$$

2.3.2 Cold dark matter and baryonic matter during matter era

The development of perturbations in CDM, δ_c, and baryons, δ_b, in the matter era, is now examined. In this era baryons have decoupled from photons and fall into potential wells due to CDM. The linear perturbation equations for the evolution of both components, assuming that the potential is due to CDM only, since $\Omega_c \delta_c \gg \Omega_b \delta_b$, are as follows

$$(2.64) \qquad \frac{\partial^2 \delta_c}{\partial \tau^2} + \mathcal{H}\frac{\partial \delta_c}{\partial \tau} = \frac{3}{2}\mathcal{H}^2(\Omega_c \delta_c + \Omega_b \delta_b) \simeq \frac{3}{2}\mathcal{H}^2 \Omega_c \delta_c;$$

$$(2.65) \qquad \frac{\partial^2 \delta_b}{\partial \tau^2} + \mathcal{H}\frac{\partial \delta_b}{\partial \tau} = \frac{3}{2}\mathcal{H}^2(\Omega_c \delta_c + \Omega_b \delta_b) \simeq \frac{3}{2}\mathcal{H}^2 \Omega_c \delta_c.$$

To solve Eq. 2.64, δ_c is assumed to be proportional to the growing mode solution for the $\Omega_m = 1$ case (see Eq. 2.43), which is a reasonable approximation after decoupling. The expression for the baryon pressure is obtained from Eq. 2.53,

$$\nabla^2 \frac{\delta P}{\bar{\rho}} \to c_s^2 (-k^2) \delta_b.$$

As noted previously, after decoupling sound speed drops significantly because it is no longer driven by radiation pressure. Specifically sound speed squared goes from $c_s^2 = 1/3(1 + R)$ to $c_s^2 = 5/3 k_b T / m_b \propto 1/a$, consistent with the assumption of a monoatomic ideal gas. Since $\Omega_m = 1$, we have it that $a \propto \tau^2$ and $\mathcal{H} = \frac{2}{\tau}$, which substituted into Eq. 2.65 afford:

$$(2.66) \qquad \tau^2 \frac{\partial^2 \delta_b}{\partial \tau^2} + \tau^2 \mathcal{H} \frac{\partial \delta_b}{\partial \tau} \tau^2 k^2 c_s^2 \delta_b = \mathcal{H}^2 \Omega_c \delta_c.$$

Considering the time dependence of the coefficients, $\tau^2 \mathcal{H} \sim 2\tau$, $\tau^2 k^2 c_s^2 \sim \tau^2 1/\tau^2$ and $\tau^2 \mathcal{H}^2 \sim 4\tau^2/\tau^2$ in Eq. 2.66, it is easy to see that the homogeneous part is amenable to power-law solutions of the type τ^n, with n determined from

$$(2.67) \qquad n(n-1) + 2n + \frac{5}{3} \frac{k_b T_*}{m_b} (k\tau_*)^2 = 0.$$

Note that the term $\tau^2 k^2 c_s^2$ is rescaled to the recombination values T_* and τ_*, as it is time-independent. Introducing the Jeans wave-number, the solution for n can be rewritten as

$$(2.68) \qquad n = \frac{-1 \pm \sqrt{1 - 24(k/k_j)}}{2};$$

Therefore the homogeneous solution is (approximately) constant in the absence of the forcing term due to CDM. This is as expected since gravity due to baryons is pretty small ($\rho_b \ll \rho_c$). The interesting part comes from the solution obtained by introducing the ansatz,

$$\delta_b = A \delta_c^* (\tau/\tau^*)^{\cdot 2}$$

which substituted in Eq. 2.66 affords

$$\left(2 + 4 + 6 \frac{k^2}{k_j^2} \right) A = 6.$$

Therefore the general solution for δ_b is,

$$(2.69) \qquad \delta_b(k) = \frac{\delta_c^* (\tau/\tau_*)^2}{1 + k^2/k_j^2} + \delta_b^{\text{hom}} \simeq \frac{\delta_c^* (\tau/\tau_*)^2}{1 + k^2/k_j^2}.$$

The implication of Eq.2.69 is that at large scales ($k \ll k_j$) the baryon fluctuations follow dark matter fluctuations.

2.3.3   The late time power spectrum

Following the evolution of matter perturbations in the radiation and matter-dominated eras, presented in section 2.2, it is now possible to describe how the matter power spectrum evolves during these epochs. As shown, during the radiation era, baryonic matter perturbations cannot grow because gravitational collapse is contrasted by radiation pressure; while CDM perturbations can only grow logarithmically. To understand how CDM amplitude is processed at different scales, it is important to distinguish between modes that are larger or smaller than the Hubble radius at the equivalence epoch (k_{eq}) (i.e. the epoch of matter-radiation equality: $\Omega_m(a_{eq}) = \Omega_r(a_{eq})$). Modes in which $k \gg k_{eq}$ become sub-Hubble during the radiation era are suppressed by a factor

$$\log\left(\frac{a_{eq}}{a_e}\right) \cdot \left(\frac{a_e(k)}{a_{eq}}\right)^2 < 1,$$

where a_e is the value of the scale factor at the time that the mode k crosses the Hubble radius during the radiation era.

In fact super-Hubble modes grow like a^2, while sub-Hubble modes grow logarithmically during the radiation era.

Since $a_e(k)/a_{eq} = k_{eq}/k$, for $k \gg k_{eq}$ at late times, when all modes are inside the Hubble radius during the matter era, we have

$$(2.70) \qquad P(k)^{\text{late}}_\phi \propto P_\phi(k) \log\left(\frac{k}{k_{eq}}\right)\left(\frac{k_{eq}}{k}\right)^2.$$

or, for matter fluctuations, considering the primordial power spectrum to be a power law and $k^2\phi \sim \delta$,

$$(2.71) \qquad P_\delta(k)^{\text{late}} = \begin{array}{ll} Ak^{ns} & k \ll k_{EQ} \\ Bk^{ns-4}\log^2\left(k/k_{eq}\right) & k \gg k_{EQ}. \end{array}$$

2.3.4   Baryon acoustic oscillation

Another important process in the early pre-recombination universe was acoustic oscillations of baryons. A detailed description of the physics is available in [53]. Briefly, photon and baryon coupling gives rise to acoustic oscillations because the in-falling of baryons into dark matter potential wells is balanced by the radiation pressure. At decoupling, photons diffuse away and, shortly after recombination, the baryons are left distributed in shells of various sizes whose characteristic scale is defined by the physical size of the sound horizon r_d, at the era of decoupling (z_d):

$$(2.72) \qquad r_d = \int_{z_d}^{\infty} \frac{c_s(z)}{H(z)} \mathrm{d}z,$$

which correspond to the largest wave-length allowed for the acoustic oscillation.

Observation of the large scale structure reveals the imprint caused by pressure waves, even in late-time clustering. The imprint is evident as a localized peak in the correlation function at the characteristic scale r_d and as a damped series of oscillations in the power spectrum. Assuming standard radiation and matter contributions to the energy density it is possible to determine the sound horizon to within 0.2% [54]. Therefore by measuring the BAO feature in correlation functions it can be used as a standard ruler. In fact the BAO feature is measured in both the transverse and line of sight (LOS) direction, which are sensitive separately to the comoving angular distance and the Hubble parameter [55]. Key improvements in BAO analyses were introduced recently including the reconstruction method which removes non-linear effects on the BAO in order to sharpen the peak and boost the precision of the constraints. These aspects are not directly relevant to the present work, but the reconstruction technique is described in detail elsewhere [56]. The present author co-authored the first BAO detection at high redshift with eBOSS DR14 quasars [23]. For this data-set reconstruction was not applied due to the low density of the quasars.

2.4 standard perturbation theory (SPT)

In the previous section the linear solutions of Eq. 2.30 were obtained and examined. Here non-linear solutions incorporating perturbation theory are examined. In particular the evolution of perturbations on non-linear scales in the low redshift Universe is examined. The background evolution will be modelled assuming that the total energy density consists of matter and a cosmological constant (ΛCDM).

The starting point for studying low-z perturbations and structure formation is to set, as the initial power spectrum, the actual primordial power spectrum, Eq. 2.70, processed during the matter and radiation epochs. Under these conditions GR formalism is not needed and Newtonian physics remains valid for characterising the main dynamics. An additional assumption is that velocity is potential (i.e. fully characterized by its divergence). This condition does not hold at small scales where the Euler equation does not exactly describe the dynamics and multi-streaming can generate vorticity. For these reasons above a certain scale a breakdown of perturbation theory is expected. The main idea behind perturbation theory is that density and velocity field can be expanded about their linear solutions. This

means (provided there is no vorticity in the velocity field) a small parameter can be chosen as variance of the linear fluctuation, $\sigma^2 = \langle \delta^2 \rangle$ which controls the transition from a linear to a non-linear regime, $\sigma^2 \ll \gg 1$.

2.4.1 Non linear equation of motion

Consider the equation of motion, (Eq. 2.30) in Fourier space [51],

$$
(2.73) \qquad \frac{\partial \delta(\mathbf{k}, \tau)}{\partial \tau} + \theta(\mathbf{k}, \tau) = - \int d^3 \mathbf{k}_1 d^3 \mathbf{k}_2 \delta_D(\mathbf{k} - \mathbf{k}_{12}) \alpha(\mathbf{k}_1, \mathbf{k}_2) \theta(\mathbf{k}_1, \tau) \delta(\mathbf{k}_2, \tau)
$$

$$
(2.74) \qquad \frac{\partial \theta(\mathbf{k}, \tau)}{\partial \tau} + \mathcal{H}\theta(\mathbf{k}, \tau) + \frac{3}{2}\mathcal{H}^2 \Omega_m \delta(\mathbf{k}, \tau) = - \int d^3 \mathbf{k}_1 d^3 \mathbf{k}_2 \delta_D(\mathbf{k} - \mathbf{k}_{12})
$$
$$
\times \beta(\mathbf{k}_1, \mathbf{k}_2) \theta(\mathbf{k}_1, \tau) \theta(\mathbf{k}_2, \tau)
$$

where the mode coupling between the evolution of δ and θ is described through the kernels α and β,

$$
(2.75) \qquad
\begin{aligned}
\alpha(\mathbf{k}_1, \mathbf{k}_2) &\equiv \frac{\mathbf{k}_{12} \cdot \mathbf{k}_1}{k_1^2}, \\
\beta(\mathbf{k}_1, \mathbf{k}_2) &\equiv \frac{k_{12}^2 (\mathbf{k}_1 \cdot \mathbf{k}_2)}{2 k_1^2 k_2^2}.
\end{aligned}
$$

and $\mathbf{k} \equiv \mathbf{k}_1 + \mathbf{k}_2$.

2.4.2 $\Omega_m = 1$ case

Consider the perturbed solution for a cosmology in which $\Omega_m = 1$. In this scenario Ω_m does not depend on time, therefore we can find separable solutions for Eqs. 2.73, 2.74 (for the fastest growing mode) that satisfy:

$$
(2.76) \qquad \delta(\mathbf{k}, a) = \sum_{n=1}^{\infty} a^n \delta_n(\mathbf{k}),
$$

$$
(2.77) \qquad \theta(\mathbf{k}, a) = -\mathcal{H} \sum_{n=1}^{\infty} a^n \theta(\mathbf{k}),
$$

where if $n = 1$ we reduce to the linear solution, $\delta_1(\mathbf{k}) = \theta_1(\mathbf{k})$.

Note that, in principle, a linear combination of both modes (growing and decaying), should be considered; however for standard cosmologies the decaying mode makes a negligible contribution in the linear evolution of δ. Taking the derivatives of Eq. 2.76 affords:

$$(2.78) \qquad \frac{\partial \delta}{\partial \tau} = \mathcal{H} \sum n a^n \delta_n$$

$$(2.79) \qquad \frac{\partial \theta}{\partial \tau} = -\mathcal{H}^2 \sum_n \left(n - \frac{1}{2}\right) a^n \theta_n$$

and substituting these relations into the equations of motion allows derivation of δ_n, θ_n in terms of the linear fluctuations:

$$(2.80) \qquad \delta_n(\mathbf{k}) = \int d^3 \mathbf{q}_1 .. \int d^3 \mathbf{q}_n \delta_D(\mathbf{k} - \mathbf{q}_{1..n}) F_n(\mathbf{q}_1,..\mathbf{q}_n) \delta_1(\mathbf{q}_1)..\delta_1(\mathbf{q}_n),$$

$$(2.81) \qquad \theta_n(\mathbf{k}) = \int d^3 \mathbf{q}_1 .. \int d^3 \mathbf{q}_n \delta_D(\mathbf{k} - \mathbf{q}_{1..n}) G_n(\mathbf{q}_1,..\mathbf{q}_n) \delta_1(\mathbf{q}_1)..\delta_1(\mathbf{q}_n).$$

$$(2.82)$$

Note the dependence on time of the coefficients in Eq. 2.82, $a \propto \tau^2$ and $3\Omega_m \mathcal{H}^2/2 \propto 6/\tau^2$ from the Friedman equation.

The kernels F_n and G_n can be found: these are homogeneous functions in $\mathbf{q}_1..\mathbf{q}_n$ that describe the coupling through $\alpha(\mathbf{k}_1, \mathbf{k}_2)$, $\beta(\mathbf{k}_1, \mathbf{k}_2)$;

$$
\begin{aligned}
F_n(\mathbf{q}_1, \ldots, \mathbf{q}_n) \quad = \quad & \sum_{m=1}^{n-1} \frac{G_m(\mathbf{q}_1, \ldots, \mathbf{q}_m)}{(2n+3)(n-1)} \Big[(2n+1)\alpha(\mathbf{k}_1, \mathbf{k}_2) F_{n-m}(\mathbf{q}_{m+1}, \ldots, \mathbf{q}_n) \\
(2.83) \quad & + 2\beta(\mathbf{k}_1, \mathbf{k}_2) G_{n-m}(\mathbf{q}_{m+1}, \ldots, \mathbf{q}_n) \Big],
\end{aligned}
$$

$$
\begin{aligned}
G_n(\mathbf{q}_1, \ldots, \mathbf{q}_n) \quad = \quad & \sum_{m=1}^{n-1} \frac{G_m(\mathbf{q}_1, \ldots, \mathbf{q}_m)}{(2n+3)(n-1)} \Big[3\alpha(\mathbf{k}_1, \mathbf{k}_2) F_{n-m}(\mathbf{q}_{m+1}, \ldots, \mathbf{q}_n) \\
(2.84) \quad & + 2n\beta(\mathbf{k}_1, \mathbf{k}_2) G_{n-m}(\mathbf{q}_{m+1}, \ldots, \mathbf{q}_n) \Big],
\end{aligned}
$$

(where $\mathbf{k}_1 \equiv \mathbf{q}_1 + \ldots + \mathbf{q}_m$, $\mathbf{k}_2 \equiv \mathbf{q}_{m+1} + \ldots + \mathbf{q}_n$, $\mathbf{k} \equiv \mathbf{k}_1 + \mathbf{k}_2$ and $F_1 = G_1 \equiv 1$ by definition).

2.4.3 Case $\Omega_m \neq 1$

In general if $\Omega_m \neq 1$, it is no longer possible to find separable forms of the solutions for δ and θ. Further details are not pertinent here but a general discussion of perturbation theory for ΛCDM can be found in [51] for example. Note, that when building a model to be tested against observations, in order to reduce the computational effort, the kernels are usually pre-computed, assuming a fiducial cosmology. This choice is discussed in [51] where its validity is shown for close-to ΛCDM scenarios, since kernel dependence on cosmology is very small. However a recent work [57] further explored this to test departures from standard ΛCDM models.

OBSERVING THE LARGE SCALE STRUCTURE

3.1   Linear redshift space distortions

Galaxy surveys provide a three-dimensional map of the large scale structure by observing the angular position of multiple galaxies in the sky and measuring their respective spectroscopic redshifts.

In a completely smooth universe where recession velocities are due solely to the expansion of the universe, $\mathbf{V} = H\mathbf{r}$, redshifts make ideal indicators of the radial distances of the galaxies. In fact due to inhomogeneities, galaxy redshifts are contaminated by peculiar velocities, $\mathbf{V} \to \mathbf{V} + \mathbf{v}$, so that the comoving redshift position $\mathbf{s}$ is defined as

$$(3.1) \qquad\qquad \mathbf{s} = \mathbf{x} + \frac{\mathbf{v} \cdot \hat{n}}{\mathcal{H}} \hat{n},$$

where $\mathbf{x}$ is the true comoving position while the second term corresponds to the *contamination* along the line of sight. While the apparent distortion of the galaxy distribution in redshift space, known as redshift space distortion (RSD), appears at first glance to be nothing more than a systematic effect, it does in fact represent a unique way to measure the growth rate of structure formation, thus allowing tests of gravity on cosmological scales [58] [59], [52]. More recent publications have modeled, tested and provided further support for this concept [60], [7].

In this section we provide a description of the RSD on large scales, where linear theory holds, while in section 3.2 we discuss models accounting for non linearities. We start with a

convenient change of variables, rescaling the peculiar velocity $\mathbf{u}$ and density Θ as

$$(3.2) \qquad \mathbf{u} \equiv \frac{-\mathbf{v}}{\mathcal{H}f},$$

$$(3.3) \qquad \Theta \equiv \nabla \cdot \mathbf{u},$$

(all the other variables remain as defined in chapter 2). Whereas according to Eq. 2.50,

$$(3.4) \qquad \mathbf{v} = -\mathcal{H}f\mathbf{u}.$$

3.1.1 Mapping from real to redshift space

All models reviewed in this section follow the plane parallel approximation whereby if an observer is very distant from the region observed (i.e. survey region), one can work with a fixed line of sight $\hat{n}$ for all observed objects, e.g. $\hat{n} \simeq \hat{z}$, with $\hat{z}$ constant versor.

Using this approximation the mapping from redshift space to real space (Eq. 3.1) is given by

$$(3.5) \qquad \mathbf{s} = \mathbf{x} - fu_z\hat{z}.$$

From Eq. 3.5 it possible to ascertain the relation between fluctuation in redshift space δ_s and real space. Assuming the number of objects observed is conserved going from one space to the other:

$$(3.6) \qquad [1 + \delta_s(\mathbf{s})]\, d^3s = [1 + \delta(\mathbf{x})]\, d^3x,$$

In Fourier space, Eq. 3.6 becomes,

$$(3.7) \qquad \int d^3s \frac{e^{-i\mathbf{ks}}}{(2\pi)^3}(1 + \delta_s) = \delta_D(\mathbf{k}) + \delta_s(\mathbf{k}) = \int \frac{d^3x}{(2\pi)^3} \exp[-i\mathbf{k}(\mathbf{x} - fu_z\hat{z})](1 + \delta),$$

which leads to,

$$(3.8) \qquad \delta_s(\mathbf{k}) + \delta_D(k) = \int \frac{d^3x}{(2\pi)^3} \exp(-i\mathbf{k}\cdot\mathbf{x})(1 + \delta)\exp\left[ifk_zu_z(\mathbf{x})\right].$$

From Eq. 3.8 it is evident that the fluctuations in redshift space distortions are given by a non-linear mapping from δ and the velocity component along the line of sight, u_z.

3.1.2 Linear regime modeling

A simple linear model describing how the fluctuations are distorted in redshift space has been developed by Kaiser [52]. The linear model, Eq. 3.8 assumes that velocities are small enough (on linear scales), to expand the exponential factor as

$$(3.9) \qquad \delta_D(\mathbf{k}) + \delta_s(\mathbf{k}) = \int \frac{d^3x}{(2\pi)^3} \exp(-i\mathbf{kx})(1 + \delta)\left[1 + ifk_zu_z(\mathbf{x})\right],$$

which translates to

$$(3.10) \qquad \delta_s(\mathbf{k}) = \delta(\mathbf{k}) + i f k_z u_z(\mathbf{x}).$$

For linear perturbation theory we have, $\nabla \mathbf{u} = \delta$ and equivalently in Fourier space, $\mathbf{u}(\mathbf{k}) = \frac{-i\mathbf{k}}{k^2}\Theta(\mathbf{k}) = \frac{-i\mathbf{k}}{k^2}\delta(\mathbf{k})$; substituting these relation in Eq. 3.9 affords the relation between δ_s and δ:

$$(3.11) \qquad \delta_s(\mathbf{k}) = \delta(\mathbf{k}) + f i k_z \frac{-i k_z}{k^2}\delta(\mathbf{k}) \equiv (1 + f\mu^2)\delta(\mathbf{k}),$$

where $\mu \equiv \frac{k_z}{k}$ is the cosine of the angle between the line of sight $\hat{z}$ and the wave-vector.

When modes perpendicular to the LOS are considered, as in Eq. 3.11, the fluctuations are unaltered from real to redshift space, since $\delta_s = \delta$ ($\mu = 0$). By contrast when observing modes parallel to the LOS ($\mu = 1$) the density fluctuations in redshift space appear enhanced by a factor $1 + f$.

Consider for example a spherical over-density contour where on average the galaxies are infalling. In redshift space the sphere appears squashed since in the perpendicular direction the size is unaltered, while in the parallel direction the size is reduced. The opposite effect happens in underdense regions, where the average outflow elongates the structure from real to redshift space. More formally we could say that the redshift space distortion generates a quadrupole moment as the spherical (isotropy) symmetry is broken along the LOS. As observed earlier, the Kaiser model provides a good description of redshift space distortions assuming that velocities are small enough for the exponential expansion to be accurate. While this assumption holds at large scales, when moving to smaller scales, towards virialized structure sizes (halos of a few Mpc), the velocities are larger than the typical size of the objects. The scenario is therefore that modes perpendicular to the LOS remain unaltered, while along the LOS the high velocities from random thermal motion generate an elongation of structures in redshift space (i.e. the quadrupole is of opposite sign than when at large scales). This is commonly referred to as the Fingers of God effect (FoG) .

3.1.3 The redshift space power spectrum

Considering the correlation of the matter overdensity in redshift space (Eq. 3.11),

$$(3.12) \qquad \langle \delta_s(\mathbf{k})\delta_s(\mathbf{k}') \rangle = \left(1 + f\mu^2\right)\left(1 + f\mu^2\right)\langle \delta(\mathbf{k})\delta(\mathbf{k}') \rangle,$$

and the definition of P , we find the relation between the redshift space power spectrum P_s and the real space one:

$$(3.13) \qquad P_s(\mathbf{k}) = P(k)\left(1 + f\mu^2\right)^2.$$

It is often convenient to decompose the angular dependence of $P_s(\mathbf{k})$ in the Legendre polynomials $\mathscr{L}_\ell(\mu)$, into

$$(3.14) \qquad P_s^\ell(k) = \frac{(2\ell+1)}{2} \int_{-1}^{1} P_s(\mathbf{k}) \mathscr{L}_\ell(\mu) \, \mathrm{d}\mu,$$

where the expansion coefficients $P_s(\mathbf{k})$ are given by

$$(3.15) \qquad P_s(\mathbf{k}) = \sum_\ell \mathscr{L}_\ell(\mu) P^\ell(k).$$

For simplicity $\mathbf{k}$ will often be used instead of (k, μ) to denote the angular dependence in redshift space. On linear scales, P_s is expected to be fully described by the first three multipoles: monopole, quadrupole and hexadecapole [61]. Moving towards smaller scales the linear description becomes increasingly inaccurate and a different theory is required, as we discuss in Sec. 3.2. Note that on smaller scales, higher order multipoles are no longer zero even though most of the information is still accounted for the first three multipoles [7]. Another important factor to be taken into account is the bias relation between the observable galaxy power spectrum and the dark matter matter density field, since galaxies and not dark matter are observed.

A simple phenomenological model often used to account for these effects is the dispersion (or streaming) model:

$$(3.16) \qquad P_s^{\mathrm{g}}(\mathbf{k}) = P^{\mathrm{g}}(k) \left(1 + \beta\mu^2\right)^2 \exp(-f^2 k^2 \mu^2 \sigma_p^2),$$

where g refers to galaxy power spectra; $\left(1 + \beta\mu^2\right)^2$ corresponds to the squashing term, in which $\beta = f/b$ and b is the linear bias; $\exp(-f^2 k^2 \mu^2 \sigma_p^2)$ is a suppression factor, in which σ_v corresponds to the pairwise velocity dispersion of galaxies within halos.

Note that the equation 3.16 is oversimplified as it considers the effects happening at the large and small scales to be independent; due to the Gaussian initial condition hypothesis at large scales as well, we expect a velocity dispersion (as the velocity field fluctuates from one point to another). Further the σ_v parameter represents an effective velocity dispersion inconsistent with the actual observable dispersion as it depends on many other factors, such as scale or bias relation.

To appreciate how this model is derived consider again the mapping between the density from real to redshift space:

$$(3.17) \qquad [1 + \delta_s(\mathbf{s})] \, \mathrm{d}^3 s = [1 + \delta(\mathbf{x})] \, \mathrm{d}^3 x,$$

where considering $\mathbf{s} = \mathbf{x} - f u_z \hat{z}$, the Jacobian is defined as

$$(3.18) \qquad J \equiv \frac{\mathrm{d}^3 s}{\mathrm{d}^3 x} = |1 - f \nabla_z u_z|.$$

This leads to

$$(3.19) \qquad 1 + \delta_s(\mathbf{s}) = \frac{1 + \delta(\mathbf{x})}{J}$$

which combined together with Eq. 3.18 gives

$$(3.20) \qquad \delta_s(\mathbf{s}) = \frac{1 + \delta(\mathbf{x}) - J}{J} = \frac{\delta(\mathbf{x}) + f \nabla_z u_z}{J}.$$

The analogous relation in Fourier space becomes,

$$(3.21) \qquad \delta_s(\mathbf{k}) = \int \frac{\mathrm{d}^3 s}{(2\pi)^3} \delta_s(\mathbf{s}) \exp(-i\mathbf{k}\cdot\mathbf{s}) =$$

$$\int (\delta + f \nabla_z u_z) f \frac{\mathrm{d}^3 s}{(2\pi)^3 J} \exp[-i\mathbf{k}\cdot(\mathbf{x} - f u_z \hat{z})],$$

and recalling that $\frac{\mathrm{d}^3 s}{J} = \mathrm{d}^3 x$, we obtain

$$(3.22) \qquad \delta_s(\mathbf{k}) = \int \frac{d^3 x}{(2\pi)^3} \exp(-i\mathbf{k}\cdot\mathbf{x}) \left[\delta(\mathbf{x}) + f \nabla_z u_z(\mathbf{x})\right] \exp(i f k_z u_z)$$

and

$$(3.23) \qquad P_s(\mathbf{k}) = \int \frac{\mathrm{d}^3 r}{(2\pi)^3} \exp(-i\mathbf{k}\cdot\mathbf{r})$$

$$\left\langle \exp(i f k_z \Delta u_z) \left[\delta(\mathbf{x}) + f \nabla_z u_z(\mathbf{x})\right] \left[\delta(\mathbf{x}') + f \nabla_z u_z(\mathbf{x}')\right] \right\rangle.$$

Where we required the translation invariance to be satisfied and defined $\Delta u_z \equiv u_z(\mathbf{x}) - u_z(\mathbf{x}')$ and $r \equiv \mathbf{x} - \mathbf{x}'$.

By making a *crude* approximation assuming Δu_z is independent of r and factorizing out of the integral the exponential term, $\exp(i f k_z \Delta u_z)$, Eq. 3.23 becomes,

$$(3.24) \quad P_s(\mathbf{k}) = \int \frac{\mathrm{d}^3 r}{(2\pi)^3} \exp(-i\mathbf{k}\mathbf{r}) \langle \exp(i f k_z \Delta u_z) \rangle \left\langle \left[\delta(\mathbf{x}) + f \nabla_z u_z(\mathbf{x})\right] \left[\delta(\mathbf{x}') + f \nabla_z u_z(\mathbf{x}')\right] \right\rangle.$$

If velocities are assumed to be Gaussian field, the $\langle \exp(i f k_z \Delta u_z) \rangle$ term transforms to:

$$(3.25) \qquad \langle \exp(f^2 k^2 \mu^2 \Delta u_z) \rangle = \exp\left(\frac{f^2 k^2 \mu^2}{2} \langle \Delta u_z^2 \rangle\right) = \exp(-f^2 k^2 \mu^2 \langle \Delta u_z^2 \rangle / 2),$$

which corresponds (qualitatively) to the expected suppression on small scales. Note that modelling the small-scale velocities as a Gaussian field is also a very simplistic assumption and therefore we expect the model to "scale breakdown" on non-linear scales. In the next section (3.2) we discuss the limitations of the model presented in Eq. 3.16 and the various attempts to extend its validity.

3.2 Non Linear redshift space distortions

Here we discuss improved models for describing non-linear distortions in the redshift space correlation function and power spectrum. We review the competing approaches and compare some of the representative models for both ξ and P and their ability to accurately describe N-body simulation.

3.2.1 Eulerian and Lagrangian perturbations

One possible approach to modelling the power spectrum in redshift space is based on Eulerian standard perturbation theory, where perturbations are performed of density and velocity fields; the key assumption, as we reviewed in Sec. 2.4, is that at linear level the amplitude of these fields represents the small parameters of the theory.

Another perturbation based approach is the Lagrangian perturbation theory (LPT), where instead we consider small deviations around the displacement vector [62]. As shown in [63], the two approach give identical results in predicting the real space matter power spectrum, when the same orders of the expansion are considered, however there are advantages and disadvantages of both approaches. One advantage of the Lagrangian prescription is that the redshift space mapping can be performed by simply adding a derivative of the original displacement in the line of sight direction. Another key point, discussed in recent works (e.g. [64]) is that the Lagrangian approach provides a more consistent description of the halo bias as opposed to that provided by the Eulerian approach. In particular [64] highlights the emergence of non local lagrangian bias terms when dealing with higher order statistics, such as the Bispectrum.

In the analysis presented in chapters 7 and 8 we do not consider higher order statistics and, given the signal to noise ratio provided by the eBOSS DR14 data, we include only the local bias terms as free parameters in our models, therefore the two perturbative schemes can be considered equivalent for the purposes of this thesis.

The following is a general description of the models for the two point correlation function, based on the Lagrangian approach. In 3.2.3 we focus instead on the power spectrum by considering the models based on the Eulerian perturbative schemes.

3.2.2 Modelling the correlation function on non-linear scales

One of the first non linear model based on the LPT scheme is presented in [63] and [65]. [63] and introduces a resummation of the LPT scheme (rLPT) [62], to describe the non linear

evolution of the large scale structures, both in real and redshift space. Improvements in the model involve a more accurate description of non-linearities on the BAO feature with respect to [62], achieved by applying resummation schemes in redshift space. Similar results have been achieved for standard perturbative schemes [66], even though the method developed in [65] and [63] has the advantage of simplicity in the formalism over the one derived in [66] as well as having a faster numerical numerical resolution. On the other hand the rLPT description becomes less accurate at scales smaller than $70h^{-1}Mpc$ where its predictive ability for the matter power spectrum deviates dramatically from N-body measurements [63].

In [11] a new formulation of LPT is introduced, known as convolution Lagrangian perturbation theory (CLPT). CLPT provides a description in real and redshift space of the dark matter and halo correlation functions; the model presented in [11], can be seen as a partial resummation of [65]. Improvements include a more accurate description of the matter correlation function in real space and of the low-multipoles in redshift space, while the deviation becomes greater for the quadrupole on quasi-linear scales. Another key advantage is that the order zero of the CLPT naturally recover the Zeldovich-approximation ([67]) for the matter correlation function [68].

Figure 3.1, from [11], presents a comparison between the CLPT based redshift space monopole matter correlation function [11] (dashed lines) and the rLPT one [65] (dotted lines) against N-body simulation (squares) described in [10], at $z = 0.55$. Linear theory (solid line) corresponds to the model formulated by [52] in configuration space. At large scales the CLPT and rLPT models overlap, while tending towards smaller scales, the model from [11] shows a better agreement with the dark matter clustering than the one in [65]. Figure 3.2, from [11], shows an analogous comparison for the redshift space quadrupole, (same notation as 3.1). In this case the CLPT model as well fails to provide an accurate description of the higher order multipoles.

The method presented in [10] studies the halo clustering in real and redshift space, using a set of $67.5h^{-3}$Gpc^3 N-body simulations. They compute corrections on the halo correlation function in redshift space proposing a non perturbative real-to-redshift space mapping on quasi-linear scales ($\sim 30 - 80h^{-1}Mpc$), which recovers the Gaussian streaming model to linear order. In a recent work [69] a further extension of the CLPT model is proposed, which combines the CLPT-real power spectrum with the scale-dependent Gaussian streaming model derived in [10], obtaining a 2% and a 4% agreement below $< 25h^{-1}Mpc$ for monopole and quadrupole.
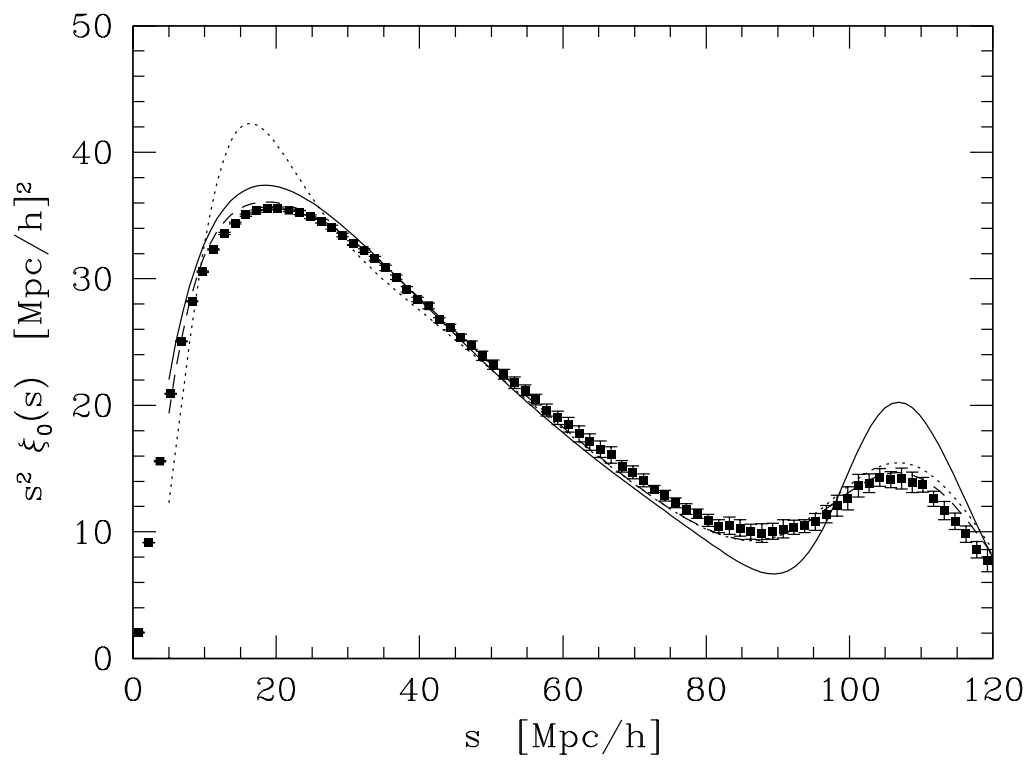
Figure 3.1: The redshift space monopole matter correlation function from CLPT (dashed lines), rLPT (dotted lines) and linear theory (solid line) compared to N-body simulation (squares) described in [10], at $z = 0.55$. (Figure taken from [11])
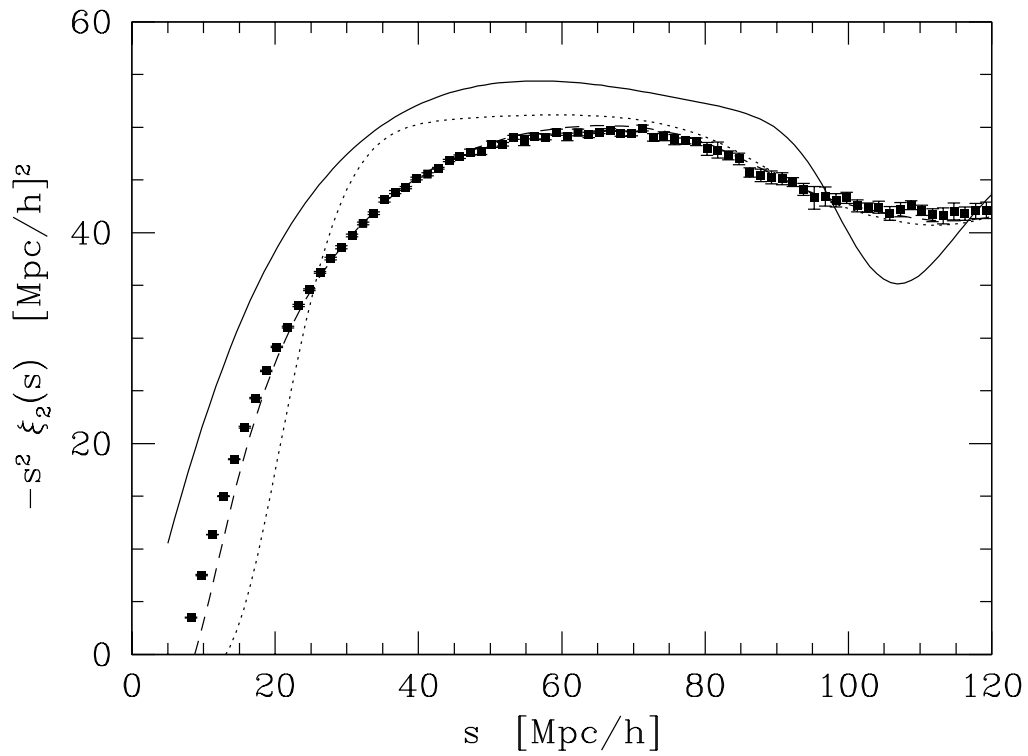
Figure 3.2: The redshift space quadrupole matter correlation function from CLPT (dashed lines), rLPT (dotted lines) and linear theory (solid line) compared to N-body simulation (squares) described in [10], at $z = 0.55$. (Figure taken from [11])

3.2.3   Modelling the power spectrum on non-linear scales

The work presented in chapters 7 and 8 has been carried out mainly considering statistics in Fourier space. As discussed in 3.2.2, all the models describing the correlation function both in real and redshift space are accurate only above a certain scale, below which any perturbation theory breaks down as we approach a non-linear regime. Moreover the signal related to a particular scale in configuration space (e.g. the BAO scale) is decomposed into different wave-numbers when going to Fourier space, for these reasons, even the best approximated model describing the correlation function at a certain range of scales would not necessarily accurately describe the power spectrum at the equivalent range of frequencies.

The following sections review the key models in Fourier space, used in this work, [70] [13] and their derivations.

3.2.3.1   Perturbation theory approach

As discussed in Sec. 2.4, the SPT approach is based on expanding the fluid equations of density and velocity around their linear solutions, while LPT consider perturbations around the displacement vector. The resultant expressions for the redshift space power spectrum are

(3.26)
$$P_{s,SPT}(k,\mu) = (1 + f\mu^2)^2 P_{lin}(k) + P_{s,1\text{-}loop}(k,\mu),$$

for SPT, and

(3.27)

$$P_{s,LPT}(k,\mu) = e^{-k^2\{1+f(f+2)\mu^2\}\sigma_v^2} \quad \times \left[P_{s,SPT}(k,\mu) + (1 + f\mu^2)^2 \left\{1 + f(f+2)\mu^2\right\} k^2 \sigma_v^2\right],$$

for LPT. See [65], [71] for the derivation of the two models.

First term in 3.26 corresponds to the Kaiser factor multiplying the linear power spectrum, while the second term encodes the mode-coupling corrections between the density and velocity fields, at one-loop order in perturbation theory. Note that those corrections arise from both gravitational clustering and redshift space distortion, which is why a naive model multiplying the Kaiser factor and the power spectrum at one-loop is not the correct approach as discussed in [70]. The second equation 3.27 is derived from LPT and includes the quantity σ_v^2 which in this case, represents the linear order estimate of the effective velocity dispersion.

Figures 3.3, 3.4 from [13] show a comparison of the results from SPT (blue dashed lines) and LPT (red dot dashed lines) with respect to the linear theory (black dashed lines) (Kaiser)
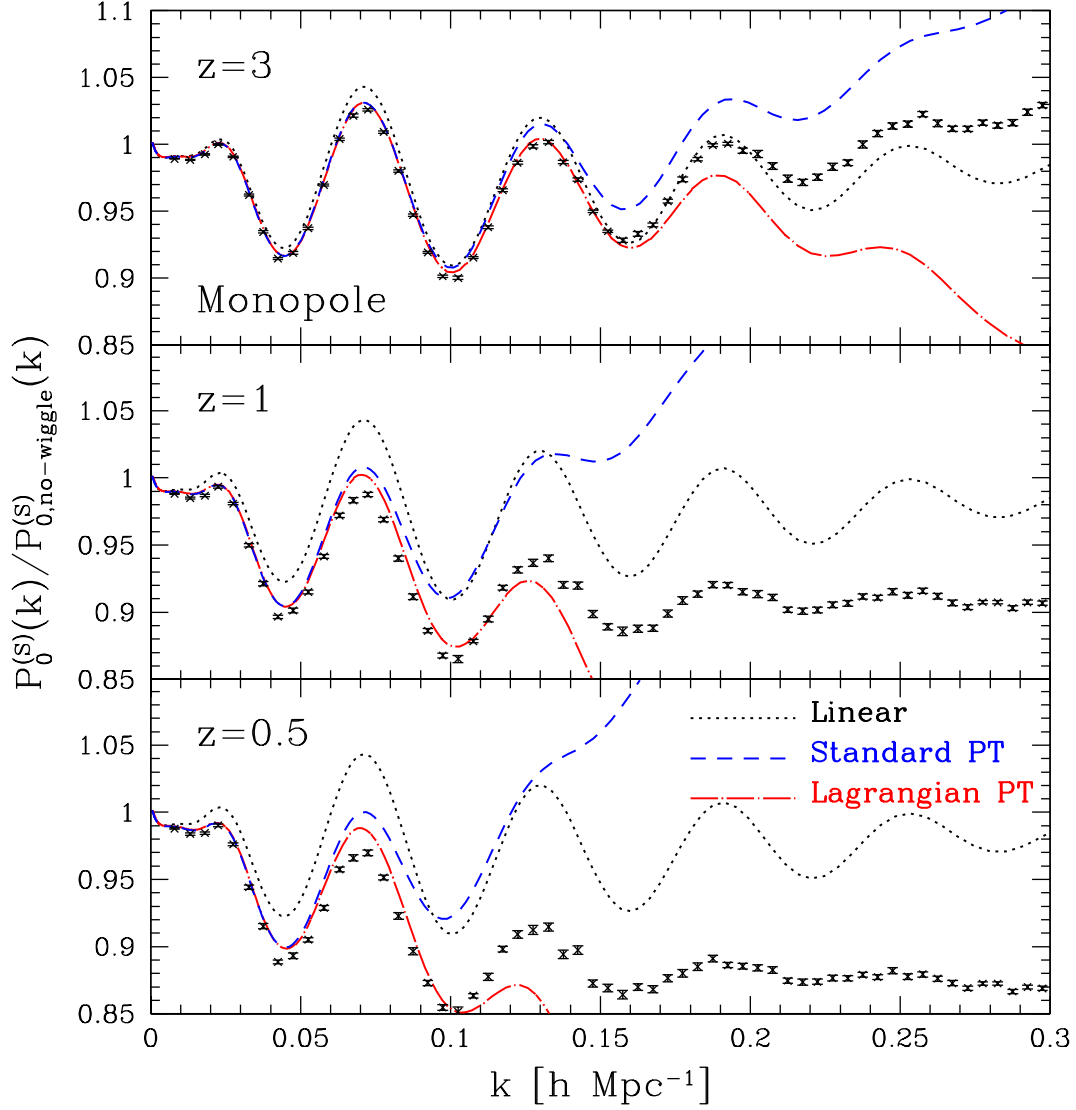
Figure 3.3: Description of the BAO feature in the monopole matter power spectrum from SPT and LPT at 1-loop (Eq. 3.26 and Eq. 3.27) with respect to the linear theory (Kaiser) and N-body simulation (crosses) [12] at $z = 0.5, 1, 3$. (Figure taken from [13])
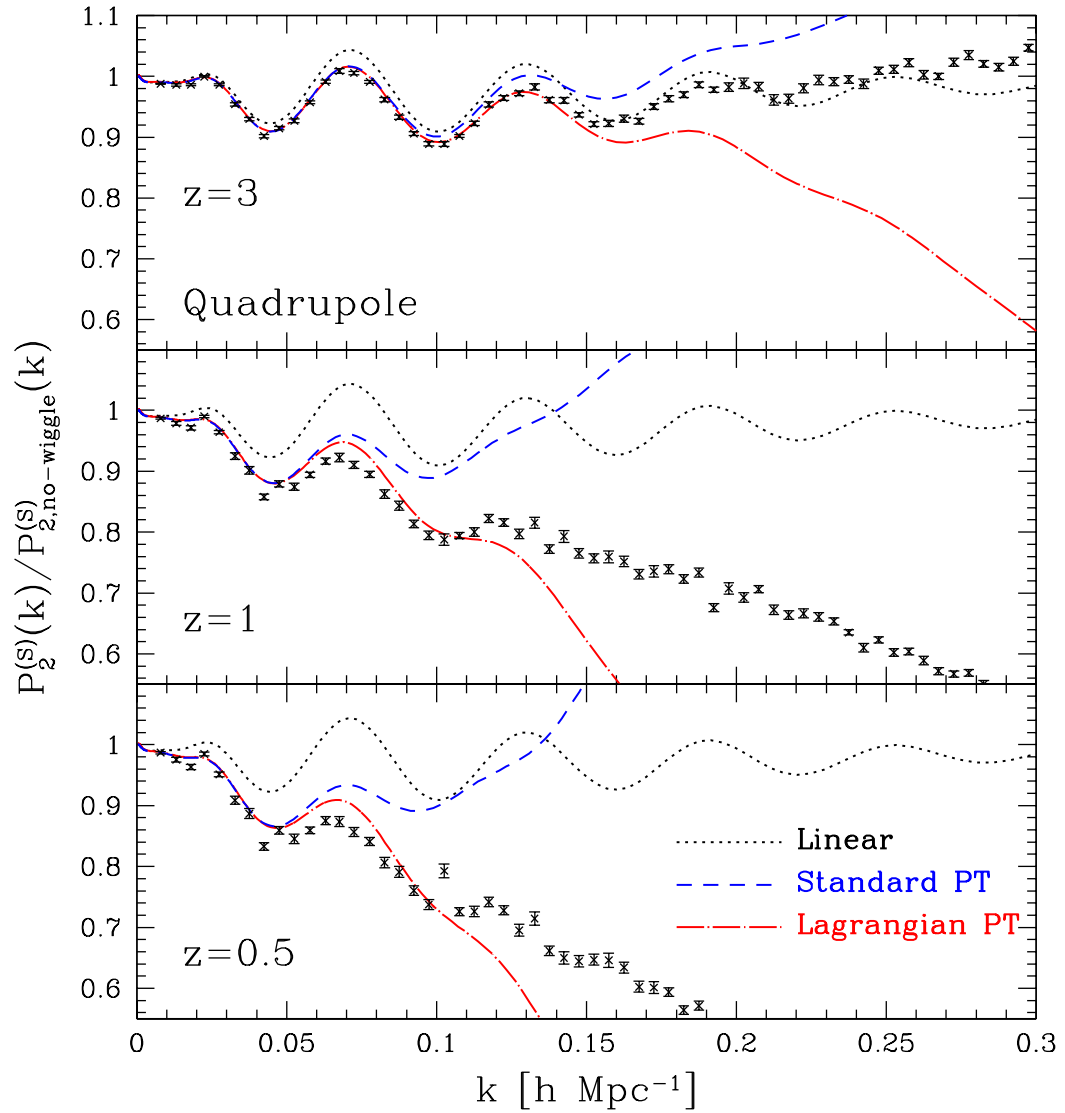
Figure 3.4: Description of the BAO feature in the quadrupole matter power spectrum from SPT and LPT at 1-loop (Eq. 3.26 and Eq. 3.27) with respect to the linear theory (Kaiser) and N-body simulation (crosses) [12] at $z = 0.5, 1, 3$. (Figure taken from [13])

and N-body simulation from [12] around the BAO feature at $z = 0.5, 1, 3$. The y-axis indicates the ratio between the predicted multipoles (monopole, Fig. 3.3 and quadrupole Fig. 3.4) and their respective no-wiggle moments. It is clear from the plots shown that both perturbative solutions do not accurately describe the baryon acoustic oscillation especially at redshifts 1 and 0.5 (middle-bottom panels), where non-linearities become more important. The LPT approach shows a slightly better agreement than does the SPT approach, but, from $k \sim 0.05$ an evident discrepancy in the amplitude with respect to the N-Body results is detected.

3.2.3.2 Phenomenological models

From the discussion above we can conclude that perturbation theory, even if it is a mathematically more rigorous approach, at $1-$loop order, cannot provide a good approximation of the redshift space multipoles. A more *successful* and efficient strategy is achieved by phenomenological models. The main phenomenological prescription, known as non-linear Kaiser model, was first introduced to extend the validity of the model [52] to non linear scales. The model, derived in [70] rigorously accounts for non linearities in mapping and in the matter power spectrum. Heading in the same direction – the so-called TNS model [13]. – extends the model presented in [70] to account for linear squashing/stretching as well as small-scale suppression.

   The following sections review the derivation of the two models, given their importance to the work in the current thesis.

3.2.3.3 Non Linear Kaiser Model

Starting from equation 3.24 and going beyond linear order affords:

$$(3.28) \quad P_s(\mathbf{k}) = \int \frac{\mathrm{d}^3 r}{(2\pi)^3} \exp(-i\mathbf{k}\mathbf{r}) \langle \exp(if k_z \Delta u_z) \rangle \big[\langle \delta(\mathbf{x})\delta(\mathbf{x}') \rangle + 2f \langle \delta(\mathbf{x})\nabla_z u_z(\mathbf{x}') \rangle$$
$$+ f^2 \langle \nabla_z u_z(\mathbf{x})\nabla_z u_z(\mathbf{x}') \rangle \big]$$

assuming a Gaussian field for the exponential term and inserting the definition of the power spectrum, the relation between the redshift and real space power spectra is,

$$(3.29) \quad P_s(\mathbf{k}) = \big(P_{\delta\delta} + 2f P_{\delta\theta} + f^2 P_{\theta\theta} \big) \cdot \exp(-f^2 k^2 \mu^2 \langle \Delta u_z^2 \rangle / 2),$$

where the subscripts δ and θ denote the correlation for density and velocity divergences, respectively.

   Some considerations of equation 3.29: the first term on the right side corresponds to the squashing (Kaiser) factor describing coherent motion of galaxies at large scales and reduces

to 3.13 at linear level, where $\delta \equiv \nabla u$ and $P_{\delta\delta} = P_{\theta\theta} = P_{\theta\delta}$. The second factor on the right, as in Eq. 3.13, represents the suppression of the correlation, due to random velocities at small scales, where galaxies belong to collapsed structures.

3.2.3.4 Non linear regime model (TNS)

[13] investigate the impact of varying the functional form of the FoG term and confirms that the discrepancies from N-body results do not vary significantly; the reason is that the higher order of the coupling between the density and velocity fields is missing when performing a first order expansion of the exponential term in Eq. 3.28, [13]. In order to account for the non linear corrections [13] consider higher-order contributions in the expansion. They present an improved version of 3.29, with a particular focus on the BAO feature. Their model, adds corrections generated from higher order coupling between density and velocities and provides a better description of both monopole and quadrupole when compared with N-body simulations. Following on from their derivation it is convenient to introduce the following notation (consistent with [13])

$$(3.30) \qquad j_1 = -i\mathbf{k}f,$$

$$(3.31) \qquad A_1 = \Delta u_z, A_2 = \delta(\mathbf{x}) + f\nabla_z u_z(\mathbf{x}), A_3 = \delta(\mathbf{x}') + f\nabla_z u_z(\mathbf{x}'),$$

into Eq. 3.21, which becomes,

$$(3.32) \qquad P^s(\mathbf{k}) = \int \mathrm{d}^3\mathbf{r}\exp(i\mathbf{k}\mathbf{r})\left\langle \exp(j_1 A_1)A_2 A_3\right\rangle.$$

We interpret the term $\langle \exp(j_1 A_1)\rangle$ as a generic characteristic function (or moment generating function) and relate it to its cumulant generation function. Being $\mathbf{A}$ a generic stochastic field with variables A_1, A_2, A_3 and j_1, j_2, j_3 some generic constant vector components, the moment generating function $\langle \exp(jA)\rangle$ is related to the cumulant generation function through the relationship

$$(3.33) \qquad \left\langle \exp(\mathbf{j}\cdot\mathbf{A})\right\rangle = \exp\left\{\langle \exp(\mathbf{j}\cdot\mathbf{A})_c\right\}$$

where the subscript c denotes the cumulant generating function.

Applying the partial derivative with respect to j_2 and j_3 on both sides of Eq. 3.33 and setting both j_2, j_3 components equal to zero affords

$$(3.34) \qquad \begin{aligned} \left\langle \exp(j_1 A_1)A_2 A_3\right\rangle &= \exp\left\{\left\langle \exp(j_1 A_1)\right\rangle_c\right\} \\ &\times \left[\left\langle \exp(j_1 A_1)A_2 A_3\right\rangle_c + \left\langle \exp(j_1 A_1)A_2\right\rangle_c \left\langle \exp(j_1 A_1)A_3\right\rangle_c\right]. \end{aligned}$$

Substituting Eq.3.34 in Eq. 3.32 we get,

$$
P^s(k, \mu) = \int d^3\mathbf{x} \exp(i\mathbf{kx}) \exp(\{\langle \exp(j_1 A_1) \rangle_c\})
$$
$$
\times \left[\langle \exp(j_1 A_1) A_2 A_3 \rangle_c + \langle \exp(j_1 A_1) A_2 \rangle_c \langle \exp(j_1 A_1) A_3 \rangle_c \right].
$$

(3.35)

If we reintroduce the A_i terms as they were defined in Eq. 3.30, the coupling between the FoG term and the density and velocity fields becomes evident at linear scales. Note also that so far no approximations have been made, a part for the plane parallel assumption, yet the full mapping was considered. In order to find first order corrections to the model in Eq. 3.29 we perturb the term within the brackets of $\exp(\{\langle \exp(j_1 A_1) \rangle_c\}$. In particular we consider the perturbation up to the second order in j_1 as:

$$
\langle \exp(j_1 A_1) A_2 A_3 \rangle_c + \langle \exp(j_1 A_1) A_2 \rangle_c \langle \exp(j_1 A_1) A_3 \rangle_c \simeq
$$
$$
\langle A_2 A_3 \rangle + j_1 \langle A_1 A_2 A_3 \rangle_c + j_1^2 \left\{ \frac{1}{2} \langle A_1^2 A_2 A_3 \rangle_c + \langle A_1 A_2 \rangle_c \langle A_1 A_3 \rangle_c \right\} + \mathcal{O}(j_1)^3.
$$

(3.36)

If we consider the A_i terms in perturbation theory (also dropping the $\langle A_1^2 A_2 A_3 \rangle_c$ term as it is of a higher order), we get,

$$
P^s(k\mu) = \exp\left\{ \langle \exp(j_1 A_1) \rangle \right\}
$$
$$
\times \left[P_{\delta\delta}(k) + 2f\mu^2 P_{\delta\theta} + f^2\mu^4 P_{\theta\theta} + A(k, \mu) + B(k, \mu) \right]
$$

(3.37)

where the exponential pre-factor can be interpreted as the suppression factor (FoG) term. A and B are the new corrections to Eq. 3.29 and correspond to,

$$
A(k, \mu) = j_1 \int d^3\mathbf{x} \exp(i\mathbf{kx}) \langle A_1 A_2 A_3 \rangle_c
$$

(3.38)

$$
B(k, \mu) = j_1^2 \int d^3\mathbf{x} \exp(i\mathbf{kx}) \langle A_1 A_2 \rangle_c \langle A_1 A_3 \rangle_c
$$

(3.39)

Figure 3.5 from [13], shows the behaviour of the two additional corrections to Eq. 3.38 in describing the BAO feature. Y-axes correspond to the matter redshift space monopole and quadrupole (left and right panels) including the A and B corrections derived in [13], divided by their respective no-wiggles spectrum [72]; the FoG term has been included assuming a Gaussian distribution for the velocity dispersion.

From both panels in 3.5 we observe that the A term for both monopole and quadrupole tends to oscillate and has a larger amplitude than the term B, which is smooth with a small amplitude. However it is evident that these corrections brings a non-negligible variation to the non-linear Kaiser model (3.29), especially for the quadrupole. Description of the BAO
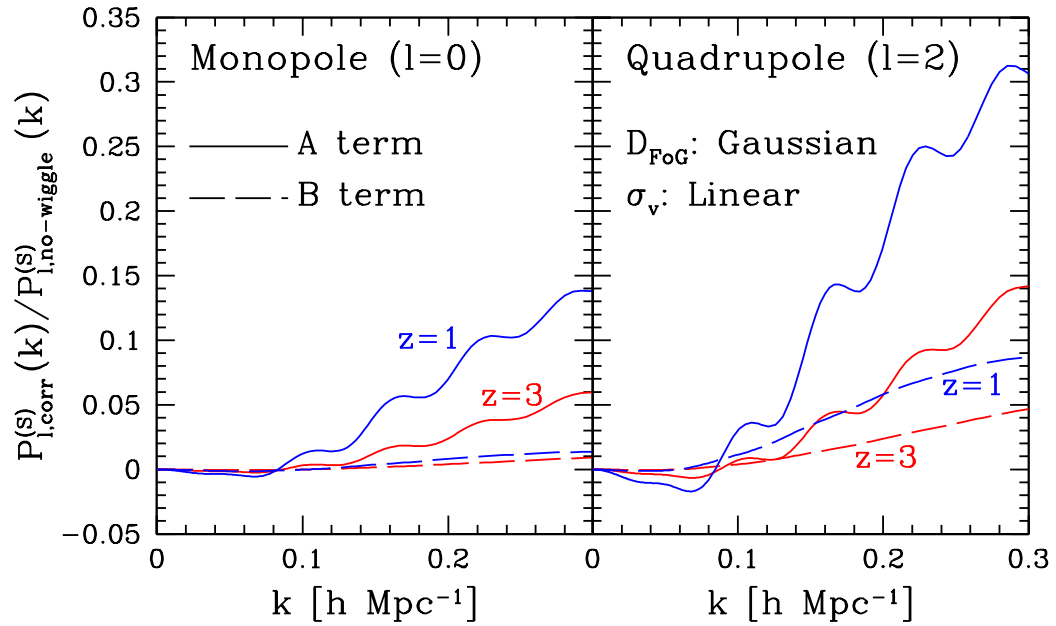
Figure 3.5: The *A* and *B* contributions to the monopole (left) and quadrupole (right) matter power spectrum. (Figure taken from [13])

feature in the monopole matter power spectrum derived with SPT and LPT with respect to the linear theory and N-body simulation at $z = 0.5, 1, 3$.

Note that when doing the approximation in Eq. 3.36, the exponential term becomes a phenomenological parameter. However, since the finger of God effect is fully non-linear and arises from the thermal motion of galaxies within halos, it is very difficult to predict the exact velocity dispersion. In fact in this and other work (e.g. [60]) it is treated as simply a nuisance parameter.

3.3 Alcock-Paczynki effect

The RSD discussed in the previous section, is not the only apparent distortion of the clustering pattern: given that the comoving distance of each galaxy is computed assuming a cosmological model, an incorrect choice of the underlying cosmology introduces artificial anisotropies in the resulting comoving clustering. In particular, assuming deviations from the true cosmology to be small when compared with the signal detected, this effect is sensitive to $H(z)$ along the line of sight and scales as the angular distance $D_A(z)$ in the transverse direction.

This apparent mismatch of the underlying cosmology, known as the Alcock-Paczynsky distortion was modelled by [73] and since then it has been used as a cosmological test in different analyses, e.g. [74] [75]. We here review how to account for this effect in our model by relating the *true* and the *observed* radial positions. We start by introducing the scaling factors,

$$
(3.40) \qquad \alpha_\parallel \quad = \frac{H^{fid}(z)r_s^{fid}(z_d)}{H(z)r_s(z_d)},
$$

$$
(3.41) \qquad \alpha_\perp \quad = \frac{D_A(z)r_s^{fid}(z_d)}{D_A^{fid}(z)r_s(z_d)},
$$

where $r_s^{fid}(z_d)$ is the fiducial sound horizon at the dragging epoch redshift (z_d) introduced in 2.3.4. The true wave-numbers $k_\parallel^t, k_\perp^t$ are then related to the observed $k_\parallel, k_\perp$ by

$$
(3.42) \qquad
\begin{aligned}
k_\parallel^t &= k_\parallel/\alpha_\parallel, \\
k_\perp^t &= k_\perp/\alpha_\perp.
\end{aligned}
$$

In this work we will deal mainly with the absolute wave-number $k = \sqrt{k_\parallel^2 + k_\perp^2}$ and the cosine of the angle to the line-of-sight μ coordinates, whose transformations, obtained from Eq.3.42, are

$$
(3.43) \qquad
\begin{aligned}
k^t &= \frac{k}{\alpha_\perp} \left[1 + \mu^2 \left(\frac{\alpha_\perp^2}{\alpha_\parallel^2} - 1 \right) \right]^{1/2}, \\
\mu^t &= \mu \frac{\alpha_\perp}{\alpha_\parallel} \left[1 + \mu^2 \left(\frac{\alpha_\perp^2}{\alpha_\parallel^2} - 1 \right) \right]^{-1/2}.
\end{aligned}
$$

3.4 Primordial Non-Gaussianity

In Sec. 1.2.5, we discussed how a standard inflationary paradigm predicts a primordial gravitational field, described by a Gaussian random field implying that the amplitude of the

initial fluctuations is also expected to follow a Gaussian distribution. On the other hand an alternative model positing a more complicated action (e.g. with a different potential term) for the Inflaton field would generate an additional non Gaussian component in the distribution of the fluctuations. This degree of non-Gaussianity can be quantified by introducing the $f_{\mathrm{N}L}$ parameter, defined in terms of the primordial (connected) Bispectrum which is expected to be equal to zero for a *perfect* Gaussian random field, divided by its tree-level component. In chapter 6, we will focus on the *local* for $f_{\mathrm{N}L}$ [76], [77] and how it is accounted in the matter power spectrum prediction (see e.g. [78]). The following is a short review of existing non-Gaussianity constraints.

$f_{\mathrm{N}L}$ **constraints from WMAP7** [40] combine 7 years of observational data on the temperature and polarization anisotropies, obtained from the WMAP satellite [79]; from the measured temperature bipectrum, local primordial non Gaussianity is constrained at 95% of accuracy to be $-10 < f_{\mathrm{N}L}^{LOC} < 74$ and $-274 < f^{LOC,eq}{}_{\mathrm{N}L} < 266$, $-410 < f^{LOC,ort}{}_{\mathrm{N}L} < 6$, using equilateral and orthogonal triangles only.

$f_{\mathrm{N}L}$ **constraints from the LSS** [14] present a measurement of $f_{\mathrm{N}L}^{LOC}$ from LSS observation competitive with the one from [40]. [14] combine three different SDSS samples: spectroscopic LRGs [17] and photometric LRGs and quasars [80] [81]. They consider the spectroscopic LRGs power spectrum on scales $k \leq 0.2h\mathrm{Mpc}^{-1}$, computed on a 4000d$eg^2$ area for $0.16 \leq z \leq 0.47$; the LRGs-angular power spectrum is computed on photometric LRGs distributed across a 3500deg^2 area between $0.2 < z < 0.6$ for $k < 0.1h\mathrm{Mpc}^{-1}$; finally they consider photometric quasars used in [81], in two different photo-z ranges, $0.65 - 1.45$ and $1.45 - 2$. As we will review in detail in chapter 6, a non negligible $f_{\mathrm{N}L}^{LOC}$ signal generates a scale-dependent bias contribution at large-scales. Quasars, as highly biased tracers of the LSS potentially provide a strong constraint on $f_{\mathrm{N}L}^{LOC}$, on the other hand they are also highly affected by systematic errors such as stellar contamination, galaxy extinction and calibration errors. More details on this can be found in [82]. Figure 3.4 shows the constraints on non Gaussianity obtained from the different samples described above; while details about the techniques used are not discussed here, it is worth noting is that no-evidence of $f_{\mathrm{N}L}^{LOC} \neq 0$ has been detected. The errors obtained (at 1σ) are comparable with those obtained in [40], (within the rande $95 - 99.7\%$).

Further constraints of $f_{\mathrm{N}L}^{LOC}$ using LSS have been presented in [83] [84]. In particular [84] find $-45 < f_{\mathrm{N}L}^{LOC} < 190$ (95% CL) on the largest effective volume using the DR9 BOSS DATA [85], (3000deg^2 footprint), within $0.43 < z < 0.7$. They also include a robust treatment of the
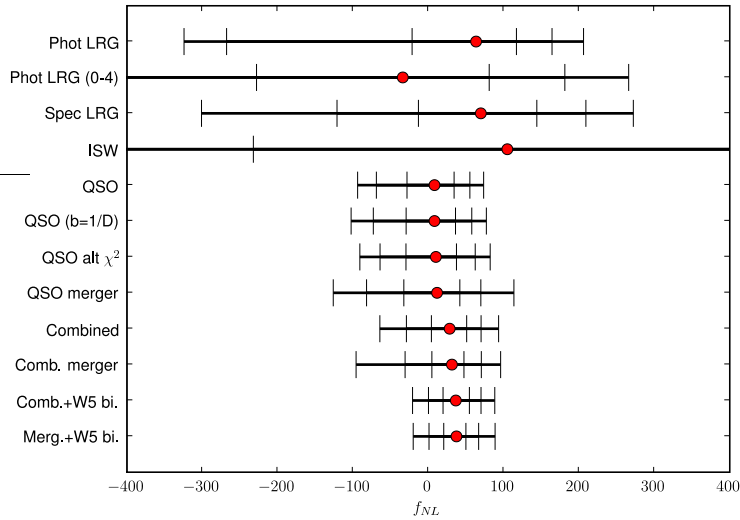
Figure 3.6: $f_{\rm NL}$ constraints (at 1,2 and 4 σ) from photometric LRGs and quasars, Integrated Sach Wolfe effect and spectroscopic LRGS. Figure taken from [14]

systematic errors such as Galactic foregrounds and their impact on the $f_{\rm NL}^{\rm LOC}$ measured. A full discussion on how to deal with the systematic bias due to stellar contamination is also included .

$f_{\rm NL}$ **constraints from Planck** In chapter 1 we have discussed the ability of the Planck experiment of studying the cosmological model by placing unprecedented constraints on the cosmological parameters. In particular with regard to local primordial non-Gaussianity, [3] obtain $f_{NL}^{LOC} = 2.5 \pm 5.7$, from the observed temperature bispectrum. This result, (at 68% CL) is consistent with a ΛCDM Universe where primordial seed perturbations have a Gaussian distribution. Planck CMB observational data represent, so far, the most powerful probe to constrain non-Gaussianity. On the other hand, the LSS measurements with future experiments will be statistically compelling thanks to the larger effective volumes being considered (Sec. 3.5.4); a comparison between future results and Planck will be then very interesting as the two probes (CMB and LSS) are almost completely independent.

In chapter 6 we propose a new technique that increases the signal to noise ratio at large scales where the non-Gaussian features would appear, on DESI-like surveys.

3.5 Measuring the power spectrum

Here we review the estimator of the power spectrum used in this thesis. The method, derived in [86], hereto FKP method, has been used in different works (see section 3.5.4 for review of

important applications) in order to measure the galaxy power spectrum from 3-dimensional redshift surveys. The FKP estimator aims to account for the target selection effects, the discreteness of the galaxy field observed and proposes an optimal weighting scheme to maximize the signal.

3.5.1 Power spectrum estimator

Three main assumptions have been made to derive the estimator;

  i the galaxies observed are a Poisson sample selected from the density field δ.

  ii There is no phase correlation between the true density field and the mask (fair-sample hypothesis).

  iii The galaxy fluctuations δ_g are Gaussian distributed. In agreement with the inflationary paradigm discussed in section 1.2.5 and consistent with observations.

Given these premises, we consider the galaxy density field defined as,

$$\delta_g = \left[n_g(\mathbf{r}) - \alpha n_s(\mathbf{r}) \right] w(\mathbf{r}), \tag{3.44}$$

where $n_g(\mathbf{r})$ is the selection function defined by the galaxy catalogue and mask, while $n_s(\mathbf{r})$ is a synthetic catalogue characterized by the same angular and radial selection function as $n_g(\mathbf{r})$ containing ($\alpha \times$ number of galaxies) objects, located at random positions, (i.e. $n_s(\mathrm{r})$ does not contain any clustering signal). The strategy includes also weight functions to optimize the signal which we discuss separately in 3.5.3.

Considering (i) and (ii) and taking the Fourier transform of the galaxy density field we obtain

$$\langle |\delta_g(\mathbf{k})|^2 \rangle = \int \frac{d^3 k'}{(2\pi)^3} P(\mathbf{k}') |G(\mathbf{k} - \mathbf{k}')|^2 + (1 + \alpha) \int d^3 x \, \bar{n}(\mathbf{x}) . \tag{3.45}$$

The first term in Eq. 3.45 consists in the *true* galaxy power spectrum convolved with the window function of the survey defined by

$$G(\mathbf{k}) \equiv \int \bar{n}(\mathbf{x}) e^{i\mathbf{k}.r} d^3 x . \tag{3.46}$$

The second term is the shotnoise contribution, modelled according to (i), which arises from the correlation of a discrete field in Fourier space.

3.5.2 Variance of the power spectrum

A further assumption, (iv), is made to compute the variance of the FKP estimator: given $G(k) \sim 1/D$ where D defines the depth of the survey, we are restrict our analysis to scale $k \gg 1/D$ so that equation 3.45 can be approximated to

$$(3.47) \qquad \langle \delta_g(\mathbf{k}) \delta_g(\delta\mathbf{k}) \rangle \simeq P(\mathbf{k}) Q(\delta\mathbf{k}) + S(\delta\mathbf{k}),$$

where S denotes the shotnoise term in equation 3.45 and

$$(3.48) \qquad Q(\mathbf{k}) \equiv \int \bar{n}^2(\mathbf{x}) e^{i\mathbf{k}\cdot\mathbf{r}} d^3x.$$

Combining together (iv) and (iii) gives that the variance of the galaxy power spectrum as

$$(3.49) \qquad \sigma_P \simeq \frac{1}{V_k} \int d^3k' |P(\mathbf{k}) Q(\delta\mathbf{k}') + S(\delta\mathbf{k}')|$$

Where V_k is the volume of the shell considered. Note that in assuming (iii), consistent with the Wick theorem, we neglected the connected galaxy four-point correlation function.

3.5.3 FKP weights

In this section we review the optimum weighting scheme proposed [86] to be applied on the galaxy density fluctuations, which depends on the average distribution in redshift $n(r)$ of the galaxies observed. In summary the FKP approach assumes that galaxies are a Poisson sample of the matter density field and that, by computing the Fourier transform of the distribution of the galaxies, deconvolving it from the window function and subtracting a Poisson shotnoise term, we get an unbiased estimator of the galaxy power spectrum. The FKP estimator, has been applied to many surveys, as we review in 3.5.4; however, as discussed in more recent works (see e.g.[87] [88]) such an estimator does not account for the many other factors involved in the relationship between the distribution of the galaxies and the matter field, such as luminosity, color and stellar mass [89] [90] [87]. Recent efforts in this direction [88] underline how the FKP estimator is in fact far from being unbiased and, instead, suggest improved approaches based on a deeper understanding of galaxy formation.

The work presented in this thesis develops and tests a new weighting scheme that accounts for the evolution in redshift of clustering by optimally combining different parts of the survey volume. However we start by briefly reviewing the *standard* FKP weights derivation.

Under the assumptions (i-iv), we select the weight function $w(\mathrm{r})$ that maximises the ratio between the variance and the power spectrum (Eq. 3.45 and Eq. 3.49, finding,

$$(3.50) \qquad w(\mathrm{r}) = \frac{1}{1 + \bar{n}(\mathrm{r})P(k)}.$$

Some considerations on Eq. 3.50; as we mentioned above this derivation has different limitations; first it describes the relationship between the galaxy and the underlying matter field in an over-simplistic way such that significant errors appear if the sampling is not Poissonian. Second in order to apply this weighting to galaxies, the scale dependence is neglected and thus the optimization is limited to a particular scale. Other work on the subject (see [88] and references within) as well as this thesis, investigate possible directions to achieve a more realistic unbiased estimator,one able to optimally extract the cosmological information from future observation.

3.5.4   Galaxy Surveys

Galaxy surveys are conducted in order to collect the angular position and redshift of a large number of galaxies in a section of the sky, so as to measure the clustering signal in 3-dimensions. When we are able to obtain the spectrum for the observed galaxies, then the *spectroscopic* redshifts measured through their emission and absorption lines have errors in the order $0,001 \sim 0.0001$, thus allowing for accurate measurements of the anisotropies along the line of sight (e.g. RSD signal).

Thanks to technical advancements, such as multi-object spectrograph (MOS), survey teams, were able to create accurate maps containing up to 10^6 galaxies, providing robust measurements of the galaxy power spectrum based on determining the statistical distribution of matter with high precision.

Significant measurements of the galaxy power spectrum using the estimator discussed in 3.5 have been presented over the last few decades and we will shortly review some of the key facilities used and the cosmological constraints achieved thanks to them. We will then focus on the ongoing eBOSS survey, whose clustering data analysis is presented in chapter 8. In the last part of this section we provide details about future surveys, discussing their respective strengths in testing cosmology with LSS measurements.

3.5.4.1   Completed and ongoing programs

2-degree Field Galaxy Redshift Survey (2dFGRS)   The 2dFGRS, completed in 2002 [19], ran for five years, with the 3.9m Anglo-Australian Telescope (AAT), covering $1500 \mathrm{deg}^2$, measuring spectroscopic redshifts for a total of 232,155 galaxies. In [15] is presented the measurement of the galaxy power spectrum, applying the FKP estimator to 221,414 galaxies, considering scales between $0.02 < k < 0.15 h \mathrm{Mpc}^{-1}$. The data constrain the total matter multiplied
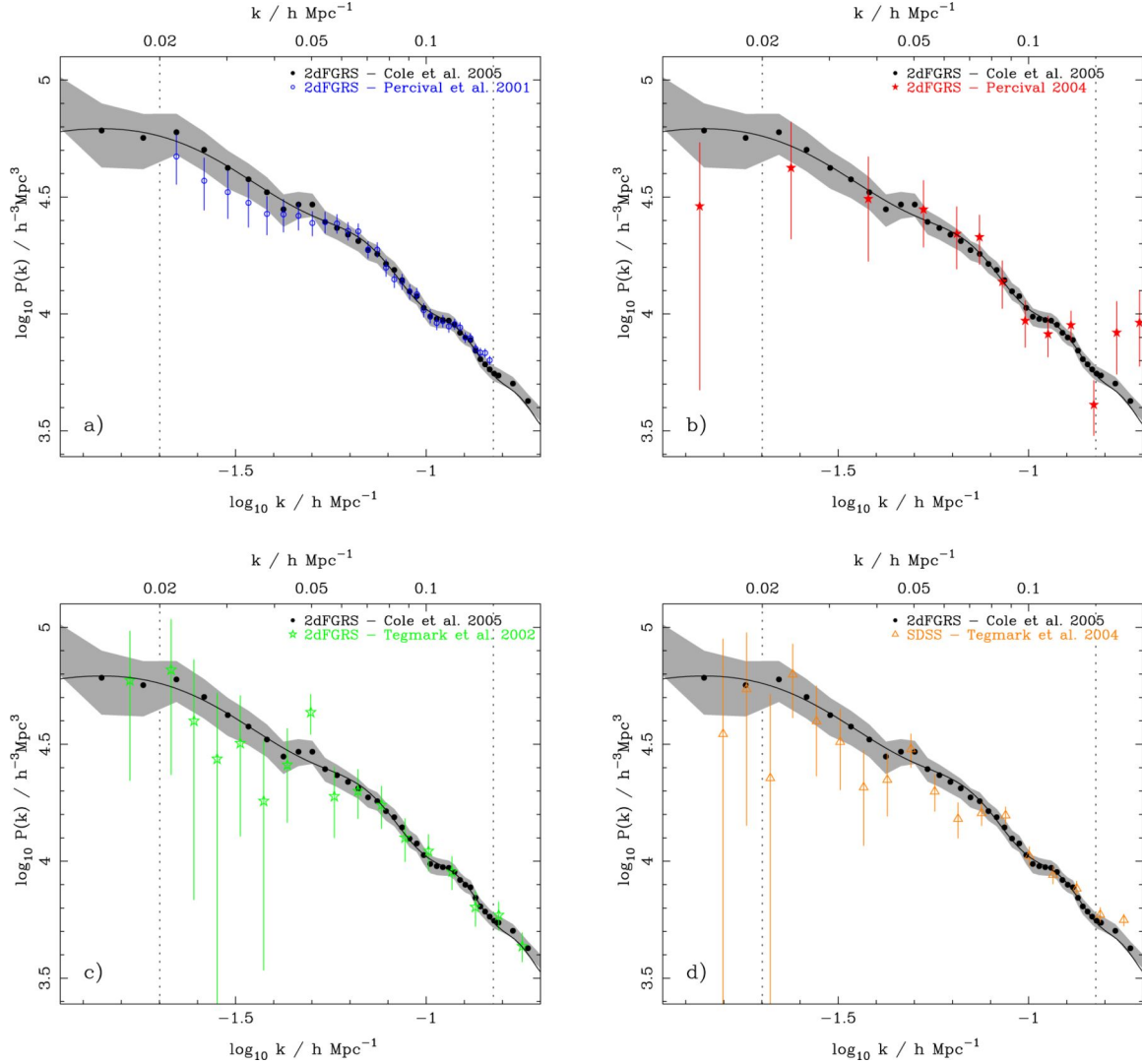
Figure 3.7: The 2dFGRS redshift space power spectrum from [15], compared with previous measurements [16][17] [18]. (Figure taken from [15])

by the Hubble parameter, at $\sim 10\%$ accuracy: $\Omega_m h = 0.168 \pm 0.016$ assuming scale invariant primordial fluctuations and the baryon fraction at $\sim 25\%$ accuracy: $\Omega_b/\Omega_m = 0.185 \pm 0.046$.

Figure 3.7 shows the redshift space power spectrum computed in [15], compared with previous measurements [16][17] [18]. Shaded regions correspond to $1 - \sigma$ confidence levels. The solid line shows the best fit obtained for the linear power spectrum normalized to match the 2dFGRS power spectrum and convoluted with the window function according to Eq. 3.45, with $\Omega_m h = 0.168$, $\Omega_b/\Omega_m = 0.17$ and $h = 0.72$.
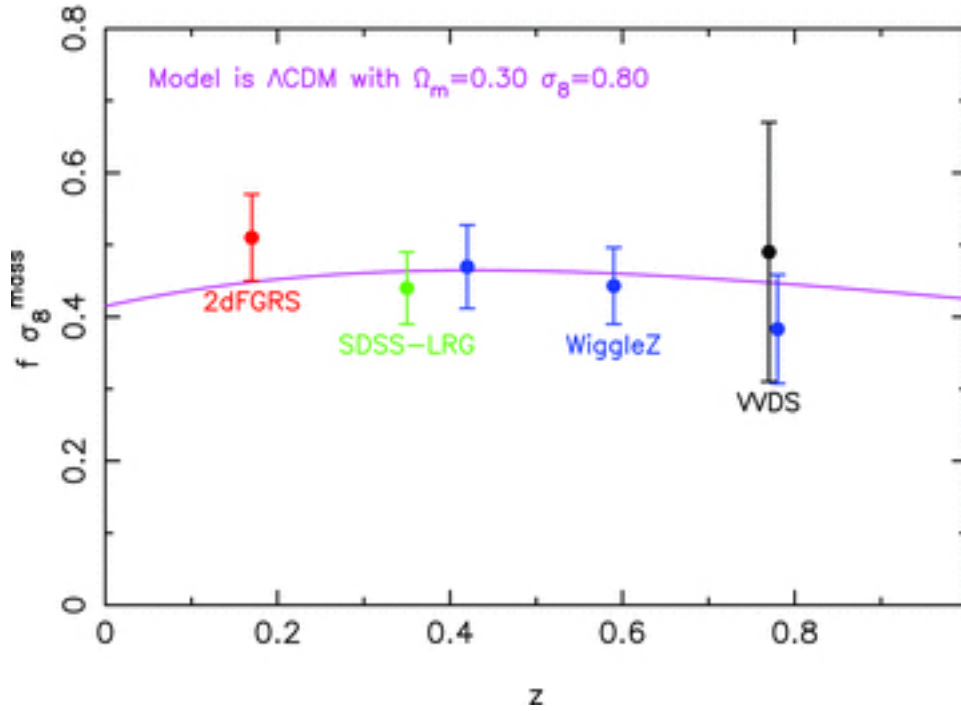
Figure 3.8: Constraints on $f\sigma_8$ obtained fitting WiggleZ data in three different redshift ranges compared to previous measurements from 2dFGRS [19], SDSS LRG [20] and VIRMOS-VLT Deep Survey [21]. (Figure taken from [22])

WiggleZ surveys   The WiggleZ Dark Energy Survey [22], completed in 2011 collected the redshifts of 240,000 galaxies in the southern sky. As for the 2dF program, the observations were carried out on the AAT using the AAOmega spectrograph, able to measure 392 spectra simultaneously. [22] present a measurement of the power spectrum, at effective redshift $z \approx 0.6$, computed on a sample of 56,159 bright emission-line galaxies observed during the WiggleZ program. The measured power spectrum is compared with a model accounting for non linear corrections and bias, at scales $k < 0.4 h\text{Mpc}^{-1}$, obtaining constraints on matter and baryon densities consistent with CMB observations. The growth rate is also measured within $\sim 20\%$ accuracy. Figure 3.8 compares the constraints on the growth rate multiplied by the amplitude term σ_8 obtained fitting WiggleZ data in three different redshift ranges, with previous measurements from 2dFGRS [19], SDSS LRG [20] and VIRMOS-VLT Deep Survey [21]. All the measurements are consistent with the ΛCDM prediction (continous line) with $\Omega_m = 0.3$, $\sigma_8 = 0.8$.

BOSS   The WiggleZ project was followed by the Baryon Oscillation Spectroscopic Survey (BOSS) [91], using the 2.5 metre telescope at Apache Point Observatory in New Mexico,

as part of the Sloan Digital Sky Survey (SDSS) collaboration. The SDSS survey in various different guises (SDSSI, SDSSI SDSSIII, see e.g. [92] [93] [91]) created the most accurate 3D map of the Universe, collecting spectra of more than three million galaxies, distributed in one third of the visible sky.

The Baryon Oscillation spectroscopic survey BOSS program from SDSSIII, 2009-2014, provided the best cosmological constraints from LSS data, by detecting the BAO using more than one million galaxies, within $0.2 < z < 0.75$. Obtaining $\sim 1.6\%$ constraint on $D_A(z)$ and at 2.3% on the Hubble parameter, [94]. From RSD analysis, [95] the growth rate is also constrained to be 0.459 ± 0.060 [95], using the first three multipoles (see Fig. 3.8 and 3.9 previous and next paragraphs).

eBOSS   The 6-year extended Baryon Oscillation Spectroscopy Survey (eBOSS) is a new redshift survey part of SDSS-IV, [96], started in July 2014, to gather the largest volume to date of any other cosmological redshift survey. The observations target multiple tracers, including more than 250,000 new luminous red galaxies (LRGs), 195, 000 emission line galaxies (ELGs) at effective redshifts of $z = 0.72, 0.87$ and over $500,000$ Quasars between $0.9 < z < 2.2$, (see 3.10). The survey goals involve distance measurement at 12% accuracy with the baryon acoustic oscillations (BAO) on the LRG sample and the first measurement at high, currently unconstrained, redshifts using the Quasars [23]. The quasars released in [97] are characterized by a lower density compared to e.g. BOSS (86 object per deg^2) but they cover an unprecedented volume $0.9 < z < 2.2$ which has allowed the first detection of the BAO at effective redshift $z = 1.52$ constraining the spherically averaged BAO distance at 3.8 per cent precision. In [98] the selection technique is presented in detail, however, in brief the quasars have been selected on imaging from SDSSI, SDSSI SDSSIII and using the Wide Field Infrared survey experiment [99], a satellite observing the entire sky in four infra-red bands. The DR14 quasar spectra were collected using the BOSS spectrograph [100] during 2 years of observations.

Systemic redshifts   Due to physical processes relative to the quasar objects, a careful treatment is required in order to infer the systemic redshift from the measured spectroscopic redshift [101]. The least biased estimate of the quasar redshift is provided by the Mg_{II} emission. However the signal to noise ratio of the Mg_{II} emission line varies significantly across the sample. For this reason the best z-estimate is based on the principal component analysis (PCA) which combines the full information from the spectra. Figure 3.9 from [23] shows the spherically averaged BAO distance measurements obtained from the DR14 quasar
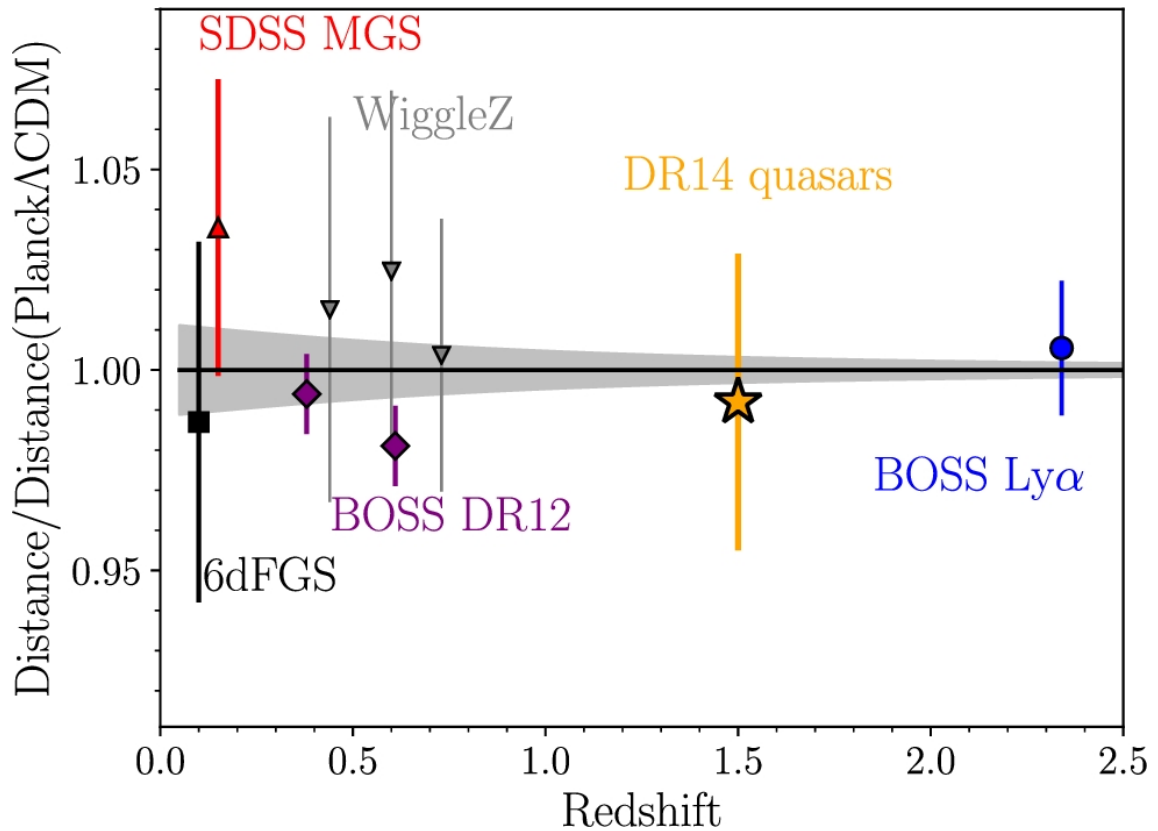
Figure 3.9: Angular distance measurements from BAO analyses (from [23]). Results from DR14 quasars [23], 6dF Galaxy Survey [24], BOSS DR12 [7], BOSS Lyα [25] and WiggleZ [26].

sample compared to the ΛCDM prediction and the previous surveys. Figure 3.9 includes results from the 6dF Galaxy Survey [24], BOSS DR12 [7] BOSS Lyα [25], WiggleZ results from [26].

3.5.4.2 Future programs

DESI The Dark-Energy Spectroscopic Instrument (DESI) is a ground based survey starting in 2019, that run for 5 years using the 4-meters Mayall telescope at the Kitt-Peak national observatory in Arizona. The Mayall telescope has been selected for its unique combination of adaptable optical and mechanical design [102]. The DESI focal plane is composed of a new 5000-fibre spectrograph covering a 3.2 deg diameter field, equipped with robotic positioners holding fiber-optic cables and sensors ensuring the alignment of the positioners. Observations during the program will observe over 30 milions galaxies producing an unprecedented map of the large scale structure covering 1/3 of the night sky (14000deg^2). The measurement of the BAO using the DESI galaxy survey will consider objects at $0.5 < z < 3.5$.
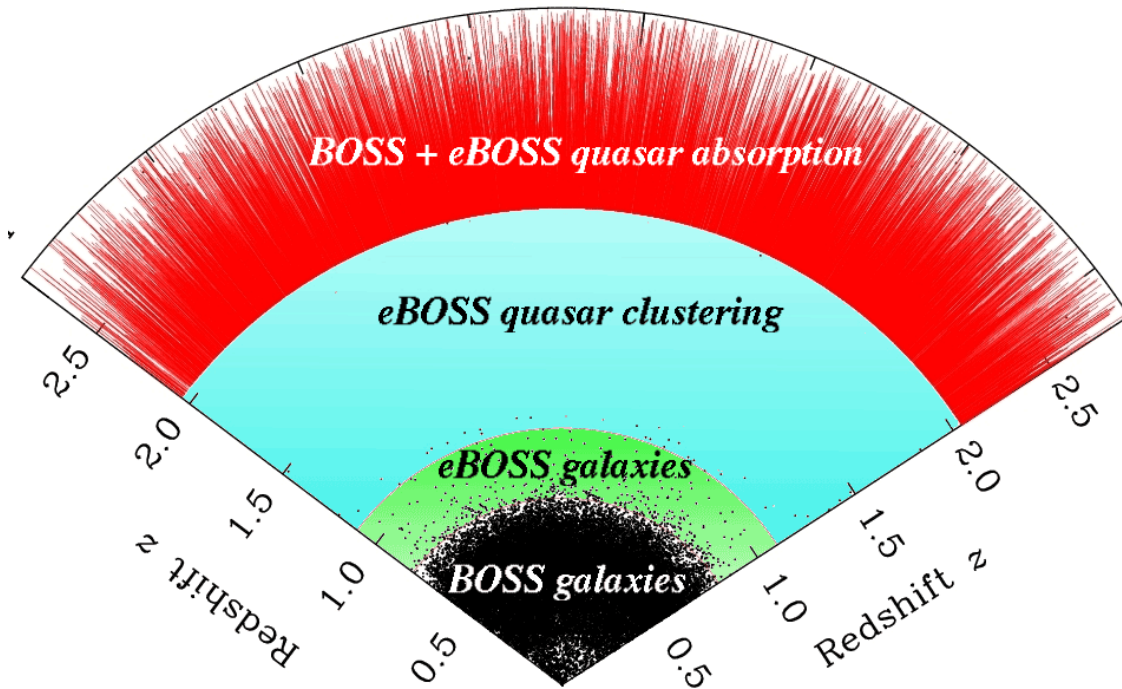
Figure 3.10: The SDSS planned coverage of the Universe (sdss.org)

The predicted number of targets to lie between 20-30 million, with a spectroscopic redshift error less than $0.001(1 + z)$, will reach the required tracer density, $1500/deg^2$, in order to optimize the BAO performance. The measurements of the distance scale are predicted to reach 1% accuracy in each redshift bin. DESI will collect spectra of bright emission galaxies (BGs) at redshifts $0 < z0.5$; luminous red galaxies (LRGs) up to $z \sim 1$ which are high massive objects, populated by old stars and therefore easily identified thanks to their red color. The survey will also select quasars from $z \sim 2.1$ up to $z \sim 3.5$ thanks to their high luminosity. Finally the main sample will be composed of ~ 30 million of emission line galaxies (ELGS) with a wide range of redshift: $0.6 < z < 1.6$

EUCLID The European Space Agency (ESA) mission Euclid [50], expected to be launched in 2020 is a major wide-field and spectroscopy space mission that is part of the Cosmic Vision 2015-2025 program. Observations will be carried out by using a 1.2 m telescope designed to provide a large field of view, working in the visible and near-infrared and mounted on the satellite to capture the shapes of galaxies with a resolution better than 0.2 arcsec. The survey will cover $15000deg^2$, observing billions of galaxies and collecting ~ 100 million galaxy redshifts. The two main probes of the survey are redshift clustering and weak lensing; for weak lensing, Euclid will measure photometric redshifts of 30 objects per $arcmin^2$

pushing the error on photo-z to be $\sigma_z/(1+z) < 0.05$, thanks to complementary photometry-ground-based data from surveys [103]. To accomplish high precision detection of the BAO, the spectroscopic survey will reach a precision on the spectroscopic redshift lower than $\sigma_z/(1+z) \leq 0.001$. Other complementary probes will be considered such as cross correlation with the CMB, strong lensing and luminosity distance through supernoave Ia in order to achieve a better understanding of the expansion history of the Universe and of the structure formation.

MEASURING THE LARGE SCALE STRUCTURES

Observed galaxy clustering exhibits local transverse statistical isotropy around the line-of-sight (LOS). The variation of the LOS across a galaxy survey complicates the measurement of the observed clustering as a function of the angle to the LOS, as fast Fourier transforms (FFTs) based on Cartesian grids, cannot individually allow for this. Recent advances in methodology for calculating LOS-dependent clustering in Fourier space include the realization that power spectrum LOS-dependent moments can be constructed from sums over galaxies, based on approximating the LOS to each pair of galaxies by the LOS to one of them. In this chapter we show that we can implement this method using multiple FFTs, each measuring the LOS-weighted clustering along different axes. The $N \log N$ nature of FFTs means that the computational speed-up is a factor of > 1000 compared with summing over galaxies. This development should be beneficial for future projects such as DESI and *Euclid* which will provide an order of magnitude more galaxies than current surveys.

The content of the work presented here refers to the collaborative research published in [104]. My contribution to this project: I decomposed the angular dependence of the clustering into a Cartesian basis; I coded the estimator and performed tests (i) and (iii) in 4.4.

4.1 Context

Although the Universe is predicted to be statistically homogeneous and isotropic as we discussed, observational effects including the Alcock-Paczynsky effect [73] and redshift-

space distortions [52] mean that the observed clustering, when translated into comoving coordinates using a fiducial distance-redshift relation exhibits local transverse statistical isotropy around the line-of-sight (LOS). The key measurement to be made from a galaxy survey is consequently the clustering as a function of the angle to the LOS. If we consider the clustering in configuration-space, then the base 'unit' is a pair of galaxies, and it is common to treat a pair as having a single LOS, usually defined as the direction to the pair centre. Any effects because the galaxies within the pair have different LOSs are called 'wide-angle effect' [105][106] and are small of the scales of interest [107][108] [109]. Thus in configuration space, measuring clustering with respect to the LOS can be easily incorporated into pair-counting algorithms [110] with a different LOS for each pair.

In Fourier-space, dealing with the varying LOS is more difficult, as fast Fourier methods do not, in general, allow for the variation of LOS. One option is to use a basis built up from spherical harmonics and Bessel functions, which naturally separates clustering with respect to the varying LOS [111] [112]. In recent works, [113] and [107] considered the Fourier decomposition as a sum over pairs of galaxies, and showed that this can be simplified (and speeded up) by assuming that the LOS to the pair is equivalent to the LOS to a single galaxy (the method is described in section 4.2). This approximately doubles the 'wide-angle effect' [114], but that is small anyway. In this chapter we consider how to implement the transform with this approximation, showing that we can use multiple fast Fourier transforms (FFTs) to perform this sum for power-law moments in $\mu \equiv \hat{\mathbf{k}} \cdot \hat{\mathbf{r}}_{LOS}$, the cosine of the angle to the LOS (this is described in § 4.3). In section 4.4 we present the results of tests of three implementations of the method, summing over galaxies, grid cells or using FFTs. We show that they provide consistent results, and compare the computational burden of each. By decomposing any moment into a sum over Legendre polynomials, we can construct any power spectrum moment using this method (§ 4.5). Such developments are necessary as one often wants to measure the power spectrum moments, not only in the data, but also in a large numbers of mock catalogues used to estimate and test for errors: for example, [115] analysed the Baryon Oscillation Spectroscopic Survey (BOSS; [116]) data and 1000 mock catalogues. Thus the computational burden of measuring LOS-dependent clustering is high.

4.2 Method

We start by defining the function [86],

$$(4.1) \qquad F(\mathbf{r}) = \frac{w(\mathbf{r})}{I^{1/2}} [n(\mathbf{r}) - \alpha n_s(\mathbf{r})],$$

where n and n_s are, respectively, the observed number density of galaxies and the number density of a synthetic catalog of *randoms*, Poisson sampled with the same mask and selection function as the survey with no other cosmological correlations, and w is the weight. α normalizes the weighted random catalogue to match the weighted galaxy catalogue. The factor I normalizes the amplitude of the observed power in accordance with its definition in a universe with no survey selection, $I \equiv \int d\mathbf{r}\, w^2 \bar{n}^2(\mathbf{r})$. From Eq. (4.1) we can define the multipole power spectrum estimator as [86][113],

$$
\begin{aligned}
\hat{P}_\ell(k) = \frac{(2\ell+1)}{I} \int \frac{d\Omega_k}{4\pi} & \left[\int d\mathbf{r}_1 \int d\mathbf{r}_2\, F(\mathbf{r}_1) F(\mathbf{r}_2) \right. \\
& \left. \times\, e^{i\mathbf{k}\cdot(\mathbf{r}_1-\mathbf{r}_2)} \mathscr{L}_\ell(\hat{\mathbf{k}}\cdot\hat{\mathbf{r}}_h) - P_\ell^{noise}(\mathbf{k}) \right],
\end{aligned}
$$
(4.2)

where $\mathbf{r}_h \equiv (\mathbf{r}_1 + \mathbf{r}_2)/2$ denotes the LOS of the pair of galaxies $\mathbf{r}_1$ and $\mathbf{r}_2$, $d\Omega_k$ is the solid angle element in k-space, $\mathscr{L}_\ell$ is the ℓ−th order Legendre polynomial and P_ℓ^{noise} is the shot noise term given by

$$
P_\ell^{noise}(\mathbf{k}) = (1 + \alpha) \int d\mathbf{r}\, \bar{n}(\mathbf{r})\, w^2(\mathbf{r}) \mathscr{L}_\ell(\hat{\mathbf{k}}\cdot\hat{\mathbf{r}}).
$$
(4.3)

For multipoles of order $\ell > 0$, $P_\ell^{noise} \ll \hat{P}_\ell$, and consequently the shot noise correction is negligible.

Denoting the number of k-modes that we want to evaluate by N_k and the number of elements that we use to perform the integral over $\mathbf{r}_1$ or $\mathbf{r}_2$ by N, we see that the computation of Eq. (4.2) will be of order $N_k \times N^2$, as the integrals in $\mathbf{r}_1$ and $\mathbf{r}_2$ are not separable. In effect this approach performs a pair-wise clustering analysis and translates into Fourier-space. As N increases the total time needed to evaluate Eq. (4.2) grows dramatically.

The FKP-estimator [86] uses the fact that the monopole is independent of the LOS, so the $\mathbf{r}_i$ integrals are separable and FFTs are trivial to apply. Consequently, the $N_k \times N^2$ process becomes a $N_k \log(N)$ one, which it is easier to handle: here N is the number of grid cells at which we sample F, so for a FFT $N = N_k$. This estimator has been successfully applied in many galaxy surveys to estimate the power spectrum and bispectrum monopoles (see e.g. [117]).

The Yamamoto estimator [113] keeps the relevant LOS information by approximating the LOS of each pair of galaxies with the LOS of one of the two galaxies, $\mathscr{L}_\ell(\hat{\mathbf{k}}\cdot\hat{\mathbf{r}}_h) \simeq \mathscr{L}_\ell(\hat{\mathbf{k}}\cdot\hat{\mathbf{r}}_2)$, which yields

$$
\begin{aligned}
\hat{P}_\ell^{Yama}(k) \;=\; \frac{(2\ell+1)}{I} \int \frac{d\Omega_k}{4\pi} & \left[\int d\mathbf{r}_1\, F(\mathbf{r}_1) e^{i\mathbf{k}\cdot\mathbf{r}_1} \right. \\
\times\; & \left. \int d\mathbf{r}_2\, F(\mathbf{r}_2) e^{-i\mathbf{k}\cdot\mathbf{r}_2} \mathscr{L}_\ell(\hat{\mathbf{k}}\cdot\hat{\mathbf{r}}_2) - P_\ell^{noise}(\mathbf{k}) \right].
\end{aligned}
$$
(4.4)

This is a reliable approximation on the scale of interest, which clearly improves on assuming a single fixed LOS for the whole survey for $l > 0$, but will eventually break down at very large scales [109]. The integrals over $\mathbf{r}_1$ and $\mathbf{r}_2$ in Eq. (4.4) are separable, so $\hat{P}_\ell^{Yama}$ becomes a $N_k \times N$ process if the integrals are solved using sums. In this chapter, we show that the efficiency of this estimator can be further improved by making use of FFT algorithms, such as FFTW[1].

4.3 FFT implementation

Here we show how to write the Yamamoto algorithm in terms of $N_k \log(N)$ processes for any multipoles. For simplicity and with no loss of generality, we focus on the monopole (which, as discussed in §4.2, reduces to the standard FKP description), the quadrupole and the hexadecapole. We proceed by defining the convenient function,

$$(4.5) \qquad A_n(\mathbf{k}) = \int d\mathbf{r} \, (\hat{\mathbf{k}} \cdot \hat{\mathbf{r}})^n F(\mathbf{r}) e^{i\mathbf{k} \cdot \mathbf{r}}.$$

With this, Eq. (4.4) reads,

$$(4.6) \qquad \hat{P}_0^{Yama}(k) = \frac{1}{I} \int \frac{d\Omega_k}{4\pi} \left[A_0(\mathbf{k}) A_0^*(\mathbf{k}) \right] - P_0^{noise}$$

$$(4.7) \qquad \hat{P}_2^{Yama}(k) = \frac{5}{2I} \int \frac{d\Omega_k}{4\pi} \, A_0(\mathbf{k}) \left[3A_2^*(\mathbf{k}) - A_0^*(\mathbf{k}) \right],$$

$$\hat{P}_4^{Yama}(k) = \frac{9}{8I} \int \frac{d\Omega_k}{4\pi} \, A_0(\mathbf{k}) \left[35A_4^*(\mathbf{k}) - 30A_2^*(\mathbf{k}) \right.$$

$$(4.8) \qquad \qquad \left. + 3A_0^*(\mathbf{k}) \right].$$

Note that the expressions for A_2 and A_4 include a k-dependent term $(\hat{\mathbf{k}} \cdot \hat{\mathbf{r}})^n$ in the integrand, which means that in this form Fourier transforms cannot directly be applied. This is the standard problem of dealing with a varying LOS across a survey. However, by means of the trivial decomposition

$$(4.9) \qquad \hat{\mathbf{k}} \cdot \hat{\mathbf{r}} = \frac{k_x r_x + k_y r_y + k_z r_z}{kr} \,,$$

A_2 can be easily re-written into a combination of smaller building blocks,

$$A_2(\mathbf{k}) = \frac{1}{k^2} \left\{ k_x^2 B_{xx}(\mathbf{k}) + k_y^2 B_{yy}(\mathbf{k}) + k_z^2 B_{zz}(\mathbf{k}) \right.$$

$$(4.10) \qquad \qquad \left. + 2 \left[k_x k_y B_{xy}(\mathbf{k}) + k_x k_z B_{xz}(\mathbf{k}) + k_y k_z B_{yz}(\mathbf{k}) \right] \right\} \,,$$

---

[1]Fastest Fourier Transform in the West: http://fftw.org

where

(4.11)
$$B_{ij}(\mathbf{k}) \equiv \int d\mathbf{r} \frac{r_i r_j}{r^2} F(\mathbf{r}) e^{i\mathbf{k}\cdot\mathbf{r}} .$$

Similarly, for A_4 we obtain,

$$\begin{aligned}
A_4(\mathbf{k}) = \frac{1}{k^4} \big\{ & k_x^4 C_{xxx} + k_y^4 C_{yyy} + k_z^4 C_{zzz} \\
& + 4 \left[k_x^3 k_y C_{xxy} + k_x^3 k_z C_{xxz} + k_y^3 k_x C_{yyx} \right. \\
& \left. + k_y^3 k_z C_{yyz} + k_z^3 k_x C_{zzx} + k_z^3 k_y C_{zzy} \right] \\
& + 6 \left[k_x^2 k_y^2 C_{xyy} + k_x^2 k_z^2 C_{xzz} + k_y^2 k_z^2 C_{yzz} \right] \\
& + 12 k_x k_y k_z \left[k_x C_{xyz} + k_y C_{yxz} + k_z C_{zxy} \right] \big\} ,
\end{aligned}$$
(4.12)

where

(4.13)
$$C_{ijl}(\mathbf{k}) \equiv \int d\mathbf{r} \frac{r_i^2 r_j r_l}{r^4} F(\mathbf{r}) e^{i\mathbf{k}\cdot\mathbf{r}} .$$

A_0, B_{ij} and C_{ijl} are all $N_k \log(N)$ processes by the use of any FFT algorithm. This provides the value of monopole, quadrupole and hexadecapole with only 1, 7 $(= 1 + 6)$ and 22 $(= 1 + 6 + 15)$ FFTs, respectively. Similar decompositions are possible for higher order multipoles.

It is important to remark that, from an analytical point of view, the above decomposition is completely equivalent to Eq. (4.4), i.e. it does not involve any further approximation. In essence, the symmetry encoded in the Yamamoto estimator of Eq. (4.4) is exactly captured by including the variation of the LOS in the relative weighting of different galaxies to FFTs, each covering a different axis direction, Eqs. (4.10) and (4.12).

4.4 Performance tests

In this section we test the following three implementations of the Yamamoto estimator, solving Eq. (4.4) using the following.

1. A sum over galaxies and randoms (the total number of points is N) and the N_k k-modes of interest. We will refer to this as *sum-gal*.

2. A sum over a gridded representation of F with N grid cells, and the N_k k-modes. We will only consider $N = N_k$ although this is not fixed as for an FFT, and refer to this as *sum-grid*.

3. An FFT-based implementation using a gridded representation of F with N grid cells and the $N_k = N$ k-modes. We will refer to this as *FFT-based*.

For the methods using sums we have optimised our code, minimizing the computations performed within the inner most loops, and using the Hermitian symmetry in k-space to reduce the number of k-modes summed over. We also only compute power spectrum moments for $k \le 0.3 h \mathrm{M} pc^{-1}$ for these methods. Additionally, for the *sum-grid* method we only include filled grid cells in the sum. We therefore consider that time taken by these algorithms is indicative of that achieved by most algorithms performing the transform using a sum.

We will test these three options using the public mock galaxy catalogues matched to the CMASS galaxy sample of the Sloan Digital Sky Survey (SDSS-III; [118]), BOSS Data Release 11 North Galactic Cap [119]. These catalogues each contain approximately 525,000 galaxies. We use the random catalogue provided with the galaxy mocks and we take the number density of the randoms to be 10 times higher than the number density of the galaxies, i.e., $\alpha^{-1} \simeq 10$. For the implementations that use a grid, we place the galaxies and randoms in a cubic box of size $L_b = 3500 \, \mathrm{M} pc h^{-1}$ using the Cloud-in-Cell (CiC) prescription, to obtain the quantity $F(\mathbf{r})$ of Eq. (4.1). In order to correct for the effects of the grid left by the CiC scheme we have corrected appropriately by the deconvolution window proposed in [120].

Fig. 4.1 displays the average power spectrum multipoles: monopole (red), quadrupole (blue) and hexadecapole (green) calculated from 50 mocks. The solid lines represent the *FFT-based* method, the dashed lines the *sum-grid*, and the dotted lines the *sum-gal*. The plot shows an almost exact agreement between the three implementations of Eq. (4.4). The results of the *sum-grid* algorithm show a few percent deviation at small scales. The origin of this is aliasing, which we have not corrected for. The aliasing effect for a 1024^3 grid is negligible for scales $k \le 0.4 h \mathrm{M} pc^{-1}$, and consequently does not appear for the *FFT-based* scheme. For comparison, adopting a 2048^3 grid we expect the aliasing to be negligible for wave numbers up to $\sim 0.6 h \mathrm{M} pc^{-1}$. Due to its small amplitude, at small k the hexadecapole is affected by numerical noise, which results in a general instability of the ratio between different methods.

In Table 4.1 we show a comparison between the computation times of the different algorithms of Fig. 4.1 for the monopole, quadrupole and hexadecapole of one realization of the DR11 CMASS NGC mocks. For the *FFT-based* implementation, we also show the computation times for different number of cells used. If we relax our assumption of 10 times randoms, and use X_{ran} times as many randoms as galaxies (for example, [115] used $X_{\mathrm{ran}} = 50$), then the computational time taken for *sum-gal* scales by approximately $(X_{\mathrm{ran}} + 1)/11$.
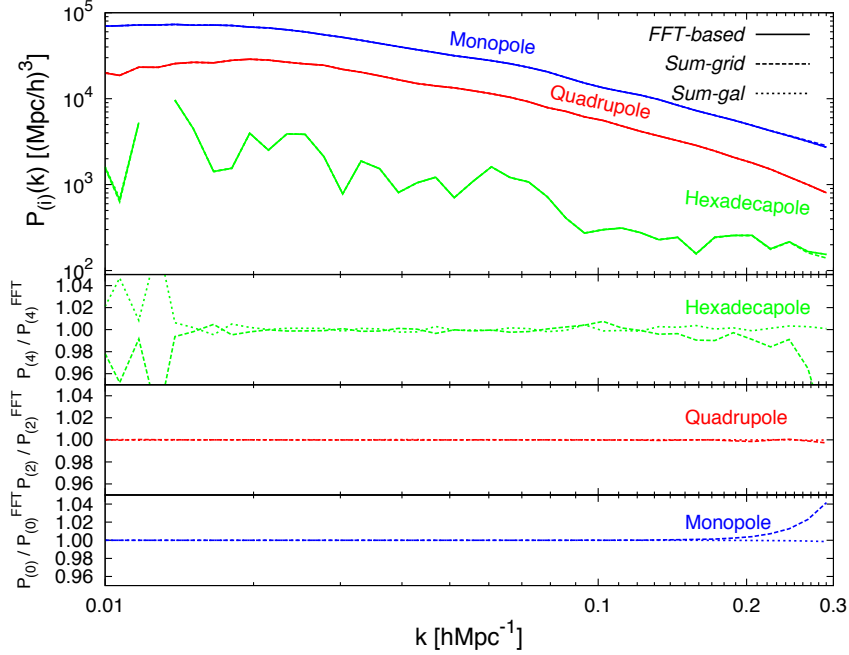
Figure 4.1: Top panel: power spectrum multipoles: monopole (blue lines), quadrupole (red lines) and hexadecapole (green lines), obtained from the average of 50 realization of PTHALOS mocks corresponding to the BOSS DR11 CMASS NGC survey geometry. The solid lines display the computation of Eq. (4.4) using the *FFT-based* method using 1024^3 grid cells. The dashed and dotted lines display the computation of the Yamamoto estimator using the *sum-grid* (with 512^3 cells) and *sum-gal* methods, respectively. In both these cases an orthonormal base of 512^3 *k*-vectors has been used. The bottom panels show the corresponding *sum-gal* and *sum-grid* multipoles divided by the *FFT-based* multipoles to highlight differences among these implementations.

	FFT-based (512^3)	FFT-based (1024^3)	FFT-based (2048^3)	sum-gal (512^3) (512^3)	sum-grid (512^3)
Time (min)	1.2	7.5	72.5	∼ 1800	∼ 2400

Table 4.1: Computation times (in minutes, using 16 processors) for the power spectrum monopole, quadrupole and hexadecapole for the three different implementations of the Yamamoto algorithm. For the *FFT-based* implementation we show the number of grid cells used: 512^3, 1024^3 and 2048^3. For the *sum-gal* algorithm the computation times are assuming $\alpha^{-1} \sim 10$ and for both *sum-gal* and *sum-grid* algorithms only computing for $k \leq 0.3h\mathrm{M}pc^{-1}$.

73

For multiple measurements for different catalogues that use the same randoms, then the time in the table reduces by a factor $1/11$ for each catalogue where the randoms do not have to be reused. However, note that in the post-reconstruction analyses of [115], the randoms are uniquely matched to each galaxy catalogue and so have to be calculated for each mock. The *sum-grid* method does not scale with the number of randoms, and is therefore faster than *sum-gal* when the number of randoms to be analysed is larger. Finally, when comparing run times, note that for *sum-gal* there is no aliasing as the galaxies and randoms are not placed on a grid, so we can use the same N_k to push to smaller k than the grid-based routines. Even allowing for these scalings, it is clear that the *FFT-based* method is significantly faster (approximately 1000 times) than either *sum-gal* or *sum-grid* for reasonable assumptions of grid size and number of randoms.

4.5   General moments of the Power Spectrum

The trick of splitting μ^n into Cartesian components employed in Eq. (4.9) will not work directly on moments of more general functions of μ. However we can still use a *FFT-based* method by decomposing the functions into Legendre polynomials and summing over the multipole-moments. For example, one proposed alternative to using multipoles is to use "Wedges" [121], where we replace $\mathscr{L}_\ell(\mu)$ in Eq. (4.4) by top hat functions in μ covering $0 \leq \mu \leq 0.5$, whose moment we denote $P_\perp$ and $0.5 < \mu \leq 1$ whose moment we denote $P_\parallel$:

$$(4.14) \qquad P_\perp(k) \;=\; \frac{2}{I} \int_0^{2\pi} \frac{d\varphi}{2\pi} \int_0^{0.5} d\mu \left[A_0(\mathbf{k}) A_0^*(\mathbf{k}) \right] - P_0^{noise},$$

$$(4.15) \qquad P_\parallel(k) \;=\; \frac{2}{I} \int_0^{2\pi} \frac{d\varphi}{2\pi} \int_{0.5}^{1} d\mu \left[A_0(\mathbf{k}) A_0^*(\mathbf{k}) \right] - P_0^{noise},$$

where φ is the azimuthal angle. Then, as discussed in [121], we can approximate these functions using the first three even Legendre polynomials as,

$$(4.16) \qquad P_\perp(k) \;\simeq\; P_0(k) - \frac{3}{8} P_2(k) + \frac{15}{128} P_4(k),$$

$$(4.17) \qquad P_\parallel(k) \;\simeq\; P_0(k) + \frac{3}{8} P_2(k) - \frac{15}{128} P_4(k).$$

In Fig. 4.2 we show the comparison between the $P_\perp$ (blue lines) and $P_\parallel$ (red lines) computed using the *sum-gal* algorithm (dashed lines), i.e. the definition of Eq. (4.14-4.15), and the combination of Eq. (4.16-4.17) computed using the *FFT-based* algorithm (solid lines). The agreement between the definition of $P_\perp$ and $P_\parallel$ and the approximation of Eq. (4.16-4.17) is very good for the range of scales studied. This suggest that the Yamamoto implementation
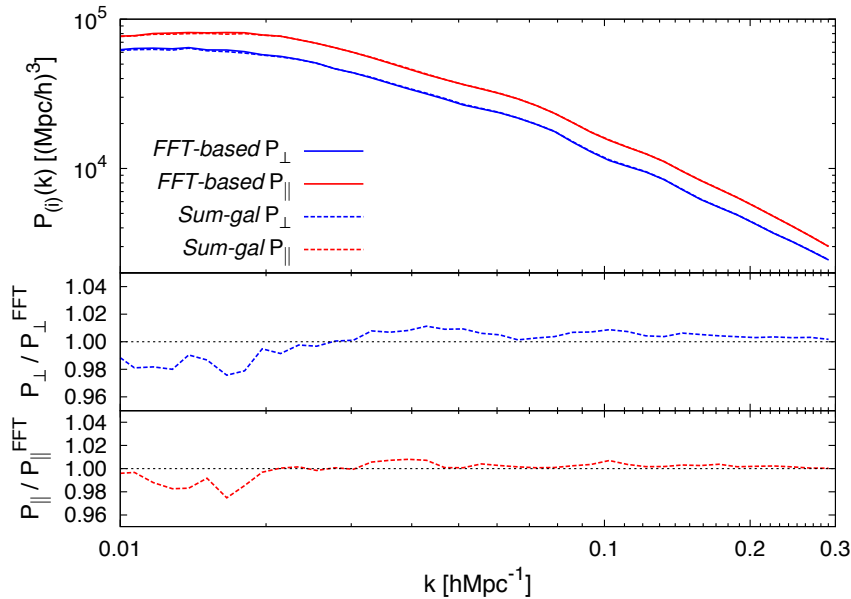
Figure 4.2: Top panel: power spectrum 'Wedges': perpendicular-to-the-LOS power spectrum monopole, $P_\perp$ (blue lines) and parallel-to-the-LOS power spectrum monopole (red lines) obtained from the average of 50 realization of PTHALOS mocks corresponding to the BOSS DR11 CMASS NGC survey geometry. The solid lines display the approximation presented by Eq. (4.16-4.17) using the monopole, quadrupole and hexadecapole computed by using the *FFT-based* method described in §4.3 placing the particles in 1024^3 grid cells. The dashed lines display the computation of the "Wedges" using *sum-gal* and Eq. (4.14-4.15), so the sum is exact. In this case an orthonormal base of 512^3 k-vector have been used. The bottom panels show the fractional differences between the *sum-gal* and the *FFT-based* method, for $P_\perp$ and $P_\parallel$ as labeled.

based on FFTs presented here is also suitable to be used to compute the wedges power spectral moments.

4.6 Summary

The main focus of this chapter has been introducing new estimators for the LOS-dependent galaxy power spectrum moments calculation. Previous method such as [113], are based on a sum over each galaxy pair assumed to be at a single LOS in order to keep the relevant angular information. However estimators implemented as in [113] are highly computationally expensive as the evaluation time required scales as N^2 with N number of galaxies (or grid-cells). In this chapter we derived and tested a new fast FFT-based estimator for the galaxy

power spectrum which decomposes the *LOS* dependence into a Cartesian grid allowing to massively reduce the computational time required for the evaluation of the power spectra multipoles ($\sim N \log(N)$). The FFT-estimator proposed can be applied to any data and it is significantly faster than pair-counting algorithms in configuration space, for this reason it will be particularly relevant in view of the next generation of redshift surveys, which will collect redshifts for more than $\sim 10^7$ of objects [122] [50].

OPTIMAL REDSHIFT WEIGHTING FOR REDSHIFT SPACE DISTORTIONS

T he low statistical errors on cosmological parameters promised by future galaxy surveys will only be realised with the development of new, fast, analysis methods that reduce potential systematic problems to low levels. We present an efficient method for measuring the evolution of the growth of structure using Redshift Space Distortions (RSD), that removes the need to make measurements in redshift shells. We provide sets of galaxy-weights that cover a wide range in redshift, but are optimised to provide differential information about cosmological evolution. These are derived to optimally measure the coefficients of a parameterisation of the redshift-dependent matter density, which provides a framework to measure deviations from the concordance ΛCDM cosmology, allowing for deviations in both geometric and/or growth. In this chapter we test the robustness of the weights by comparing with alternative schemes and investigate the impact of galaxy bias. We extend the results to measure the combined anisotropic Baryon Acoustic Oscillation (BAO) and RSD signals. The content of the work presented here refers to the research published in [123];

5.1   Wide redshift survey analysis

As we discussed in chapter 2 the large-scale galaxy distribution is expected to follow a Gaussian random field, for which the statistical information is fully encoded in 2-point

statistics, therefore the central quantities in the analysis of galaxy surveys are the Correlation Function and its Fourier-space analogue, the Power Spectrum. The observed projections of these quantities encode significant cosmological information, including the positions of the Baryonic Acoustic Oscillations (BAO), which can be used as standard rulers to reconstruct the expansion history of the Universe, [124]. The statistics also encode Redshift Space Distortions (RSD), which provide information about the large-scale growth of cosmological structure, [61].

As we discussed, to be able to reach the statistical precision promised by forthcoming surveys including DESI, [122] and Euclid, [50], at least an order of magnitude beyond current measurements, an effort to improve the methods to analyse the data is a main requirement. This includes recent key developments such as "reconstruction" to remove non-linear BAO damping, [125] or the development of fast methods to measure the anisotropic clustering signal, [104][126], as we discussed in chapter 4.

In this chapter we address one additional question: how best to combine future data from different volumes within the surveys, without losing information from galaxy pairs that span different bins, if using a binned approach and to optimally recover the desired signal. To deal with the first concern, we can make the transition from splitting into redshift-bins, to instead adopting weights that act to provide smoother windows on the data.

To optimise the weights, we must consider two factors: the first concerns changes in the observational efficiency as a function of position on the sky and redshift, and leads to weights that vary as a function of observed galaxy density, [86], and bias , [87]. The second concerns the cosmological models that we wish to distinguish between: [86], [87] wished to optimally measure a power spectrum, which was assumed to be fixed within a survey volume. If instead, we wish to measure cosmological parameters that vary across a sample, for example a quantity that evolves with redshift, then the weights must additionally be optimised to measure this evolution.

In general, RSD measurements are made for a particular volume, presented as a single measurement at an effective redshift; if e.g. the growth factor varies in a non-linear way across the sample, the effective redshift is not a good approximation, by contrast by weighting the sample we allow for variation in redshift of all the measured quantities.

[127] presented weights optimised for measuring the distance-redshift relationship using the BAO signal. They considered a second-order expansion of the distance-redshift relationship around a fiducial cosmological model, and provided sets of weights for the monopole and quadrupole moments of the correlation function (or power spectrum) designed to optimally measure these parameters. In this work we extend this derivation to

the measurement of Redshift-Space Distortions, considering the weights required for these measurements, and how they compare to the BAO-optimised weights.

The outline of the chapter is as follows. In Sec. 5.2 we briefly go through the method of linear data compression and we underline the advantages related. In Sec. 5.3 we present the cosmological model.

In Sec. 5.4 we build to a derivation of the optimal weighting scheme for redshift space distortion measurements parametrized with respect to the matter energy density evolution in redshift, $\Omega_m(z)$. The choice of Ω_m parametrization allows to easily extend the results for more general clustering models which include both redshift space distortion and Alcock & Paczyński effects (1979), AP. In the second part of the section we compare them with other possible weights optimized for RSD measurements and we discuss our assumption for linear bias model. In Sec. 5.5 we derive the generalisation of optimal weights for RSD and AP test combined measurements.

5.2 Optimal Weights

The derivation of optimal weights is equivalent to the problem of optimal data compression: we use the weights to reduce the number of data points that need to be analysed to recover the cosmological parameters. We will now review how to optimally linearly compress our data, in the case of a covariance matrix known a priori, as described in [128]. Further details on the Karhunen-Loève methods in e.g. [129] and [130].

Given the n-dimensional data-set $\mathbf{x}$, assumed to be Gaussian distributed with mean μ and covariance C, it can be linearly compressed into a new data-set y,

$$(5.1) \qquad y = \mathbf{w}^T \mathbf{x},$$

where $\mathbf{w}$ is a n-dimensional vector of weights. The measurement y has mean $\mathbf{w}^T \mu$ and variance $\mathbf{w}^T C \mathbf{w}$.

The Fisher information matrix F is defined as the second derivative of the logarithmic likelihood function $\mathscr{L} \equiv -\ln L$,

$$(5.2) \qquad F_{ij} \equiv \left\langle \frac{\partial^2 \mathscr{L}}{\partial \theta_i \partial \theta_j} \right\rangle,$$

for a set of parameters to be measured θ_i. For a single parameter θ_i,

$$(5.3) \qquad F_{ii} = \frac{1}{2} \left(\frac{\mathbf{w}^T C_{,i} \mathbf{w}}{\mathbf{w}^T C \mathbf{w}} \right)^2 + \frac{\left(\mathbf{w}^T \mu_{,i} \right)^2}{\mathbf{w}^T C \mathbf{w}},$$

where the index $,i$ denotes $\partial/\partial\theta_i$. Note that the normalisation of the weights is arbitrary The search for optimal weights is equivalent to maximising F_{ii} with respect to $\mathbf{w}$.

For a measurement of 2-point statistics from a galaxy survey, we should consider that $\mathbf{x}$ is the arrays formed by the measurements of the over-density squared, δ^2 in configuration or Fourier space. Working in Fourier space, the covariance matrix C of the power spectrum of the modes in the absence of a survey window is diagonal; for each redshift slice with volume dV and expected galaxy density $\overline{n}(r)$,

$$(5.4) \qquad\qquad C \sim \left(P_{\mathrm{fid}} + 1/\overline{n}(r)\right)^2 \frac{1}{dV},$$

where we have made the assumption that around the likelihood maxima, the power spectra P_{fid} are drawn from a Gaussian distribution with fixed covariance matrix, e.g. [131]. In this case, the first term in Eq. (5.3) vanishes. Maximising F_{ii} with respect to $\mathbf{w}$, we find the only non-trivial eigenvector to be

$$(5.5) \qquad\qquad \mathbf{w}^T = C^{-1}\mu_{,i},$$

and the new compressed data set reduces to

$$(5.6) \qquad\qquad y = \mu_{,i}^T C^{-1}\mathbf{x}.$$

Note that, to linear order, y contains the same information as $\mathbf{x}$, which can be checked by substituting $\mathbf{w} = C^{-1}\mu_{,i}$ in Eq. (5.3), and seeing that F remains unchanged. Eq. (5.5) forms the basis for our derivation of optimal weights.

Eq. (5.3) shows why it does not make sense to optimise for the set of δ (as opposed to δ^2). This is because, although now the second term in Eq. (5.3) now vanishes as $\langle\delta\rangle = 0$, the resulting eigenvector equation derived from the first term shows that there is no single set of optimal weights, even under the simplifying assumption of a diagonal covariance matrix. We can still apply the weights derived for δ^2 to individual galaxies if we assume that the scales upon which clustering is being measured are small with respect to the cosmological changes that affect the relative weights. We would then simply weight each galaxy (and the expected density used to estimate δ) by $\mathbf{w}_{gal} = \sqrt{\mathbf{w}_{\delta^2}}$.

Note that the optimal set of weights given in Eq. (5.5) depends upon the derivatives of $\mu_i = P_{,i}$. Consequently in the rest of the work presented here, we concentrate our analysis on the form of $P_{,i}$, which directly gives the form for the weights. If $P_{,i}$ matches for different measurements, then the optimal weights will also match.

The weights can be seen as a generalisation of the FKP weights presented in [86]. The FKP weights are obtained by minimising the fractional variance in the power under the

assumption that fluctuations are Gaussian and have the form

$$(5.7) \qquad w_{\mathrm{FKP}}(r) = \frac{1}{1 + \overline{n}(r)P(k)};$$

The weights defined by Eq. (5.5) depend on the inverse of the covariance matrix: assuming the redshift slices to be independent we can invert the Covariance matrix for a chosen scale and recover the FKP weights.

The cosmological model-dependent weights depend on the covariance matrix assumed and on the derivative of the mean value of the model with respect to the parameter that we want to estimate. Thus, once these quantities are fixed, it is not trivial to adapt a particular set of weights for different models. However, it would be very useful to set up weights that can be applied to make different measurements: both for computational reasons and in order to perform joint fits to the data. In this work we will start by deriving weights to be applied to RSD measurements and then we will broaden this to consider jointly measuring the RSD and the AP effect. Comparing the set of weights in these different situations shows whether it is likely that a single set of weights can be used to make optimal measurements in both situations.

5.3 Cosmological Model

5.3.1 Fiducial Cosmology

The ΛCDM scenario predicts the nature of dark energy as a cosmological constant with equation of state parameter $w = -1$ where the dynamical expansion of the Universe is specified by Friedmann equation

$$(5.8) \qquad \frac{H_{\mathrm{fid}}^2(z)}{H_{0,\mathrm{fid}}^2} = \Omega_{m,0,\mathrm{fid}}(1+z)^3 + \Omega_{k,\mathrm{fid}}(1+z)^2 + \Omega_{\Lambda,\mathrm{fid}}(z),$$

where the subscript the "0" stands for quantities evaluated at $z = 0$ while "fid" denotes fiducial quantities. With $\Omega_{\Lambda,\mathrm{fid}}$ dark energy density, $\Omega_{k,\mathrm{fid}} = 1 - \Omega_{m,\mathrm{fid}} - \Omega_{\Lambda,\mathrm{fid}}$ curvature, and H_0 the present-day Hubble parameter. We have

$$(5.9) \qquad \Omega_{m,\mathrm{fid}}(z) = \frac{\Omega_{m,0,\mathrm{fid}}(1+z)^3}{H_{\mathrm{fid}}^2(z)/H_{0,\mathrm{fid}}^2},$$

where $\Omega_{m,0}$ refers to energy density evaluated at $z = 0$. In a Friedmann-Roberston-Walker universe the solution for the linear growth factor $D_{\mathrm{fid}}(z)$ and the dimensionless linear growth

rate f are given by

(5.10)
$$
\begin{aligned}
g_{\mathrm{fid}}(\Omega_{m,\mathrm{fid}}(z)) &\equiv \frac{D_{\mathrm{fid}}(z)}{a} \\
&= \frac{5\Omega_{m,\mathrm{fid}}(z)\,H_{\mathrm{fid}}^3(z)}{2(1+z)^2} \int_z^\infty \mathrm{d}z'\,\frac{(1+z')}{H_{\mathrm{fid}}^3(z')}
\end{aligned}
$$

with scale factor a;

(5.11)
$$
\begin{aligned}
f_{\mathrm{fid}}(\Omega_{m,\mathrm{fid}}(z)) = {}&-1 - \frac{\Omega_{m,\mathrm{fid}}(z)}{2} + \Omega_{\Lambda,\mathrm{fid}}(z) \\
&+ \frac{5\Omega_{m,\mathrm{fid}}(z)}{2g_{\mathrm{fid}}(z)}.
\end{aligned}
$$

Under the assumption of a flat universe i.e. $\Omega_{k,\mathrm{fid}} = 0$, we have $\Omega_{\Lambda,\mathrm{fid}}(z) = 1 - \Omega_{m,\mathrm{fid}}(z)$.

For the fiducial galaxy bias model we choose a simple *ad hoc* functional form as used in [132], which is approximately correct for the $H\alpha$ galaxies to be observed by the Euclid survey,

(5.12)
$$
b_{\mathrm{fid}} = \sqrt{1+z}.
$$

5.3.2   Parametrising deviations

The derivation presented in Sec. 2 required us to define the parameters that we wish to optimise measurement of. We wish to choose parameters that allow us to measure deviations from the ΛCDM model. In the absence of compelling alternative cosmological models, we choose parameters that define an expansion in redshift of the cosmological behaviour we wish to understand - in our case the structure growth rate, and the expansion rate. Both of these can be modelled by deviations in $\Omega_m(z)$ away from the fiducial model, and we adopt this quantity as the redshift-evolving quantity that we wish to understand, rather than the distance-redshift relation considered by [127], which does not easily extend to structure growth differences. We expand $\Omega_m(z)$ around the fiducial model as,

(5.13)
$$
\frac{\Omega_m(z)}{\Omega_{m,\mathrm{fid}}(z)} = q_0\left(1 + q_1 y(z) + \frac{1}{2}q_2 y(z)^2\right),
$$

we fix a pivot redshift z_p within the survey redshift range and y is defined as $y(z) + 1 \equiv \frac{\Omega_{m,\mathrm{fid}}(z)}{\Omega_{m,\mathrm{fid}}(z_p)}$; the expansion parameters q_0, q_1, q_2 are obtained from Eq. 7.4 and its first and

second derivatives evaluated at z_p;

(5.14)
$$
\begin{aligned}
q_0 &= \frac{\Omega_m(z_p)}{\Omega_{m,\text{fid}}(z_p)}, \\
q_1 &= \frac{\Omega_{m,\text{fid}}(z_p)}{\Omega_m(z_p)} \frac{d\Omega_m/dz|_{z_p}}{d\Omega_{m,\text{fid}}/dz|_{z_p}} - 1, \\
q_2 &= \Bigg[\frac{\Omega_{m,\text{fid}}(z_p)}{\Omega_m(z_p)} \frac{d^2\Omega_m}{dz^2}\Big|_{z_p} - \frac{d^2\Omega_{m,\text{fid}}}{dz^2}\Big|_{z_p} \\
&\quad - \left(\frac{\Omega_{m,fid}(z_p)}{\Omega_m(z_p)} \frac{d\Omega_m/dz|_{z_p}}{d\Omega_{m,\text{fid}}/dz|_{z_p}} - 1 \right)\left(\frac{2}{\Omega_{m,\text{fid}}(z_p)} \right. \\
&\quad \left. \left(\frac{d\Omega_{m,\text{fid}}}{dz} \right)^2 \Big|_{z_p} + \frac{d^2\Omega_{m,\text{fid}}}{dz^2}\Big|_{z_p} \right) \Bigg] \frac{\Omega_{m,\text{fid}}(z_p)}{\left(d\Omega_{m,\text{fid}}/dz|_{z_p} \right)^2}.
\end{aligned}
$$

The Hubble parameter with respect to $\Omega_m(z)$ is

(5.15)
$$
\frac{H^2(z)}{H_0^2} = \frac{\Omega_{m,0}(1+z)^3}{\Omega_m(z)},
$$

where we have assumed that the dark matter equation of state is fixed,

(5.16)
$$
\mathscr{P} = w\rho; \; w = 0
$$

with pressure $\mathscr{P}$ and matter density ρ.

A broader range of models could be derived by perturbing the homogeneous solution of the Einstein equations, but in this work we restrict ourselves to deviations close to ΛCDM in the dark energy and curvature components. The Ω_m parametrisation allows for many deviations from ΛCDM: all the standard cosmological parameters can be written in terms of the q_i parameters e.g. if we want to allow for modified gravity models we can parametrize the growth factor as a function of $\Omega_m(z)$. Alternatively, if we are studying the deviations from a fiducial geometry we can parametrize the AP parameters. We assume that Eqns. (7.10) & (7.7) hold for the perturbed $\Omega_m(z)$, which fix how the parameters q_i lead to deviations in the growth rate away from the fiducial model.

5.4 Redshift weighting assuming known distance-redshift relation

In this section we derive a set of optimal weights to measure $\Omega_m(z)$ and the bias when the distance-redshift relation is assumed known, i.e we derive the weights for an observed power spectrum that contains only the distortion due to RSD and not due to AP effect.

We will discuss three different cases with different assumptions about parameters assumed known: the first two aim to estimate $\Omega_m(z)$ and the third the bias, parametrised by $b\sigma_8(z)$. In 5.4.2 we consider the case in which the bias is known and fixed to a fiducial model; in this case we are considering that the information about Ω_m is coming from all the terms of the Power Spectrum multipoles. We discuss this set of weight with respect to different fiducial models for the bias in order to test how knowing the bias would affect the results. However this first set of weights does not match the actual RSD measurements condition in which the bias is unknown. We then consider in 5.4.3 a case for RSD measurements where we assume the growth information is not coming from tangential power and the only information to be considered comes from $f\sigma_8$. Bias evolution plays an important role for clustering measurements even if, in the redshift range of interest for future and current surveys, Ω_m is significantly more sensitive to redshift than bias, (see Sec. 5.3). As our last case, in 5.4.4, we consider for completeness a set of weight to measure the bias relation as a function of redshift.

5.4.1   Modelling the observed power spectrum

For simplicity we adopt a linear model for the redshift-space distortions, assume that we are working in the plane parallel approximation, and assume a linear deterministic bias model so that the power spectrum in redshift space, P^s is related to the real power spectrum P by

$$(5.17) \qquad P^s(\mathbf{k}) = (b + f\mu_{\mathbf{k}}^2)^2 P(k)$$

where $P(k)$ is the linear real space power spectrum and where $\mu_{\mathbf{k}} \equiv \hat{\mathbf{z}} \cdot \hat{\mathbf{k}}$ is the cosine of the angle between the wavevector $\mathbf{k}$ and the line of sight $\hat{\mathbf{z}}$, [52].

It is common to decompose P^s into an orthonormal basis of Legendre polynomials such that, in linear regime, the redshift power spectrum is well described by its first three non-null moments: monopole P_0, quadrupole P_2 and hexadecapole P_4.

$$(5.18) \qquad P^s(\mathbf{k}) = \mathscr{P}_0(\mu_{\mathbf{k}})P_0(k) + \mathscr{P}_2(\mu_{\mathbf{k}})P_2(k) + \mathscr{P}_4(\mu_{\mathbf{k}})P_4(k),$$

related with $P(k)$ through ,

$$(5.19) \qquad P_0(k) = \left(b^2 + \frac{2}{3}bf + \frac{1}{5}f^2 \right) P(k)$$

,

$$(5.20) \qquad P_2(k) = \left(\frac{4}{3}bf + \frac{4}{7}f^2 \right) P(k),$$

(5.21)
$$P_4(k) = \left(\frac{8}{35}f^2\right)P(k).$$

We normalise the power spectrum using the standard variance of the galaxy distribution smoothed on scale $R = 8h^{-1}$Mpc, $\sigma_8(z)$, where

(5.22)
$$\sigma_8(z) = \sigma_{8,0}D(z) = \sigma_{8,0}\frac{g(z)}{1+z}.$$

This normalisation enters into Eq. (5.17) in a way that is perfectly degenerate with b and f, which could be replaced by new parameters $(b\sigma_8)$ and $(f\sigma_8)$.

5.4.2 Optimal weights to measure $\Omega_m(z)$ assuming known bias

We build optimal weights by taking the derivative of the power spectrum model with respect to the parameters q_i, As discussed in section 5.2, hereafter we only consider the component of these weights that varies with $P_{,i}$, which we denote for the monopole, quadrupole and hexadecapole, respectively w_0, w_2, w_4. For simplicity we refer to these as the "weights", but it is worth remembering that there is a missing inverse variance component.

(5.23)
$$w_{\ell,q_i} = \frac{\partial P_\ell}{\partial q_i}$$

We explicitly write the redshift dependence of P on the q_i parameters, so that the right side of Eq. (5.23) becomes

(5.24)
$$\frac{\partial P_\ell}{\partial q_i} = \frac{\partial P_\ell}{\partial f}\frac{\partial f}{\partial q_i} + \frac{\partial P_\ell}{\partial \sigma_8}\frac{\partial \sigma_8}{\partial q_i}$$

This second term assumes that we are recovering information from both radial and transverse modes. This is true for the transverse component if the bias is known perfectly. We build our set of weights as a function of redshift, for the monopole we have

(5.25)
$$w_{0,i} = \left(\frac{2}{3}b + \frac{2}{5}f\right)\sigma_8^2\frac{\partial f}{\partial q_i} + \left(b^2 + \frac{2}{3}bf + \frac{1}{5}f^2\right)2\sigma_8\frac{\partial \sigma_8}{\partial q_i}$$

with

(5.26)
$$\frac{\partial f(z)}{q_i} = \frac{\partial \Omega_m(z)}{\partial q_i}\left(\frac{5}{2g(z)} - \frac{1}{2}\right) - \frac{\partial \Omega_m(z)}{\partial q_i} - \frac{5}{2}\frac{\Omega_m(z)}{g^2(z)}\frac{\partial g(z)}{\partial q_i},$$

(5.27)
$$\frac{\partial \sigma_8(z)}{\partial q_i} = \frac{\sigma_{8,0}}{1+z}\frac{\partial g(z)}{\partial q_i};$$

where

(5.28)
$$\frac{\partial g(z)}{\partial q_i} = \frac{5}{2(1+z)^2} \left(\frac{\partial \Omega_m(z)}{\partial q_i} H^3(z) + 3H^2(z) \frac{\partial H(z)}{\partial q_i} \Omega_m(z) \right) \cdot$$
$$\int_z^\infty dz' \frac{(1+z')}{H^3(z')} - \frac{15\Omega_m(z)H^3(z)}{2(1+z)^2} \int_z^\infty dz' \frac{(1+z')}{H^4(z')} \frac{\partial H(z')}{\partial q_i}$$

(5.29)
$$\frac{\partial H(z)}{\partial q_i} = H_0 \frac{1}{2} \left(\frac{\Omega_{m,0}(1+z)^3}{\Omega_m(z)} \right)^{-1/2} \frac{(1+z)^3}{\Omega_m(z)}$$
$$\cdot \left(\frac{\partial \Omega_{m,0}}{\partial q_i} - \frac{\Omega_{m,0}}{\Omega_m} \frac{\partial \Omega_m(z)}{\partial q_i} \right),$$

with

(5.30)
$$\frac{\partial \Omega_m}{\partial q_0} = \Omega_{m,fid}(z),$$
$$\frac{\partial \Omega_m}{\partial q_1} = \Omega_{m,\text{fid}}(z) y(z),$$
$$\frac{\partial \Omega_m}{\partial q_2} = \Omega_{m,\text{fid}}(z) \frac{y^2(z)}{2}.$$

Note that in the equations above the $P(k)$ term has been factored out; all the terms are evaluated at $q_0 = 1$ since we are ignoring the weights dependence on cosmology.

Similarly for the quadrupole and for the hexadecapole

(5.31)
$$w_{2,q_i} = \left(\frac{4}{3}b + \frac{8}{7}f \right) \sigma_8^2 \frac{\partial f}{\partial q_i} + \left(\frac{4}{3}bf + \frac{4}{7}f^2 \right) 2\sigma_8 \frac{\partial \sigma_8}{\partial q_i},$$

$$w_{4,i} = \frac{16}{35} f \sigma_8^2 \frac{\partial f}{\partial q_i} + \frac{8}{35} f^2 2\sigma_8 \frac{\partial \sigma_8}{\partial q_i}.$$

Figure 5.1 shows the set of weights for the monopole, quadrupole and hexadecapole, with a convenient normalization. All the plot are generated considering a ΛCDM model with $\Omega_{m,0} = 0.31$ as the fiducial cosmology. We explore a wide redshift range to see general trends, as if we are analysing data from a range of surveys. We fix a pivot redshift in $z_p = 0.4$. All three weights with respect to parameters q_0 (blue lines) show a peak at redshift $z \sim 0.1 - 0.2$; this is due to $\partial\Omega_m/\partial q_i$ term which rapidly grows until about $z \sim 2$ and then tends to a constant. The peak corresponds to the $\Omega_m \sim \Omega_\Lambda$ epoch: the weights aim to highlight the deviations from the fiducial cosmology ΛCDM, and therefore peak approximately in the range of the equivalence between matter and Λ. At higher redshifts the weights decrease due to the decreasing dependence of $\Omega_m(z)$ on f and σ_8.

The weights about the *slope parameters*, q_1 (orange line), rapidly grow at low redshift driven by $\partial \Omega_m / \partial q_1$ and $\partial P_\ell / \partial \sigma_8$, and then start decreasing as $\partial f / \partial \Omega_m$ and $\partial P_\ell / \Omega_m$ dominate. We see that they pickup small differences about the peak due to the different dependencies on P_ℓ.

The green lines displays the weights with respect to the second order parameter q_2: they are similar, with a minimum about $z \sim 0.5$: this difference with respect to q_0 and q_1 is due to the $\partial \Omega_m / \partial q_2$ term, which starts decreasing with z until about $z \sim 0.4$ and then slowly increases. Comparing the monopole, quadrupole and hexadecapole weights we see that the weights behave in a similar way for all three statistics; the hexadecapole weights show a faster decrease for all three parameters, due to the absence of the bias dependence. However the differences with monopole and quadrupole are small, confirming our assumption that the bias choice does not drastically change the weights in the region of interest.

5.4.2.1 Application of the method

We have derived a set of weights that compress the information available in the power spectrum across a range of redshifts. In practice, to apply the method, we weight galaxies, assuming $\mathbf{w}_{gal} = \sqrt{\mathbf{w}_{\delta^2}}$, to obtain a set of monopole, quadrupole and hexadecapole for each set of weights.

If we were only interested in a single parameter, (e.g. q_0) and we thought all the information came from the monopole, we would measure the weighted $P_{w,0}$ by applying the w_{0,q_0} to each galaxy; we would then fit q_0 by comparing the data with the theoretical prediction for the monopole, weighted at different redshifts as

$$(5.32) \qquad P_{0,w_{0,q_0} \mathrm{model}}(k) = \int dz \, P_0(k,z) \cdot w_{0,q_0}(z).$$

Where the $P_0(k,z,q_0)$ corresponds to the monopole prediction, e.g Eq.5.19 and we have ignored the window effects. If we further assume the simple linear model for RSD, [52],

$$(5.33) \qquad P_0(k,z) = \left(b^2 + \frac{2}{3} b f(\Omega_m(q_0,z)) + \frac{1}{5} f(\Omega_m(q_0,z))^2 \right) P(k);$$

we can express f in terms of $\Omega_m(q_0,z)$ according to Eq. 7.7.

In order to simultaneously measure all three q_i parameters, we measure each multipole weighted to be optimal for each q_i parameters, i.e. we weight galaxies with the different w_{i,q_j} functions and we build a data vector Π as,

$$(5.34) \qquad \Pi^T = (P_{0,w_0,q_0}, P_{0,w_0,q_1}, P_{0,w_0,q_2} \dots P_{4,w_4,q_2})^{\mathrm{T}}.$$
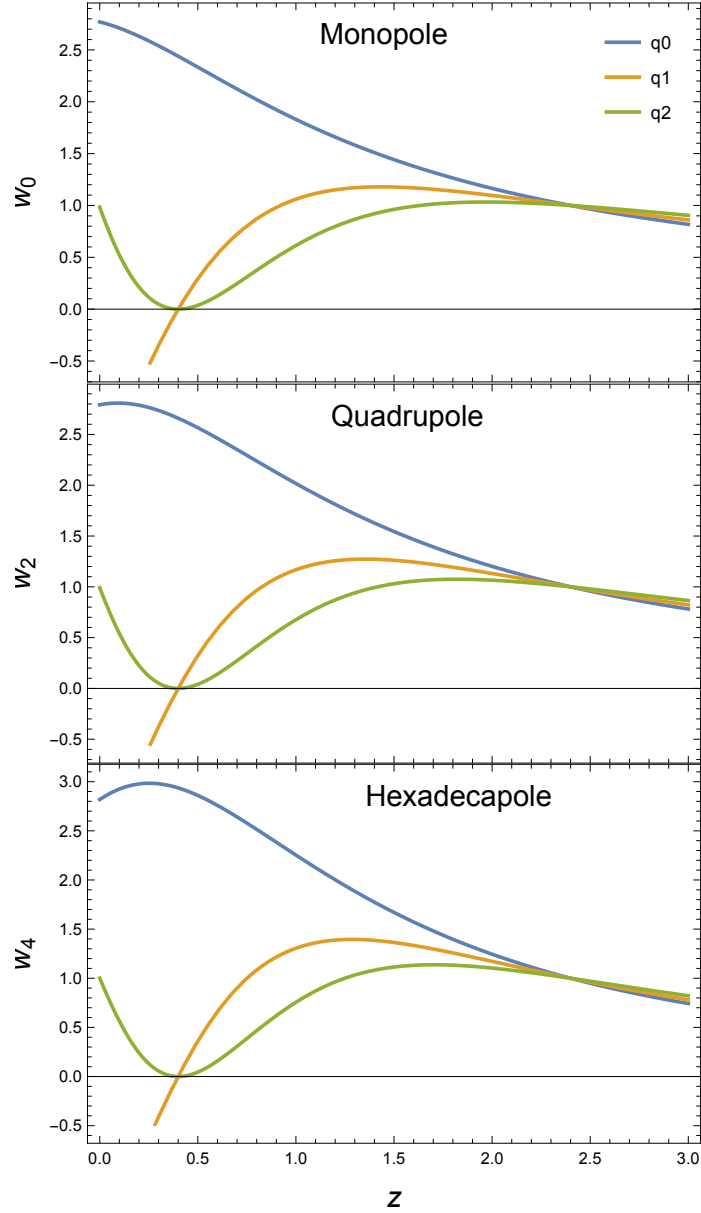
Figure 5.1: The weights for the monopole (w_0) , quadrupole (w_2) and hexadecapole (w_4) with respect to the q_i parameters: blue lines indicate the weight with respect to q_0, orange lines indicate the weight with respect to q_1 and the green lines the weight with respect to q_2. These weights assume a fiducial bias evolving as $b = \sqrt{1+z}$ and were calculated for RSD measurements assuming that the bias is known, as described in Sec. 5.4.2.

Note that each weighted multipole $P_{i,w_{i,q_j}}$ provides a particular piece of information about $\Omega_m(z)$ that optimizes the measurement of each q_i. We constrain the three q_i by jointly fitting from the data-vector Π compared with a Π_{model}. In practice we assume a Gaussian likelihood and minimize

$$\chi^2 \propto (\Pi - \Pi_{model})^{\mathrm{T}} C^{-1} (\Pi - \Pi_{model}); \tag{5.35}$$

where each $P_{i,w_{i,q_j}}$ inside Π_{model} is modeled as in Eq. 5.32. The C^{-1} term corresponds to the joint covariance matrix.

5.4.2.2 The dependence on the fiducial bias model

We now test the robustness of the set of weights for Ω_m, presented in 5.4.2, with respect to the bias model. To do this we compute sets of weights from different choices of $b(z)$. We first derive the set of weights presented in Sec. 5.4, parametrized with respect to Ω_m, fixing a constant bias, $b = 1.024$, which is our fiducial value at $z = 0.45$, then we repeat for $b = 1/D_{\mathrm{fid}}(z)$.

Figures 5.2, 5.3 show that the behaviour of the weights with redshift is similar to previous results and there are no significant differences in the shapes. As expected the differences are more visible in the monopole (top panel) than in the quadrupole (bottom panel) since the former is more sensitive to galaxy bias. We exclude the weights for the hexadecapole since it does not depend on galaxy bias.

5.4.3 Optimal weights to measure $\Omega_m(z)$ with unknown bias

RSD measurements constrain the product of the two key parameters f and σ_8 and it is common to consider a single measurement of $[f\sigma_8]$, marginalising over an unknown bias. Therefore we present a set of weights that matches the philosophy of current RSD measurements: we consider the term $[b\sigma_8]$ to be *independent* from $[f\sigma_8]$ since we marginalize over the bias. Considering e.g. the monopole

$$P_0 = \left([b\sigma_8]^2 + \frac{2}{3}[b\sigma_8][f\sigma_8](z) + \frac{1}{5}[f\sigma_8]^2(z) \right) P(k)/(\sigma_8^2) \tag{5.36}$$

for unknown bias the dependence on the q_i parameters is only through $[f\sigma_8]$. We derive the set of weight by taking the derivative of P_0, P_2, P_4 with respect to q_1, q_2, q_3,

$$w_{0,q_i} \equiv \left(\frac{2}{3}[b\sigma_8] + \frac{2}{5}[f\sigma_8](z) \right) \frac{\partial[f\sigma_8]}{\partial q_i}(z), \tag{5.37}$$
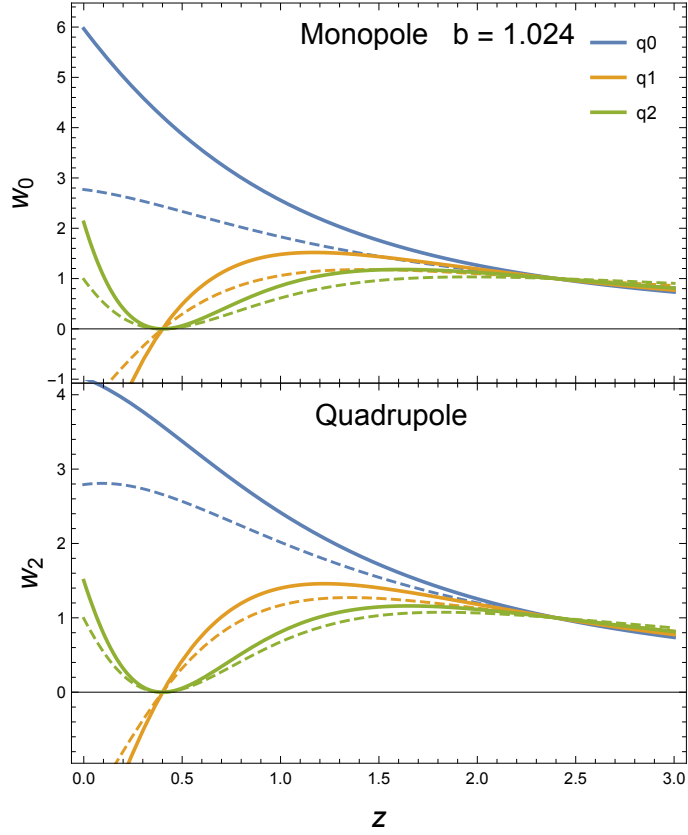
Figure 5.2: Solid lines as Fig. 5.4.2, but assuming a constant bias $b = 1.024$. We compare this set of weights with the results presented in Fig 5.4.2, (dashed lines), obtained assuming a bias evolving as $b = \sqrt{1 + z}$.

$$(5.38) \qquad w_{2,q_i} \equiv \left(\frac{4}{3}[b\sigma_8] + \frac{8}{7}[f\sigma_8](z) \right) \frac{\partial[f\sigma_8]}{\partial q_i}(z),$$

$$(5.39) \qquad w_{4,q_i} \equiv \left(\frac{16}{35}[f\sigma_8](z) \right) \frac{\partial[f\sigma_8]}{\partial q_i}(z),$$

where the derivatives $\partial[f\sigma_8]/\partial q_i(z)$ are obtained using Eq. 5.26 and 5.27.

Figure 5.4, shows the set of weights for the monopole, quadrupole and hexadecapole parametrized with respect to q_0, q_1, q_2, when ignoring the information contained in $[b\sigma_8]$, conveniently normalised. We compare them with the weights derived in 5.4.2, presented in Fig 5.4.2, (dashed lines). The main difference between the two set of weights lies on the assumptions we make for galaxy bias: if we are setting it as completely unknown, considering only the information contained in $[f\sigma_8]$ or if we are including $[b\sigma_8]$ term, constraining $b(z)$ to a fiducial model; however the plots show a very similar behaviour between the two cases,
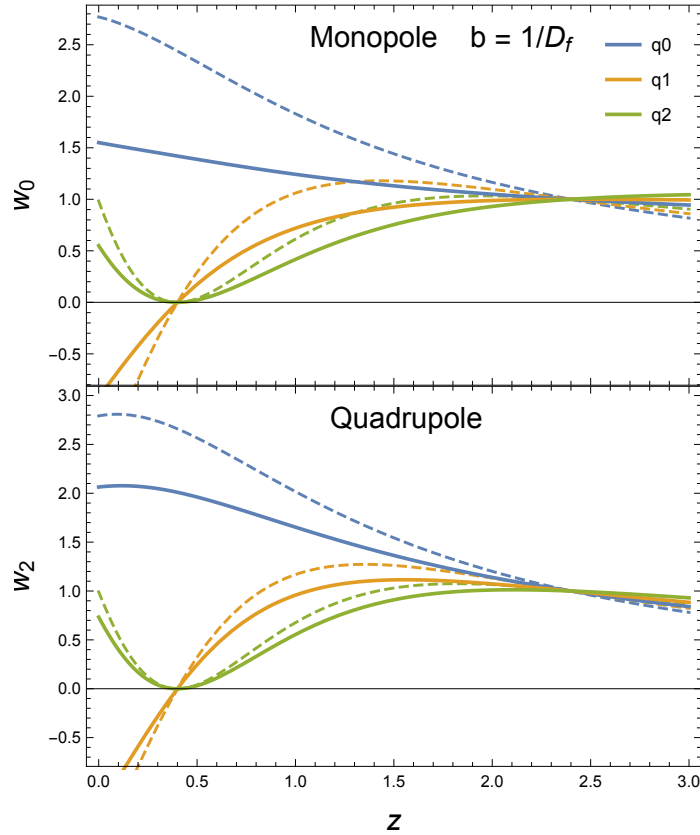
Figure 5.3: Solid lines as Fig. 5.4.2, but assuming a fiducial bias evolving with redshift as $b = 1/D_f(z)$. We compare this set of weights with the results presented in Fig 5.4.2, (dashed lines), obtained assuming a bias evolving as $b = \sqrt{1+z}$.

it is clear then that the tangential modes do not play a large role in determining optimal weights.

5.4.4 Optimal weights to measure bias

For completeness we will show how to derive weights that optimally measure the evolution of the bias parameter around the fiducial model.

In an analogous manner to Eq. 7.4 we model $[b\sigma_8](z)$ as an expansion about a fiducial model $[b\sigma_8]_{\text{fid}}$:

$$(5.40) \qquad \frac{[b\sigma_8](z)}{[b\sigma_8]_{\text{fid}}(z)} = \eta_0\left(1 + \eta_1 x + \frac{1}{2}\eta_2 x^2\right)$$

about a pivot redshift z_p, where $1 + x \equiv \frac{[b\sigma_8]_{\text{fid}}(z)}{[b\sigma_8]_{\text{fid}}(z_p)}$.
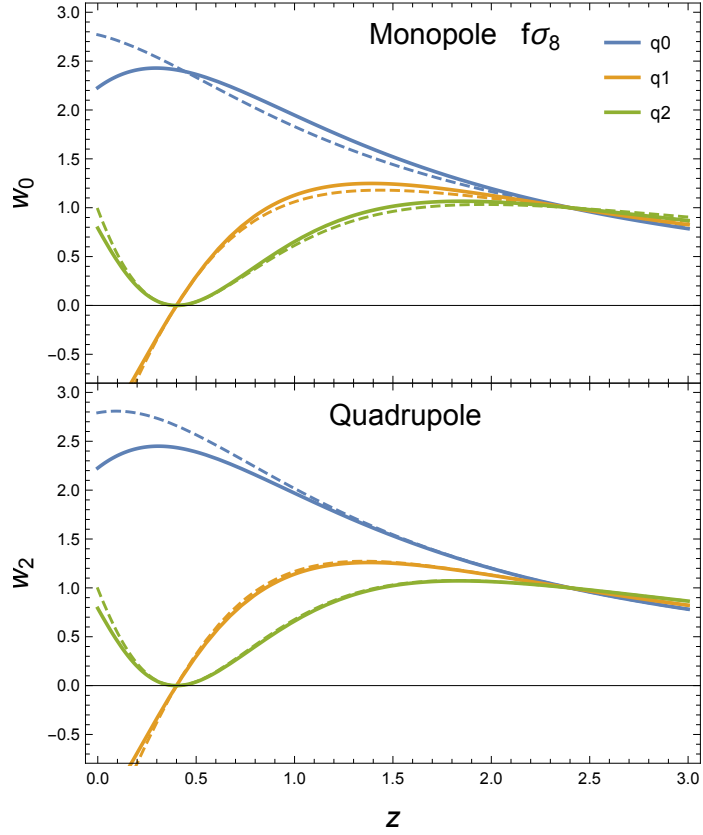
Figure 5.4: Solid lines show weights for the monopole (w_0) quadrupole (w_2) and hexade-capole (w_4) , with respect to the q_i parameters ignoring the information in $b\sigma_8$ term, as described in Sec. 7.2.2. These are compared with the weights presented in Fig. 5.4.2 (dashed lines), which assume the bias is known.

The η parameters correspond to the derivative 0,1,2 of $[b\sigma_8](z)$ relation evaluated at z_p.

In analogy with measuring q_i, we can derive a set of weights that optimally estimate the bias-redshift through the η_j parameters,

$$(5.41) \qquad\qquad w_{\ell, \eta_j} = \frac{\partial P_\ell}{\partial [b\sigma_8]} \frac{\partial [b\sigma_8]}{\eta_j}$$

This set of weights can be applied instead of the set of weights with respect to Ω_m in case we want to measure deviations from the fiducial model chosen for the bias. We do not plot these weights for simplicity but include the derivation to show how they could be calculated.

5.5 Redshift weighting assuming unknown distance-redshift relation

Our previous results provide an optimal scheme specific for RSD measurements; as pointed out in the introduction it would be very useful to optimize at the same time geometric measurements and thus enable measurements that include all the parameters both for computational costs either for accuracy of the results. An optimal weighted scheme for BAO measurements has been recently presented in [127] where the authors describe a weighting scheme parametrized with respect to the distance-redshift relation, including the AP effect modelled as

<div align="right">(5.42)</div>

$$k_\perp \to \alpha^{-1}(1+\epsilon)k_\perp,$$
$$k_\parallel \to \alpha^{-1}(1+\epsilon)^{-2}k_\parallel,$$

with parameters α, for isotropic deformation and ϵ, for anisotropic. The method optimises only BAO measurements, constraining the covariance matrix at BAO scales and ignoring the growth parameters.

In this section we will account for both distortions due to peculiar velocities and distortions due to incorrect choice of geometry described by Alcock-Paczyński effect. We still use a parametrization of $\Omega_m(z)$ to define deviations from our fiducial model as described in Eq. 7.4.

5.5.1 Modelling AP and RSD in the observed $P(k)$

We denote k^t and k the true and observed coordinates respectively, then assuming an incorrect geometry transforms the coordinates

<div align="right">(5.43)</div>

$$k^t = \frac{k}{\alpha_\perp}\left[1+\mu^2\left(\frac{\alpha_\perp^2}{\alpha_\parallel^2}-1\right)\right]^{1/2},$$
$$\mu^t = \mu\frac{\alpha_\perp}{\alpha_\parallel}\left[1+\mu^2\left(\frac{\alpha_\perp^2}{\alpha_\parallel^2}-1\right)\right]^{-1/2},$$

with $\alpha_\parallel$ defined as the ratio between the observed and the true Hubble parameter, $H(z)/H_t(z)$ and $\alpha_\perp$ defined as ratio between the true and the observed angular diameter distance $D_{A,t}(z)$ / $D_A(z)$; the multipoles at the observed k are related to the Power Spectrum at k^t, through

<div align="right">(5.44)</div>

$$P_\ell(k) = \frac{2\ell+1}{2}\int_{-1}^{1}d\mu P(k^t,\mu^t)\mathscr{L}_\ell(\mu)$$

For linear redshift space distortion, [52], inserting the transformation of the coordinates given by Eq. 5.43, the galaxy power spectrum at the true wavenumber is

$$
P^s(k^t, \mu^t) = \frac{1}{\alpha_\perp^2 \alpha_\parallel} P\left[\frac{k}{\alpha_\perp} \left[1 + \mu^2 \left(\frac{\alpha_\perp^2}{\alpha_\parallel^2} - 1 \right) \right]^{1/2} \right]
$$

$$
\left[1 + \mu^2 \left(\frac{\alpha_\perp^2}{\alpha_\parallel^2} - 1 \right) \right]^{-2} \left\{ 1 + \mu^2 \left[(\beta + 1) \frac{\alpha_\perp^2}{\alpha_\parallel^2} - 1 \right] \right\}^2 .
$$

(5.45)

We use the notation $\beta \equiv f/b$ for simplicity with equations. We expand at first order P in the right side of Eq. 5.45, in order to get analytical derivatives with respect to the expansion parameters. We have tested numerically that this approximation does not influence our conclusions. Introducing $\varphi \equiv \frac{\alpha_\perp^2}{\alpha_\parallel^2} - 1$, we can expand the right side of Eq. 5.45 to first order about $(\alpha_\perp, \varphi) = (1, 0)$, using

$$
P\left[\frac{k}{\alpha_\perp} \left(1 + \mu^2 \varphi \right)^{1/2} \right] \approx P(k) +
$$

$$
(\alpha_\perp - 1) \frac{\partial P}{\partial k} \frac{\partial k}{\partial k^t} \frac{\partial k^t}{\partial \alpha_\perp} \Big|_{\substack{\alpha_\perp = 1 \\ \varphi = 0}} + \varphi \frac{\partial P}{\partial k} \frac{\partial k}{\partial k^t} \frac{\partial k^t}{\partial \varphi} \Big|_{\substack{\alpha_\perp = 1 \\ \varphi = 0}}
$$

(5.46)

Substituting in Eq. 5.45 and then in Eq. 5.44, we obtain models of the multipoles accounting for both RSD and AP effects to be

$$
P_\ell(k) = \frac{2\ell + 1}{2} \int_{-1}^{1} d\mu \mathcal{L}_\ell(\mu) \left\{ P(k) \left(1 + \mu^2 \beta \right)^2 + \right.
$$

$$
\varphi \left[\frac{1}{2} \frac{\partial P}{\partial \ln k} \mu^2 \left(1 + \mu^2 \beta \right)^2 + P(k)(-2\mu^2)(1 + \beta \mu^2)^2 + \right.
$$

$$
\left. 2\mu^2 (1 + \beta \mu^2)(1 + \beta) P(k) - \frac{1}{2} P(k)(1 + \mu^2 \beta)^2 \right] +
$$

$$
\left. (1 - \alpha_\perp)(1 + \mu^2 \beta)^2 \left(\frac{\partial P}{\partial \ln k} + 3P(k) \right) \right\}
$$

(5.47)

In particular it holds that $P^s(k)$ at linear order is described by the first three multipoles, as discussed in 3. The monopole, quadrupole and hexadecapole are

$$
\begin{aligned}
P_0(k) &= \frac{1}{2}\sigma_8^2 \Bigg\{ \left(2 + \frac{4}{3}\beta + \frac{2}{5}\beta^2\right) P(k) + \varphi\left[\left(\frac{1}{3} + \frac{2}{5}\beta + \frac{1}{7}\beta^2\right)\right. \\
&\quad \frac{\partial P}{\partial \ln k} - \left(1 + \frac{2}{15}\beta - \frac{1}{35}\beta^2\right) P(k)\Bigg] + (1 - \alpha_\perp)\Big(2 \\
&\quad + \frac{4}{3}\beta + \frac{2}{5}\beta^2\Big)\left(\frac{\partial P}{\partial \ln k} + 3P(k)\right)\Bigg\}, \\
P_2(k) &= \frac{5}{2}\sigma_8^2\Bigg\{\left(\frac{8}{15}\beta + \frac{8}{35}\beta^2\right) P(k) + \varphi\left[\left(\frac{2}{15} + \frac{8}{35}\beta\right.\right. \\
&\quad + \frac{2}{21}\beta^2\Big)\frac{\partial P}{\partial \ln k} - \left(\frac{4}{21}\beta + \frac{4}{105}\beta^2\right) P(k)\Bigg] + (1- \\
&\quad \alpha_\perp)\left(\frac{8}{15}\beta + \frac{8}{35}\beta^2\right)\left(\frac{\partial P}{\partial \ln k} + 3P(k)\right)\Bigg\}, \\
P_4(k) &= \frac{9}{2}\sigma_8^2\Bigg\{\frac{16}{315}\beta^2 P(k) + \varphi\left[\left(\frac{16}{315}\beta + \frac{8}{231}\beta^2\right)\frac{\partial P}{\partial \ln k}\right. \\
&\quad - \left(\frac{32}{315}\beta + \frac{24}{385}\beta^2\right) P(k)\Bigg] + (1 - \alpha_\perp)\frac{16}{315}\beta^2\Big(\frac{\partial P}{\partial \ln k} + \\
&\quad 3P(k)\Big)\Bigg\}.
\end{aligned}
\tag{5.48}
$$

5.5.2 AP and RSD weights derivation, assuming known bias

As before, the weights for the power spectrum multipoles, assuming information from both RSD and AP effects, are obtained by taking the derivative of the P_i with respect to the q_i parameters defined in 5.3.2,

$$
\begin{aligned}
w_{\ell,q_i} = \frac{\partial P_\ell}{\partial q_i} &= \frac{\partial P_\ell}{\partial \varphi}\frac{\partial \varphi}{\partial q_i} + \frac{\partial P_\ell}{\partial \alpha_\perp}\frac{\partial \alpha_\perp}{\partial q_i} \\
&\quad + \frac{\partial P_\ell}{\partial \beta}\frac{\partial \beta}{\partial f}\frac{\partial f}{\partial q_i} + \frac{\partial P_\ell}{\partial \sigma_8}\frac{\partial \sigma_8}{\partial q_i}.
\end{aligned}
\tag{5.49}
$$

all the derivatives are evaluated at the fiducial model. In case of flat universe we have

$$
\alpha_\perp(z) = \frac{\int_0^z dz' \, 1/H(q_i, z')}{\int_0^z dz'' \, 1/H_{\text{fid}}(z'')}
\tag{5.50}
$$

Inserting the definition of β and φ,

$$
\begin{aligned}
\frac{\partial \beta}{\partial f} &= \frac{1}{b}, \\
\frac{\partial \varphi}{\partial q_i} &= -\frac{2\alpha_\perp^3}{\alpha_\parallel^3}\left(\frac{1}{\alpha_\perp}\frac{\partial \alpha_\parallel}{\partial q_i} + \frac{-\alpha_\parallel}{\alpha_\perp^2}\frac{\partial \alpha_\perp}{\partial q_i}\right),
\end{aligned}
\tag{5.51}
$$

95

where

$$
\begin{aligned}
\frac{\partial \alpha_\parallel}{\partial q_i} &= -\frac{1}{H_{\text{fid}}(z)} \frac{\partial H}{\partial q_i}, \\
\frac{\partial \alpha_\perp}{\partial q_i} &== \frac{\int_0^z dz' - \frac{1}{H_{\text{fid}}^2(z')} \frac{\partial H}{\partial q_i}}{\int_0^z dz'' 1/H_{\text{fid}}(z'')}.
\end{aligned}
\tag{5.52}
$$

The weights have arbitrary normalization but we cannot factor out the scale dependence as we did for the RSD weights since we now have two different k-dependent terms P and $dP/d\ln k$. However we tested this and found that this dependence is very weak.

Figure 5.5 shows the weights optimal for RSD and AP measurements evaluated at $k = 0.1$ $h\,\text{M}Pc^{-1}$, for the monopole, quadrupole and hexadecapole respectively. Blue lines indicate the weights with respect to q_0, orange lines with respect to q_1 and green lines with respect to q_2. Comparing with the previous result that assumed a known distance-redshift relation (dashed lines), it is possible to see that the behaviour of the three weights does not change drastically. In general the redshift dependence is stronger including also the AP effect and the new weights show a more enhanced maximum. Since the contribution from φ and $\alpha_\perp$ vanish for q_0, the weights w_{i,q_0} are equivalent to the previous weights without AP effect. (Fig 7.1).

5.5.3 AP-RSD weights assuming unknown bias

If we now neglect the information given by $[b\sigma_8]$, as we did for one set of RSD weights, we substitute $\beta = f/b$, then we change the Eq. 5.52 to

$$
\begin{aligned}
w_{\ell,q_i} = \frac{\partial P_\ell}{\partial q_i} = & \frac{\partial P_\ell}{\partial \varphi} \frac{\partial \varphi}{\partial i} + \frac{\partial P_\ell}{\partial \alpha_\perp} \frac{\partial \alpha_\perp}{\partial q_i} \\
& + \frac{\partial P_\ell}{\partial f\sigma_8} \frac{\partial f\sigma_8}{\partial q_i},
\end{aligned}
\tag{5.53}
$$

where we have assumed that $\partial[b\sigma_8]/\partial q_i = 0$.

In Sec 5.4 we showed that there are no significant differences between the cases in which $b\sigma_8$ is known and unknown, however, for the reasons discussed in Sec. 4, they are more consistent with the RSD measurements. We do not plot any new results since the differences are very small.
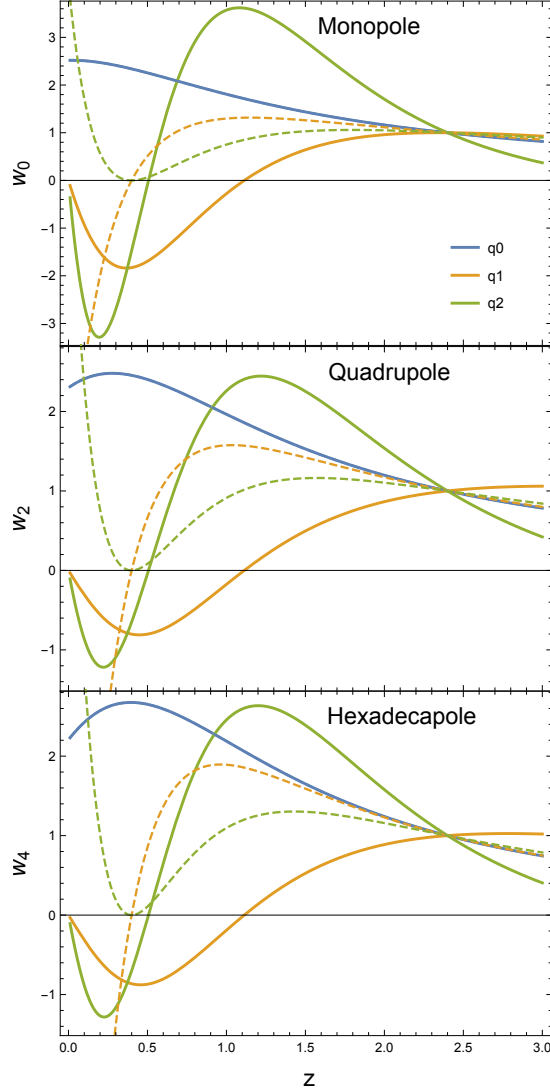
Figure 5.5: The RSD + AP optimal weights for the monopole w_0, quadrupole w_2, hexade-capole w_4. Blue lines indicate the weights with respect to the q_0 parameter. Orange lines indicate the weights with respect to the q_1 parameter and green lines indicates the weights with respect to the q_2 parameter. We compare them with previous results, where the distance-redshift relation was fixed (dashed lines); the weights w_{ℓ,q_0} (blue lines) are equivalent to the previous weights without AP effect since the contribute from φ and $\alpha_\perp$ vanish because of $\partial H(q_i)/\partial q_0 = 0$. The RSD+AP weights show enhanced features due to AP parameters, whose importance increases with redshift.

97

5.6   Summary

In this chapter, we have proposed a new technique to optimize the anisotropic clustering measurements in deep redshift surveys. The optimization applies weights to galaxies and compresses the information into the redshift direction. In this way, we avoid splitting the sample in bins while preserving our ability to maintain sensitivity to the evolution of the underlying cosmology. We derived and tested the weights for a ΛCDM scenario and investigated the impact of different bias models on the weighting scheme. The next steps will be including the weights in the estimator presented in 4, testing the pipeline on N-body simulations (chapter 7) and then applying it to the eBOSS DR14 quasars (chapter 8).

OPTIMISING PRIMORDIAL NON-GAUSSIANITY MEASUREMENTS

FROM GALAXY SURVEYS

Galaxy clustering data from current and upcoming large scale structure surveys can provide strong constraints on primordial non-Gaussianity through the scale-dependent halo bias. To fully exploit the information from galaxy surveys, optimal analysis methods need to be developed and applied to the data. Since the halo bias is sensitive to local non-Gaussianity predominately at large scales, the volume of a given survey is crucial. Consequently, for such analyses we do not want to split into redshift bins, which would lead to information loss due to edge effects, but instead analyse the full sample. We apply an optimal technique, with the approach presented in chapter 5, to directly constrain local non-Gaussianity parametrised by $f_{\mathrm{NL}}^{\mathrm{loc}}$, from galaxy clustering. Similarly to the work presented in 5 focused on RSD, we here derive a set of weights to optimally measure the amplitude of local non-Gaussianity, $f_{\mathrm{NL}}^{\mathrm{loc}}$. We discuss the redshift weighted power spectrum estimators, outline the implementation procedure and test our weighting scheme against Lognormal catalogs for two different surveys: the quasar sample of the Extended Baryon Oscillation Spectroscopic Survey (eBOSS) and the emission line galaxy sample of the Dark Energy Spectroscopic Instrument (DESI) survey. We find an improvement of 30 percent for eBOSS and 6 percent for DESI compared to the standard Feldman, Kaiser & Peacock weights, although these predictions are sensitive to the bias model assumed.

This chapter describes a collaborative research project published in [133]. My major contribution to this project is the derivation of the redshift weights (equations 6.18-6.23).

6.1   Introduction

Primordial non-Gaussianity (PNG) is one of the most promising probes to distinguish between different models of inflation, a theory to describe an era of exponential expansion of the very early universe that was first introduced to solve problems within the Big Bang model. Inflation can solve the horizon problem as well as the flatness problem, and can also explain the origin of structure formation through the creation of initial fluctuations. Currently, the best constraints on PNG are provided by measurements of the cosmic microwave background (CMB) with the Planck satellite [30].

Even though current constraints from large scale structure (LSS) data (i.g. [84]) are weaker than the CMB results, future galaxy surveys have the potential to significantly improve upon these limits (see e.g. [134–136, 136–142]) by constraining the scale dependent halo bias induced by PNG [14, 76, 143, 144]. Upcoming spectroscopic surveys such as the extended Baryon acoustic Oscillation Spectroscopic Survey (eBOSS) [1], the Euclid mission [145], as well as the Dark Energy Spectroscopic Instrument (DESI) [146] survey are expected to constrain the amplitude of local non-Gaussianity, $f_{\mathrm{NL}}^{\mathrm{loc}}$, around a few (from here on we will drop the subscript 'loc' for simplicity); however, to achieve that level of accuracy, analysing techniques need to be optimised to fully exploit the LSS information. Indeed, most galaxy redshift survey analyses fall short of their expected results predicted using Fisher Matrix techniques.

It was recently realised [127] that that some of the missing signal is lost because analyses are generally performed after splitting a galaxy sample into redshift shells. Instead, they proposed adopting an analysis strategy that relies on assigning weights to the galaxies over a broad redshift range, showing that this retains more information provided that the weights take the redshift evolution of the underlying physical theory into account. This has the potential to notably improve cosmological constraints from LSS surveys.

[127] focussed on optimising LSS surveys for BAO measurements, and their method was shown to work using mock catalogs in [147]. In subsequent work, redshift weights were derived to constrain modified gravity through Redshift Space Distortions (RSD) in [123]. These weights can be interpreted as a natural extension of the Feldman, Kaiser & Peacock (FKP) weights [86], that balance galaxies according to their number densities, for the case that the cosmological observables of interest evolve with time. If the underlying physical theory is independent of redshift then the weights reduce to the standard FKP weights. In the future, multiple galaxy surveys will cover a large redshift range, $0 < z < 3$, making the redshift weighting technique particularly efficient as well as necessary to avoid information loss

due to edge effects and disjoint bins. Furthermore, the computational time can be reduced significantly since the redshift weighting technique only requires a single analysis instead of measuring each redshift bin separately. Redshift weighting also removes the need to define an effective redshift of a survey by providing measurements with known variation over the redshift range.

In this work, we derive and assess the redshift weights for optimising LSS surveys for local f_{NL} measurements. Avoiding redshift binning is particularly relevant for non-Gaussianity measurements since the effect of the scale dependent bias dominants on very large scales. Breaking the survey into redshift bins (for example, considering the clustering in bins of width $\Delta z = 0.1$), removes large-scale clustering signal. For the correlation function it is clear that such binning removes pairs of galaxies, where galaxies lie in different bins. For the power spectrum, the binning introduces a window function, correlating large-scale modes, and decreasing the effective number of modes.

The chapter is organised as follows: In Section 6.2 we summarise modelling of the power spectrum as well as the observable effects of non-Gaussianity on the power spectrum. We introduce the concept of redshift weighting in Section 6.3.1 and derive the optimal weights for f_{NL} measurements in Section 6.3.2. We outline the procedure of how to apply the weights to the data in Section 6.3.3. In Section 6.3.4 we discuss the modelling of the redshift weighted power spectrum and in Section 6.4 we estimate the improvement of using f_{NL} weights compared to FKP weights by simulating the redshift weighted power spectrum estimators using Lognormal catalogs. Finally, Section 6.5 contains a discussion of this project key results.

6.2 Physical Model

In this Section we provide a brief summary of the scale dependent halo bias induced by non-Gaussianity. In the framework of local non-Gaussianity, i.e. a type of non-Gaussianity that only depends on the local value of the potential, the primordial potential can be parametrised as [148, 149]

$$\Phi = \phi + f_{\mathrm{NL}}(\phi^2 - \langle \phi^2 \rangle) \tag{6.1}$$

where ϕ is a Gaussian random field and f_{NL} describes the amplitude of the quadratic correction to the potential. The potential can then be related to the density field via $\delta(k) = \alpha(k)\Phi(k)$, with

$$\alpha(k) = \frac{2k^2 T(k) D(z)}{3\Omega_m} \frac{c^2}{H_0^2} \frac{g(0)}{g(\infty)} \tag{6.2}$$

with the transfer function $T(k)$, the linear growth factor $D(z)$ normalised to be unity at $z = 0$, the matter density today Ω_m, the speed of light c and the Hubble parameter today H_0. The factor $g(\infty)/g(0)$, with $g(z) = (1 + z)D(z)$, arises due to our normalisation of $D(z)$ and can be omitted if D(z) is normalised to equal the scale factor during the matter dominated era. Here we are using the CMB convention for f_{NL} assuming Φ is the primordial potential. Note that some authors have previously adopted a "LSS convention" that assumes Φ is extrapolated to $z = 0$, with $f_{\text{NL}}^{\text{LSS}} = g(\infty)/g(0)f_{\text{NL}}^{\text{CMB}} \approx 1.3\ f_{\text{NL}}^{\text{CMB}}$. We do not do this as we consider it unnecessary and potentially confusing.

The scale dependent halo bias $\Delta b(k)$ in the local Ansatz is then given by [14, 76]

$$\Delta b(k) = 2(b - p)f_{\text{NL}}\frac{\delta_{\text{crit}}}{\alpha(k)} \tag{6.3}$$

where $\delta_{\text{crit}} = 1.686$ and $1 < p < 1.6$ depending on the type of tracer. Here we follow [14] assuming $p = 1$ for luminous red galaxies (LRGs) and emission line galaxies (ELGs) and $p = 1.6$ for quasars.

The total bias, including local non-Gaussianity is then $b_{\text{tot}} = b + \Delta b(k)$.

In the limit of the plane parallel approximation, the linear matter power spectrum P in redshift space is [52]

$$P(k, \mu) = \left(b_{\text{tot}} + f\mu^2\right)^2 P_M(k) \tag{6.4}$$

where f is the linear growth rate, μ is the cosine of the angle between the wavevector k and the line of sight and $P_M(k)$ is the linear matter power spectrum. The effect of f_{NL} is included in the definition of the total bias. From an observational point of view it is more convenient to consider the power spectrum multipoles defined as

$$P_l(k) = \frac{2l + 1}{2}\int_{-1}^{1}d\mu P(k, \mu)\mathcal{L}_l(\mu) \tag{6.5}$$

where $\mathcal{L}_l(\mu)$ are the Legendre polynomials, instead of the linear power spectrum given by equation (6.4). Even though the power spectrum is fully defined by its first three moments at linear order, only the monopole

$$P_0(k) = \left(b_{\text{tot}}^2 + \frac{2}{3}f b_{\text{tot}} + \frac{1}{5}f^2\right)P_M(k) \tag{6.6}$$

as well as the quadrupole

$$P_2(k) = \left(\frac{4}{3}b_{\text{tot}}f + \frac{4}{7}f^2\right)P_M(k) \tag{6.7}$$

depend on the bias. Therefore we focus our analysis to these multipoles.
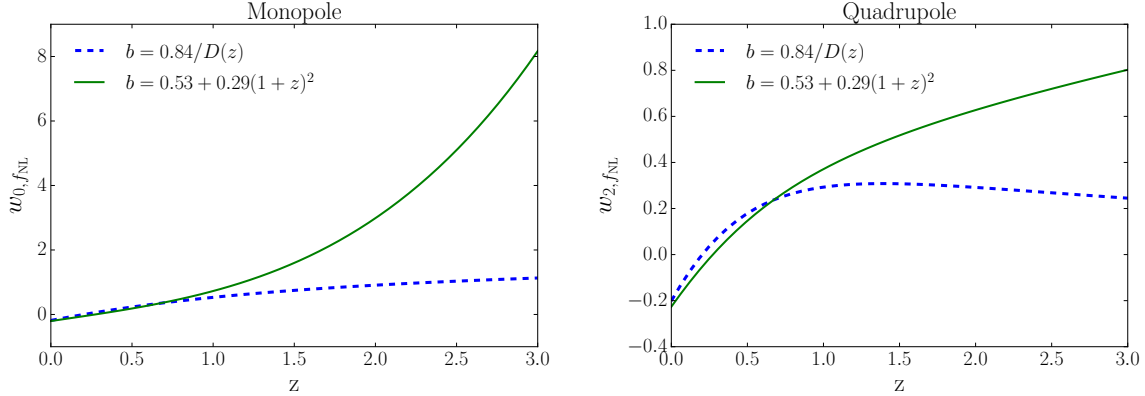
Figure 6.1: Optimal redshift weights for local non-Gaussianity, f_{NL}, measurements as a function of redshift for the power spectrum monopole [left panel] and quadrupole [right panel]. Blue dashed lines assume a bias model $b(z) = 0.53 + 0.29(1 + z)^2$ and $p = 1.6$ referring to quasars as tracer of the underlying matter density, while green lines are for $b(z) = 0.84/D(z)$ and $p = 1.0$, referring to ELGs. The assumptions on the fiducial value of f_{NL} have an negligible effect on the weights. For these plots we assume a fiducial of $f_{\mathrm{NL}} = 0$

6.3 Optimal weights

6.3.1 Redshift weights

Following the procedure outlined in [123] and [147] we can derive the optimal redshift weights by maximising the Fisher information matrix F defined as

$$(6.8) \qquad F_{ij} \equiv \left\langle \frac{\partial^2 \mathscr{L}}{\partial \theta_i \partial \theta_j} \right\rangle,$$

(6.9)

with the likelihood function $\mathscr{L}$ and the parameters θ_i. Assuming a Gaussian likelihood, the fisher matrix for a single parameter of the weighted data set can be calculated as

$$(6.10) \qquad F_{ii} = \frac{1}{2} \left(\frac{\mathbf{w}^T C_{,i} \mathbf{w}}{\mathbf{w}^T C \mathbf{w}} \right)^2 + \frac{(\mathbf{w}^T \mu_{,i})^2}{\mathbf{w}^T C \mathbf{w}}$$

with the covariance matrix C, the mean μ, the weights $\mathbf{w}$ and the index $, i$ denoting the partial derivative $\partial/\partial \theta_i$ [see e.g. 128, 129].

The first term in equation (6.10) vanishes assuming the covariance matrix is known and independent of the cosmological parameters. The second term is maximised for

$$(6.11) \qquad \mathbf{w}^T = C^{-1} \mu_{,i}.$$

Defining $w_i = \mu_{,i}^T$ as well as $d\mathcal{W} \equiv C^{-1}$ the weights for parameter θ_i can be written as

$$\mathbf{w} = w_i \, d\mathcal{W}. \tag{6.12}$$

The factor $d\mathcal{W}$ takes the statistical uncertainty of the observable into consideration whereas w_i factors in the redshift evolution of the theoretical model. The normalisation of the weights is arbitrary and does not affect the cosmological constraints. We choose the normalisation,

$$N_i = \int w_i \, d\mathcal{W} \tag{6.13}$$

leading to normalised weights $\hat{\mathbf{w}}$ defined as

$$\hat{\mathbf{w}} \equiv \frac{1}{N_i} w_i \, d\mathcal{W}. \tag{6.14}$$

Note first, that the index i refers to the same cosmological parameter but does not imply Einstein summation and second, that our normalisation differs from the one in [147] by a factor of w_i.

6.3.2 Redshift weights for local non-Gaussianity

For the power spectrum P(k), the inverse covariance matrix in each redshift slice can be approximated by

$$d\mathcal{W} \equiv C^{-1} = \left(\frac{\bar{n}}{\bar{n}P + 1} \right)^2 dV \tag{6.15}$$

depending on the galaxy density $\bar{n}$ as well as the survey volume dV. Since in this analysis we are interested in using measurements of the power spectrum monopole and quadrupole to constrain the non-Gaussianity parameter f_{NL}, the part of weights referring to the redshift evolution of f_{NL} are given by

$$w_{l,f_{\mathrm{NL}}} = \frac{\partial P_l}{\partial f_{\mathrm{NL}}}. \tag{6.16}$$

The total weights

$$\mathbf{w} = w_{l,f_{\mathrm{NL}}} d\mathcal{W} \tag{6.17}$$

are then a combination of the volume factor $d\mathcal{W}$ and the f_{NL} weights. In the following we will use the term "redshift weights" to refer to $w_{l,f_{\mathrm{NL}}}$ but one should keep in mind that the total weights also include the volume factor $d\mathcal{W}$. For $w_i = 1$ the weights reduce to the commonly used FKP weights. However, if one is interested in a theory that is more sensitive at high

redshifts, for instance, more total weight will be given to galaxies at higher redshifts than in the case of FKP weights.

Using equation (7.22) and equation (6.3) together with equation (6.6), the weight of the monopole reads as

$$(6.18) \qquad w_{0,f_{\mathrm{NL}}} = \left(2b_{\mathrm{tot}} + \frac{2}{3}f\right)\frac{\partial b_{\mathrm{tot}}}{\partial f_{\mathrm{NL}}}P_M(k,z)$$

and furthermore assuming a fiducial value for $f_{\mathrm{NL,fid}} = 0$ simplifies to

$$(6.19) \qquad w_{0,f_{\mathrm{NL}}} = \left(2b + \frac{2}{3}f\right)2(b-p)\frac{\delta_{\mathrm{crit}}}{\alpha(k,z)}P_M(k,z).$$

Factoring out the explicit redshift dependency as $\alpha(k,z) = \alpha(k,z_0)D(z)$ and $P_M(k,z) = P_M(k,z_0)D(z)^2$ as well as normalising the weights according to equation (6.13), the normalised weights can be written independent of the wavevector k. Without the loss of generality, the weights can be redefined as

$$(6.20) \qquad \hat{w}_{0,f_{\mathrm{NL}}} = \frac{1}{N_{0,f_{\mathrm{NL}}}}w_{0,f_{\mathrm{NL}}}$$

where

$$(6.21) \qquad w_{0,f_{\mathrm{NL}}} = \left(b + \frac{1}{3}f\right)(b-p)D(z)$$

$$(6.22) \qquad N_{0,f_{\mathrm{NL}}} = \int w_{0,f_{\mathrm{NL}}}\, d\mathcal{W}.$$

Similarly the quadrupole weight can be defined as

$$(6.23) \qquad w_{2,f_{\mathrm{NL}}} = \frac{4}{3}f(b-p)D(z).$$

It should be emphasised the scale independence of these weights significantly simplifies their application (see Section 6.3.3).

Fig. 6.1 shows the weight for the monopole $w_{0,f_{\mathrm{NL}}}$ [left panel] and the quadrupole $w_{2,f_{\mathrm{NL}}}$ [right panel] as a function of redshift z assuming a bias of $b(z) = 0.53 + 0.29(1+z)^2$ (blue dashed lines) and $p = 1.6$ as well as $b(z) = 0.84/D(z)$ and $p = 1$ (green lines), bias models previously proposed for eBOSS quasars [1] and DESI ELGs [2] respectively. The weights at low redshifts, $z < 0.75$, are similar for both, but deviate for higher redshifts due to increasing differences in the bias models, with a strong high-redshift bias leading to larger weights at high redshifts. In general, the f_{NL} weights are also larger for higher redshifts since the f_{NL} model is also sensitive to the redshift evolution of the the growth rate.

6.3.3   Implementation procedure

The implementation procedure was outlined in [127] analysing the real space correlation
function as well as in [123] for the power spectrum in Fourier space. For completeness, we
summarise some of the key-points here. The redshifts weights can be applied to the data
and randoms as an extension of the usual FKP weighting scheme following the prescription
of [86],

$$(6.24) \qquad w_{\text{FKP}} = \frac{1}{1 + \bar{n}(z) P(k_0)}$$

where $\bar{n}(z)$ is the mean number density at the galaxies's redshift z, and k_0 is commonly
assumed to be approximately the BAO scale. The redshift dependent weights are applied in
the following way: In real space, each galaxy pair (or pair of randoms) is weighted by $w_{l, f_{\text{NL}}}$
as well as w_{FKP}

$$(6.25) \qquad \widetilde{XY} = \sum_z w_{l, f_{\text{NL}}} w_{\text{FKP}}^2 XY$$

where $\widetilde{XY} = \{DD, DR, RR\}$ refer to the data-data, data-random and random-random pairs
of the sample. The standard [110] estimator

$$(6.26) \qquad \xi_{l, f_{\text{NL}}} = \frac{\widetilde{DD} - 2\widetilde{DR} + \widetilde{RR}}{RR}$$

can then be used to calculate the weighted correlation function, where RR are the un-
weighted random-random pairs.

In Fourier space the procedure is similar. Each galaxy is weighted by a product of FKP
weight and the f_{NL} specific weights as derived in Section 6.3.1

$$(6.27) \qquad w = \sqrt{w_{\text{FKP}} \times w_{l, f_{\text{NL}}}}.$$

Note, that even though we derived the weights within the framework of the power spectrum,
following the assumption that the clustering evolves over larger scales than those being
measured, we can approximate the weights applied to the galaxies as the root of the power
spectrum weights $w_g = \sqrt{w_P}$.

6.3.4   Modelling the weighted power spectrum

The model to be fitted to the measured, weighted power, also depends on the weights. i.e. we
need both the data and model to be sensitive to the same redshifts. We model the theoretical
weighted power spectrum multipoles by compressing them into the redshift direction as

$$(6.28) \qquad P_{l,w}(k) \equiv \frac{1}{N_i} \int d\mathcal{W}(z) \, w_{l,i}(z) P_l(k, z)$$
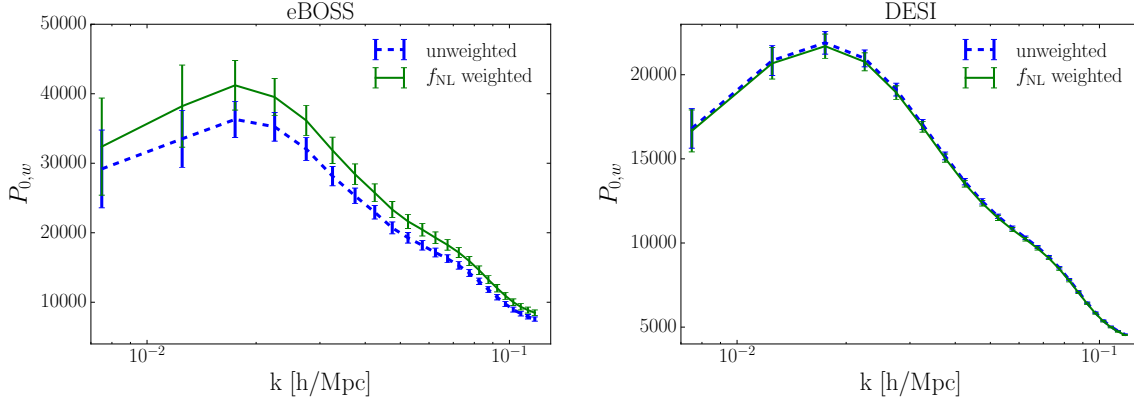
Figure 6.2: Redshift weighted power spectrum monopole for eBOSS [left panel] and DESI [right panel]. Blue dashed lines correspond to the 'unweighted' (or FKP)-weighted monopole (assuming $w_0 = 1$) and green lines represent the f_{NL}-weighted monopole. Details on the survey assumptions are summarised in Tab. 6.1.

with

$$w_{\mathrm{unweighted}} = 1 \tag{6.29}$$

$$w_{0, f_{\mathrm{NL}}} = \left(b + \frac{1}{3} f \right)(b - p) D(z) \tag{6.30}$$

$$w_{2, f_{\mathrm{NL}}} = \frac{4}{3} f (b - p) D(z) \tag{6.31}$$

with the normalisation N_i given by the equation (6.13).

In general, the theoretical power spectrum includes a convolution with the survey window function. However, considering the galaxy power spectrum as an evolving quantity requires a redefinition of the survey window function (for details see Ruggeri et al., in prep.).

6.4 Testing the redshift weights

In order to test the weights, we generate an ensemble of mock catalogues, based on overdensities drawn from a Lognormal distribution [150]. Lognormal-random fields were used for convenience because they approximate the present-day non-linear fluctuation field, and they obey the physical limit $\delta > -1$, which means that they can be Poisson sampled to provide a galaxy distribution with shot-noise and sample variance matching those expected. Although both the assumptions of a Lognormal overdensity field and Poisson-sampled galaxies are crude approximations, they are fit for our purpose of testing the weights.

107

Table 6.1: We are modelling the eBOSS quasar sample and the DESI ELG sample with
the number of galaxies given in Tabel 2 of [1] and Table 2.3 in [2] respectively. We are not
considering the complete surveys but rather select specific samples to highlight the range of
results that can be expected for different survey specification.

survey	tracer	redshift range	sky coverage	bias model
eBOSS	Quasars	$0.6 < z < 2.2$	$7{,}500 \deg^2$	$b(z) = 0.53 + 0.29(1 + z)^2$
DESI	ELGs	$0.6 < z < 1.8$	$14{,}000 \deg^2$	$b(z) = 0.84/D(z)$

We generate 10,000 mock catalogues in redshift shells of $\delta z = 0.025$ with the number
densities, redshift range, sky coverage and bias model as expected for the eBOSS quasar
sample and DESI ELGs. A summary of the survey specifications can be found in Table 6.1.
We assume a box size of $L = V^{1/3}$ with the volume referring to the shell of a given survey
calculated as

$$(6.32) \qquad V(z) = \frac{4\pi}{3} f_{\text{sky}} \left(\chi(z_{\text{max}})^3 - \chi(z_{\text{min}})^3 \right)$$

with the sky coverage fraction f_{sky} and the comoving distance χ. Within each redshift shell
we assume no density gradient, simplifying our analysis to avoid a detailed modelling of
survey window function. The simulations assume a flat ΛCDM cosmology with $\Omega_m = 0.3$,
$\Omega_b = 0.045$, $h = 0.7$, $n_s = 1.0$, $\sigma_8 = 0.8$ and $f_{\text{NL}} = 0$ as our fiducial cosmology. We compute the
spherically averaged power-spectrum monopole in 23 bins of width $\Delta k = 0.005 \, h/\text{Mpc}$ from
$0.005 \, h/\text{Mpc} < k < 0.12 \, h/\text{Mpc}$ using

$$(6.33) \qquad P_0(k, z) = \frac{3}{2} \sum |\tilde{\delta}(k)|^2 \mathscr{L}_0(\mu(k))$$

where $\mathscr{L}_0(\mu)$ is the 0th order Legendre polynomial and $|\tilde{\delta}(k)|^2$ is the squared modulus of the
Fourier transform of the overdensity $\delta(r)$ at position r and the sum is over all wavevectors
in the range $|k| \pm \Delta k/2$ [see e.g., 151]. For each mock we then calculate the weighted and
unweighted power spectra via equation (6.28).

In the following analysis we only consider constraints from the monopole as a proof of
concept and do not consider constraints from the quadrupole since most of the information
on f_{NL} is contained in the monopole [84]. For each mock the weighted power spectrum is
then calculated using equation (6.28). We calculate the covariance matrix as

$$(6.34) \qquad C_{ij} = \frac{1}{N_m - 1} \sum_{n=1}^{N_m} \left[d_n(k_i) - \bar{d}(k_i) \right] \left[d_n(k_j) - \bar{d}(k_j) \right]$$

where N_m is the total number of mocks, $d_n(k)$ is the power spectrum monopole from the
nth mock.
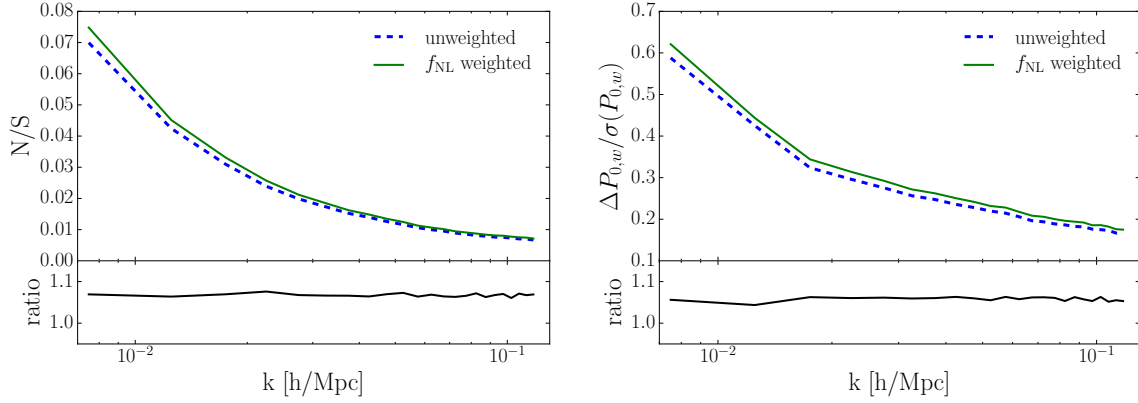
Figure 6.3: Noise-to-signal of the weighted power spectrum monopole [left panel] and the difference of the weighted power spectrum assuming $f_{NL} = 10$ and $f_{NL} = 0$ over the noise, $\Delta P_{0,w}/\sigma(P_{0,w}) = \left(P_{0,w}(f_{NL} = 10) - P_{0,w}(f_{NL} = 0)\right)/\sigma(P_{0,X})$, [right panel]. Blue dashed lines refer to the 'unweighted' power spectrum monopole and green lines to the f_{NL}-weighted monopole. The lower panel shows the ratio between the 'unweighted' and f_{NL}-weighted case. Even though the unweighted monopole has a higher level of noise, the sensitivity to f_{NL} is higher for the f_{NL}-weighted monopole and with that the capacity to constrain to f_{NL}.

Fig. 6.2 shows the f_{NL}-weighted and 'unweighted' power spectrum monopole for eBOSS [left panel] and DESI [right panel]. The effect of the f_{NL}-weights is greater for eBOSS due to the adaption of a bias model that evolves more strongly with redshift as well as due to the larger redshift range of the survey. Note, that the normalisation factor for both surveys is different.

The redshift weighting scheme takes the redshift evolution of the underlying theory into account, potentially shifting the weights towards regions with higher noise in the clustering signal. Therefore, applying redshift weights does not automatically lead to higher signal to noise in the power spectrum itself. Instead, redshift weighting leads to the observable that can constrain the underlying theory the most. In the case of local non-Gaussianity, more weight is given to galaxies at higher redshifts despite the larger statistical uncertainty at these redshifts, because the effect of f_{NL} on the powers spectrum is greater at higher redshifts. Fig. 6.3 depicts the noise-to-signal as a function of scale for the f_{NL}-weighted and 'unweighted' power spectrum monopole for DESI [left panel], as well as the difference of the redshift weighted power spectrum for $f_{NL} = 10$ and $f_{NL} = 0$ over the noise [right panel]. Even though the N/S is larger for the f_{NL}-weighted power spectrum, it has a greater capability to constrain f_{NL} than the FKP-weighted power spectrum because it is more sensitive to the f_{NL}.

To get an estimate on the error achievable on a measurement of f_{NL} from both surveys, we calculate the χ^2 surface

$$(6.35) \qquad\qquad \chi^2 = (\vec{m} - \vec{d})^T C^{-1} (\vec{m} - \vec{d})$$

where $\vec{d}$ is the data vector calculated from the mocks and $\vec{m}$ is the model vector. For both surveys we can then calculate the expected likelihood. For eBOSS we find an uncertainty on f_{NL} of $\sigma(f_{\mathrm{NL}}) = 21.63$ at 68% C.L. for the FKP-weighted case and $\sigma(f_{\mathrm{NL}}) = 16.66$ for the f_{NL}-weighting scheme, an improvement of 30%. The improvement for DESI is slightly lower at around 6%. Our analysis currently uses a scale-dependent FKP weight (i.e. P is allowed to vary with k in the weights). If the FKP weight were fixed, as is often assumed when analysing data for simplicity, then we would expect less good constraints on f_{NL} because of increased cosmic variance and/or shot noise. We would also have a different fractional improvement from the redshift weights, with the improvement increasing if the FKP weights are fixed for $P(k)$ with k on larger scales: those where the f_{NL} signal is stronger and the redshift-weights more effective. For example if the FKP weight is fixed at $k_0 = 0.0475$ the improvement increases to 42% for eBOSS.

The Fisher matrix forecasts for eBOSS quasars are $\sigma(f_{\mathrm{NL}}) = 15.74$ [1] with fixing the bias. The redshift weighting technique yields results closer to the predicted uncertainty compared to the unweighted analysis. We do not quite reach the Fisher forecast accuracy because we only consider the monopole and assume a slightly smaller k-range. The Fisher forecasts for DESI are $\sigma(f_{\mathrm{NL}}) = 3.8$ [146], yet these constraints are for the full DESI survey and not just the ELG sample.

The difference between the improvement for eBOSS and DESI from adding the new weights is driven by the range of bias assumed across the sample under consideration, and so will not be fully known for DESI until the survey starts. Even so, this analysis is a proof of principle that the fNL-redshift weighting can lead to stronger constraints on fNL than a simple FKP-weighted power spectrum.

6.5 Discussion

The optimal weights we have derived to measure f_{NL} balance sample variance, shot noise and the redshift evolution of the scale dependent halo bias induced by non-Gaussianity. The weights depend on the properties of the galaxy sample through the evolving bias of the sample. As the bias is generally increasing with redshift, we end up weighting galaxies at
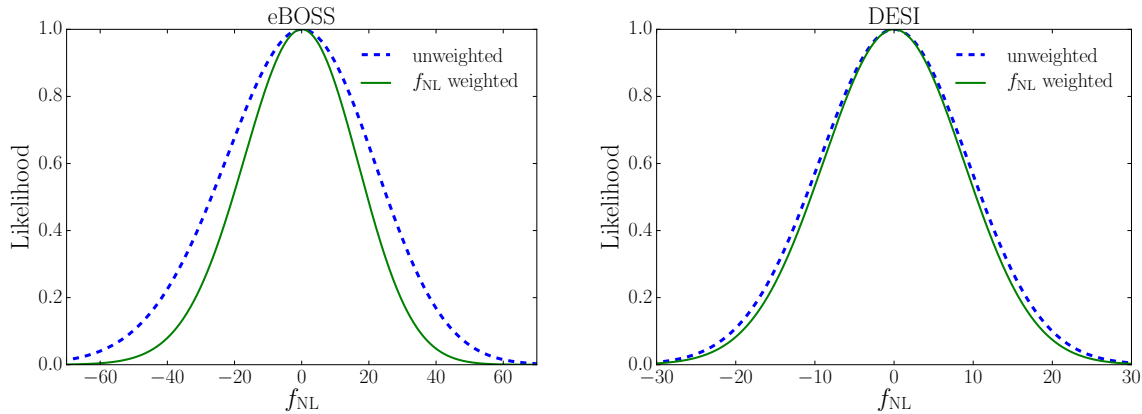
Figure 6.4: Projected likelihood for f_{NL} measurements from eBOSS quasars [left panel] and DESI ELGs [right panel] for an 'unweighted' (green lines) and f_{NL}-weighted (blue dashed lines) power spectrum monopole. The redshift weighting technique can improve the constraints on f_{NL} by 30% for eBOSS quasars and 6% for DESI ELGs. The improvement is larger for eBOSS due to the strong redshift evolution of the assumed bias model as well as a larger redshift range.

high redshift more strongly than at low redshifts, even if the signal-to-noise of the clustering signal is weaker.

We assessed the potential of the f_{NL} weights using mock catalogs generated with a Log-normal code simulating the upcoming eBOSS and DESI surveys. We find that the uncertainty on f_{NL} is minimised when applying the f_{NL} redshift weights, yielding an improvement of 6% up to 30% for DESI and eBOSS respectively compared to analysing an FKP-weighted power spectrum.

There are a few caveats to our analysis: First, the redshift weights to optimally measure local non-Gaussianity depend strongly on the assumed galaxy bias. If the fiducial bias model is inaccurate, then the weights will not be optimal and lead to looser constraints on f_{NL} then expected. However, the redshift weighted power spectrum will still be unbiased. Second, for tracers with no strongly evolving bias the underlying theory is only mildly redshift dependent limiting the overall improvement of the redshift weighting technique. In general, the improvement from the f_{NL}-weighting increases with the redshift range of the survey but also depends on the tracer of the sample, with the improvement being stronger where the range of bias across a sample is larger.

6.6 Summary

Following the same procedure presented in chapter 5, in this chapter we have derived a set
of weights to optimize the measurement of f_{NL}; we assessed the potential of these weights
using mock catalogs generated though a Lognormal code simulating the upcoming eBOSS
and DESI surveys. We found that the uncertainty on f_{NL} is minimised when applying the f_{NL}
redshift weights, yielding an improvement of 6% up to 30% for DESI and eBOSS respectively
compared to analysing an FKP-weighted power spectrum.

We have discussed the potential of redshift weighting to constrain f_{NL} for eBOSS and
DESI, but there are also other future surveys for which this technique is highly relevant, for
instance the Euclid mission [145] and SPHEREx [152]. Euclid is a space based, spectroscopic
survey of Hα-selected emission line galaxies with galaxies in redshift range range $0.7 < z <
2.0$, expected to constrain local non-Gaussianity in addition to BAO and RSD measurements.
SPHEREx is a all-sky spectroscopic satellite survey covering a very wide redshift range that
was particularly designed to measure non-Gaussianity. It has an evolving redshift accuracy
up to $\sigma_z/(1 + z) < 0.2$ with low redshifts being more accurately measured than high redshifts.
However, we expect the lower redshift accuracy not to be problematic when applying the
redshift weights as long as the uncertainty in redshift is taken into account as an additional
contribution to the covariance when calculating the weights.

TESTING A NEW APPROACH TO MEASURE THE EVOLUTION OF THE STRUCTURE GROWTH

The extended Baryon Oscillation Spectroscopic Survey (eBOSS) is one of the first of a new generation of galaxy redshift surveys that will cover a large range in redshift with sufficient resolution to measure the baryon acoustic oscillations (BAO) signal. As we discussed in chapters 5 and 6, for surveys covering a large redshift range we can no longer ignore cosmological evolution, meaning that either the redshift shells analysed have to be significantly narrower than the survey, or we have to allow for the averaging over evolving quantities. Both of these have the potential to remove signal: analyzing small volumes increases the size of the Fourier window function, reducing the large-scale information, while averaging over evolving quantities can, if not performed carefully, remove differential information. It will be important to measure cosmological evolution from these surveys to explore and discriminate between models. We apply the method described in chapter 5, to optimally extract this differential information to mock catalogues designed to mimic the eBOSS quasar sample. By applying a set of weights to extract redshift space distortion measurements as a function of redshift, we demonstrate an analysis that does not invoke the problems discussed above. We show that our estimator gives unbiased constraints.

The content of the work presented here refers to the research published in [153].

7.1 Clustering analysis strategies for eBOSS

The eBOSS survey [96], [1] [28], which commenced in July 2014, will cover the largest volume
to date of any cosmological redshift survey with a density sufficient to extract useful cosmo-
logical information. eBOSS observations will target multiple density-field tracers, including
more than $250,000$ luminous red galaxies (LRGs), $195,000$ emission line galaxies (ELGs) at
effective redshifts $z = 0.72, 0.87$ and over $500,000$ quasars between $0.8 < z < 2.2$. The survey's
goals include the distance measurement at $1 - 2\%$ accuracy with the BAO peak on the LRG
sample and the first BAO measurements using quasars as density tracers over the redshift
range $1 < z < 2$ (the first clustering measurements were recently presented in [23]). The
wide redshift range covered, compared with that in previous redshift surveys represents an
unique opportunity to test and discriminate between different cosmological scenarios on
the basis of their evolution in redshift. Full survey details can be found in [96].

The clustering analysis strategy adopted for most recent galaxy survey analyses was
based on computing the correlation function or the power spectrum for individual samples
or subsamples, overwhich the parameters being measured were assumed to be unvarying
with redshift. The measurements were then considered to have been made at an effective
redshift: see e.g. [7], [154]. In particular [7], divided the full The Baryon Oscillation Spectro-
scopic Survey (BOSS) survey volume in three overlapping redshift bins and repeated the
measurement in each sub-volume. This technique has many disadvantages: the choice of
bins is a balance between having enough data for a significant detection in each bin leading
to Gaussian errors and having bins small enough that there is no cosmological evolution
across them, leading to a degrading compromise. The technique also ignores information
from the cross-correlation between galaxies in different redshift bins, potentially ignoring
signal. Sharp cuts in redshift will also introduce ringing artefacts in the Fourier-space, po-
tentially causing complications in the analysis. To complicate analyses further, many mock
catalogues currently used to compare to the data intrinsically lack evolution, or "lightcone"
effects, being drawn from simulation snapshots. Although this is a separate problem, these
differences limit the tests of the effects of evolution that can be performed, and have the
potential to hide biases caused by evolution.

In chapters 5 and 6, we introduced an alternative approach to the redshift binning. The
idea is to consider the whole volume of the survey and optimally compress the information
in the redshift direction by applying a set of redshift weights to all galaxies, and only then
computing the weighted correlation function. Comparing measurements made using differ-
ent sets of redshift weights maintains the sensitivity to the underlying evolving theory. The

sets of weights are derived in order to minimize the error on the parameters of interest. In addition, by applying the redshift weighting technique instead of splitting the survey, is it possible to compute the correlation function to larger scales whilst accounting for the evolution in redshift; this was particularly clear in what derived in chapter 6, which considered this method to optimize the measurement of local primordial non Gaussianity, which relies on large scales. Further, [147] showed that the application of a weighting scheme rather than splitting into bins also improves BAO measurements.

As already mentioned, the need to correctly deal with evolution will increase for the DESI and Euclid experiments, which will cover a broad redshift range and have significantly reduced statistical measurement errors compared to current surveys in any particular redshift range. The Dark Energy Spectroscopic Instrument (DESI)[1] is a new MOS currently under construction for the 4-meter Mayall telescope on Kitt Peak. DESI will be able to obtain 5000 simultaneous spectra, which coupled with the increased collecting area of the telescope compared with the 2.5-meter Sloan telescope, means that it can create a spectroscopic survey of galaxies ~ 20 times more quickly than eBOSS. In 2020 the European Space Agency will launch the Euclid[2] satellite mission. Euclid is an ESA medium class astronomy and astrophysics space mission, and will undertake a galaxy redshift survey over the redshift range $0.9 < z < 1.8$, while simultaneously performing an imaging survey in both visible and near-infrared bands. The complete survey will provide hundreds of thousands images and several tens of Petabytes of data. About 10 billion sources will be observed by Euclid out of which several tens of million galaxy redshifts will be measured and used to make galaxy clustering measurements.

In the current work we test the redshift weighting approach by analysing a set of 1000 mocks catalogues [155] designed to match the eBOSS quasar sample. This quasar sample has a low density (82.6 objects/deg^2) compared to that of recent galaxy samples, and covers a total area over 7500 deg^2. The quasars are highly biased targets and we expect their bias to evolve with redshift, $b(z) \propto c_1 + c_2(1 + z)^2$, with constant values $c_1 = 0.607 \pm 0.257$, $c_2 = 0.274 \pm 0.035$, as measured in [156].

Although the mocks are not drawn from N-body simulations, they have been calibrated to match one of the BigMultiDark (BigMD) [157], a high resolution N-body simulation, with 3840^3 particles covering a volume of $(2500h^{-1}Mpc)^3$. The BigMD simulations were performed using GADGET-2 [158], with ΛCDM Planck cosmological constraints as a fiducial cosmology. $\Omega_m = 0.307$, $\Omega_b = 0.048206$, $\sigma_8 = 0.8288$, $n_s = 0.96$, $H_0 = 100h$kms^{-1}Mpc^{-1}

---

[1]http://desi.lbl.gov/
[2]http://sci.esa.int/euclid

and $h = 0.6777$. In [155] the authors showed that EZ-mocks are nearly indistinguishable from the full N-body solutions: they reproduce the power spectrum within 1%, up to $k = 0.65h\mathrm{Mpc}^{-1}$. The mocks are created using a new efficient methodology based on the effective Zel'dovich approximation approach including stochastic scale-dependent, non-local and nonlinear biasing contribution. In particular, the halo bias and the non linearities are accounted for by introducing a number of effective free parameters, directly calibrated from the clustering observation or from a N-body mock; the current analysis uses light-cone catalogues calibrated directly from the DR14Q clustering. The light-cone is implemented coating 7 different snapshots at $z = 0.9, 1.1, 1.3, 1.5, 1.6, 1.7, 2.0$. Given the noise of the DR14 sample, we are not interested in extending the analysis presented here to explore non-linear bias parameters, which in fact, are kept in chapter 8 as well, as nuisance parameters. For this reason, the resolution given by the EZ mocks light-cone is sufficient for validating the analysis on eBOSS data. However, the step-wise implementation of the light-cone, as we discuss in 7.6.2, limits our ability to constrain the slope of the growth rate parameter and to investigate the impact of the evolution in redshift of the velocity dispersion. A key requirement for future work will be to reproduce the tests discussed here on a more realistic set of mocks with an higher resolution and a proper light-cone implementation.

In the next chapter (8), we will apply the weighting scheme to measure redshift-space distortions from the eBOSS DR 14 quasar data. In this paper, we validate the procedure and test for optimality. By fitting to the evolution with a model for bias and cosmology, we are able to fit simultaneously the evolution of the growth rate $f(z)$, the amplitude of the dark matter density fluctuations $\sigma_8(z)$ and the galaxy bias $b(z)$; breaking part of the degeneracy inherent in standard measurements of $f\sigma_8$ and $b\sigma_8$ when only one effective redshift is considered. We show that the redshift weighting scheme gives unbiased measurements.

The weights can be applied in both configuration or Fourier space. In this paper, we focus Fourier space, as there is some evidence that this provides stronger redshift space distortions (RSD) constrains, given the current scale limits within which the clustering can be modelled to a reasonable accuracy [7]. In addition, the calculation of the power spectrum moments is significantly faster than the correlation function as discussed in chapter 4. Working in Fourier-space requires a reformulation of the window selection to account for an evolving power spectrum.

The chapter is organized as follows; Section 7.2 reviews the derivation of optimal weights, presenting two schemes that differ in the cosmological model to be tested. In Section 7.3 we review the redshift space power spectrum model at a single redshift. In Section 7.4 we model the power spectrum and the window function to obtain the redshift evolving power

spectrum. In Section 7.5 we present the result of our analysis.

7.2   Optimal Weights

We make use of two different sets of weights; the first explores deviations from the ΛCDM model by altering the evolution of Ω_m in redshift. This model ties together growth and geometry, but can also be used after fixing the expansion rate to match the prediction of the ΛCDM model. The second parametrizes the $f\sigma_8$ parameter combination measured by RSD, allowing for a more standard test of deviations from ΛCDM. Here, the growth and geometry are artificially kept separate as $f\sigma_8$ only affects cosmological growth. In both cases the weights are computed selecting a flat ΛCDM scenario as fiducial model. Note that, as discussed in Chap. 5 and [127], the choice of an inaccurate fiducial model for the weights would only affect the variance of the quantities constrained and not the best-fit values.

The weight functions act as a smooth window on the data and allow us to combine the information coming from the whole volume sampled. These weights are derived by minimising the error on the redshift space distortion measurements, as predicted by a simple Fisher matrix analysis, as shown in chapter 5. Their derivation allows for the evolution with redshift of the cosmological parameters we want to estimate from the data. Optimizing the measurements of the generic parameter θ from the power spectrum moments P_j, $j = 0, 2, 4..$ we obtain the following weights,

$$(7.1) \qquad\qquad w(z) = C^{-1}\partial P_j(z)/\partial \theta_i.$$

We assume the covariance matrix of P, C to be parameter independent and, in absence of a survey window, to be described as

$$(7.2) \qquad\qquad C \sim (P_{\text{fid}} + 1/\overline{n})^2 1/dV,$$

for each volume element, dV within the survey. The weights can be seen as an extension of the FKP weights presented in [86], which have the form,

$$(7.3) \qquad\qquad w_{\text{FKP}}(r) = \frac{1}{1 + \overline{n}(r)P(k)},$$

by including the redshift component $\partial P_j(z)/\partial \theta_i$.

Note that the weights as they are reported in Eq. (7.1), aim to compress different *measurements* of the power spectrum across a range of different redshifts. In fact, we apply weights to each galaxy in order to avoid binning, by assuming the relation $w_{gal} = \sqrt{w_P}$, with w_P denoting the weights defined in Eq. 7.1, which relies on the scale-dependence of the weights being smooth on the scale of interests for clustering.

7.2.1 Optimal Weights for Ω_m

As described in chapter 5, it is empirically convenient to test for deviations from the ΛCDM model by considering the evolution of the matter density with redshift. To do this, we consider a Taylor expansion up to second order about the fiducial model,

$$(7.4) \qquad \frac{\Omega_m(z)}{\Omega_{m,\text{fid}}(z)} = q_0 \left[1 + q_1 y(z) + \frac{1}{2} q_2 y(z)^2 \right],$$

where z_p is the pivot redshift i.e. a selected redshift within the redshift range of the survey and $y(z) + 1 \equiv \Omega_{m,\text{fid}}(z)/\Omega_{m,\text{fid}}(z_p)$.   Note that as shown in [147] the analysis does not depend on the choice of a particular z_p. The q_i parameters correspond to the first and second derivatives of $\Omega_m(z)|_{z_p}$, evaluated at z_p, and incorporate potential deviations about the fiducial model $\Omega_{m,\text{fid}}$.

The choice of parameterising Ω_m (and hence the Hubble parameter, the angular diameter distance and the growth rate) in terms of q_0, q_1 and q_2 allows us to simultaneously investigate small deviations using a common framework; e.g. departures from a fiducial cosmology and geometry are accounted through the fiducial Hubble constant and angular diameter distance $H(\Omega_m)$, $D_A(\Omega_m)$; further, modified gravity models can be accounted through the growth rate, $f(\Omega_m)$.

By matching to the standard Friedman equation, we parametrize the redshift evolution of the Hubble parameter in term of $\Omega_m(z)$ as,

$$(7.5) \qquad H^2(z) = H_0^2 \frac{\Omega_{m,0}(1+z)^3}{\Omega_m(z)}.$$

Assuming a flat Universe ($\Omega_k = 0$) in agreement with CMB measurements [54], we have $\Omega_\Lambda(z) = 1 - \Omega_m(z)$. The subscript "0" denotes quantities evaluated at $z = 0$. For simplicity of notation we omit the q_i dependence from all the parameters: we refer to $\Omega_m(z, q_i)$ as $\Omega_m(z)$, and we denote with $\Omega_{m,\text{fid}}$ the fiducial ΛCDM matter density.

For the scenarios considered, we assume the solution for the linear growth factor $D(z)$ and the dimensionless linear growth rate f have the same dependence on $\Omega_m(z)$ as in the ΛCDM model,

$$(7.6) \qquad g(z) \equiv (1+z)D(z) = \frac{5\Omega_m(z)H^3(z)}{2(1+z)^2} \int_z^\infty dz' \frac{(1+z')}{H^3(z')}$$

$$(7.7) \qquad f(z) = -1 - \frac{\Omega_m(z)}{2} + \Omega_\Lambda(z) + \frac{5\Omega_m(z)}{2g(z)}.$$

Fig. 7.1 shows an example of the weights as derived in chapter 5, that optimize the measurements of the q_i parameters in a ΛCDM fiducial background for a redshift-space
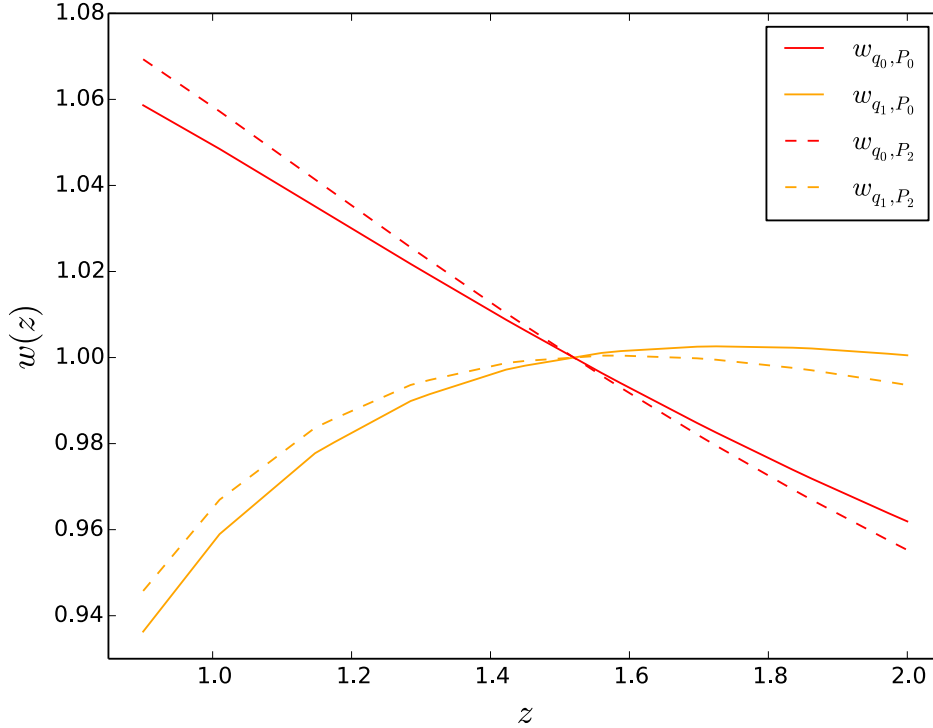
Figure 7.1: The weights for the monopole and quadrupole with respect to the q_i parameters.

power spectrum. Since each multipole contains information about $\Omega_m(z)$, our set of weights is derived to be optimal for the first two non-null moments of the power spectrum on the Legendre polynomial basis for each q_i parameter. Continuous lines indicate the weights for the monopole with respect to q_0 (red line) and q_1 (orange line); dashed lines indicate the weights for the quadrupole with respect q_0, q_1 (red and orange lines). All the weights are normalized to be equal 1 at the pivot redshift;

7.2.2 Optimal Weights for $f\sigma_8$

RSD measurements constrain the amplitude of the velocity power spectrum, and its cosmological dependence in the linear regime is commonly parameterized by the product of the two parameters f and σ_8, which provides a good discriminator of modified gravity models [159]. We compare results obtained from the Ω_m parametrisation with those derived using a set of weights parametrised with respect to $[f\sigma_8](z)$. In an analogous way to the consideration in Section 7.2.1, we can expand $[f\sigma_8](z)$ about a fiducial model, so Eq. (7.4)

119

becomes

$$(7.8) \qquad [f\sigma_8](z) = [f\sigma_8]_{fid}(z) p_0\left(1 + p_1 x + p_2 \frac{x^2}{2}\right),$$

where $x \equiv [f\sigma_8]_{fid}(z)/[f\sigma_8]_{fid}(z_p) - 1$. The p_i parameters correspond to the first and second derivatives of $[f\sigma_8](z)|_{z_p}$, evaluated at z_p, and incorporate potential deviations about the fiducial model $[f\sigma_8]_{fid}$.

As a fiducial model for $[f\sigma_8]_{fid}$ to compute the weights, we select the solution of linear perturbation theory in a flat ΛCDM scenario, where the growth rate evolves with redshift as

$$(7.9) \qquad \begin{aligned} [f\sigma_8]_{fid}(z) = &\left[-1 - \frac{\Omega_{m,fid}(z)}{2} + \Omega_{\Lambda,fid}(z) + \frac{5\Omega_{m,fid}(z)}{2g_{fid}(z)}\right] \\ &\times \sigma_{8,0} \frac{g_{fid}(z)}{(1+z)^2}, \end{aligned}$$

with g_{fid}, fiducial growth factor,

$$(7.10) \qquad g_{fid}(z) = \frac{5\Omega_{m,fid}(z) H_{fid}^3(z)}{2(1+z)^2} \int_z^\infty dz' \frac{(1+z')}{H_{fid}^3(z')}$$

The galaxy bias parameter is assumed to be independent of f and σ_8. For simplicity, we consider $[b\sigma_8]$ to be *independent* from $[f\sigma_8]$ as well. Considering e.g. the galaxy monopole with respect to the linear matter power spectrum P,

$$(7.11) \qquad P_0 = \left([b\sigma_8]^2 + \frac{2}{3}[b\sigma_8][f\sigma_8](z) + \frac{1}{5}[f\sigma_8]^2(z)\right) P(k),$$

the dependence on the p_i parameters is given only through $[f\sigma_8]$. We derive the set of weights by taking the derivative of P_0, P_2, P_4 with respect to p_1, p_2, p_3. For completeness we include the weights here as they were not included in chapter 5.

$$(7.12) \qquad w_{i,q_0} = N_i, \quad w_{i,q_1} = N_i y, \quad w_{i,q_2} = N_i \frac{1}{2} y^2,$$

where

$$(7.13) \qquad N_0 \equiv \left(\frac{2}{3}[b\sigma_8] + \frac{2}{5}[f\sigma_8](z)\right)[f\sigma_8](z),$$

$$(7.14) \qquad N_2 \equiv \left(\frac{4}{3}[b\sigma_8] + \frac{8}{7}[f\sigma_8](z)\right)[f\sigma_8](z),$$

$$(7.15) \qquad N_2 \equiv \left(\frac{16}{35}[f\sigma_8](z)\right)[f\sigma_8](z).$$

A strong effect on the set of weights is caused by the assumptions we make for galaxy bias. If we set the bias as an unknown parameter, and we marginalize over it, then we cannot deduce any information about structure growth from the amplitude of the density power spectrum. This is the case for the expansion around $[f\sigma_8]$, where we considered $[b\sigma_8]$ and $[f\sigma_8]$ as independent parameters. However, if we constrain $b(z)$ to match a fiducial model, we will derive weights that make use of the information coming from the amplitude of the power spectrum. For the expansion around Ω_m, we can choose whether or not to include this information.

7.3 Modelling the anisotropic galaxy power spectrum at a single redshift

We model the power spectrum using perturbation theory (PT) up to 1-loop order. We include the non linear redshift space distortions effects as in [70] and [13] (TSN model),

$$
\begin{aligned}
P_{\mathrm{g}}(k,\mu) = \exp\left\{-(fk\mu\sigma_v)^2\right\} \Big[&P_{\mathrm{g},\delta\delta}(k) \\
&+ 2f\mu^2 P_{\mathrm{g},\delta\theta}(k) + f^2\mu^4 P_{\theta\theta}(k) \\
&+ b^3 A(k,\mu,\beta) + b^4 B(k,\mu,\beta) \Big],
\end{aligned}
$$
(7.16)

where μ is the cosine of the angle between the wave-vector $\mathbf{k}$ and the line of sight. $P_{\theta\theta}$ and $P_{\delta\theta}$ are the *velocity-velocity* and *matter-velocity* power spectra terms that correspond to the extended linear model of [52] as derived in [70]. θ denotes the Fourier transform of the comoving velocity field divergence, $\theta(\mathbf{k}) \equiv -i\mathbf{k}\cdot\mathbf{u}(k)$ where $\nabla\mathbf{u} = -\nabla\mathbf{v}/\big[af(a)H(a)\big]$ with velocity field v and dimensionless linear growth rate f. The exponential term represents the damping due to the "Fingers of God" effect, where σ_v denotes the velocity dispersion term, here treated as free parameter. The A, B terms come from the TNS model which take into account further corrections due to the non linear coupling between the density and velocity fields [13]. Note that at linear level $P_{\theta\theta} = P_{\delta\theta} = P_{\delta\delta}$.

We model $P_{\mathrm{g},\delta\delta}$ and $P_{\mathrm{g},\delta\theta}$ as

$$
\begin{aligned}
P_{\mathrm{g},\delta\delta}(k) = b^2 P_{\delta\delta}(k) &+ 2b_2 b P_{b2,\delta}(k) + 2b_{s2} b P_{bs2,\delta}(k) \\
&+ 2b_{3nl} b \sigma_3^2(k) P(k) + b_2^2 P_{b22}(k) \\
&+ 2b_2 b_{s2} P_{b2s2}(k) + b_{s2}^2 P_{bs22}(k) + S,
\end{aligned}
$$
(7.17)

(7.18)

$$P_{g,\delta\theta}(k) = b P_{\delta\theta}(k) + b_2 P_{b2,\theta}(k) + b_{s2} P_{bs2,\theta}(k)$$
$$+ b_{3nl}\sigma_3^2(k)P(k),$$

(7.19)

The bias is modelled following recent studies [64][160] that showed the importance of non-local contributions. We account for those effects introducing as galaxy bias parameters: the linear b, second order local b_2, non local b_{s2}, and the third order non-local b_{3nl} bias parameters, and the constant stochasticity shotnoise term S. We numerically evaluate the non-linear matter power spectra, $P_{\delta\delta}$, $P_{\delta\theta}$, $P_{\theta\theta}$, at 1-loop order in standard perturbation theory (SPT) using the linear power spectrum input from CAMB [161].

In the current analysis we make use of the first three non-zero moments of the power spectrum, projected into an orthonormal basis of Legendre polynomials $\mathscr{L}_\ell(\mu)$ such that,

$$P_\ell(k) = \frac{2\ell+1}{2}\int_{-1}^{1} d\mu P(k,\mu)\mathscr{L}_\ell(\mu),$$

(7.20)

with the monopole $\ell = 0$, quadrupole $\ell = 2$ and hexadecapole $\ell = 4$, respectively. In this paper we do not consider geometrical deviations and we are only concerned with growth measurements in a fixed background. However, we note that such deviations can be included as follows. The geometrical deviations from the fiducial cosmology can be included through the Alcock-Paczynski effect, [73]. Here, revised mode numbers k', μ' for the cosmological model being tested, are related to those observed k, μ assuming the fiducial cosmology by the transformations

$$k' = \frac{k}{\alpha_\perp}\left[1 + \mu^2\left(\frac{\alpha_\perp^2}{\alpha_\parallel^2} - 1\right)\right]^{1/2}$$

(7.21)

$$\mu' = \frac{\mu\alpha_\perp}{\alpha_\parallel}\left[1 + \mu^2\left(\frac{\alpha_\perp^2}{\alpha_\parallel^2} - 1\right)\right]^{-1/2}$$

where the scaling factors $\alpha_\parallel$ and $\alpha_\perp$ are defined as

$$\alpha_\parallel = \frac{H^{\text{fid}}(z)}{H(z)},$$

(7.22)

$$\alpha_\perp = \frac{D_A(z)}{D_A^{\text{fid}}(z)}.$$

By applying the transformations of Eq. (7.22) to Eq. (7.20), the multipoles at the observed k and μ, relate to the power spectrum at the true variables k' and μ' through

$$P_\ell(k) = \frac{(2\ell+1)}{2\alpha_\perp^2\alpha_\parallel}\int_{-1}^{1} d\mu P_g(k',\mu')\mathscr{L}_\ell(\mu).$$

(7.23)

7.4 Modelling the evolving galaxy power spectrum

7.4.1 Redshift weighted multipoles without window function

We model the redshift dependence of f, σ_8, $\alpha_\parallel$, and $\alpha_\perp$ as described above, and the bias evolution (see Sec. 7.4.3). In principle we can compute the weighted multipoles by integrating the power spectrum moments as given in Eq. (7.23) over redshift, including the redshift weighting,

$$
(7.24) \qquad\qquad P_{\ell w_{\ell,q_j}} = \int dz\, P_\ell(k,z)\, w_{\ell,q_j}.
$$

In general when estimating the power spectrum of a three-dimensional redshift survey, that measured is the underlying power spectrum convolved with the window function. Therefore to compare the model with the data we first convolve it with the window determined by the survey geometry. In the next section we derive a general relation between the measured P and the window function to extend the treatment of [86], (Eq. 2.1.4) to the case where the power spectrum is evolving with redshift.

7.4.2 Redshift weighted multipoles including the survey window effect

We study the window function for the evolving power spectrum using a generalized Hankel transformation between power spectrum and correlation function moments, where the window applied is also decomposed into a set of multipoles. This is an extension of the work by [162] and [95], which presented a method to convolve model power spectra with the window function for a non-evolving power spectrum. We consider the case where the underlying correlation function ξ is dependent on both the separation $r = |r_i - r_j|$ (with r_i and r_j position of galaxies of each pair) and the mean redshift of each galaxy pair $\xi[r_i(z_i), |r_i - r_j|]$. Here we have assumed that cosmological evolution is negligible over the range of redshifts covered by every pair, so we can quantify the clustering of each using the correlation function at the mean redshift.

The multipole moments of the power spectrum in the local plane-parallel approximation

can be written as,

$$
\begin{aligned}
\hat{P}_\ell(k) = &\frac{2\ell+1}{2}\int d\mu_k \int \frac{d\phi}{2\pi}\int d\mathbf{x}_1 \int d\mathbf{x}_2\, e^{i\mathbf{k}\cdot\mathbf{x}_1}e^{-i\mathbf{k}\cdot\mathbf{x}_2}\\
&\langle\delta(\mathbf{x}_1)\delta(\mathbf{x}_2)W(\mathbf{x}_1)W(\mathbf{x}_2)\rangle\,\mathcal{L}_\ell(\hat{\mathbf{k}}\cdot\hat{\mathbf{x}}_h)\\
= &\frac{2\ell+1}{2}\int d\mu_k \int \frac{d\phi}{2\pi}\int d\mathbf{x}_1 \int d\mathbf{s}\times\\
&\left(\sum_L \xi_L[s,z(x_1)]\mathcal{L}_L(\hat{\mathbf{x}}_h\cdot\hat{\mathbf{s}})\right)\times\\
&W(\mathbf{x}_1)W(\mathbf{x}_1+\mathbf{s})e^{-i\mathbf{k}\cdot\mathbf{s}}\mathcal{L}_\ell(\hat{\mathbf{k}}\cdot\hat{\mathbf{x}}_h),
\end{aligned}
\tag{7.25}
$$

where $\int d\mu_k$ is the integral over all the possible cosine angles between $\hat{\mathbf{k}}$ and $\hat{\mathbf{x}}_h$ and W defines the mask. ξ_L denotes the correlation function moments in the Legendre basis. Note that Eq. (7.25) differs from equation A.16 in [95], only in the $\xi_L[s,z(x_1)]$ term; for a single redshift slice we would only have $\xi_L(s)$. We make use of the relations,

$$
e^{-i\mathbf{k}\cdot\mathbf{s}} = \sum_p (i)^p(2p+1)j_p(ks)\mathcal{L}_p(\hat{\mathbf{k}}\cdot\hat{\mathbf{s}}),
\tag{7.26}
$$

$$
\int d\mu_k \int \frac{d\phi}{2\pi}\mathcal{L}_\ell(\hat{\mathbf{k}}\cdot\hat{\mathbf{x}}_h)\mathcal{L}_p(\hat{\mathbf{k}}\cdot\hat{\mathbf{s}}) = \frac{2}{2\ell+1}\mathcal{L}_\ell(\hat{\mathbf{s}}\cdot\hat{\mathbf{x}}_h)\delta_{\ell p},
\tag{7.27}
$$

which, when combined with Eq. (7.25), give

$$
\begin{aligned}
\hat{P}_\ell(k) = &i^\ell(2\ell+1)\int d\mathbf{x}_1\int d\mathbf{s}\sum_L \xi_L[s,z(x_1)]j_\ell(ks)\times\\
&W(\mathbf{x}_1)W(\mathbf{x}_1+\mathbf{s})\mathcal{L}_\ell(\hat{\mathbf{x}}_h\cdot\hat{\mathbf{s}})\mathcal{L}_L(\hat{\mathbf{x}}_h\cdot\hat{\mathbf{s}}).
\end{aligned}
\tag{7.28}
$$

Substituting the Bailey relation, $\mathcal{L}_\ell\mathcal{L}_p = \sum_t a^\ell_{pt}\mathcal{L}_t$, Eq. (7.28) becomes,

$$
\begin{aligned}
\hat{P}_\ell(k) = &i^\ell(2\ell+1)\int d\mathbf{x}_1\int d\mathbf{s}\sum_L \xi_L[s,z(x_1)]j_\ell(ks)\times\\
&W(\mathbf{x}_1)W(\mathbf{x}_1+\mathbf{s})\mathcal{L}_\ell(\hat{\mathbf{x}}_h\cdot\hat{\mathbf{s}})\sum_t a^\ell_{Lt}\mathcal{L}_t(\hat{\mathbf{x}}_h\cdot\hat{\mathbf{s}}).\\
= &i^\ell(2\ell+1)\int 2\pi s^2 ds\, j_\ell(ks)\sum_L\sum_t a^\ell_{Lt}\int d\mu_s\int\frac{d\phi}{2\pi}\\
&\times\int d\mathbf{x}_1\,\xi_L[s,z(x_1)]W(\mathbf{x}_1)W(\mathbf{x}_1+\mathbf{s})\mathcal{L}_t(\hat{\mathbf{x}}_h\cdot\hat{\mathbf{s}})
\end{aligned}
\tag{7.29}
$$

At this stage, in contrast to Eq. $A.19$ in [95], we cannot bring ξ_L out of the integral over x_1. Since we are not able to decouple the mask from ξ, in principle, we would have to compute the integral over x_1 for every model ξ fitted to the data. However we can reduce drastically the

computational time required by assuming that ξ is well behaved such that we can split the integral over x_1 into a sum over a small number of x_i ranges. This is different from measuring the clustering in shells - we are still calculating and modelling the power spectrum as a continuously weighted function calculated using every galaxy pair; we are simply making an assumption about the smooth behaviour in redshift of the expected clustering.

$$
\begin{aligned}
\hat{P}_\ell(k) = i^\ell (2\ell+1) \int 2\pi s^2 ds \, j_\ell(ks) \sum_L \sum_t a_{Lt}^\ell \int d\mu_s \int \frac{d\phi}{2\pi} \\
\times \sum_i \int_{x_i} d\mathbf{x}_1 \, \xi_L(s, z(x_i)) W(\mathbf{x}_i) W(\mathbf{x}_i + \mathbf{s}) \mathscr{L}_t(\hat{\mathbf{x}}_h \cdot \hat{\mathbf{s}}).
\end{aligned}
$$
(7.30)

Assuming that $\xi_L(s, z(x_i))$ is constant over each sub-integral range x_i we can take it out of the integrals,

$$
\begin{aligned}
\hat{P}_\ell(k) = i^\ell (2\ell+1) \int 2\pi s^2 ds \, j_\ell(ks) \sum_L \sum_t a_{Lt}^\ell \times \\
\sum_i \xi_L(s, z(x_i)) \int d\mu_s \int \frac{d\phi}{2\pi} \int_{x_i} d\mathbf{x}_i \, W(\mathbf{x}_i) W(\mathbf{x}_i + \mathbf{s}) \mathscr{L}_t(\hat{\mathbf{x}}_h \cdot \hat{\mathbf{s}}),
\end{aligned}
$$
(7.31)

and redefine the sub-window function multipoles $W_{p,z_i}^2(s)$ for $p = 0, 2, 4..$ as

$$
\begin{aligned}
W_{p,z_i}^2(s) = \frac{2p+1}{2} \int d\mu_s \int \frac{d\phi}{2\pi} \int_{z_i} d\mathbf{x}_i \\
\times W(\mathbf{x}_i) W(\mathbf{x}_i + \mathbf{s}) \mathscr{L}_p(\mu_s).
\end{aligned}
$$
(7.32)

Using the definition of the sub-window function multipoles of Eq. 7.32, we can write Eq. (7.31) to be

$$
\begin{aligned}
\hat{P}_\ell(k) = i^\ell (2\ell+1) \int 2\pi s^2 ds \, j_\ell(ks) \times \\
\sum_L \sum_t \frac{2}{2t+1} a_{Lt}^\ell \sum_i \xi_L(s, z_i) W_{t,z_i}^2(s).
\end{aligned}
$$
(7.33)

which generalizes Eq. A.23 in [95] to the case of a redshift-evolving power spectrum.

Note that when computing the mask $W(\mathbf{x})$ using the random catalog we include the redshift weights, in the same way the standard FKP weights have been included in traditional analyses e.g. [95].

7.4.3 Bias evolution

evolution in redshift of the galaxy bias, $b(z)$ strongly depends on the targets considered. In Chap. 5 we compared the weights for different $b(z)$ relations and showed that the weights are not significantly sensitive to the different $b(z)$ considered;

The fitting formula for the linear bias parameter of the quasar sample suggests that the linear bias redshift evolves as, [156],

$$b(z) = 0.53 + 0.29(1 + z)^2. \tag{7.34}$$

We model the evolution of b about the pivot redshift times σ_8 as,

$$b\sigma_8(z) = b\sigma_8(z_{\mathrm{p}}) + \partial b\sigma_8/\partial z|_{z_p}(z - z_{\mathrm{p}}) + ... \tag{7.35}$$

We neglect the redshift dependence for the non linear bias parameter b_2, so we assume this is constant with redshift, $b_2\sigma_8(z_{\mathrm{p}})$. We fix the 2nd-order non-local bias, bs_2 and 3rd-order non-local bias, b_{3nl} terms to their predicted values according to non-local Lagrangian models,[64], [160],

$$
\begin{aligned}
b_{s2} &= -\frac{4}{7}(b-1), \\
b_{3nl} &= \frac{32}{315}(b-1).
\end{aligned}
\tag{7.36}
$$

7.5 Fitting to the mock data

7.5.1 Power spectrum measurement

To compute the power spectrum moments with respect to the line of sight (LOS), we make use of the estimator introduced in chapter 4. This fourier transform (FT) - based algorithm uses multiple FTs to track the multipole moments, in the local plane-parallel approximation where we have a single LOS for each pair of galaxies. This estimator has been already used in recent analysis [95], that confirmed the advantages of using such decomposition: it reduces the computational time from N^2 associated to naive pair counting analysis [113] to $\sim N log N$.

Redshift weights are included in the estimator, by defining the weighted galaxy number density as $n_g(\mathbf{r})w$. As discussed in Section 7.2 we have derived the galaxy weights from the square-root of the power spectrum weights, under the assumption that the scale dependence in the weights is smooth compared to the scale of interest for our clustering measurements.

The result is a set of weighted multipoles, $P_{0,2,w_{0,1,2}}$, where each P_{i,w_j} corresponds to a particular set of weights that optimizes each of the q_i or p_i measurement, i.e. for the set of weights w_{i,q_j} (or w_{i,p_j} for the $f\sigma_8$ weights) functions and we build a data vector Π as,

$$\Pi^T = (P_{0,w_0,q_0}, P_{0,w_0,q_1}, P_{0,w_0,q_2} ... P_{2,w_2,q_2})^{\mathrm{T}}. \tag{7.37}$$

7.5.2 Covariance matrix estimation

We evaluate the covariance matrix for the data vector Π^T using 1000 EZ mock described in Section 7.1. For each mock, we compute the weighted monopole and quadrupole moments for each set of optimal redshift weights, for $n_b = 10$ k-bins in the range of $k = 0.01 - 0.2 h \text{Mpc}^{-1}$. From these, we derive the covariance matrix as

$$
(7.38) \quad C = \frac{1}{N_T - 1} \sum_{n=1}^{N_T} \left[P_{n,\ell,w_{\ell,q_t}}(k_i) - \hat{P}_{\ell,w_{\ell,q_t}}(k_i) \right]
$$
$$
\times \left[P_{n,\ell,w_{\ell,q_t}}(k_j) - \hat{P}_{\ell,w_{\ell,q_t}}(k_j) \right],
$$

where $N_T = 1000$ is the number of mock catalogues, w_{ℓ,q_t} denotes each set of weights for each parameter q_t (or p_t) and $\hat{P}_{\ell,w_{\ell,q_t}}(k_i) = \frac{1}{N_T} \sum_{n=1}^{N_T} P_{n,\ell,w_{\ell,q_t}}(k_i)$.

Note that when inverting the covariance matrix we include the Hartlap factor [163] to account for the fact that C is inferred from mock catalogues. choice of $n_b = 10$ given $N_T = 1000$ mocks available, ensures that the covariance matrix is positive definite.

7.5.3 Maximising the Likelihood

Since each weighted multipole $P_{i,w_{i,q_j}}$ is optimized with respect to a particular piece of information (e.g. $\Omega_m[z]$),we jointly fit all three q_i (or p_i) parameters simultaneously. We compare the measured Π^T to modelled weighted power spectra multipoles, convolved with the window function as explained in Section 7.4.2. We assume a Gaussian likelihood and minimize

$$
(7.39) \quad \chi^2 \propto (\Pi - \Pi_{\text{m}odel})^{\text{T}} C^{-1} (\Pi - \Pi_{\text{m}odel});
$$

Where $\Pi_{\text{m}odel}$ refers to the window convolved $P_{i,w_{i,q_j}}$. The C^{-1} term corresponds to the joint covariance derived in Eq. (8.4). We repeat the fit for both the Ω_m and $f\sigma_8$ optimized sets of weights.

In the current analysis we limit ourselves to linear order deviations about our fiducial ΛCDM model, for both $f\sigma_8(z)$ and $\Omega_m(z)$ described in Sections 7.2.1 and 7.2.2, since the data cannot capture second-order deviations.

7.6 Measuring RSD with the evolving galaxy power specturm

The fits presented in this section are performed using a Monte Carlo Markov Chain (MCMC) code, implemented to efficiently account for the degeneracies between the parameters; in

all the fit performed we select a range between $k = 0.01 - 0.2 h\mathrm{Mpc}^{-1}$. For each scenario explored we run 10 independent chains, satisfying the Gelman-Rubin convergence criteria [164] with the requirement of $R - 1 < 10^4$; where R corresponds to the ratio between the variance of chain mean and the mean of chain variances. All the results presented are obtained after marginalizing on the full set of parameters, including the nuisance parameters (shotnoise and velocity dispersion). All the contour plots are produced using the public getdist libraries[3].

We fit the weighted monopole and quadrupole computed on a subset of 20 EZ mocks, for both the Ω_m and the $f\sigma_8$-optimized weights, while keeping the distance-redshift relation fixed to the fiducial cosmology, i.e. $\alpha_\parallel = \alpha_\perp = 1$.

We do not consider the full set of 1000 EZ mocks for the following reasons; first we are limited by the EZ-mock accuracy in describing non linearities in galaxy bias and velocities; further by the accuracy in the light-cone describing the redshift evolution for $f\sigma_8$ which is included as a step function. Thus we do not believe that the mocks supports us looking at deviations from the model at better accuracy than this. However, the error on our constraints is still $1/\sqrt{20}$ smaller than what we expect on the eBOSS quasars constraints. The analysis has been performed on different subset of 20 mocks out of the 1000 available to verify that the outcomes do not depend on a particular sub-sample choice.

Our analysis is presented as follow; in 7.6.1 we present the result obtained with the Ω_m weights fitting for q_0, q_1, $b\sigma_8(z_\mathrm{p})$, $\partial b\sigma_8/\partial z|_{z_p}$, b_2, σ_v, and shotnoise S. In parallel we present the fit for $p_0, p_1, b\sigma_8(z_\mathrm{p})$, $\partial b\sigma_8/\partial z|_{z_p}$, b_2, σ_v when applying the $f\sigma_8$ weights.

In 7.6.2 we investigate the impact of the bias assumption on the constraints, showing a comparison between bias evolving and constant with redshift.

In 7.6.3 we compare the results obtained with the redshift weights approach with the analysis performed considering one *constant* redshift slice i.e. considering all the parameters $(f\sigma_8, b\sigma_8, \sigma_v, b_2, S)$ in the power spectra at their value at the pivot redshift $z_p = 1.55$ and applying FKP weights only (for simplicity of the notation from now on we refer to this as *traditional* analysis).

Differently from [147], we compare the redshift weights analysis with the standard analysis used for previous RSD measurements (see e.g. [95]) rather than testing the weights $w_{q,i}, w_{p,i} = 1$. The main focus of this work is to test that our analysis is not biased by introducing evolution in the power spectrum and in the window function. We rely on the Fisher matrix theory correctly selecting the set of weights optimal with respect to the q_i, p_i errors.

---

[3]http://getdist.readthedocs.io/
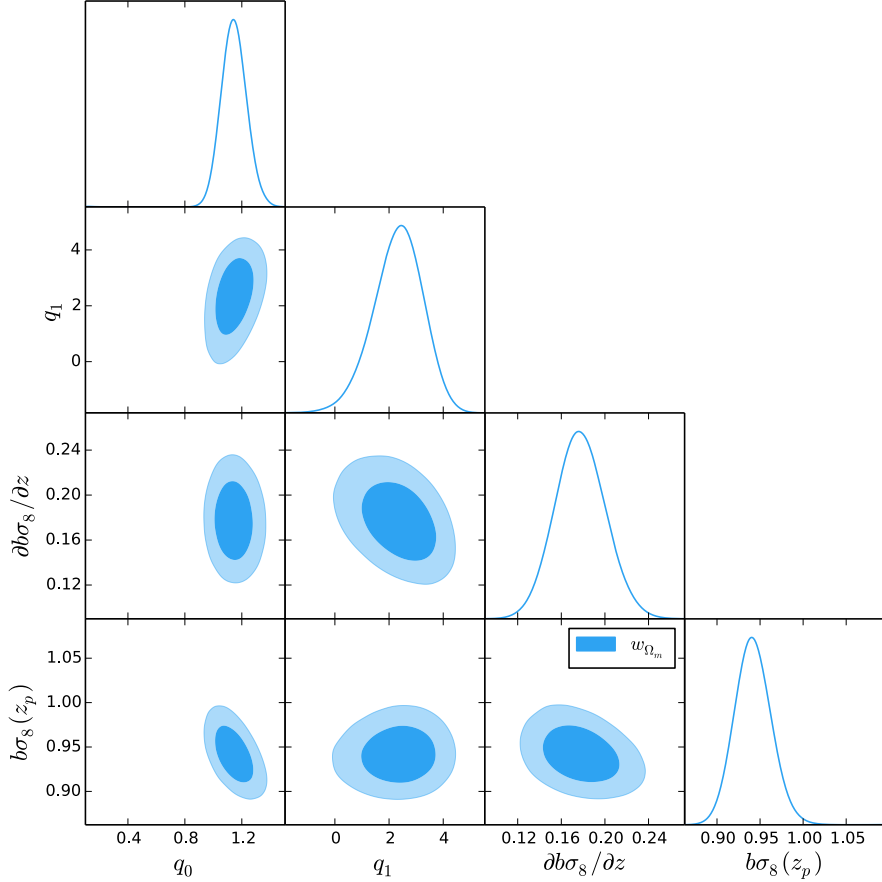
Figure 7.2: Likelihood distributions for the analysis of the average of 20 EZ mock. We show the results for q_0, q_1, $b\sigma_8(z_p)$, $\partial b\sigma_8/\partial z$, marginalized over the full set parameters (including $b_2\sigma_8(z_p)$, σ_v, S not displayed here). We multi-fit two weighted monopoles and two weighted quadrupoles (one for each weight function (w_{0,p_i}, w_{2,p_i}) The fitting range is $k = 0.01 - 0.2h$Mpc^{-1} for both the monopole and quadrupole.

7.6.1 Redshift weights fit

Fig. 7.2 shows the posterior likelihood distributions from the analysis performed with the set of redshift weights optimized to constrain $\Omega_m(z)$ (blue contour plots), using the monopole and the quadrupole; we fit for q_0, q_1 which describe up to linear order deviations in the evolution of $\Omega_m(z)$ according to ΛCDM model; we also vary the galaxy bias parameters modelled as in section 7.4.3, while we fix the 2nd-order non-local bias, bs_2 and 3rd-order non-local bias, b_{3nl} terms as shown in Eq. 7.36. To summarize we fit for 7 parameters: q_0, q_1, $b\sigma_8(z_p)$, $\partial b\sigma_8/\partial z|_{z_p}$, $b_2\sigma_8(z_p)$, σ_v, and shotnoise S.

Fig 7.3 presents the results of the analysis while using the set of redshift weights optimized to constrain $f\sigma_8(z)$, as introduced in Sec. 7.2.2; the structure is the same as in Fig. 7.2. We fit
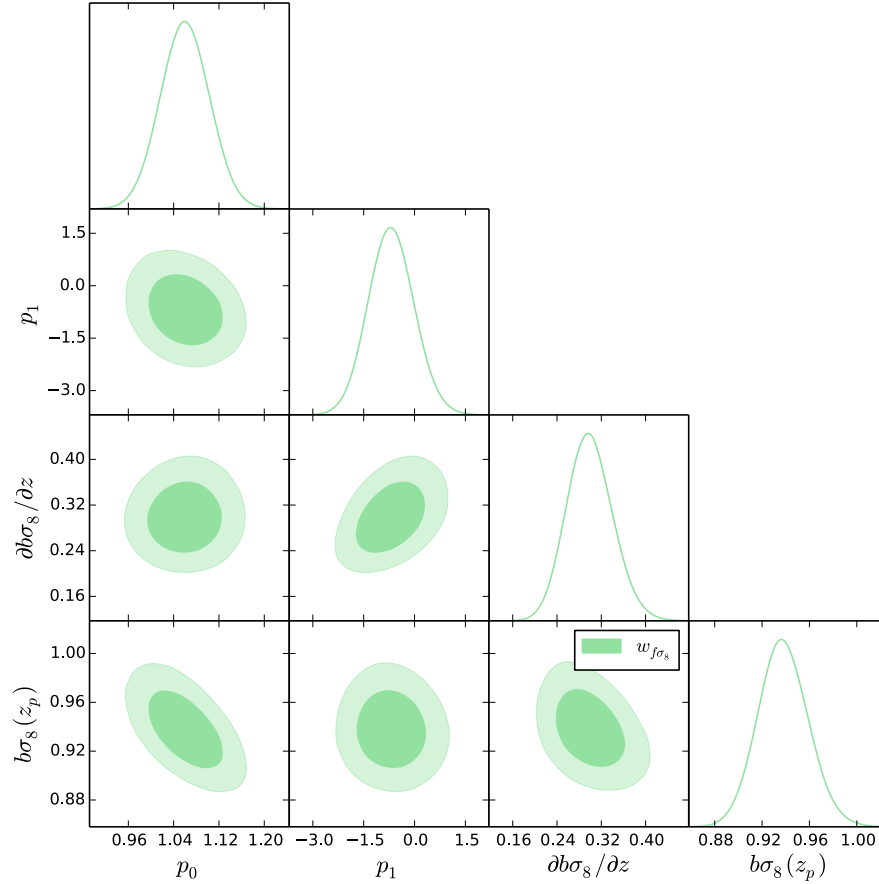
Figure 7.3: Likelihood distributions for the analysis of the average of 20 EZ mock. We show the results for p_0, p_1, $b\sigma_8(z_p)$, $\partial b\sigma_8/\partial z$, marginalized on the full set parameters (including $b_2\sigma_8(z_p)$, σ_v, S not displayed here). We multi-fit two weigthed monopoles and two weighted quadrupoles (one for each weight function (w_{0,p_i}, w_{2,p_i}) The fitting range is $k = 0.01 - 0.2h\mathrm{Mpc}^{-1}$ for both the monopole and quadrupole.

for p_0, p_1 to constrain $f\sigma_8(z)$ deviations about the fiducial $f\sigma_8(z)$ according to ΛCDM; we also fit for $b\sigma_8(z_p)$, $\partial b\sigma_8(z)/\partial z$, $b_2\sigma_8(z_p)$, σ_v, S, 7 parameters in total as for the other set of weights.

We obtained the covariance and correlation matrix for the full set of parameters of the MCMC chains using getdist libraries.

The resulting posteriors in both Figures 7.2 and 7.3 show a correlation between the zero order parameters, q_0 (p_0) and $b\sigma_8(z_p)$, of magnitude of ~ 0.5. We also detect a relevant anti-correlation ~ -0.4 between the slope parameter q_1 (p_1) and the gradient $\partial b\sigma_8(z)/\partial z$.

These non-zero correlations lead to a mild dependency between the assumed bias model (linear and non linear in k and in z) and the slope parameter q_1 (p_1) without however

Figure 7.4: The reconstructed evolution of $f\sigma_8$ and 68% confidence level regions using the average of 20 mocks; blue shaded region shows the constraint on the evolution of $f\sigma_8$ obtained by the fit of $\Omega_m(z, q_i)$ using the w_{Ω_m} optimal weights and deriving at each redshift $f[\Omega_m(z, q_i)]$ times $\sigma_8[\Omega_m(z, q_i)]$; green shaded region shows the resulting evolution when fitting for $f\sigma_8(z, p_i)$ at each redshift. The red point indicates the results obtained when performing the traditional analysis, with $z_p = 1.55$.

affecting (within $\sim 1\sigma$) the constraints on $f\sigma_8$. In 7.6.2 we illustrate the impact of the bias evolution on the growth rate in more details.

Due to the stepwise implementation of the growth rate and bias model in the mocks, the fiducial values of q_0, q_1 (p_0, p_1) are not well defined. Therefore, we do not display an expected value for p_i and q_i as those cannot be inferred from the $f\sigma_8$ evolution included as a non-smooth step function in the mocks. However, within 1 to 2sigma we recover the smooth ΛCDM expectation values of $q_0 = 1$ and $q_1 = 0$.

Fig. 7.4 shows the redshift evolution reconstructed from p_0, p_1, (green shaded regions), compared with the evolution reconstructed from the q_0, q_1 (blue shaded regions). The red point indicates the constraints at one single redshift (traditional analysis, with $z = 1.55$) for $f\sigma_8$. We overplot the evolution of $f\sigma_8(z)$ as accounted in the mock light-cone (black dashed line). The plot shows that the $f\sigma_8$ evolution obtained for both the Ω_m and $f\sigma_8$ weighting schemes is fully consistent with the cosmology contained in the mock and in full agreement with the constraints coming from the traditional analysis. For both parametrizations the errors obtained at the pivot redshift is comparable with the error we get from the traditional

analysis. Note that the error from redshift weighting analysis comes from the marginalization over a set of 7 parameters in contrast to the traditional analysis limited to only 5 free parameters.

Away from from the pivot redshift, the errors becomes larger for both parametrizations. At these redshifts, the major contribution to the error comes from the slope constraints (q_1, p_1) and the S/N is lowered due to the low number density $n(z)$, [23]. The number of quasars observed as a function of redshift also helps to explain the differences in the error as a function of redshift, with a larger error found where there are fewer quasars. For both parametrizations, the slope parameters are degenerate with the non linear bias parameters.

In 7.6.1 we modelled the bias evolution with a Taylor expansion up to linear order about the pivot redshift (see Eq. 7.4.3). Fig. 7.5 shows the $b\sigma_8(z)$ evolution measured using the Ω_m and $f\sigma_8$ weighting schemes (blue and green shaded regions). We reconstruct $b\sigma_8(z)$ at the different redshifts from the fit of $b\sigma_8(z_p)$ and $\partial b\sigma_8(z)/\partial z$. We overplot the evolution of $b\sigma_8(z)$ as included in the mocks (black dashed line). The red point indicates the constraints obtained by using the traditional analysis; we find full agreement at the pivot redshift between the three different analysis and within 1σ of the value included in the mocks. The bias depends significantly on redshift and in the mocks is modelled as a step function, which leads to small discrepancies with respect to both the constant and linear evolution in $b\sigma_8$. We redid the fit extending the analysis to second order in bias and found consistent results but with error too large to see any improvements (high degeneracy). For the purpose of fitting eBOSS quasar sample this is more than enough and we leave for future work a more careful study of the bias effects/evolution to be performed on more accurate N-body mocks.

7.6.2 Constant bias vs evolving bias

We now investigate how a particular choice for the bias evolution in redshift can affect and impact the constraints on $f\sigma_8(z)$. To do this, we repeat the analysis as presented in 7.6.1 using the Ω_m and $f\sigma_8$ weights, we model $\Omega_m(z)$ and $f\sigma_8(z)$ in the same way as in 7.6.1, but now assuming that the bias is constant with redshift i.e we set $\partial b\sigma_8(z)/\partial z = 0$.

In Figures 7.6, 7.7 we show the comparison between the results obtained with the constant bias. We display the posterior likelihood for all the quantities evaluated at the pivot redshift, $f\sigma_8(z_p)$ $b\sigma_8(z_p)$, σ_v, b_2, S. In Figure 7.6, blue contours show the likelihood distributions obtained when using the Ω_m weights and considering $b\sigma_8$ evolving as in Eq. 7.4.3. Dark blue contours indicate the constraints obtained when considering $\partial b\sigma_8(z)/\partial z = 0$. In Figure 7.7 we present the analogous results when using the $f\sigma_8$ parametrization; green contours show the likelihood distributions obtained when using the $f\sigma_8$ weights considering the
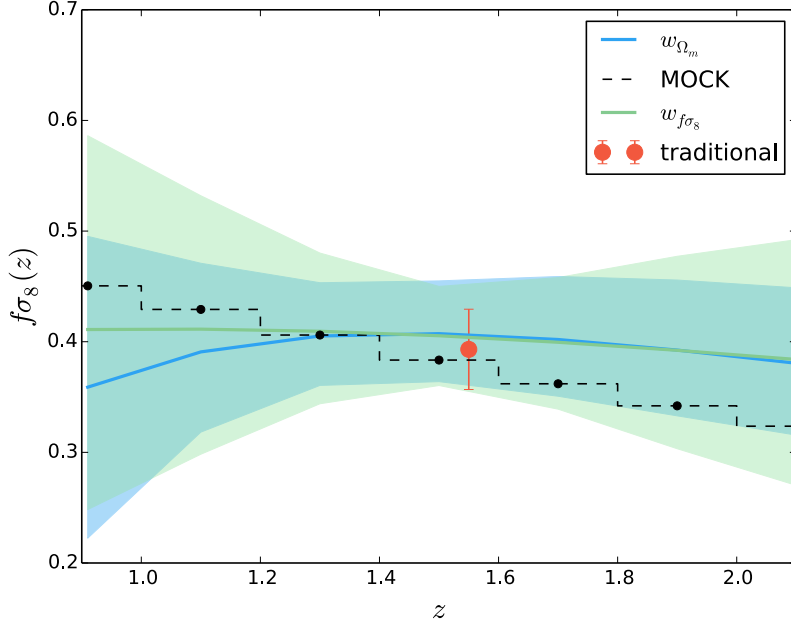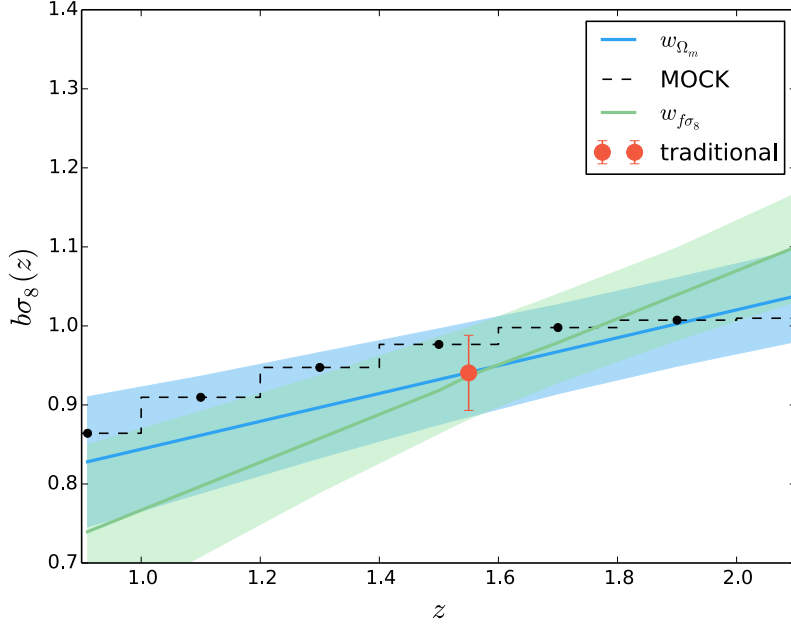
Figure 7.5: The reconstructed evolution for $b\sigma_8(z)$ and 68% confidence level regions using the average of 20 mocks; we fit the evolution for $b\sigma_8$, modelled as a Taylor expansion about the pivot redshift, up to linear order. Blue shaded regions show the evolution of $b\sigma_8$ through the fit of $b\sigma_8(z_p)$, $\partial b\sigma_8(z)/\partial z$, obtained for the $\Omega_m(q_i)$ analysis; green shaded regions show the analogous resulting $b\sigma_8(z)$ when fitting for $f\sigma_8(z, p_i)$ at each redshift. The red point indicates the results obtained for $f\sigma_8(z_p)$ when performing the traditional analysis.

bias evolving as in Eq. 7.4.3. Dark green contours correspond to the constraints obtained when we set $\partial b\sigma_8(z)/\partial z$ equal to zero. The results obtained from the different models are consistent, but, whereas the constraints for $b\sigma_8(z_p)$ remain unchanged there is an evident impact on the $f\sigma_8$ constraints at the pivot redshift. Forcing the bias to be constant with redshift lead to an higher value for $f\sigma_8$.

This should be more important for future surveys, for which higher precision is expected: for these surveys, a careful study/treatment of the bias will be required. One approach would be to have free functions to describe the bias (e.g Taylor expanding cosmological quantities as in the present case), and making sure there is enough freedom in the other parameters so that the measurements are applicable to a wide range of cosmological models and targets, with few assumptions. For higher S/N and more realistic mocks it would be interesting to investigate the evolution in redshift of the non linear bias parameters and the possible impact on $f\sigma_8$. In this work all of the non linear quantities are considered at a single redshift and our tests are limited to verify that the bias does not affect the measurement of the growth, which is adequate for the current signal-to-noise level.
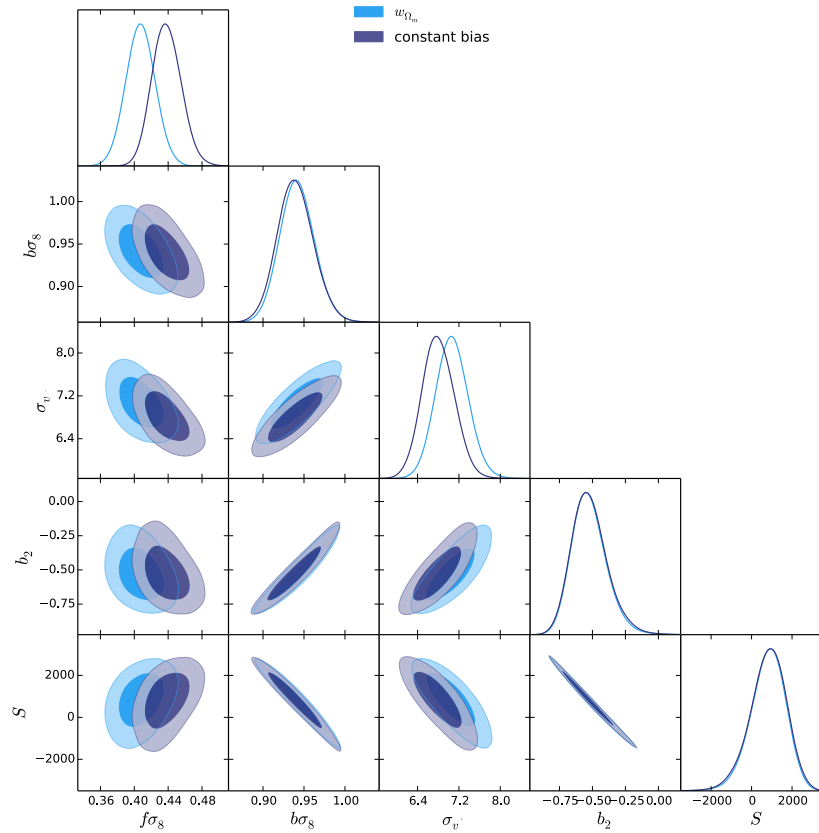
Figure 7.6: Comparison between evolving and constant bias for the Ω_m - weights analysis. Blue likelihood contours indicate the constraints obtained when fitting for $b\sigma_8(z_p)$ and $\partial b\sigma_8(z)/\partial z$; dark blue contours indicate the constraints obtained when setting $\partial b\sigma_8(z)/\partial z = 0$ and fitting only for $b\sigma_8(z_p)$.

7.6.3 Weights vs no Weights

We compare the analysis performed using the redshift weights approach, as presented in 7.6.1 with the *traditional* analysis at one constant redshift.

The traditional analysis makes use of the power spectrum moments, modelled as in Sec. 7.3, to constrain $f\sigma_8$ and $b\sigma_8$ at one single epoch which corresponds to the effective redshift of the survey ($z = 1.55$). We do the comparison for both the Ω_m $f\sigma_8$ weighting schemes;

Figure 7.8 shows the comparison between the redshift weights analysis for Ω_m (blue contours), $f\sigma_8$ (green contours) and the constant redshift analysis (brown contours). In order to make the comparison between the three different analysis we infer from the MCMC chains of q_i and p_i, the $f\sigma_8[z, \Omega_m(q_i)]$ and $f\sigma_8(z, p_i)$ valued at the pivot redshifts. We then compare those values with the $f\sigma_8(z_p)$, $b\sigma_8(z_p)$ as obtained from the traditional analysis. The last two panels in Fig. 7.8 show that we recover the same value for b_2, and S where the
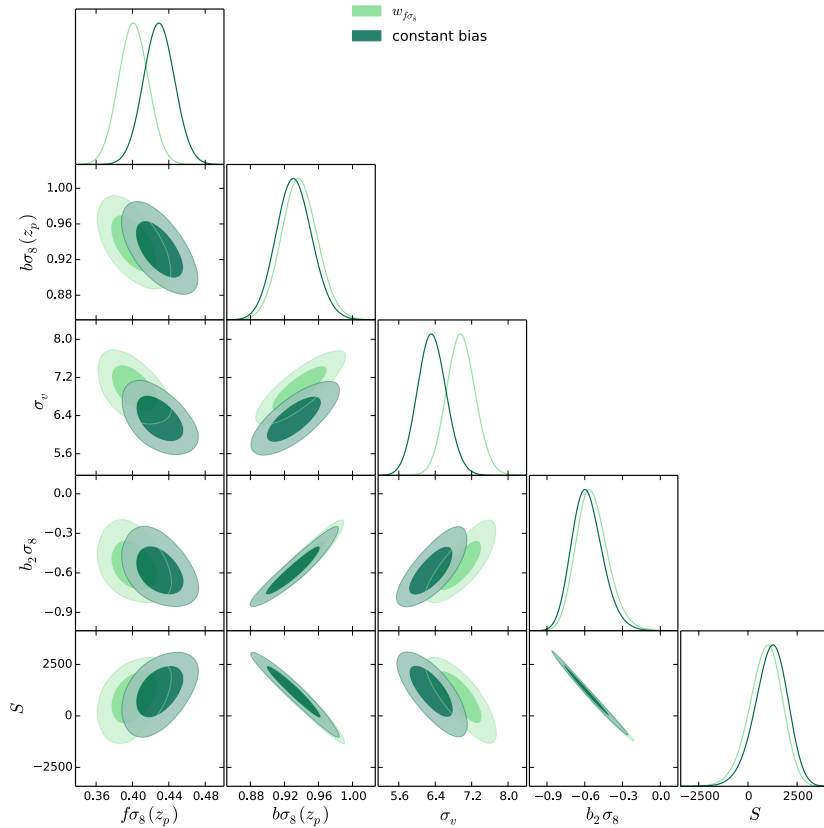
Figure 7.7: Comparison between evolving and constant bias for the $f\sigma_8$-weights analysis. Green likelihood contours indicate the constraints obtained when fitting for $b\sigma_8(z_p)$ and $\partial b\sigma_8(z)/\partial z$; dark green contours indicate the constraints obtained when setting $\partial b\sigma_8(z)/\partial z = 0$ and fitting only for $b\sigma_8(z_p)$.

evolution in redshift is not considered in all the three different analysis; the other constraints on $f\sigma_8$, $b\sigma_8$ and σ_v are fully consistent within $\sim 1\sigma$.

7.7 Summary

In this chapter we introduced the pipeline to be used in chapter 8 on eBOSS data and discussed relative tests performed using the EZ mocks. We have focused on two different parametrizations to model the evolution in redshift of $f\sigma_8$; the first account for the evolution in redshift through $\Omega_m(z)$ allowing simultaneously for deviations in both geometry and growth with respect to the ΛCDM scenario. The second, investigates deviations in the evolution of $f\sigma_8(z)$ about the fiducial cosmology; in this case the growth and the geometry deviations are artificially kept separated. To compare the constraints on $f\sigma_8$ with the
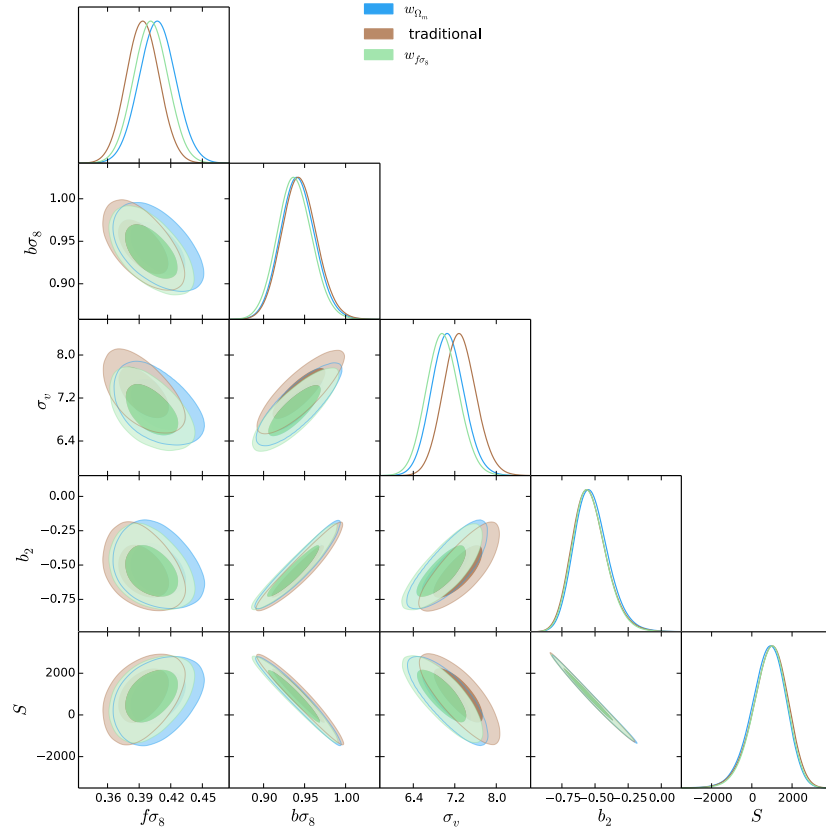
Figure 7.8: The comparison between the redshift weights analysis and the traditional analysis. Likelihood contours for $f\sigma_8$, $b\sigma_8$, σ_v b_2, S quantities, at their pivot redshift values. Blue likelihood contours show the results obtained with the $\Omega_m(q_i)$ analysis; green contours show the results from the $f\sigma_8(p_i)$ analysis. Brown contours indicate the results obtained with the traditional analysis.

traditional method, performed at a single epoch, we computed $f\sigma_8(z_p)$ from the evolving constraints, finding full agreement between the three different methods.

We perform the same analysis first by fixing the geometrical projection, given by H, D_A: in this case as expected both redshift weight methods give exactly the same constraints of $f\sigma_8$. We then considered an anisotropic fit, including the AP parameters in our models. In this case the constraints from $\Omega_m(z)$ differ with the other analyses since $\alpha_{\parallel,\perp}$ are not included as free independent parameters but their evolution is described through $\Omega_m(z)$. Also in this scenario we find good agreement (within 1σ) between the parameters of interest.

The tests presented in this chapter validate the pipeline to be used for eBOSS data; however as we discussed in chapter 6, the method can be used for different probes.

MEASURING THE EVOLUTION OF THE GROWTH RATE USING REDSHIFT SPACE DISTORTIONS BETWEEN REDSHIFT 0.8 AND 2.2

We measure the growth rate and its evolution using the anisotropic clustering of the extended Baryon Oscillation Spectroscopic Survey (eBOSS) Data Release 14 (DR14) quasar sample, which includes 148 659 quasars covering the wide redshift range of $0.8 < z < 2.2$ and a sky area of 2112.90 deg^2. To optimise measurements we deploy a redshift-dependent weighting scheme following the procedure discussed in 7, which allows us to avoid binning, and perform the data analysis consistently including the redshift evolution across the sample. We perform the analysis in Fourier space and use the redshift evolving power spectrum multipoles to measure the redshift space distortion parameter $f\sigma_8$ and parameters controlling the anisotropic projection of the cosmological perturbations. We measure $f\sigma_8(z = 1.52) = 0.43 \pm 0.05$ and $df\sigma_8/dz(z = 1.52) = -0.16 \pm 0.08$, consistent with the expectation for a ΛCDM cosmology as constrained by the Planck experiment.

The content of the work presented here refers to the research published in [165].

8.1 Context of the analysis

The positions of galaxies signpost peaks in the density field, and consequently measuring their clustering provides a wealth of cosmological information. Two components of the clustering are particularly important: Baryon Acoustic Oscillations (BAO) act as a robust

standard ruler, allowing geometrical measurements from measurements of their projected sizes, while Redshift-Space Distortions (RSD) change the clustering amplitude in a way that is anisotropic around the line-of-sight. The strength of the RSD signal depends on the rate of structure growth at the redshifts of the galaxies, and therefore allows tests of General Relativity on extremely large scales. The combination of these measurements is able to distinguish between competing models of Dark Energy, the phenomenon driving the accelerated expansion of the Universe.

Dark Energy starts to dominate the Universe at a redshift $z \sim 0.7$ and, in order to understand the physics behind this in detail, we desire BAO and RSD measurements covering a wide range of redshifts. In particular, measurements at redshifts significantly greater than 0.7 allow us to measure the amplitude of fluctuations before Dark Energy dominates, normalising measurements of acceleration at lower redshifts. The extended Baryon Oscillation Spectroscopic Survey (eBOSS; [96]), part of the SDSS-IV experiment [28] was designed with this specific goal in mind [1], with the dominant target for observations being quasars between the redshifts of $0.8 < z < 2.2$, at a relatively low density of $82.6/\deg^2$.

We expect significant evolution in such a sample with redshift: for example, the bias of these quasars is expected to evolve as $b(z) \simeq 0.28[(1+z)^2 - 6.6] + 2.4$ [166][156], thus ranging from 1.6 to 3.4 across the survey. Consequently, when analysing data we need to be careful to allow for this evolution, both when optimising any kind of analysis as well as to make sure measurements are unbiased. The method of "redshift-weights" does this by constructing sets of weights applied to all of the data, before calculating clustering statistics (such as the power spectrum multipoles). The weights are designed to allow the optimal measurement of evolving cosmological parameters. The cosmological parameters could be, for example, the coefficients of a Taylor expansion of the growth rate with redshift.

[127] calculated and analysed weights optimised to measure the distance-redshift relation from BAO. Recently, these ideas were applied to mock catalogues for BAO [147] and RSD as we discuss in chapters 5, 7, demonstrating their potential. The technique is now ready to be applied to data, and the characteristics of the eBOSS quasar sample make it the ideal choice for such analysis. In [167] and [168], a different methodology is used to measure the evolving RSD and BAO signals: standard measurements are made as if for a narrow redshift interval, but instead for weighted distributions of the quasars. A cosmological model can be tested by using the supplied sets of weights to determine the effective RSD and BAO in the model given that kernel, and comparing to the corresponding measurements.

In our work, we apply the method presented in chapter 7, and consider two sets of weights designed to test for deviations from the ΛCDM model, by altering $\Omega_m(z)$, or $f\sigma_8(z)$.

The first choice can change both growth and geometry, unless we explicitly fix one of these, while the second only tests the cosmological growth rate. We also consider a traditional analysis, where we only apply weights matching those of [86]. This corresponds to a limit of the redshift-weighting approach as the redshift-weights tend towards the FKP form in the limit where the error associated with a cosmological parameter does not vary with redshift. The chapter is laid out as follows: In Section 8.2 we briefly review the eBOSS data. Section 8.3 provides an overview of the method, focusing on the eBOSS specific aspects. The results are presented Section 8.5.

8.2   The eBOSS DR14 dataset

The eBOSS survey [96], [1] will provide a redshift survey covering the largest volume to date at a density where it can provide useful cosmological measurements. Full survey details can be found in [96]: observations will ultimately include 250,000 luminous red galaxies (LRGs), 195,000 emission line galaxies (ELGs) and over 500,000 quasars. The main goal is to make BAO distance measurements at 1–2% accuracy [1]. Using the same samples the goal for the RSD analysis is to constrain $f\sigma_8$ at 2.5%, 3.3% and 2.8% accuracy for LRGs, ELGs and Clustering Quasars respectively. For the current analysis we make use of the quasar catalogues from the eBOSS DR14 dataset described in chapter 3. The target selection algorithm is presented in [98]: quasars were selected from the combination of SDSS imaging data [169], and that from the WISE satellite [170]. The SDSS imaging data were taken using the Sloan telescope [171] and spectra were taken using the BOSS spectrographs [100]. Redshifts were measured using the standard BOSS pipeline [172], coupled with various updates and visual inspection of a subset as outlined in [97], which describes the DR14Q quasar catalogue.

The quasar sample, covers a wide redshift range, $0.8 < z < 2.2$ with a low density, $82.6/\text{deg}^2$, compared with other targets, and is designed to ultimately cover a total area of $7500\,\text{deg}^2$. In this work we use the intermediate data sample referred to as DR14 [97]. This sample contains 98577 quasars covering the wide redshift range of $0.8 < z < 2.2$ and a sky area of $1001.25\,\text{deg}^2$. Early measurements of the bias of this sample are presented in [156], showing excellent agreement with those measured from earlier catalogues [166]. In this work we make use of the *fiducial* redshift estimates, obtained as a combination of the three different estimates (z_{MgII}, z_{PCA}, z_{PL}), presented in [97] and we show the constraints obtained when measuring the full NGC + SGC samples. The comparison between the results from different redshift estimates and the discussion for the analysis on NGC (SGC) only is

presented in [173], [174]

We apply a number of weights in order to correct for various features of the data. First, we apply a set of systematic weights designed to correct for trends observed in the target catalogue, where the density of targets varies with observational parameters. These weights are presented in [173] and our treatment is consistent with this. We upweight the nearest neighbour to correct for close-pairs. Redshift failures are corrected by down-weighting the random catalogue used to define the survey mask, as a function of the plate position: which alters the expected signal-to-noise [173]. In addition, we apply redshift-dependent weights optimised to measure the value and derivative of a cosmological parameter (chosen to be $\Omega_m(z)$ or $f\sigma_8(z)$) beyond a fiducial ΛCDM model, around a pivot redshift. The design of these weights considers the information available and the dependence on the cosmological parameter of interest. For the eBOSS quasar data, it is not useful to probe beyond the first derivative of the parameters around a pivot redshift because of the limited constraining power of the data set. The derivation of the weights was presented in chapter 5

In the following sections we briefly review the key points of the analysis.

8.3   Modelling the data

We contrast three methods:

1. A traditional analysis, fitting with one set of weights, matching those introduced by [86], commonly known as FKP weights,

2. Redshift-weighted, with two sets of weights optimised to measure $\Omega_m(z)$; we refer to this method also as w_{Ω_m}.

3. Redshift-weighted, with two sets of weights optimised to measure $f\sigma_8(z)$. we refer to this method also as $w_{f\sigma_8}$

We perform fits either allowing the anisotropic geometrical projection parameters (also know as the AP parameters [73], $\alpha_\parallel$ and $\alpha_\perp$ to be simultaneously fitted, or keeping them fixed at their fiducial value.

We derive and fit models for all three of these methods using the same procedure, as described in chapter 7. Briefly, we calculate the TNS model [13] for each model to be tested at a discrete series of redshifts and apply the redshift weights to give models of the redshift-space moments. In order to account for the coupling between redshift evolution in the cosmological parameters and the survey geometry on the power spectra moments we

discretize the window convolution, creating sub-windows at redshifts 0.87, 1.01, 1.15, 1.29, 1.43, 1.57, 1.71, 1.85, 1.99, 2.13, following the procedure described in [123].

The TNS model includes corrections from the non-linear coupling between the density and velocity fields, it requires us to calculate the non-linear matter power spectra, $P_{\delta\delta}$, $P_{\delta\theta}$, $P_{\theta\theta}$, which we do at 1-loop order in standard perturbation theory (SPT) using the linear power spectrum output from CAMB [161].

Quasar bias is modelled including non-local contributions as in chapter 7, with parameters corresponding to the linear b, second order local b_2, non local b_{s2}, and the third order non-local b_{3nl} bias parameters. We make the approximations $b_{s2} = -4/7(b-1)$ and $b_{3nl} = 32/315(b-1)$ following [160] and [175] respectively; we fit only a local bias model as the quasar data do not contain enough small-scale information to fit for non local bias parameters.

We assume b linearly evolves with redshift, and that b_2 does not vary with redshift. In fact we know that the bias evolves strongly with redshift [176][156] but, given that we wish to constrain cosmological evolution across the sample, this should be simultaneously fitted with the cosmological measurements to avoid double-counting information. We perform a linear fit to match the linear cosmological measurements as a Taylor expansion with respect to the value of $b\sigma_8$ at the pivot redshift,

$$(8.1) \qquad b\sigma_8(z) = b\sigma_8(z_p) + \partial b\sigma_8/\partial z|_{z_p}(z - z_p).$$

With $b\sigma_8(z_p)$ and $\partial b\sigma_8/\partial z|_{z_p}$ free parameters. We also fit for a constant shotnoise term S.

The *traditional analysis*, method 1, makes measurements at a single effective epoch ($z_p = 1.52$), using only FKP weights, so we have a single weighted monopole moment, and a single weighted quadrupole moment to be fitted with five free parameters in total: $f\sigma_8$, $b\sigma_8$, σ_v, $b_2\sigma_8$, S. Where S accounts for deviations from the Poisson shot-noise and σ_v is a phenomenological parameters from the TNS model.

When allowing the background geometry to vary, this parameter set is extended to seven, $f\sigma_8$, $b\sigma_8$, σ_v, $b_2\sigma_8$, S, $\alpha_\parallel$, $\alpha_\perp$, including the projection parameters. To validate this model we fitted to a single snapshot drawn from the Outerim simulation [177], with results presented in [173]. Good agreement was recovered. We compare our traditional measurement with other results obtained from similar analyses in [167, 173, 174, 178]

Method 2 explores deviations from ΛCDM through the evolution of Ω_m in redshift. To do so we model $\Omega_m(z)$ as a Taylor expansion about the fiducial model $\Omega_{m,\text{fid}}$,

$$(8.2) \qquad \Omega_m(z) = \Omega_{m,\text{fid}} q_0[1 + q_1 y(z)]$$

with $y(z) = \Omega_{m,\text{fid}}(z)/\Omega_{m,\text{fid}}(z_p)$; q_0 and q_1 are free parameters giving the overall normalisation and first derivative of $\Omega_m(z)$ at the pivot redshift. In this work, we use a pivot redshift $z_p = 1.52$, matching the effective redshift of the quasar sample. To test the robustness of the analysis we perform the same analysis selecting $z_p = 1.1$; $z_p = 1.7$ confirming that there is no dependence on the pivot redshift selected; For this method we have two sets of weights for the monopole and two sets of the quadrupole, so we simultaneously fit to four moments in total.

As we discussed in details in chapter 7, this parametrisation provides a common framework to test for deviations from the fiducial cosmology both in terms of geometry (distance-redshift relation) and growth rate ($f\sigma_8$), by considering these quantities as a function of $\Omega_m(q_0, q_1)$. The strategy is to assume that, for expected small deviations, the standard equations, linking the Hubble parameter and the Angular Diameter distance to $\Omega_m(z)$, are the same as in the ΛCDM model.

Once we have measured q_0, and q_1, we can project them back to $\alpha_\parallel$, $\alpha_\perp$ and $f\sigma_8$ at any epoch. The physical limit that Ω_m cannot be negative at any epoch places a physical motivated prior on $\alpha_\parallel$, $\alpha_\perp$ and $f\sigma_8$; the impact of such priors is discussed in detail in Section 8.5

The third parametrisation, method 3 explores the evolution of $f\sigma_8$; it represents a more direct way to measure deviations in structure growth, where the latter are artificially kept separate from the geometrical evolution. Here we directly Taylor expand $f\sigma_8(z)$:

$$(8.3) \qquad [f\sigma_8](z) = [f\sigma_8]_{\text{fid}}(z)p_0[1 + p_1 x(z)],$$

where $x = [f\sigma_8]_{\text{fid}}(z)/[f\sigma_8]_{\text{fid}}(z_p)$, and p_0 and p_1 are free parameters giving the overall normalisation and first derivative of $f\sigma_8(z)$ at the pivot redshift. This model allows a wider range of deviations from the ΛCDM scenario, as it does not assume any particular form or relation for f and σ_8. For this method we have two sets of weights for the monopole and two sets of the quadrupole, so we simultaneously fit to four moments in total.

In chapter 7, we compare the *traditional analysis* to the measurement from the redshift weights techniques projected at the pivot redshift using mock catalogues, confirming that the redshift weights analysis give unbiased constraints. Weights optimised to look for deviations from ΛCDM using changes in either Ω_m or $f\sigma_8$, provide complementary measurements given the different deviations, and dependencies on observations. Both can be used to measure $f\sigma_8$ at any particular redshift, and be compared to the more traditional way of looking for deviations.

8.4 Fitting models to the data

We now fit to the quasar data with each of the three models, traditional, Ω_m, $f\sigma_8$, described in Section 8.3. We fit to the NGC and SGC data independently, assuming they are uncorrelated, a reasonable assumption given their physical separation, and then combine the likelihoods to give our result from the full NGC + SGC sample. The results presented in the following sections have been obtained by simultaneously fitting the full set of parameters using a MCMC approach, and then marginalising over the parameters not plotted or measured, including the nuisance parameters S and σ_v, common to all methods.

We measure the weighted moments of the power spectrum, using the method described in chapter 4, with different sets of weights. We select 30 k-bins, $0.001 < k < 0.3 \, \mathrm{hMpc}^{-1}$. To test the robustness of the results we repeated the same analysis reducing the maximum k fitted $k_{\max}$ to $0.2 h/Mpc^{-1}$ obtaining fully consistent fits, albeit with increased errors. In method 1 we fit simultaneously monopole and quadrupole (for SGC and NGC with 2 different windows) adopting a 120x120 covariance. In methods 2 and 3 we perform a joint fit of the weighted monopole and quadrupole, P_{i,w_j}, each calculated using the appropriate set of weights for q_0 and q_1 (and p_0, p_1); for a 240x240 total covariance including NGC and SGC samples.

We compute the covariance matrix from the 1000 EZ mocks, including all weights as,

$$(8.4) \qquad C = \frac{1}{999} \sum_{n=1}^{1000} [\mathbf{d}_n(k_i) - \hat{\mathbf{d}}(k_i)][\mathbf{d}_n(k_j) - \hat{\mathbf{d}}(k_j)]^T,$$

where $\mathbf{d}_n$ is the vector formed of the multiple weighted moments being fitted, and $\hat{\mathbf{d}}$ is the mean value. Note that when inverting the covariance matrix we include the small Hartlap factor [163] and the Dodelson & Schneider error [179] to account for the fact that C is inferred from mock catalogues. An alternative approach would have been to adjust the Gaussian assumption [180].

Parameter constraints are derived from a MCMC routine, optimised for this problem. Multiple chains are run for each fit, and convergence is checked both using the [164] convergence criteria and by testing consistency of results from independent chains, starting at different positions.

8.5 Results

In this section we present the results obtained from the traditional 1, Ω_m 2 and $f\sigma_8$ 3 analyses; we first present the results obtained assuming a fixed fiducial distance-redshift
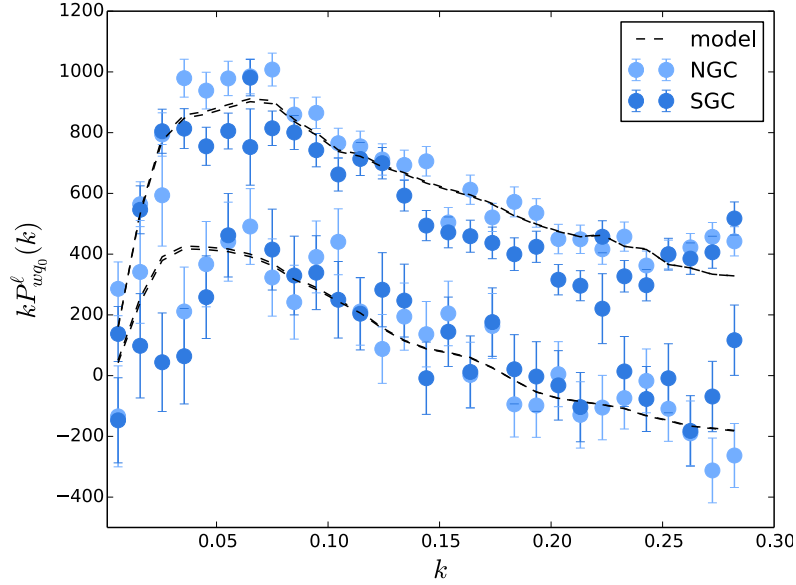
Figure 8.1: The weighted monopole (top) and quadrupole (bottom) for Ω_m weights; we display the measurement of the weighted moments computed using the NGC (light blue points) and SGC (blue points) samples. Black dashed lines correspond to the best fit models obtained from the joint fit of the 2 samples; the 2 best fit dashed lines differ at large scales since convoluted with two different window functions accounting for the different survey geometries and systematics between the 2 samples.

relation, i.e. setting $\alpha_\parallel$ and $\alpha_\perp$ both equal to unity in our pipeline (Section 8.5.2); while in Section 8.5.4 we allow them to vary, fitting simultaneously the growth and the geometry. In Section 8.5.6 we compare the key results of this work with parallel work performed at a single redshift (as in our traditional analysis) in configuration space [173] and Fourier space [174], where the analysis has been extended to include the hexadecapole moment of the power spectrum. We also compare our results with the redshift weights based-analysis of [167] in Section 8.5.6, which makes a number of different assumptions and explores alternative cosmological models.

Fiducial cosmology: we analyse the data in a flat ΛCDM cosmological model with total and baryonic components $\Omega_m(z = 0)= 0.31$, $\Omega_b(z = 0) = 0.0325$; neutrino masses $\sum m_v = 0.06 eV$, ampltude of the clustering $\sigma_8(z = 0) = 0.8$, spectral index $n_s = 0.97$ and dimensionless hubble parameter $h = 0.676$;

8.5.1 The weighted multipole measurements

In Fig. 8.1, we present the moments calculated for the Ω_m set of weights. They all look very similar for all the weights, showing consistency with the fiducial ΛCDM model. It is only if
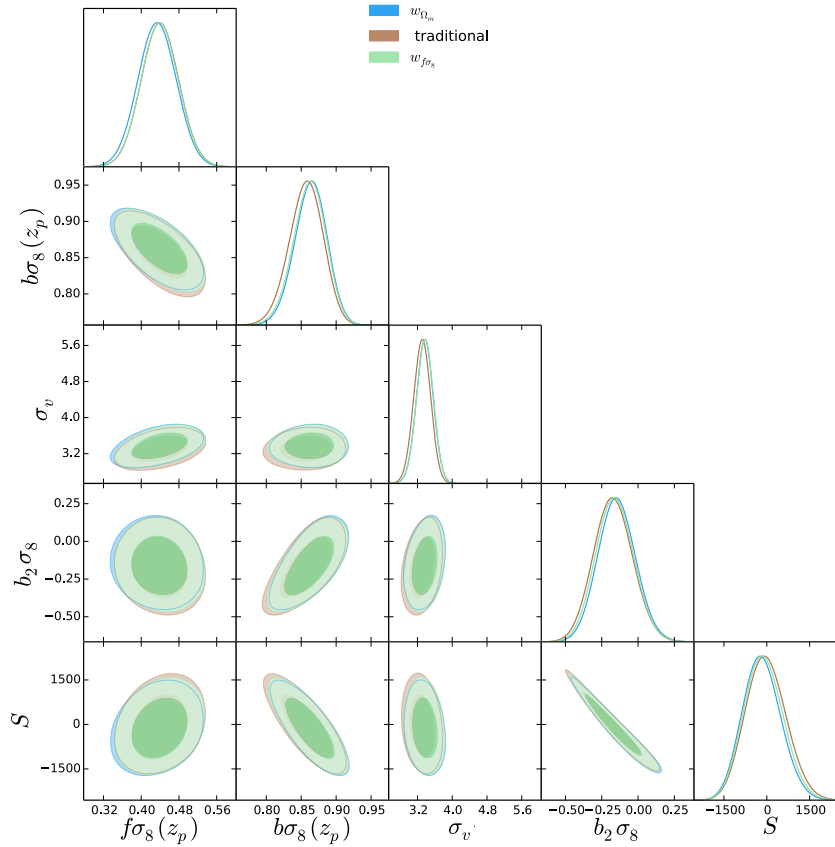
Figure 8.2: A comparison between the values of $f\sigma_8$, $b\sigma_8$, σ_v, S obtained by the three different methods when the background geometry is fixed. Blue and green contours indicates the projected values from the Ω_m and $f\sigma_8$ analysis (7 free parameters) respectively; brown contours correspond to the constraints obtained from the single-epoch traditional analysis (5 free parameters).

we were to find an inconsistency with this model, that we would see an anomaly here for a particular set of weights. i.e. the constraining power lies in the fact that if the cosmology was very different from the fiducial ΛCDM value, these would look very different from each other.

8.5.2   Fitting growth in a fixed background geometry

As described in Section 8.3, the traditional analysis constrains the clustering at a single effective epoch allowing for 5 free parameters $f\sigma_8(z_p)$, $b\sigma_8(z_p)$ + nuisance parameters. In contrast, the weighted analyses fits the evolution of Ω_m and $f\sigma_8$ with redshift, and requires a fit with 7 parameters: q_0, q_1 (p_0, p_1) to model the normalisation and evolution in

the growth, $b\sigma_8(z_p)\, \partial b\sigma_8/\partial z$ to account for the evolution in the linear bias $b(z)$, together with nuisance parameters $b_2\sigma_8$, $\sigma_{\rm v}$ and S. As we are interested in measuring cosmological evolution, we need to carefully consider if the nuisance parameters also need to allow for evolution. Regarding the σ_v parameter, it would theoretically be possible to allow this to vary with redshift, but we have checked using N-body simulations, that for $k < 0.3\, h\mathrm{Mpc}^{-1}$, the evolution does not impact $f\sigma_8$; if we were instead interested in the measurements of non-local bias, for example, allowing for this evolution would have been a key requirement. We do allow the bias to be simultaneously fitted as described in Section 8.3.

In order to compare the redshift-weight measurements with the traditional one, we projected the 7 parameter MCMC chains ($q_0, q_1, b\sigma_8, \partial b\sigma_8/\partial z$ + nuisance parameters) into the 5-dimensions parameter space by computing $f[\Omega_m(q_0, q_1, z_p)]$, $f(p_0, p_1, z_p)]$ and $b(z_p)$. The results are displayed in Fig. 8.2 where we show likelihood contours for $f\sigma_8(z_p)$, $b\sigma_8(z_p)$, etc as derived obtained from the three different analysis, traditional (brown contours), w_{Ω_m} (blue contours) and $w_{f\sigma_8}$ (green contours) when imposing $\alpha_{\parallel} = \alpha_{\perp} = 1$. It is worth noting that all three methods fully agree at the pivot redshift confirming the previous tests made on the mocks. Moreover the redshift weighted analysis give constraints of the same order as those obtained in the traditional analysis even though the latter marginalizes over one less free parameter. This suggests that the information in the data about the evolution of $f\sigma_8$ is available in addition to the information obtained at the effective redshift.

8.5.3   The evolution of $f\sigma_8(z)$, $\Omega_m(z)$, $b(z)$

As described and discussed in chapter 5 in general the redshift-weights allows us to account for the evolution in the clustering measurements. In this work, through Eq. (8.2), and Eq. (8.3) we are able to reconstruct the evolution for $f\sigma_8$ from both q_0, q_1 and p_0, p_1 parameters. We also modelled a linear evolution of the linear bias as described by Eq. (8.1). We show the resulting constraints on the evolution of $f\sigma_8$, $b(z)$, $\Omega_m(z)$, in Fig. 8.3.

The lower panel of Fig. 8.3 shows the evolution in redshift of $f\sigma_8$ obtained applying w_{Ω_m} (blue shaded regions) and $w_{f\sigma_8}$ (green shaded regions). We overplot the constraints coming from the single epoch (traditional) analysis at redshift 1.52. We find good agreement between the different techniques over the full redshift range. The dashed line indicates the fiducial cosmology used. We detect a similar slope in the evolution to that in the fiducial cosmology, and all of our measurement methods provide results that agree within one sigma with the fiducial cosmology. The error on $f\sigma_8$ increases while moving from the pivot redshift in both directions as uncertainties in q_1 and p_1 become relevant. As we are fixing the projection, varying $\Omega_m(z)$ only affects the growth rate, explaining the good agreement
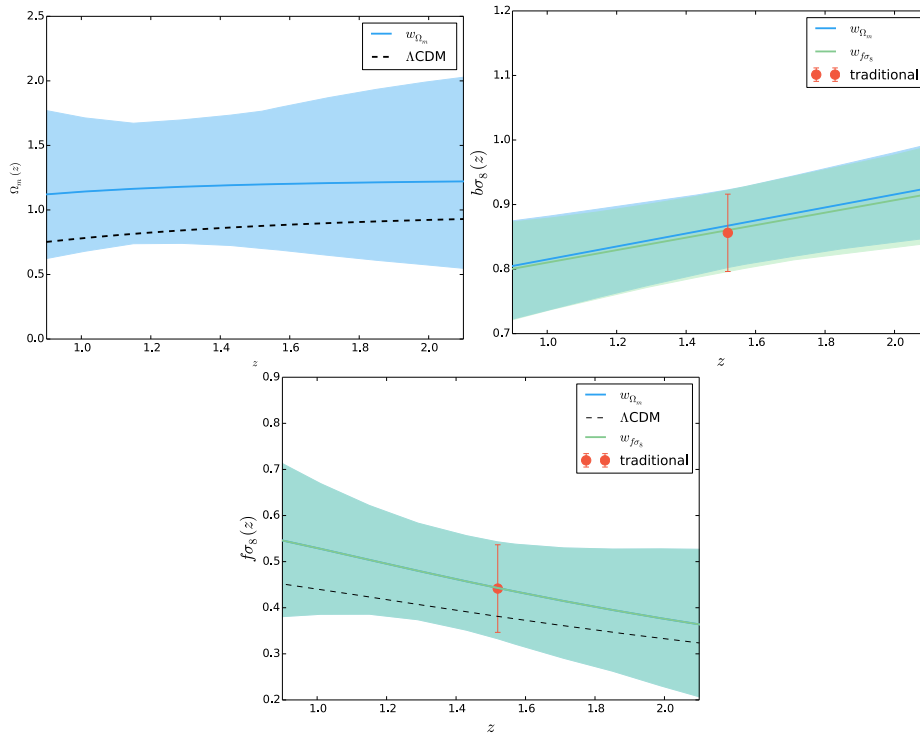
Figure 8.3: Top Panel: the evolution of $\Omega_m(z)$ measured via the parameters q_0, q_1. Middle Panel: the evolution of the linear bias times σ_8 fitted using Ω_m parametrization (blue shaded regions), $f\sigma_8$ parametrizations (green shaded regions); red point indicates the single-epoch constraints of $b\sigma_8(z_p)$ from the traditional analysis. Bottom Panel: the evolution of $f\sigma_8$ from the three different analysis; notation and colors as above; all the errors correspond to 68% confidence level.

between measurements made using both sets of weights: they are both testing for the same sort of departures from the ΛCDM model.

The middle panel of Fig. 8.3 shows our constraints on the linear redshift evolving bias parameter. Also in this case, we find full agreement between the different techniques. As mentioned in Section 8.3 we do not go beyond linear evolution in the bias, matching our allowed evolution in the cosmological parameters of interest. As we are not interested in the recovered bias parameters, we just want to make sure that the assumptions cannot affect the constraints we get on the growth rate. In chapter 7 we validated that in this case, the linear assumption is valid.

8.5.4 Simultaneously fitting growth and geometry

We repeat our analysis, using all three methods, but now including the projection (AP) parameters in our models. Given the weak detection of the anisotropic BAO signal in the

quasar sample (see [23]), a full fit of the monopole and quadrupole is not enough to give
independent strong constraints on the full set of parameters covering both geometrical
and growth-rate deviations. i.e. with only wide uniform physical priors on the parameters,
the degeneracies between the parameters, particularly the shotnoise term together with
$f\sigma_8$, $b\sigma_8$ $\alpha_\parallel$ and $\alpha_\perp$, does not allow our chains to converge (after $10^5 - 10^6$ steps). However,
as pointed out in [181], beyond certain values of $\alpha_\parallel$ and $\alpha_\perp$, the full background used to
analyse the data loses any meaning. Measurements from independent cosmological probes
in almost all cosmological models that we would want to test already put tight constraints
on these quantities [54]. We therefore include a broad prior on both $\alpha_\parallel$ and $\alpha_\perp$, setting
$0.75 < \alpha_\parallel < 1.25$, $0.85 < \alpha_\perp < 1.25$. We keep the uniform priors on the other parameters:
± 10000 for S and ± 100 for $f\sigma_8$ and $b\sigma_8$. To test the robustness of our analysis with respect
the choice of the priors we performed prior-free analysis exploring the likelihood surfaces
outside of those regions.

In the traditional and $w_{f\sigma_8}$ analyses we include $\alpha_\parallel$ and $\alpha_\perp$ as two additional free parame-
ters. For the w_{Ω_m} analysis, however, we do not add any further free parameters: we account
for the departures from the fiducial geometry by including $\alpha_\parallel[\Omega_m(q_0, q_1)]$, $\alpha_\perp[\Omega_m(q_0, q_1)]$
in our models (as discussed in Section 8.3). This procedure requires us to impose a prior
on the value of $\Omega_m(z)$ which has to be positive definite at any redshift to avoid numerical
problem; we illustrate the effect of these prior on the constraints in Fig. 8.5.

Fig. 8.4 shows the likelihood contours obtained from the three different analysis when
allowing for unknown projection parameters (the AP parameters). Dark brown contours
refer to 1; The constraints for the w_{Ω_m}, $w_{f\sigma_8}$ analysis (dark blu $w_{\Omega_m,AP}$ and dark green,
$w_{f\sigma_8,AP}$) are obtained projecting q_0, q_1 and p_0, p_1 into $f\sigma_8(q_i)$ (p_i); also in this scenario
we confirm a good agreement between the three analyses; as explained, $\alpha_\parallel$ and $\alpha_\perp$ are
not free in the w_{Ω_m} analysis but we derive them from the constraints of q_0, q_1. This is the
reason why the two parameters are highly correlated, as shown in the Figure. Note that the
w_{Ω_m} method has two less free parameters with respect $w_{f\sigma_8}$ and one less with respect the
traditional analysis. In Figure 8.5 we compare the *evolution* parameters $q_{0,1}, b\sigma_8, \partial b\sigma_8/\partial z|_{z_p}$
obtained (dark blue contours, $w_{\Omega_m,AP}$), with previous results when the geometry has been
fixed (blue contours, $w_{\Omega_m,NOAP}$). We find a good agreement between the two; the shapes
of q_1 likelihoods show the effect of the physical priors we are including: $\Omega_m(z_p) > 0$ for
$w_{\Omega_m NOAP}$ and $\Omega_m(z) > 0$, $0.0 < z < 2.2$ for $w_{\Omega_m AP}$. Fig. 8.6 is structured in the same way as
Fig. 8.5; we compare the results from $w_{f\sigma_8,AP}$ with previous results of $w_{f\sigma_8,NOAP}$ method.
We find a good agreement with the best fit values obtained; note that here we do not assume
physical priors on the sign of Ω_m. Finally in Fig. 8.7 we compare the constraints at the pivot
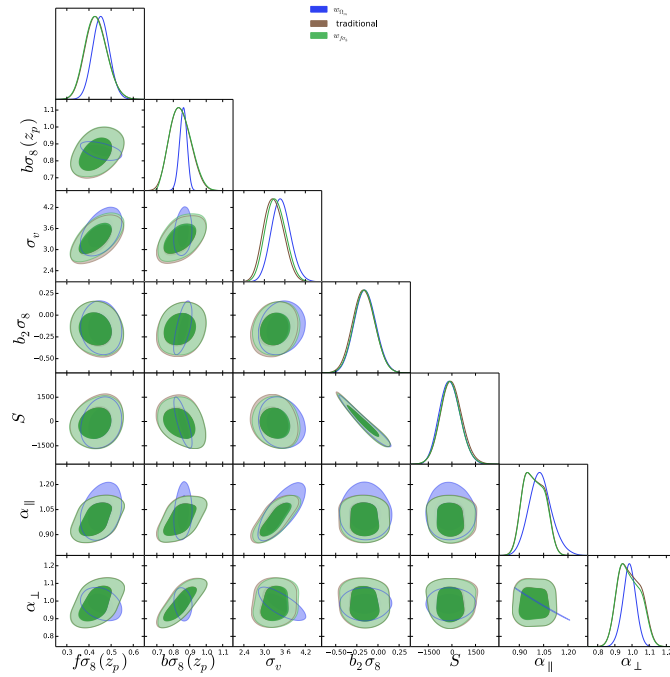
Figure 8.4: A comparison between the values of $f\sigma_8$, $b\sigma_8$, σ_v, S obtained from the three different methods (1,2, 3) when the background geometry is allowed to vary thought the AP parameters. Green contours correspond to the projected values from the $f\sigma_8$ analysis ($f\sigma_8(p_0, p_1)$, $b\sigma_8(z_p)$, σ_v, S, $\alpha_\parallel$, $\alpha_\perp$). Blue contours represent the projected constraints from Ω_m analysis ($f\sigma_8(q_0, q_1)$, $b\sigma_8(z_p)$, σ_v, S, $\alpha_\parallel(q_0, q_1)$, $\alpha_\perp(q_0, q_1)$) Brown contours indicate the constraints from the single-epoch traditional analysis at the pivot redshift $z_\mathrm{p} = 1.52$

redshift for $f\sigma_8$ and $b\sigma_8$ with and without AP, for method 1, 2 and 3 (brown, blue, green contours); we confirm the good agreement on the constraints for $f\sigma_8$ with and without fixing the geometry. When performing the anisotropic fit we get a larger error as expected; note that for the w_{Ω_m} analysis we get the constraints to be of the same order: as explained, in this scenario, we tie together geometry and growth, thus $\alpha_\parallel$ and $\alpha_\perp$ are not independent parameters.

Finally in Figures 8.8, we present the results of the three different analysis, as in Fig. 8.3. Note that, since in the w_{Ω_m} analysis $\alpha_\parallel$ and $\alpha_\perp$ are not independent but are included as functions of $\Omega(q_0, q_1, z)$, we obtain a marginalized error smaller than the one obtained in the case of the $w_{f\sigma_8}$ analysis.
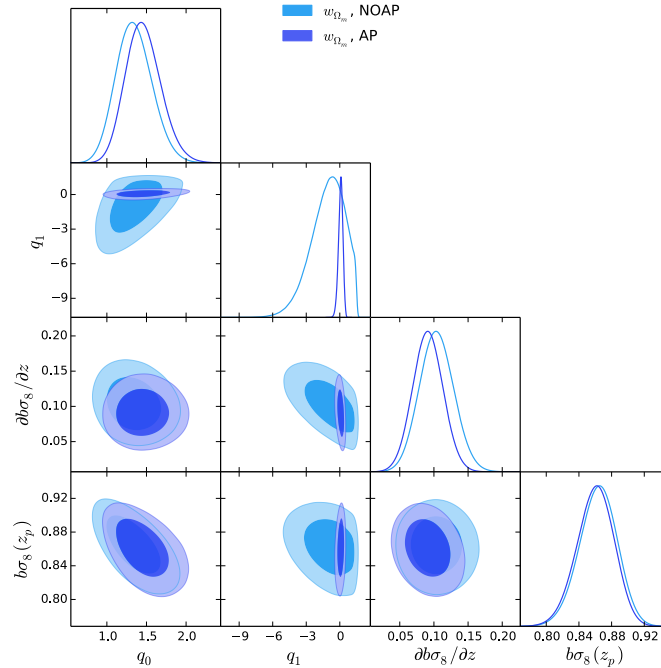
Figure 8.5: A comparison between the constraints on the *evolution parameters* obtained
from the Ω_m analysis with and without fixing the anisotropic projection parameters (Blue
and light blue contours respectively).

8.5.5 Bestfit measurements

In Table 8.5.5 we summarize the results from the different analysis (1, 2, 3) with and without
free AP parameters (bottom and top panel). We display the best fit values (first column)
the mean values $\pm 1\sigma$ (second column); The first section of the table shows the fit to the
monopole and quadrupole fixing the AP parameters. While the second section of the table
shows the fit results allowing the AP parameters to be simultaneously fitted. The fitting range
is $k = 0.01$ - 0.3hMpc for both the monopole and quadrupole. We consider the results from
combining both North Galactic Cap (NGC) and South Galactic Cap (SGC) using standard
redshifts estimates. The error-bars are obtained by marginalising over all other parameters.

8.5.6 Consensus with other projects

The current analysis has been compared with similar analysis performed on the same
data set [173] [178] [167] [174]; we refer to [173] for a longer discussion on the different
methodologies and we here focus on the comparison only between analyses measuring the
redshift evolution of the growth rate. In particular we compare our results with analyses

Table 8.1: The best fitting measurements for the DR14 quasar data over the redshift range $(0.8 < z < 2.2)$. Top panel for results with fixed anisotropic projection parameters (NOAP). Bottom panel for results with free anisotropic projection parameters (AP). These are the marginalised constraints made from the chains presented in Figs 8.3, 8.6 and 8.8.

	NOAP		
Traditional			
	max. like.	mean $\pm 1\sigma$	
$f(z)\sigma_8(z)$	0.435	0.44	$\pm\, 0.04$
$b\sigma_8$	0.86	0.86	$\pm\, 0.02$
σ_v	3.30	3.30	$\pm\, 0.19$
$b_2\sigma_8$	-0.18	-0.17	$\pm\, 0.13$
S	-340	-270	$\pm\, 697$
χ^2	113/(120 - 5)		
Ω_m weights			
q_0	1.31	1.34	$\pm\, 0.23$
q_1	-1.07	-1.09	$\pm\, 1.50$
$b\sigma_8(z_p)$	0.10	0.10	$\pm\, 0.025$
$\partial b\sigma_8/\partial z|_{z_p}$	0.87	0.86	$\pm\, 0.02$
σ_v	3.39	3.34	$\pm\, 0.19$
$b_2\sigma_8$	-0.15	-0.15	$\pm\, 0.13$
S	-208	-174	$\pm\, 660$
χ^2	221/(240 - 7)		
$f\sigma_8$ weights			
p_0	1.11	1.12	$\pm\, 0.11$
p_1	0.35	0.28	$\pm\, 0.69$
$b\sigma_8(z_p)$	0.865	0.86	$\pm\, 0.02$
$\partial b\sigma_8/\partial z|_{z_p}$	0.10	0.10	$\pm\, 0.03$
σ_v	3.33	3.37	$\pm\, 0.19$
$b_2\sigma_8$	-0.15	-0.16	$\pm\, 0.13$
S	-218	-106	$\pm\, 676$
χ^2	223/(240 - 7)		

|	AP		
Traditional			
	max. like.	mean $\pm 1\sigma$	
$f(z)\sigma_8(z)$	0.40	0.43	± 0.05
$b\sigma_8$	0.79	0.84	± 0.06
σ_v	3.0	3.2	± 0.29
$b_2\sigma_8$	-0.16	-0.17	± 0.13
S	28	-37	± 685
$\alpha_{\parallel}$	0.95	0.99	± 0.065
$\alpha_{\perp}$	0.94	0.99	± 0.06
χ^2	112/(120 - 7)		
Ω_m weights			
q_0	1.42	1.46	± 0.22
q_1	0.07	0.07	± 0.20
$b\sigma_8(z_p)$	0.86	0.09	± 0.02
$\partial b\sigma_8/\partial z\vert_{z_p}$	0.09	0.09	± 0.02
σ_v	3.44	3.48	± 0.28
$b_2\sigma_8$	-0.16	-0.15	± 0.13
S	-145	-124	± 653
χ^2	222/(240 - 7)		
$f\sigma_8$ weights			
p_0	1.11	1.11	± 0.13
p_1	0.16	0.29	± 0.69
$b\sigma_8(z_p)$	0.79	0.85	± 0.06
$\partial b\sigma_8/\partial z\vert_{z_p}$	0.09	0.10	± 0.03
σ_v	3.19	3.33	± 0.29
$b_2\sigma_8$	-0.13	-0.16	± 0.13
S	-205	-95	± 664
$\alpha_{\parallel}$	0.94	0.99	± 0.06
$\alpha_{\perp}$	0.94	0.98	± 0.06
χ^2	222/(240 - 9)		
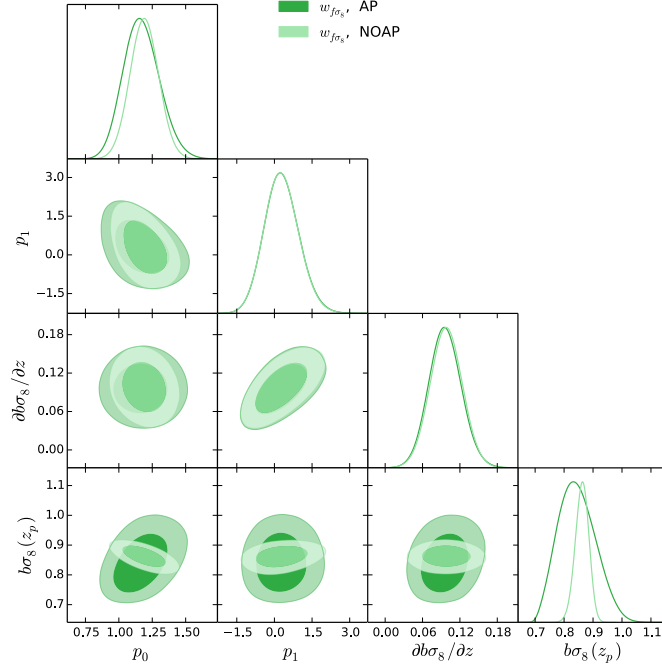
Figure 8.6: A comparison between the constraints on the *evolution parameters* obtained from the $f\sigma_8$ analysis with and without fixing the anisotropic projection parameters (Green and light green contours respectively).

presented in [174] and [167]. In [174] the evolution of $f\sigma_8$ have been studied performing an analysis in three different overlapping redshift bins: $0.8 < z < 1.5$, $1.2 < z < 1.8$, $1.5 < z < 2.2$, corresponding to effective redshifts $1.19; 1.5; 1.83$; This standard analysis considers the first three moments of the power spectrum, $P_{0,2,4}$, up to $k = 0.3h\text{Mpc}^{-1}$; the measurements are fitted with the TNS model computed up to 2-loop in standard perturbation theory; the window survey effect is accounted following [162]. In [167] they perform a joint BAO and RSD analysis using the monopole and quadrupole (in the k-range of $0.02 \leq k\,[h\text{Mpc}^{-1}] \leq 0.30$) and comparing with a TNS redshift space power spectrum template at 2-loop level in perturbation theory; They derive redshift weights following the lines of [127][123] to optimize the constraints on $\alpha_\perp, \alpha_\parallel$ and $f\sigma_8$ at four effective redshifts, namely, $z_{\text{eff}} = 0.98, 1.23, 1.53$ and 1.94. In contrast to the analysis presented in this work where the whole redshift range is considered and the weighted multipoles are combined in a joint fit, in [167] the redshift weights act to divide the sample into *smooth* z-bins. In each bin they perform the same analysis to constrain $f\sigma_8(z_{\text{eff}}), \alpha_{\parallel,\perp}(z_{\text{eff}})$ at the four effective redshifts. Thus this approach is a hybrid between redshift-weighting and standard analyses. [167] use an optimisation to find the best redshift kernels and then perform a standard analysis for each, assuming the
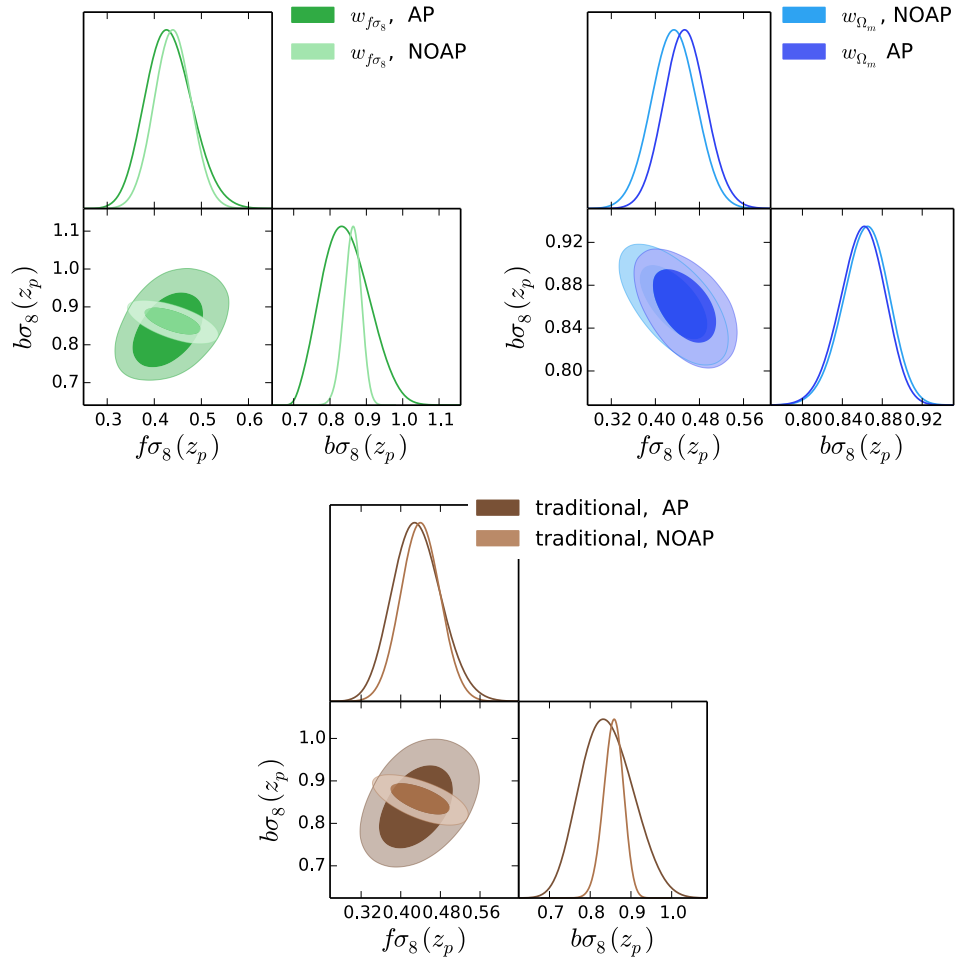
Figure 8.7: A comparison between the different analysis with AP (darker colors) and
without AP (lighter colors). Bottom panel shows the constraints from the traditional
analysis of $f\sigma_8(z_p)$ and $b\sigma_8(z_p)$. Middle and top panel for the projected constraints of
$f\sigma_8(q_0, q_1), b\sigma_8(q_0, q_1)$ (blue and light blue contours) and $f\sigma_8(p_0, p_1), b\sigma_8(p_0, p_1)$ (green
and dark green contours) in the $w_{f\sigma_8}$ w_{Ω_m} analysis.
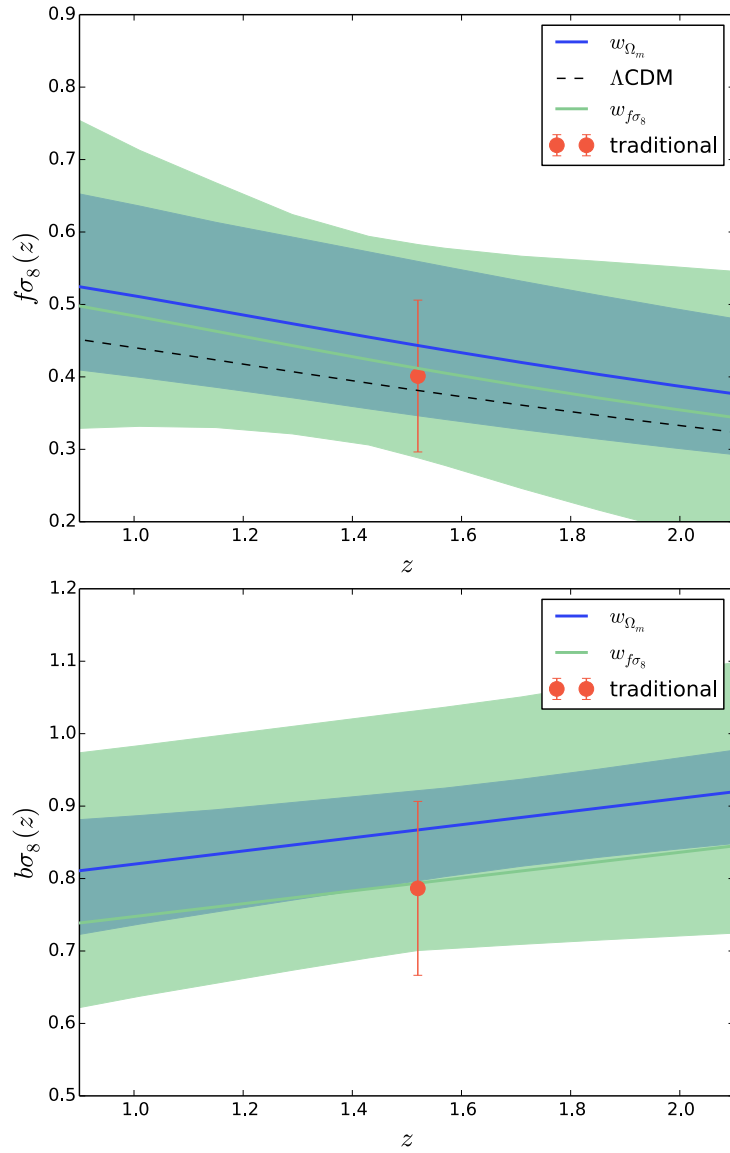
Figure 8.8: The evolution of $f\sigma_8(z)$ and $b\sigma_8(z)$ when including the AP effect; notation and colors same as in 8.3; all the errors correspond to 68% confidence level.
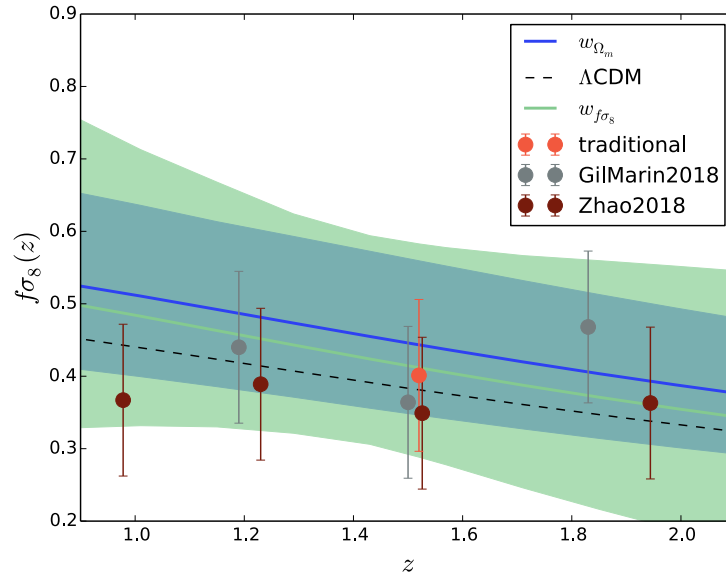
Figure 8.9: comparison of $f\sigma_8$ evolution as obtained by different analysis. All the errors correspond to 68% confidence level.

measurements being at one effective redshift. In contrast we directly measure parameters controlling the redshift evolution. In Figure 8.9 we show the constraints from the different analysis. The red point and blue and green band correspond to the traditional and redshift weight analysis results 1, 2, 3 presented in this work. Grey points correspond to the redshift bin analysis presented in [174], while dark red points correspond to the analysis of [167]. We confirm the good agreement between the different techniques in measuring $f\sigma_8(z)$. Note that the marginalized error bars for the red, grey, dark red points refer to analyses with 7 free parameters ($f\sigma_8(z_{\mathrm{eff}}), b\sigma_8(z_{\mathrm{eff}}), \alpha_\parallel, \alpha_\perp +$ nuisance) while redshift weights methods (blue and green band) include 7 and 9 free parameters respectively ($q_0, q_1, b\sigma_8, \partial b\sigma_8/\partial z + nuisance$), ($p_0, p_1, b\sigma_8, \partial b\sigma_8/\partial z \alpha_\parallel, \alpha_\perp, +nuisance$).

8.6 Summary

In this chapter we presented the first anisotropic analysis on the latest eBOSS quasar sample, DR14. The DR14 quasar sample is particularly interesting as it is characterized by a a wide redshift range $0.8 - 2.2$ opening up new possibilities such as directly investigating the evolution of the growth of the structure, but, on the other hand it is also characterized by a low density compared to previous samples, such as the BOSS LRG sample; for this reason, cutting the sample into different redshift bins may significantly impact the S/N. In order to

optimize the measurements we adopted instead the weighting technique strategy presented in chapters 5, 7, which considers the entire sample together and weights galaxies with respect to their redshift to account for the evolution of the matter density field across the survey volume. In this work, we choose to constrain the growth rate and its first derivative obtaining consistent results with the standard analyses. We also explored different parametrizations to model the redshift evolution in the power spectra finding good agreement between them. We expect the analysis presented here to be particularly interesting in view of future surveys for example the DESI ELGs sample discussed Sec. 3.5.4 that will cover a wide redshift range but will also benefit from an higher density with respect to the quasar sample.

CONCLUSIONS

This thesis has presented new algorithms to reduce computational load when processing large data-sets; explored new methodologies to analyse data using N-body simulations; and shown how these can be applied to process the latest available astronomic data.

In chapter 4 new estimators for calculating LOS-dependent moments of the galaxy power spectrum were presented. Following on from developments presented elsewhere [113] [182], it was shown that use of multiple FFTs to measure LOS-dependent clustering is both fast and efficient. The method is faster than previous sums-over-galaxies methods, and is also faster than pair-counting algorithms [110] themselves derived to calculate configuration-space monopole, quadrupole and hexadecapole moments of the correlation function. These developments will be important for the coming generation of galaxy redshift surveys, including DESI [122] and Euclid [50], that will provide an order of magnitude more galaxies to evaluate than currently available surveys, rendering data evaluation and processing considerably more challenging. The developments presented here should also find applications for measuring the galaxy bispectrum, and hence enhance our ability to extract the cosmological information provided by galaxy surveys.

Chapter 5 was concerned with how to more efficiently process data from a wide range of redshifts. It was shown that data from different volumes of space could be combined without loosing information; and a set of optimal redshift-dependent weightings for RSD measurements was developed and presented. These allow optimal compression of original datasets while minimising the *a priori* error provided by the Fisher matrix. In contrast to current RSD measurements, which compare the data with the model at a single effective

redshift, the weightings presented account for the redshift evolution of the underlying cosmology. The method is based on the particular choice of a (fiducial) model describing the evolution in redshift, in the redshift range being measured/investigated.

The set of weightings optimally estimates deviations from a ΛCDM background, modelled using variations of $\Omega_m(z)$. $\Omega_m(z)$ was modelled as a polynomial expansion in terms of parameters q_i about a fixed fiducial model; the compression method [128] was then applied and the set of weighting that optimally estimates the expansion parameters derived. As discussed in the chapter, the weights derived generalise the FKP weightings, taking account of the galaxy density distribution through the covariance matrix, and allowing sensitivity to the redshift dependence of the statistics being measured.

Initially a fixed distance-redshift relation was included, and two separate cases considered: one in which the bias was known and constrained to a fiducial model, and one in which the bias was unknown. These were compared and it was shown that they were consistent – implying that bias did not play a major role in determining the weightings. The assumptions of the fiducial bias model were tested by deriving the results for the two bias models. It was again shown that the weighting were not significantly sensitive to $b(z)$. For completeness a further set of weightings that optimizes the measurement of bias has been derived. In order to improve future measurements the previous weightings were then extended to the more general case that the distance-redshift relation was unknown: the observed power spectrum including the AP effect was modelled, with two new distortion parameters $\alpha_\parallel$, $\alpha_\perp$ in $P(k)$ describing the AP effect.

The set of weightings obtained for RSD and AP measurements is scale dependent through the ratio of $P(k)$ to its logarithmic derivative. This is not a major issue for future applications since the dependence is predicted to be very weak. Furthermore, considering e.g. CAMB, computing the P(k) model or its derivative in real space will not require massive computational resources, provided the weightings are applied after calculating the power. [127] did not have face this problem since they constrained every quantity on the BAO scale ($k \approx 0.1 h\mathrm{Mpc}^{-1}$). Subsequently the new results were compared with those produced with weightings accounting for RSD only at the BAO scale and it was found that the redshift dependence was increased by the inclusion of the AP parameters.

In order to be able to correctly apply the weighting scheme, it will be necessary to understand how the weightings designed to correct for systematic density field distortions should be combined. The derivations presented made a number of assumptions (e.g. that the shaper of the power spectrum is the same equal for each redshift slice and that P has a Gaussian distribution). It would be interesting to see if the weightings change when these

assumptions are relaxed – a topic for future investigations.

Chapter 6 explored an alternative weighting scheme to constrain primordial non Gaussianity. Although in the present work the focus was on measuring the redshift space distortions signal, non Gaussianity is an interesting topic and provides a good test for the redshift weighting improvements, since fewer evolving parameters are involved. The scale dependent bias is a strong probe of non-Gaussianity and the upcoming LSS surveys will put tight constraints on the amplitude of the primordial fluctuations, f_{NL}. Since these surveys cover a wide range of redshifts, z-weighting is a promising way of more fully exploiting LSS information. Redshift weighting is of particular importance for investigating the primordial universe since non-Gausssianity alters large scales more strongly than small scales. Not splitting the data into small redshift slices therefore increases the effective number of scale modes that are included in any analysis. In fact, applying redshift weighting will be crucial for obtaining the accuracy predicted by Fisher forecasts, which implicitly assume that all of the information is extracted – in effect assuming that optimised weighting are used. In the present thesis, only weightings optimised to measure non-Gaussianity within the local framework were considered. Future investigations will doubtless be concerned with weightings for more complex models, such as equilateral or orthogonal shapes, or shapes with specific angle dependency, or models with non-zero running of f_{NL} A natural extension would be to apply the redshift weighting technique to multiple tracer samples, thereby combining optimal redshift weightings with weightings designed to better exploit the additional information coming from multi-tracer methods.

Chapter 7 presented a new pipeline to measure the redshift space distortions inherent in surveys covering a wide range of redshifts. The redshift weighting technique was applied to investigate small deviations from ΛCDM. Two parametrizations were selected that allowed for deviations in matter-energy density, and evolution of the growth rate. Multiple sets of weightings were derived to optimize each order of deviations. The window function derivation was extended so as to account for the redshift evolution of the power spectrum. The results obtained were compared with those obtained using the "traditional" analysis, i.e. analysis performed considering the clustering as constant across the whole volume. It was found that the redshift weighting technique gave unbiased constraints over the whole redshift range, in full agreement with the traditional analysis performed at the effective redshift.

The constraints obtained fully validate the analysis, presented in chapter 8 to measure RSD on the eBOSS quasar sample, where the expected error $f\sigma_8$ was about 5%. To apply the same pipeline to future surveys designed to achieve greater accuracy, further work will

be required: first it will be necessary to consider quadratic deviations in the evolution of both q_i and galaxy bias parameters. In the present thesis only deviations aimed to test the robustness of fit were considered, whereas the signal expected from the quasar sample will not be able to constrain quadratic evolution.

Another interesting project would be to account for the AP parameters and their evolution in redshift. To perform such analysis, a set of N-body simulations that accurately describe non-linearities/light-cone evolution will also be required, so as to reduce degeneracies and reduce statistical error. Here growth alone was considered: with better data it will be possible to include AP and growth together. As illustrated in chapter 8 for the eBOSS sample, the constraints are too weak to do this without introducing priors.

In chapter 8 the new technique was applied to DR14 the latest eBOSS quasar sample. The DR14 quasar sample allows testing of the cosmological model at previously unexplored epochs. It also covers a wide range of redshifts and opens up the possibility of directly investigating the evolution of the cosmological parameters. Standard analyses investigated the evolution of the growth rate at different epochs by cutting volumes into slices characterized by different redshifts. The DR14 quasar sample is characterized by a lower density than previous samples (e.g. BOSS LRG) so slicing can have a significant impact on the S/N ratio.

Two parametrizations were explored to model the evolution in redshift of $f\sigma_8$. The first modelled the evolution in redshift through Ω_m making it possible to account simultaneously for deviations in both geometry and growth. The second investigated deviations in the evolution of $f\sigma_8$ about the fiducial cosmology: in this case the growth and geometry deviations were kept artificially separated. To compare the constraints on $f\sigma_8$ using the "traditional" method at a single epoch, with the methods described above, $f\sigma_8$ was estimated from the evolving constraints: full agreement between the three different methods was found.

Chapters 5, 7, 8 constituted a step-by-step demonstration of how to include the redshift weightings in the analyses. They also demonstrated that evolution in the models could easily be accounted for re-deriving the window function; and confirmed that the redshift weighting method afforded unbiased constraints. Future surveys are expected to reduce the statistical error by an order of magnitude over a wide redshift range. Thus, it will be increasingly important to account for evolution in the models. The larger range of dynamic redshift covered will open up the possibility of distinguishing different cosmological scenarios. This will be accomplished using the evolution of the key parameters to remove part of the degeneracy between them.

In particular Euclid mission and DESI, approved and currently being planned will map the large scale structure over unprecedented areas (14,000 to 18,000 deg^2) and large redshift

ranges, (0.9 < z < 2.1, 0.5 < z < 3.5) that will allow us to accurately reconstruct the geometry of the universe and the cosmic structure formation using cosmological probes. Preliminary evaluations of their ability to constrain cosmological parameters have been based, so far, on reasonable but rather crude approximations, e.g. with respect to survey geometry and volume; in particular the power spectrum estimates typically assume the survey footprint to be a relatively compact region of the sky and the underlying galaxy distribution to be approximately homogeneous, without significant redshift evolution. The actual analysis, on the other hand, will necessarily have to consider the redshift evolution in order to reach the promised improvements.

The measurement of the BAO using the DESI galaxy survey will consider objects at $0.5 < z < 3.5$. The predicted number of targets between 20-30 million, with a spectroscopic redshift error less than $0.001(1 + z)$, will reach the required tracer density, $1500/\mathrm{d}eg^2$, in order to optimize the BAO performance. The measurements of the distance scale are predicted to reach 1% accuracy in each redshift bin. However the binning method would require the repeated analysis 35 times on $\sim 2 \cdot 10^7/35$ targets and will not consider the correlation between the different portions of the sky covered. For these surveys, the optimal weights technique will be a more efficient and accurate alternative; considering the whole sample and applying to each galaxy the redshift weights, we will be able to compute the correlation from all the galaxy pairs. We expect this to enhance the S/N on the detection of the BAO feature: recent studies [127] showed a 30% improvements on the errorbars for the eBOSS survey at $0.9 < z < 2.1$, using a set of redshift weights. For the DESI redshift range, which is almost three times eBOSS, the improvement will be significantly larger.

[1]   G.-B. Zhao, Y. Wang, A. J. Ross, S. Shandera, W. J. Percival, K. S. Dawson, J.-P. Kneib, A. D. Myers, J. R. Brownstein, J. Comparat, T. Delubac, P. Gao, A. Hojjati, K. Koyama, C. K. McBride, A. Meza, J. A. Newman, N. Palanque-Delabrouille, L. Pogosian, F. Prada, G. Rossi, D. P. Schneider, H.-J. Seo, C. Tao, D. Wang, C. Yèche, H. Zhang, Y. Zhang, X. Zhou, F. Zhu, and H. Zou, "The extended Baryon Oscillation Spectroscopic Survey: a cosmological forecast," *MNRAS*, vol. 457, pp. 2377–2390, Apr. 2016.

[2]   DESI Collaboration, A. Aghamousa, J. Aguilar, S. Ahlen, S. Alam, L. E. Allen, C. Allende Prieto, J. Annis, S. Bailey, C. Balland, and et al., "The DESI Experiment Part I: Science,Targeting, and Survey Design," *ArXiv e-prints*, Oct. 2016.

[3]   Planck Collaboration, N. Aghanim, Y. Akrami, M. Ashdown, J. Aumont, C. Baccigalupi, M. Ballardini, A. J. Banday, R. B. Barreiro, N. Bartolo, S. Basak, R. Battye, K. Benabed, J.-P. Bernard, M. Bersanelli, P. Bielewicz, J. J. Bock, J. R. Bond, J. Borrill, F. R. Bouchet, F. Boulanger, M. Bucher, C. Burigana, R. C. Butler, E. Calabrese, J.-F. Cardoso, J. Carron, A. Challinor, H. C. Chiang, J. Chluba, L. P. L. Colombo, C. Combet, D. Contreras, B. P. Crill, F. Cuttaia, P. de Bernardis, G. de Zotti, J. Delabrouille, J.-M. Delouis, E. Di Valentino, J. M. Diego, O. Doré, M. Douspis, A. Ducout, X. Dupac, S. Dusini, G. Efstathiou, F. Elsner, T. A. Enßlin, H. K. Eriksen, Y. Fantaye, M. Farhang, J. Fergusson, R. Fernandez-Cobos, F. Finelli, F. Forastieri, M. Frailis, E. Franceschi, A. Frolov, S. Galeotta, S. Galli, K. Ganga, R. T. Génova-Santos, M. Gerbino, T. Ghosh, J. González-Nuevo, K. M. Górski, S. Gratton, A. Gruppuso, J. E. Gudmundsson, J. Hamann, W. Handley, D. Herranz, E. Hivon, Z. Huang, A. H. Jaffe, W. C. Jones, A. Karakci, E. Keihänen, R. Keskitalo, K. Kiiveri, J. Kim, T. S. Kisner, L. Knox, N. Krachmalnicoff, M. Kunz, H. Kurki-Suonio, G. Lagache, J.-M. Lamarre, A. Lasenby, M. Lattanzi, C. R. Lawrence, M. Le Jeune, P. Lemos, J. Lesgourgues, F. Levrier, A. Lewis, M. Liguori, P. B. Lilje, M. Lilley, V. Lindholm, M. López-Caniego, P. M. Lubin, Y.-Z. Ma, J. F. Macías-Pérez, G. Maggio, D. Maino, N. Mandolesi, A. Mangilli, A. Marcos-Caballero, M. Maris, P. G. Martin, M. Martinelli, E. Martínez-

González, S. Matarrese, N. Mauri, J. D. McEwen, P. R. Meinhold, A. Melchiorri, A. Mennella, M. Migliaccio, M. Millea, S. Mitra, M.-A. Miville-Deschênes, D. Molinari, L. Montier, G. Morgante, A. Moss, P. Natoli, H. U. Nørgaard-Nielsen, L. Pagano, D. Paoletti, B. Partridge, G. Patanchon, H. V. Peiris, F. Perrotta, V. Pettorino, F. Piacentini, L. Polastri, G. Polenta, J.-L. Puget, J. P. Rachen, M. Reinecke, M. Remazeilles, A. Renzi, G. Rocha, C. Rosset, G. Roudier, J. A. Rubiño-Martín, B. Ruiz-Granados, L. Salvati, M. Sandri, M. Savelainen, D. Scott, E. P. S. Shellard, C. Sirignano, G. Sirri, L. D. Spencer, R. Sunyaev, A.-S. Suur-Uski, J. A. Tauber, D. Tavagnacco, M. Tenti, L. Toffolatti, M. Tomasi, T. Trombetti, L. Valenziano, J. Valiviita, B. Van Tent, L. Vibert, P. Vielva, F. Villa, N. Vittorio, B. D. Wandelt, I. K. Wehus, M. White, S. D. M. White, A. Zacchei, and A. Zonca, "Planck 2018 results. VI. Cosmological parameters," *ArXiv e-prints*, July 2018.

[4]   A. G. Riess, A. V. Filippenko, P. Challis, A. Clocchiatti, A. Diercks, P. M. Garnavich, R. L. Gilliland, C. J. Hogan, S. Jha, R. P. Kirshner, B. Leibundgut, M. M. Phillips, D. Reiss, B. P. Schmidt, R. A. Schommer, R. C. Smith, J. Spyromilio, C. Stubbs, N. B. Suntzeff, and J. Tonry, "Observational Evidence from Supernovae for an Accelerating Universe and a Cosmological Constant," *AJ*, vol. 116, pp. 1009–1038, Sept. 1998.

[5]   H. Hildebrandt, M. Viola, C. Heymans, S. Joudaki, K. Kuijken, C. Blake, T. Erben, B. Joachimi, D. Klaes, L. Miller, C. B. Morrison, R. Nakajima, G. Verdoes Kleijn, A. Amon, A. Choi, G. Covone, J. T. A. de Jong, A. Dvornik, I. Fenech Conti, A. Grado, J. Harnois-Déraps, R. Herbonnet, H. Hoekstra, F. Köhlinger, J. McFarland, A. Mead, J. Merten, N. Napolitano, J. A. Peacock, M. Radovich, P. Schneider, P. Simon, E. A. Valentijn, J. L. van den Busch, E. van Uitert, and L. Van Waerbeke, "KiDS-450: cosmological parameter constraints from tomographic weak gravitational lensing," *MNRAS*, vol. 465, pp. 1454–1498, Feb. 2017.

[6]   M. A. Troxel, N. MacCrann, J. Zuntz, T. F. Eifler, E. Krause, S. Dodelson, D. Gruen, J. Blazek, O. Friedrich, S. Samuroff, J. Prat, L. F. Secco, C. Davis, A. Ferté, J. DeRose, A. Alarcon, A. Amara, E. Baxter, M. R. Becker, G. M. Bernstein, S. L. Bridle, R. Cawthon, C. Chang, A. Choi, J. De Vicente, A. Drlica-Wagner, J. Elvin-Poole, J. Frieman, M. Gatti, W. G. Hartley, K. Honscheid, B. Hoyle, E. M. Huff, D. Huterer, B. Jain, M. Jarvis, T. Kacprzak, D. Kirk, N. Kokron, C. Krawiec, O. Lahav, A. R. Liddle, J. Peacock, M. M. Rau, A. Refregier, R. P. Rollins, E. Rozo, E. S. Rykoff, C. Sánchez, I. Sevilla-Noarbe, E. Sheldon, A. Stebbins, T. N. Varga, P. Vielzeuf,

M. Wang, R. H. Wechsler, B. Yanny, T. M. C. Abbott, F. B. Abdalla, S. Allam, J. Annis, K. Bechtol, A. Benoit-Lévy, E. Bertin, D. Brooks, E. Buckley-Geer, D. L. Burke, A. Carnero Rosell, M. Carrasco Kind, J. Carretero, F. J. Castander, M. Crocce, C. E. Cunha, C. B. D'Andrea, L. N. da Costa, D. L. DePoy, S. Desai, H. T. Diehl, J. P. Dietrich, P. Doel, E. Fernandez, B. Flaugher, P. Fosalba, J. García-Bellido, E. Gaztanaga, D. W. Gerdes, T. Giannantonio, D. A. Goldstein, R. A. Gruendl, J. Gschwend, G. Gutierrez, D. J. James, T. Jeltema, M. W. G. Johnson, M. D. Johnson, S. Kent, K. Kuehn, S. Kuhlmann, N. Kuropatkin, T. S. Li, M. Lima, H. Lin, M. A. G. Maia, M. March, J. L. Marshall, P. Martini, P. Melchior, F. Menanteau, R. Miquel, J. J. Mohr, E. Neilsen, R. C. Nichol, B. Nord, D. Petravick, A. A. Plazas, A. K. Romer, A. Roodman, M. Sako, E. Sanchez, V. Scarpine, R. Schindler, M. Schubnell, M. Smith, R. C. Smith, M. Soares-Santos, F. Sobreira, E. Suchyta, M. E. C. Swanson, G. Tarle, D. Thomas, D. L. Tucker, V. Vikram, A. R. Walker, J. Weller, Y. Zhang, and DES Collaboration, "Dark Energy Survey Year 1 results: Cosmological constraints from cosmic shear," *Phys. Rev. D*, vol. 98, p. 043528, Aug. 2018.

[7]   S. Alam, M. Ata, S. Bailey, F. Beutler, D. Bizyaev, J. A. Blazek, A. S. Bolton, J. R. Brownstein, A. Burden, C.-H. Chuang, J. Comparat, A. J. Cuesta, K. S. Dawson, D. J. Eisenstein, S. Escoffier, H. Gil-Marín, J. N. Grieb, N. Hand, S. Ho, K. Kinemuchi, D. Kirkby, F. Kitaura, E. Malanushenko, V. Malanushenko, C. Maraston, C. K. McBride, R. C. Nichol, M. D. Olmstead, D. Oravetz, N. Padmanabhan, N. Palanque-Delabrouille, K. Pan, M. Pellejero-Ibanez, W. J. Percival, P. Petitjean, F. Prada, A. M. Price-Whelan, B. A. Reid, S. A. Rodríguez-Torres, N. A. Roe, A. J. Ross, N. P. Ross, G. Rossi, J. A. Rubiño-Martín, S. Saito, S. Salazar-Albornoz, L. Samushia, A. G. Sánchez, S. Satpathy, D. J. Schlegel, D. P. Schneider, C. G. Scóccola, H.-J. Seo, E. S. Sheldon, A. Simmons, A. Slosar, M. A. Strauss, M. E. C. Swanson, D. Thomas, J. L. Tinker, R. Tojeiro, M. V. Magaña, J. A. Vazquez, L. Verde, D. A. Wake, Y. Wang, D. H. Weinberg, M. White, W. M. Wood-Vasey, C. Yèche, I. Zehavi, Z. Zhai, and G.-B. Zhao, "The clustering of galaxies in the completed SDSS-III Baryon Oscillation Spectroscopic Survey: cosmological analysis of the DR12 galaxy sample," *MNRAS*, vol. 470, pp. 2617–2652, Sept. 2017.

[8]   The Dark Energy Survey Collaboration, T. M. C. Abbott, F. B. Abdalla, A. Alarcon, S. Allam, F. Andrade-Oliveira, J. Annis, S. Avila, M. Banerji, N. Banik, K. Bechtol, G. M. Bernstein, R. A. Bernstein, E. Bertin, D. Brooks, E. Buckley-Geer, D. L. Burke, H. Camacho, A. Carnero Rosell, M. Carrasco Kind, J. Carretero, F. J. Castander,

R. Cawthon, K. C. Chan, M. Crocce, C. E. Cunha, C. B. D'Andrea, L. N. da Costa, C. Davis, J. De Vicente, D. L. DePoy, S. Desai, H. T. Diehl, P. Doel, A. Drlica-Wagner, T. F. Eifler, J. Elvin-Poole, J. Estrada, A. E. Evrard, B. Flaugher, P. Fosalba, J. Frieman, J. Garcia-Bellido, E. Gaztanaga, D. W. Gerdes, T. Giannantonio, D. Gruen, R. A. Gruendl, J. Gschwend, G. Gutierrez, W. G. Hartley, D. Hollowood, K. Honscheid, B. Hoyle, B. Jain, D. J. James, T. Jeltema, M. D. Johnson, S. Kent, N. Kokron, E. Krause, K. Kuehn, S. Kuhlmann, N. Kuropatkin, F. Lacasa, O. Lahav, M. Lima, H. Lin, M. A. G. Maia, M. Manera, J. Marriner, J. L. Marshall, P. Martini, P. Melchior, F. Menanteau, C. J. Miller, R. Miquel, J. J. Mohr, E. Neilsen, W. J. Percival, A. A. Plazas, A. Porredon, A. K. Romer, A. Roodman, R. Rosenfeld, A. J. Ross, E. Rozo, E. S. Rykoff, M. Sako, E. Sanchez, B. Santiago, V. Scarpine, R. Schindler, M. Schubnell, S. Serrano, I. Sevilla-Noarbe, E. Sheldon, R. C. Smith, M. Smith, F. Sobreira, E. Suchyta, M. E. C. Swanson, G. Tarle, D. Thomas, M. A. Troxel, D. L. Tucker, V. Vikram, A. R. Walker, R. H. Wechsler, J. Weller, B. Yanny, and Y. Zhang, "Dark Energy Survey Year 1 Results: Measurement of the Baryon Acoustic Oscillation scale in the distribution of galaxies to redshift 1," *ArXiv e-prints*, Dec. 2017.

[9] D. M. Scolnic, D. O. Jones, A. Rest, Y. C. Pan, R. Chornock, R. J. Foley, M. E. Huber, R. Kessler, G. Narayan, A. G. Riess, S. Rodney, E. Berger, D. J. Brout, P. J. Challis, M. Drout, D. Finkbeiner, R. Lunnan, R. P. Kirshner, N. E. Sanders, E. Schlafly, S. Smartt, C. W. Stubbs, J. Tonry, W. M. Wood-Vasey, M. Foley, J. Hand, E. Johnson, W. S. Burgett, K. C. Chambers, P. W. Draper, K. W. Hodapp, N. Kaiser, R. P. Kudritzki, E. A. Magnier, N. Metcalfe, F. Bresolin, E. Gall, R. Kotak, M. McCrum, and K. W. Smith, "The Complete Light-curve Sample of Spectroscopically Confirmed SNe Ia from Pan-STARRS1 and Cosmological Constraints from the Combined Pantheon Sample," *ApJ*, vol. 859, p. 101, June 2018.

[10] B. A. Reid and M. White, "Towards an accurate model of the redshift-space clustering of haloes in the quasi-linear regime," *MNRAS*, vol. 417, pp. 1913–1927, Nov. 2011.

[11] J. Carlson, B. Reid, and M. White, "Convolution Lagrangian perturbation theory for biased tracers," *MNRAS*, vol. 429, pp. 1674–1685, Feb. 2013.

[12] A. Taruya, T. Nishimichi, S. Saito, and T. Hiramatsu, "Nonlinear evolution of baryon acoustic oscillations from improved perturbation theory in real and redshift spaces," *Phys. Rev. D*, vol. 80, p. 123503, Dec. 2009.

[13]   A. Taruya, T. Nishimichi, and S. Saito, "Baryon acoustic oscillations in 2D: Modeling redshift-space power spectrum from perturbation theory," *Phys. Rev. D*, vol. 82, p. 063522, Sept. 2010.

[14]   A. Slosar, C. Hirata, U. Seljak, S. Ho, and N. Padmanabhan, "Constraints on local primordial non-Gaussianity from large scale structure," *JCAP*, vol. 8, p. 031, Aug. 2008.

[15]   S. Cole, W. J. Percival, J. A. Peacock, P. Norberg, C. M. Baugh, C. S. Frenk, I. Baldry, J. Bland-Hawthorn, T. Bridges, R. Cannon, M. Colless, C. Collins, W. Couch, N. J. G. Cross, G. Dalton, V. R. Eke, R. De Propris, S. P. Driver, G. Efstathiou, R. S. Ellis, K. Glazebrook, C. Jackson, A. Jenkins, O. Lahav, I. Lewis, S. Lumsden, S. Maddox, D. Madgwick, B. A. Peterson, W. Sutherland, and K. Taylor, "The 2dF Galaxy Redshift Survey: power-spectrum analysis of the final data set and cosmological implications," *MNRAS*, vol. 362, pp. 505–534, Sept. 2005.

[16]   W. J. Percival, C. M. Baugh, J. Bland-Hawthorn, T. Bridges, R. Cannon, S. Cole, M. Colless, C. Collins, W. Couch, G. Dalton, R. De Propris, S. P. Driver, G. Efstathiou, R. S. Ellis, C. S. Frenk, K. Glazebrook, C. Jackson, O. Lahav, I. Lewis, S. Lumsden, S. Maddox, S. Moody, P. Norberg, J. A. Peacock, B. A. Peterson, W. Sutherland, and K. Taylor, "The 2dF Galaxy Redshift Survey: the power spectrum and the matter content of the Universe," *MNRAS*, vol. 327, pp. 1297–1306, Nov. 2001.

[17]   M. Tegmark, A. J. S. Hamilton, and Y. Xu, "The power spectrum of galaxies in the 2dF 100k redshift survey," *MNRAS*, vol. 335, pp. 887–908, Oct. 2002.

[18]   W. J. Percival, "Markov chain reconstruction of the 2dF Galaxy Redshift Survey real-space power spectrum," *MNRAS*, vol. 356, pp. 1168–1176, Jan. 2005.

[19]   M. Colless, B. A. Peterson, C. Jackson, J. A. Peacock, S. Cole, P. Norberg, I. K. Baldry, C. M. Baugh, J. Bland-Hawthorn, T. Bridges, R. Cannon, C. Collins, W. Couch, N. Cross, G. Dalton, R. De Propris, S. P. Driver, G. Efstathiou, R. S. Ellis, C. S. Frenk, K. Glazebrook, O. Lahav, I. Lewis, S. Lumsden, S. Maddox, D. Madgwick, W. Sutherland, and K. Taylor, "The 2dF Galaxy Redshift Survey: Final Data Release," *ArXiv Astrophysics e-prints*, June 2003.

[20]   D. J. Eisenstein, J. Annis, J. E. Gunn, A. S. Szalay, A. J. Connolly, R. C. Nichol, N. A. Bahcall, M. Bernardi, S. Burles, F. J. Castander, M. Fukugita, D. W. Hogg, Ž. Ivezić, G. R. Knapp, R. H. Lupton, V. Narayanan, M. Postman, D. E. Reichart, M. Richmond,

D. P. Schneider, D. J. Schlegel, M. A. Strauss, M. SubbaRao, D. L. Tucker, D. Vanden Berk, M. S. Vogeley, D. H. Weinberg, and B. Yanny, "Spectroscopic Target Selection for the Sloan Digital Sky Survey: The Luminous Red Galaxy Sample," *AJ*, vol. 122, pp. 2267–2280, Nov. 2001.

[21]   A. Pollo, L. Guzzo, O. Le Fèvre, B. Meneux, A. Cappi, H. J. McCracken, A. Iovino, C. Marinoni, D. Bottini, B. Garilli, V. L. Le Brun, D. Maccagni, J. P. Picat, R. Scaramella, M. Scodeggio, L. Tresse, G. Vettolani, A. Zanichelli, C. Adami, S. Arnouts, S. Bardelli, M. Bolzonella, S. Charlot, P. Ciliegi, T. Contini, S. Foucaud, P. Franzetti, I. Gavignaud, O. Ilbert, B. Marano, A. Mazure, R. Merighi, S. Paltani, R. Pellò, L. Pozzetti, M. Radovich, G. Zamorani, E. Zucca, M. Bondi, A. Bongiorno, J. Brinchmann, O. Cucciati, S. de la Torre, F. Lamareille, Y. Mellier, P. Merluzzi, S. Temporin, D. Vergani, and C. J. Walcher, "The VIRMOS-VLT Deep Survey: the Last 10 Billion Years of Evolution of Galaxy Clustering," in *Deepest Astronomical Surveys* (J. Afonso, H. C. Ferguson, B. Mobasher, and R. Norris, eds.), vol. 380 of *Astronomical Society of the Pacific Conference Series*, p. 533, Dec. 2007.

[22]   C. Blake, S. Brough, M. Colless, W. Couch, S. Croom, T. Davis, M. J. Drinkwater, K. Forster, K. Glazebrook, B. Jelliffe, R. J. Jurek, I.-H. Li, B. Madore, C. Martin, K. Pimbblet, G. B. Poole, M. Pracy, R. Sharp, E. Wisnioski, D. Woods, and T. Wyder, "The WiggleZ Dark Energy Survey: the selection function and z = 0.6 galaxy power spectrum," *MNRAS*, vol. 406, pp. 803–821, Aug. 2010.

[23]   M. Ata, F. Baumgarten, J. Bautista, F. Beutler, D. Bizyaev, M. R. Blanton, J. A. Blazek, A. S. Bolton, J. Brinkmann, J. R. Brownstein, E. Burtin, C.-H. Chuang, J. Comparat, K. S. Dawson, A. de la Macorra, W. Du, H. du Mas des Bourboux, D. J. Eisenstein, H. Gil-Marín, K. Grabowski, J. Guy, N. Hand, S. Ho, T. A. Hutchinson, M. M. Ivanov, F.-S. Kitaura, J.-P. Kneib, P. Laurent, J.-M. Le Goff, J. E. McEwen, E.-M. Mueller, A. D. Myers, J. A. Newman, N. Palanque-Delabrouille, K. Pan, I. Pâris, M. Pellejero-Ibanez, W. J. Percival, P. Petitjean, F. Prada, A. Prakash, S. A. Rodríguez-Torres, A. J. Ross, G. Rossi, R. Ruggeri, A. G. Sánchez, S. Satpathy, D. J. Schlegel, D. P. Schneider, H.-J. Seo, A. Slosar, A. Streblyanska, J. L. Tinker, R. Tojeiro, M. Vargas Magaña, M. Vivek, Y. Wang, C. Yèche, L. Yu, P. Zarrouk, C. Zhao, G.-B. Zhao, and F. Zhu, "The clustering of the SDSS-IV extended Baryon Oscillation Spectroscopic Survey DR14 quasar sample: first measurement of baryon acoustic oscillations between redshift 0.8 and 2.2," *MNRAS*, vol. 473, pp. 4773–4794, Feb. 2018.

[24] F. Beutler, C. Blake, M. Colless, D. H. Jones, L. Staveley-Smith, L. Campbell, Q. Parker, W. Saunders, and F. Watson, "The 6dF Galaxy Survey: baryon acoustic oscillations and the local Hubble constant," *MNRAS*, vol. 416, pp. 3017–3032, Oct. 2011.

[25] J. E. Bautista, N. G. Busca, J. Guy, J. Rich, M. Blomqvist, H. du Mas des Bourboux, M. M. Pieri, A. Font-Ribera, S. Bailey, T. Delubac, D. Kirkby, J.-M. Le Goff, D. Margala, A. Slosar, J. A. Vazquez, J. R. Brownstein, K. S. Dawson, D. J. Eisenstein, J. Miralda-Escudé, P. Noterdaeme, N. Palanque-Delabrouille, I. Pâris, P. Petitjean, N. P. Ross, D. P. Schneider, D. H. Weinberg, and C. Yèche, "Measurement of baryon acoustic oscillation correlations at z = 2.3 with SDSS DR12 Lyα-Forests," *A&A*, vol. 603, p. A12, June 2017.

[26] E. A. Kazin, J. Koda, C. Blake, N. Padmanabhan, S. Brough, M. Colless, C. Contreras, W. Couch, S. Croom, D. J. Croton, T. M. Davis, M. J. Drinkwater, K. Forster, D. Gilbank, M. Gladders, K. Glazebrook, B. Jelliffe, R. J. Jurek, I.-h. Li, B. Madore, D. C. Martin, K. Pimbblet, G. B. Poole, M. Pracy, R. Sharp, E. Wisnioski, D. Woods, T. K. Wyder, and H. K. C. Yee, "The WiggleZ Dark Energy Survey: improved distance measurements to z = 1 with reconstruction of the baryonic acoustic feature," *MNRAS*, vol. 441, pp. 3524–3542, July 2014.

[27] S. Perlmutter, G. Aldering, G. Goldhaber, R. A. Knop, P. Nugent, P. G. Castro, S. Deustua, S. Fabbro, A. Goobar, D. E. Groom, I. M. Hook, A. G. Kim, M. Y. Kim, J. C. Lee, N. J. Nunes, R. Pain, C. R. Pennypacker, R. Quimby, C. Lidman, R. S. Ellis, M. Irwin, R. G. McMahon, P. Ruiz-Lapuente, N. Walton, B. Schaefer, B. J. Boyle, A. V. Filippenko, T. Matheson, A. S. Fruchter, N. Panagia, H. J. M. Newberg, W. J. Couch, and T. S. C. Project, "Measurements of Ω and Λ from 42 High-Redshift Supernovae," *ApJ*, vol. 517, pp. 565–586, June 1999.

[28] M. R. Blanton, M. A. Bershady, B. Abolfathi, F. D. Albareti, C. Allende Prieto, A. Almeida, J. Alonso-García, F. Anders, S. F. Anderson, B. Andrews, and et al., "Sloan Digital Sky Survey IV: Mapping the Milky Way, Nearby Galaxies, and the Distant Universe," *AJ*, vol. 154, p. 28, July 2017.

[29] A. Einstein, "The Foundation of the General Theory of Relativity," *Annalen Phys.*, vol. 49, no. 7, pp. 769–822, 1916. [Annalen Phys.14,517(2005)].

[30] Planck Collaboration, P. A. R. Ade, N. Aghanim, M. Arnaud, F. Arroja, M. Ashdown, J. Aumont, C. Baccigalupi, M. Ballardini, A. J. Banday, and et al., "Planck 2015

results. XVII. Constraints on primordial non-Gaussianity," *A&A*, vol. 594, p. A17, Sept. 2016.

[31] D. Langlois, "Inflation and Cosmological Perturbations," in *Lecture Notes in Physics, Berlin Springer Verlag* (G. Wolschin, ed.), vol. 800 of *Lecture Notes in Physics, Berlin Springer Verlag*, pp. 1–57, Mar. 2010.

[32] S. Weinberg, "The Cosmological Constant Problem," *Rev. Mod. Phys.*, vol. 61, pp. 1–23, 1989.
[,569(1988)].

[33] P. J. Peebles and B. Ratra, "The cosmological constant and dark energy," *Reviews of Modern Physics*, vol. 75, pp. 559–606, Apr. 2003.

[34] T. Padmanabhan, "Cosmological constant-the weight of the vacuum," *Phys. Rep.*.

[35] T. P. Sotiriou and V. Faraoni, "f(R) theories of gravity," *Reviews of Modern Physics*, vol. 82, pp. 451–497, Jan. 2010.

[36] J. C. Mather, E. S. Cheng, D. A. Cottingham, R. E. Eplee, Jr., D. J. Fixsen, T. Hewagama, R. B. Isaacman, K. A. Jensen, S. S. Meyer, P. D. Noerdlinger, S. M. Read, L. P. Rosen, R. A. Shafer, E. L. Wright, C. L. Bennett, N. W. Boggess, M. G. Hauser, T. Kelsall, S. H. Moseley, Jr., R. F. Silverberg, G. F. Smoot, R. Weiss, and D. T. Wilkinson, "Measurement of the cosmic microwave background spectrum by the COBE FIRAS instrument," *ApJ*, vol. 420, pp. 439–444, Jan. 1994.

[37] D. J. Fixsen, E. S. Cheng, J. M. Gales, J. C. Mather, R. A. Shafer, and E. L. Wright, "The Cosmic Microwave Background Spectrum from the Full COBE FIRAS Data Set," *ApJ*, vol. 473, p. 576, Dec. 1996.

[38] R. Keisler, C. L. Reichardt, K. A. Aird, B. A. Benson, L. E. Bleem, J. E. Carlstrom, C. L. Chang, H. M. Cho, T. M. Crawford, A. T. Crites, T. de Haan, M. A. Dobbs, J. Dudley, E. M. George, N. W. Halverson, G. P. Holder, W. L. Holzapfel, S. Hoover, Z. Hou, J. D. Hrubes, M. Joy, L. Knox, A. T. Lee, E. M. Leitch, M. Lueker, D. Luong-Van, J. J. McMahon, J. Mehl, S. S. Meyer, M. Millea, J. J. Mohr, T. E. Montroy, T. Natoli, S. Padin, T. Plagge, C. Pryke, J. E. Ruhl, K. K. Schaffer, L. Shaw, E. Shirokoff, H. G. Spieler, Z. Staniszewski, A. A. Stark, K. Story, A. van Engelen, K. Vanderlinde, J. D. Vieira, R. Williamson, and O. Zahn, "A Measurement of the Damping Tail of the Cosmic Microwave Background Power Spectrum with the South Pole Telescope," *ApJ*, vol. 743, p. 28, Dec. 2011.

[39] S. Das, B. D. Sherwin, P. Aguirre, J. W. Appel, J. R. Bond, C. S. Carvalho, M. J. Devlin, J. Dunkley, R. Dünner, T. Essinger-Hileman, J. W. Fowler, A. Hajian, M. Halpern, M. Hasselfield, A. D. Hincks, R. Hlozek, K. M. Huffenberger, J. P. Hughes, K. D. Irwin, J. Klein, A. Kosowsky, R. H. Lupton, T. A. Marriage, D. Marsden, F. Menanteau, K. Moodley, M. D. Niemack, M. R. Nolta, L. A. Page, L. Parker, E. D. Reese, B. L. Schmitt, N. Sehgal, J. Sievers, D. N. Spergel, S. T. Staggs, D. S. Swetz, E. R. Switzer, R. Thornton, K. Visnjic, and E. Wollack, "Detection of the Power Spectrum of Cosmic Microwave Background Lensing by the Atacama Cosmology Telescope," *Physical Review Letters*, vol. 107, p. 021301, July 2011.

[40] E. Komatsu, K. M. Smith, J. Dunkley, C. L. Bennett, B. Gold, G. Hinshaw, N. Jarosik, D. Larson, M. R. Nolta, L. Page, D. N. Spergel, M. Halpern, R. S. Hill, A. Kogut, M. Limon, S. S. Meyer, N. Odegard, G. S. Tucker, J. L. Weiland, E. Wollack, and E. L. Wright, "Seven-year Wilkinson Microwave Anisotropy Probe (WMAP) Observations: Cosmological Interpretation," *ApJS*, vol. 192, p. 18, Feb. 2011.

[41] M. Betoule, R. Kessler, J. Guy, J. Mosher, D. Hardin, R. Biswas, P. Astier, P. El-Hage, M. Konig, S. Kuhlmann, J. Marriner, R. Pain, N. Regnault, C. Balland, B. A. Bassett, P. J. Brown, H. Campbell, R. G. Carlberg, F. Cellier-Holzem, D. Cinabro, A. Conley, C. B. D'Andrea, D. L. DePoy, M. Doi, R. S. Ellis, S. Fabbro, A. V. Filippenko, R. J. Foley, J. A. Frieman, D. Fouchez, L. Galbany, A. Goobar, R. R. Gupta, G. J. Hill, R. Hlozek, C. J. Hogan, I. M. Hook, D. A. Howell, S. W. Jha, L. Le Guillou, G. Leloudas, C. Lidman, J. L. Marshall, A. Möller, A. M. Mourão, J. Neveu, R. Nichol, M. D. Olmstead, N. Palanque-Delabrouille, S. Perlmutter, J. L. Prieto, C. J. Pritchet, M. Richmond, A. G. Riess, V. Ruhlmann-Kleider, M. Sako, K. Schahmaneche, D. P. Schneider, M. Smith, J. Sollerman, M. Sullivan, N. A. Walton, and C. J. Wheeler, "Improved cosmological constraints from a joint analysis of the SDSS-II and SNLS supernova samples," *A&A*, vol. 568, p. A22, Aug. 2014.

[42] A. G. Riess, L. Macri, S. Casertano, H. Lampeitl, H. C. Ferguson, A. V. Filippenko, S. W. Jha, W. Li, and R. Chornock, "A 3% Solution: Determination of the Hubble Constant with the Hubble Space Telescope and Wide Field Camera 3," *ApJ*, vol. 730, p. 119, Apr. 2011.

[43] LSST Science Collaboration, P. A. Abell, J. Allison, S. F. Anderson, J. R. Andrew, J. R. P. Angel, L. Armus, D. Arnett, S. J. Asztalos, T. S. Axelrod, and et al., "LSST Science Book, Version 2.0," *ArXiv e-prints*, Dec. 2009.

[44]   M. Bartelmann, "TOPICAL REVIEW Gravitational lensing," *Classical and Quantum Gravity*, vol. 27, p. 233001, Dec. 2010.

[45]   H. Hoekstra, "Weak lensing constraints on galaxy halos," in *EAS Publications Series* (G. A. Mamon, F. Combes, C. Deffayet, and B. Fort, eds.), vol. 20 of *EAS Publications Series*, pp. 153–160, 2006.

[46]   F. Köhlinger, M. Viola, B. Joachimi, H. Hoekstra, E. van Uitert, H. Hildebrandt, A. Choi, T. Erben, C. Heymans, S. Joudaki, D. Klaes, K. Kuijken, J. Merten, L. Miller, P. Schneider, and E. A. Valentijn, "KiDS-450: the tomographic weak lensing power spectrum and constraints on cosmological parameters," *MNRAS*, vol. 471, pp. 4412–4435, Nov. 2017.

[47]   C. Heymans, L. Van Waerbeke, L. Miller, T. Erben, H. Hildebrandt, H. Hoekstra, T. D. Kitching, Y. Mellier, P. Simon, C. Bonnett, J. Coupon, L. Fu, J. Harnois Déraps, M. J. Hudson, M. Kilbinger, K. Kuijken, B. Rowe, T. Schrabback, E. Semboloni, E. van Uitert, S. Vafaei, and M. Velander, "CFHTLenS: the Canada-France-Hawaii Telescope Lensing Survey," *MNRAS*, vol. 427, pp. 146–166, Nov. 2012.

[48]   J. T. A. de Jong, G. A. Verdois Kleijn, T. Erben, H. Hildebrandt, K. Kuijken, G. Sikkema, M. Brescia, M. Bilicki, N. R. Napolitano, V. Amaro, K. G. Begeman, D. R. Boxhoorn, H. Buddelmeijer, S. Cavuoti, F. Getman, A. Grado, E. Helmich, Z. Huang, N. Irisarri, F. La Barbera, G. Longo, J. P. McFarland, R. Nakajima, M. Paolillo, E. Puddu, M. Radovich, A. Rifatto, C. Tortora, E. A. Valentijn, C. Vellucci, W.-J. Vriend, A. Amon, C. Blake, A. Choi, I. F. Conti, S. D. J. Gwyn, R. Herbonnet, C. Heymans, H. Hoekstra, D. Klaes, J. Merten, L. Miller, P. Schneider, and M. Viola, "The third data release of the Kilo-Degree Survey and associated data products," *A&A*, vol. 604, p. A134, Aug. 2017.

[49]   Dark Energy Survey Collaboration, T. Abbott, F. B. Abdalla, J. Aleksić, S. Allam, A. Amara, D. Bacon, E. Balbinot, M. Banerji, K. Bechtol, A. Benoit-Lévy, G. M. Bernstein, E. Bertin, J. Blazek, C. Bonnett, S. Bridle, D. Brooks, R. J. Brunner, E. Buckley-Geer, D. L. Burke, G. B. Caminha, D. Capozzi, J. Carlsen, A. Carnero-Rosell, M. Carollo, M. Carrasco-Kind, J. Carretero, F. J. Castander, L. Clerkin, T. Collett, C. Conselice, M. Crocce, C. E. Cunha, C. B. D'Andrea, L. N. da Costa, T. M. Davis, S. Desai, H. T. Diehl, J. P. Dietrich, S. Dodelson, P. Doel, A. Drlica-Wagner, J. Estrada, J. Etherington, A. E. Evrard, J. Fabbri, D. A. Finley, B. Flaugher, R. J. Foley, P. Fosalba, J. Frieman, J. García-Bellido, E. Gaztanaga, D. W. Gerdes, T. Giannantonio, D. A. Goldstein,

D. Gruen, R. A. Gruendl, P. Guarnieri, G. Gutierrez, W. Hartley, K. Honscheid, B. Jain, D. J. James, T. Jeltema, S. Jouvel, R. Kessler, A. King, D. Kirk, R. Kron, K. Kuehn, N. Kuropatkin, O. Lahav, T. S. Li, M. Lima, H. Lin, M. A. G. Maia, M. Makler, M. Manera, C. Maraston, J. L. Marshall, P. Martini, R. G. McMahon, P. Melchior, A. Merson, C. J. Miller, R. Miquel, J. J. Mohr, X. Morice-Atkinson, K. Naidoo, E. Neilsen, R. C. Nichol, B. Nord, R. Ogando, F. Ostrovski, A. Palmese, A. Papadopoulos, H. V. Peiris, J. Peoples, W. J. Percival, A. A. Plazas, S. L. Reed, A. Refregier, A. K. Romer, A. Roodman, A. Ross, E. Rozo, E. S. Rykoff, I. Sadeh, M. Sako, C. Sánchez, E. Sanchez, B. Santiago, V. Scarpine, M. Schubnell, I. Sevilla-Noarbe, E. Sheldon, M. Smith, R. C. Smith, M. Soares-Santos, F. Sobreira, M. Soumagnac, E. Suchyta, M. Sullivan, M. Swanson, G. Tarle, J. Thaler, D. Thomas, R. C. Thomas, D. Tucker, J. D. Vieira, V. Vikram, A. R. Walker, R. H. Wechsler, J. Weller, W. Wester, L. Whiteway, H. Wilcox, B. Yanny, Y. Zhang, and J. Zuntz, "The Dark Energy Survey: more than dark energy - an overview," *MNRAS*, vol. 460, pp. 1270–1299, Aug. 2016.

[50] R. Laureijs, J. Amiaux, S. Arduini, J. . Auguères, J. Brinchmann, R. Cole, M. Cropper, C. Dabin, L. Duvet, A. Ealet, and et al., "Euclid Definition Study Report," *ArXiv e-prints*, Oct. 2011.

[51] F. Bernardeau, S. Colombi, E. Gaztañaga, and R. Scoccimarro, "Large-scale structure of the Universe and cosmological perturbation theory," *Phys. Rep.*, vol. 367, pp. 1–248, Sept. 2002.

[52] N. Kaiser, "Clustering in real space and in redshift space," *MNRAS*, vol. 227, pp. 1–21, July 1987.

[53] D. H. Weinberg, M. J. Mortonson, D. J. Eisenstein, C. Hirata, A. G. Riess, and E. Rozo, "Observational probes of cosmic acceleration," *Phys. Rep.*, vol. 530, pp. 87–255, Sept. 2013.

[54] Planck Collaboration, P. A. R. Ade, N. Aghanim, M. Arnaud, M. Ashdown, J. Aumont, C. Baccigalupi, A. J. Banday, R. B. Barreiro, J. G. Bartlett, and et al., "Planck 2015 results. XIII. Cosmological parameters," *A&A*, vol. 594, p. A13, Sept. 2016.

[55] T. Padmanabhan, "Dark energy and gravity," *General Relativity and Gravitation*, vol. 40, pp. 529–564, Feb. 2008.

[56] D. J. Eisenstein, H.-J. Seo, E. Sirko, and D. N. Spergel, "Improving Cosmological Distance Measurements by Reconstruction of the Baryon Acoustic Peak," *ApJ*, vol. 664, pp. 675–679, Aug. 2007.

[57] B. Bose and K. Koyama, "A perturbative approach to the redshift space power spectrum: beyond the Standard Model," *JCAP*, vol. 8, p. 032, Aug. 2016.

[58] L. Guzzo, M. Pierleoni, B. Meneux, E. Branchini, O. Le Fèvre, C. Marinoni, B. Garilli, J. Blaizot, G. De Lucia, A. Pollo, H. J. McCracken, D. Bottini, V. Le Brun, D. Maccagni, J. P. Picat, R. Scaramella, M. Scodeggio, L. Tresse, G. Vettolani, A. Zanichelli, C. Adami, S. Arnouts, S. Bardelli, M. Bolzonella, A. Bongiorno, A. Cappi, S. Charlot, P. Ciliegi, T. Contini, O. Cucciati, S. de la Torre, K. Dolag, S. Foucaud, P. Franzetti, I. Gavignaud, O. Ilbert, A. Iovino, F. Lamareille, B. Marano, A. Mazure, P. Memeo, R. Merighi, L. Moscardini, S. Paltani, R. Pellò, E. Perez-Montero, L. Pozzetti, M. Radovich, D. Vergani, G. Zamorani, and E. Zucca, "A test of the nature of cosmic acceleration using galaxy redshift distortions," *Nature*, vol. 451, pp. 541–544, Jan. 2008.

[59] J. A. Peacock, S. Cole, P. Norberg, C. M. Baugh, J. Bland-Hawthorn, T. Bridges, R. D. Cannon, M. Colless, C. Collins, W. Couch, G. Dalton, K. Deeley, R. De Propris, S. P. Driver, G. Efstathiou, R. S. Ellis, C. S. Frenk, K. Glazebrook, C. Jackson, O. Lahav, I. Lewis, S. Lumsden, S. Maddox, W. J. Percival, B. A. Peterson, I. Price, W. Sutherland, and K. Taylor, "A measurement of the cosmological mass density from clustering in the 2dF Galaxy Redshift Survey," *Nature*, vol. 410, pp. 169–173, Mar. 2001.

[60] F. Beutler, S. Saito, H.-J. Seo, J. Brinkmann, K. S. Dawson, D. J. Eisenstein, A. Font-Ribera, S. Ho, C. K. McBride, F. Montesano, W. J. Percival, A. J. Ross, N. P. Ross, L. Samushia, D. J. Schlegel, A. G. Sánchez, J. L. Tinker, and B. A. Weaver, "The clustering of galaxies in the SDSS-III Baryon Oscillation Spectroscopic Survey: testing gravity with redshift space distortions using the power spectrum multipoles," *MNRAS*, vol. 443, pp. 1065–1089, Sept. 2014.

[61] A. J. S. Hamilton, "Linear Redshift Distortions: a Review," in *The Evolving Universe* (D. Hamilton, ed.), vol. 231 of *Astrophysics and Space Science Library*, p. 185, 1998.

[62] T. Buchert, "Lagrangian theory of gravitational instability of Friedman-Lemaitre cosmologies and the 'Zel'dovich approximation'," *MNRAS*, vol. 254, pp. 729–737, Feb. 1992.

[63] T. Matsubara, "Nonlinear perturbation theory with halo bias and redshift-space distortions via the Lagrangian picture," *Phys. Rev. D*, vol. 78, p. 083519, Oct. 2008.

[64] K. C. Chan, R. Scoccimarro, and R. K. Sheth, "Gravity and large-scale nonlocal bias," *Phys. Rev. D*, vol. 85, p. 083509, Apr. 2012.

[65] T. Matsubara, "Resumming cosmological perturbations via the Lagrangian picture: One-loop results in real space and in redshift space," *Phys. Rev. D*, vol. 77, p. 063530, Mar. 2008.

[66] M. Crocce and R. Scoccimarro, "Renormalized cosmological perturbation theory," *Phys. Rev. D*, vol. 73, p. 063519, Mar. 2006.

[67] P. J. E. Peebles, *The large-scale structure of the universe.* 1980.

[68] Y. B. Zel'dovich, "Gravitational instability: An approximate theory for large density perturbations.," *A&A*, vol. 5, pp. 84–89, Mar. 1970.

[69] L. Wang, B. Reid, and M. White, "An analytic model for redshift-space distortions," *MNRAS*, vol. 437, pp. 588–599, Jan. 2014.

[70] R. Scoccimarro, "Redshift-space distortions, pairwise velocities, and nonlinearities," *Phys. Rev. D*, vol. 70, p. 083007, Oct. 2004.

[71] A. F. Heavens, S. Matarrese, and L. Verde, "The non-linear redshift-space power spectrum of galaxies," *MNRAS*, vol. 301, pp. 797–808, Dec. 1998.

[72] D. J. Eisenstein and W. Hu, "Baryonic Features in the Matter Transfer Function," *ApJ*, vol. 496, pp. 605–614, Mar. 1998.

[73] C. Alcock and B. Paczynski, "An evolution free test for non-zero cosmological constant," *Nature*, vol. 281, p. 358, Oct. 1979.

[74] T. Matsubara and Y. Suto, "Cosmological Redshift Distortion of Correlation Functions as a Probe of the Density Parameter and the Cosmological Constant," *ApJL*, vol. 470, p. L1, Oct. 1996.

[75] W. E. Ballinger, J. A. Peacock, and A. F. Heavens, "Measuring the cosmological constant with redshift surveys," *MNRAS*, vol. 282, p. 877, Oct. 1996.

[76] N. Dalal, O. Doré, D. Huterer, and A. Shirokov, "Imprints of primordial non-Gaussianities on large-scale structure: Scale-dependent bias and abundance of virialized objects," *Phys. Rev. D*, vol. 77, p. 123514, June 2008.

[77] N. Bartolo, E. Komatsu, S. Matarrese, and A. Riotto, "Non-Gaussianity from inflation: theory and observations," *Phys. Rep.*, vol. 402, pp. 103–266, Nov. 2004.

[78] P. Creminelli, L. Senatore, and M. Zaldarriaga, "Estimators for local non-Gaussianities," *JCAP*, vol. 0703, p. 019, 2007.

[79] C. L. Bennett, M. Halpern, G. Hinshaw, N. Jarosik, A. Kogut, M. Limon, S. S. Meyer, L. Page, D. N. Spergel, G. S. Tucker, E. Wollack, E. L. Wright, C. Barnes, M. R. Greason, R. S. Hill, E. Komatsu, M. R. Nolta, N. Odegard, H. V. Peiris, L. Verde, and J. L. Weiland, "First-Year Wilkinson Microwave Anisotropy Probe (WMAP) Observations: Preliminary Maps and Basic Results," *ApJS*, vol. 148, pp. 1–27, Sept. 2003.

[80] N. Padmanabhan, T. Budavári, D. J. Schlegel, T. Bridges, J. Brinkmann, R. Cannon, A. J. Connolly, S. M. Croom, I. Csabai, M. Drinkwater, D. J. Eisenstein, P. C. Hewett, J. Loveday, R. C. Nichol, K. A. Pimbblet, R. De Propris, D. P. Schneider, R. Scranton, U. Seljak, T. Shanks, I. Szapudi, A. S. Szalay, and D. Wake, "Calibrating photometric redshifts of luminous red galaxies," *MNRAS*, vol. 359, pp. 237–250, May 2005.

[81] G. T. Richards, X. Fan, H. J. Newberg, M. A. Strauss, D. E. Vanden Berk, D. P. Schneider, B. Yanny, A. Boucher, S. Burles, J. A. Frieman, J. E. Gunn, P. B. Hall, Ž. Ivezić, S. Kent, J. Loveday, R. H. Lupton, C. M. Rockosi, D. J. Schlegel, C. Stoughton, M. SubbaRao, and D. G. York, "Spectroscopic Target Selection in the Sloan Digital Sky Survey: The Quasar Sample," *AJ*, vol. 123, pp. 2945–2975, June 2002.

[82] S. Ho, C. Hirata, N. Padmanabhan, U. Seljak, and N. Bahcall, "Correlation of CMB with large-scale structure. I. Integrated Sachs-Wolfe tomography and cosmological implications," *Phys. Rev. D*, vol. 78, p. 043519, Aug. 2008.

[83] J.-Q. Xia, C. Baccigalupi, S. Matarrese, L. Verde, and M. Viel, "Constraints on primordial non-Gaussianity from large scale structure probes," *JCAP*, vol. 8, p. 033, Aug. 2011.

[84] A. J. Ross, W. J. Percival, A. Carnero, G.-b. Zhao, M. Manera, A. Raccanelli, E. Aubourg, D. Bizyaev, H. Brewington, J. Brinkmann, J. R. Brownstein, A. J. Cuesta, L. A. N. da Costa, D. J. Eisenstein, G. Ebelke, H. Guo, J.-C. Hamilton, M. V. Magaña,

E. Malanushenko, V. Malanushenko, C. Maraston, F. Montesano, R. C. Nichol, D. Oravetz, K. Pan, F. Prada, A. G. Sánchez, L. Samushia, D. J. Schlegel, D. P. Schnei-der, H.-J. Seo, A. Sheldon, A. Simmons, S. Snedden, M. E. C. Swanson, D. Thomas, J. L. Tinker, R. Tojeiro, and I. Zehavi, "The clustering of galaxies in the SDSS-III DR9 Baryon Oscillation Spectroscopic Survey: constraints on primordial non-Gaussianity," *MNRAS*, vol. 428, pp. 1116–1127, Jan. 2013.

[85] C. P. Ahn, R. Alexandroff, C. Allende Prieto, S. F. Anderson, T. Anderton, B. H. Andrews, É. Aubourg, S. Bailey, E. Balbinot, R. Barnes, and et al., "The Ninth Data Release of the Sloan Digital Sky Survey: First Spectroscopic Data from the SDSS-III Baryon Oscillation Spectroscopic Survey," *ApJS*, vol. 203, p. 21, Dec. 2012.

[86] H. A. Feldman, N. Kaiser, and J. A. Peacock, "Power-spectrum analysis of three-dimensional redshift surveys," *ApJ*, vol. 426, pp. 23–37, May 1994.

[87] W. J. Percival, L. Verde, and J. A. Peacock, "Fourier analysis of luminosity-dependent galaxy clustering," *MNRAS*, vol. 347, pp. 645–653, Jan. 2004.

[88] R. E. Smith and L. Marian, "Towards optimal estimation of the galaxy power spectrum," *MNRAS*, vol. 454, pp. 1266–1289, Dec. 2015.

[89] C. Park, M. S. Vogeley, M. J. Geller, and J. P. Huchra, "Power spectrum, correlation function, and tests for luminosity bias in the CfA redshift survey," *ApJ*, vol. 431, pp. 569–585, Aug. 1994.

[90] M. J. I. Brown, R. L. Webster, and B. J. Boyle, "The clustering of colour-selected galaxies," *MNRAS*, vol. 317, pp. 782–794, Oct. 2000.

[91] A. J. Ross, F. Beutler, C.-H. Chuang, M. Pellejero-Ibanez, H.-J. Seo, M. Vargas-Magaña, A. J. Cuesta, W. J. Percival, A. Burden, A. G. Sánchez, J. N. Grieb, B. Reid, J. R. Brown-stein, K. S. Dawson, D. J. Eisenstein, S. Ho, F.-S. Kitaura, R. C. Nichol, M. D. Olm-stead, F. Prada, S. A. Rodríguez-Torres, S. Saito, S. Salazar-Albornoz, D. P. Schneider, D. Thomas, J. Tinker, R. Tojeiro, Y. Wang, M. White, and G.-b. Zhao, "The clustering of galaxies in the completed SDSS-III Baryon Oscillation Spectroscopic Survey: observational systematics and baryon acoustic oscillations in the correlation func-tion," *MNRAS*, vol. 464, pp. 1168–1191, Jan. 2017.

[92] D. J. Eisenstein, I. Zehavi, D. W. Hogg, R. Scoccimarro, M. R. Blanton, R. C. Nichol, R. Scranton, H.-J. Seo, M. Tegmark, Z. Zheng, S. F. Anderson, J. Annis, N. Bahcall,

J. Brinkmann, S. Burles, F. J. Castander, A. Connolly, I. Csabai, M. Doi, M. Fukugita, J. A. Frieman, K. Glazebrook, J. E. Gunn, J. S. Hendry, G. Hennessy, Z. Ivezić, S. Kent, G. R. Knapp, H. Lin, Y.-S. Loh, R. H. Lupton, B. Margon, T. A. McKay, A. Meiksin, J. A. Munn, A. Pope, M. W. Richmond, D. Schlegel, D. P. Schneider, K. Shimasaku, C. Stoughton, M. A. Strauss, M. SubbaRao, A. S. Szalay, I. Szapudi, D. L. Tucker, B. Yanny, and D. G. York, "Detection of the Baryon Acoustic Peak in the Large-Scale Correlation Function of SDSS Luminous Red Galaxies," *ApJ*, vol. 633, pp. 560–574, Nov. 2005.

[93] W. J. Percival, B. A. Reid, D. J. Eisenstein, N. A. Bahcall, T. Budavari, J. A. Frieman, M. Fukugita, J. E. Gunn, Ž. Ivezić, G. R. Knapp, R. G. Kron, J. Loveday, R. H. Lupton, T. A. McKay, A. Meiksin, R. C. Nichol, A. C. Pope, D. J. Schlegel, D. P. Schneider, D. N. Spergel, C. Stoughton, M. A. Strauss, A. S. Szalay, M. Tegmark, M. S. Vogeley, D. H. Weinberg, D. G. York, and I. Zehavi, "Baryon acoustic oscillations in the Sloan Digital Sky Survey Data Release 7 galaxy sample," *MNRAS*, vol. 401, pp. 2148–2168, Feb. 2010.

[94] F. Beutler, H.-J. Seo, A. J. Ross, P. McDonald, S. Saito, A. S. Bolton, J. R. Brownstein, C.-H. Chuang, A. J. Cuesta, D. J. Eisenstein, A. Font-Ribera, J. N. Grieb, N. Hand, F.-S. Kitaura, C. Modi, R. C. Nichol, W. J. Percival, F. Prada, S. Rodriguez-Torres, N. A. Roe, N. P. Ross, S. Salazar-Albornoz, A. G. Sánchez, D. P. Schneider, A. Slosar, J. Tinker, R. Tojeiro, M. Vargas-Magaña, and J. A. Vazquez, "The clustering of galaxies in the completed SDSS-III Baryon Oscillation Spectroscopic Survey: baryon acoustic oscillations in the Fourier space," *MNRAS*, vol. 464, pp. 3409–3430, Jan. 2017.

[95] F. Beutler, H.-J. Seo, S. Saito, C.-H. Chuang, A. J. Cuesta, D. J. Eisenstein, H. Gil-Marín, J. N. Grieb, N. Hand, F.-S. Kitaura, C. Modi, R. C. Nichol, M. D. Olmstead, W. J. Percival, F. Prada, A. G. Sánchez, S. Rodriguez-Torres, A. J. Ross, N. P. Ross, D. P. Schneider, J. Tinker, R. Tojeiro, and M. Vargas-Magaña, "The clustering of galaxies in the completed SDSS-III Baryon Oscillation Spectroscopic Survey: anisotropic galaxy clustering in Fourier space," *MNRAS*, vol. 466, pp. 2242–2260, Apr. 2017.

[96] K. S. Dawson, J.-P. Kneib, W. J. Percival, S. Alam, F. D. Albareti, S. F. Anderson, E. Armengaud, É. Aubourg, S. Bailey, J. E. Bautista, A. A. Berlind, M. A. Bershady, F. Beutler, D. Bizyaev, M. R. Blanton, M. Blomqvist, A. S. Bolton, J. Bovy, W. N. Brandt, J. Brinkmann, J. R. Brownstein, E. Burtin, N. G. Busca, Z. Cai, C.-H. Chuang, N. Clerc, J. Comparat, F. Cope, R. A. C. Croft, I. Cruz-Gonzalez, L. N. da Costa,

M.-C. Cousinou, J. Darling, A. de la Macorra, S. de la Torre, T. Delubac, H. du Mas des Bourboux, T. Dwelly, A. Ealet, D. J. Eisenstein, M. Eracleous, S. Escoffier, X. Fan, A. Finoguenov, A. Font-Ribera, P. Frinchaboy, P. Gaulme, A. Georgakakis, P. Green, H. Guo, J. Guy, S. Ho, D. Holder, J. Huehnerhoff, T. Hutchinson, Y. Jing, E. Jullo, V. Kamble, K. Kinemuchi, D. Kirkby, F.-S. Kitaura, M. A. Klaene, R. R. Laher, D. Lang, P. Laurent, J.-M. Le Goff, C. Li, Y. Liang, M. Lima, Q. Lin, W. Lin, Y.-T. Lin, D. C. Long, B. Lundgren, N. MacDonald, M. A. Geimba Maia, E. Malanushenko, V. Malanushenko, V. Mariappan, C. K. McBride, I. D. McGreer, B. Ménard, A. Merloni, A. Meza, A. D. Montero-Dorta, D. Muna, A. D. Myers, K. Nandra, T. Naugle, J. A. Newman, P. Noterdaeme, P. Nugent, R. Ogando, M. D. Olmstead, A. Oravetz, D. J. Oravetz, N. Padmanabhan, N. Palanque-Delabrouille, K. Pan, J. K. Parejko, I. Pâris, J. A. Peacock, P. Petitjean, M. M. Pieri, A. Pisani, F. Prada, A. Prakash, A. Raichoor, B. Reid, J. Rich, J. Ridl, S. Rodriguez-Torres, A. Carnero Rosell, A. J. Ross, G. Rossi, J. Ruan, M. Salvato, C. Sayres, D. P. Schneider, D. J. Schlegel, U. Seljak, H.-J. Seo, B. Sesar, S. Shandera, Y. Shu, A. Slosar, F. Sobreira, A. Streblyanska, N. Suzuki, D. Taylor, C. Tao, J. L. Tinker, R. Tojeiro, M. Vargas-Magaña, Y. Wang, B. A. Weaver, D. H. Weinberg, M. White, W. M. Wood-Vasey, C. Yeche, Z. Zhai, C. Zhao, G.-b. Zhao, Z. Zheng, G. Ben Zhu, and H. Zou, "The SDSS-IV Extended Baryon Oscillation Spectroscopic Survey: Overview and Early Data," *AJ*, vol. 151, p. 44, Feb. 2016.

[97] B. Abolfathi, D. S. Aguado, G. Aguilar, C. Allende Prieto, A. Almeida, T. T. Ananna, F. Anders, S. F. Anderson, B. H. Andrews, B. Anguiano, and et al., "The Fourteenth Data Release of the Sloan Digital Sky Survey: First Spectroscopic Data from the Extended Baryon Oscillation Spectroscopic Survey and from the Second Phase of the Apache Point Observatory Galactic Evolution Experiment," *ApJS*, vol. 235, p. 42, Apr. 2018.

[98] A. D. Myers, N. Palanque-Delabrouille, A. Prakash, I. Pâris, C. Yeche, K. S. Dawson, J. Bovy, D. Lang, D. J. Schlegel, J. A. Newman, P. Petitjean, J.-P. Kneib, P. Laurent, W. J. Percival, A. J. Ross, H.-J. Seo, J. L. Tinker, E. Armengaud, J. Brownstein, E. Burtin, Z. Cai, J. Comparat, M. Kasliwal, S. R. Kulkarni, R. Laher, D. Levitan, C. K. McBride, I. D. McGreer, A. A. Miller, P. Nugent, E. Ofek, G. Rossi, J. Ruan, D. P. Schneider, B. Sesar, A. Streblyanska, and J. Surace, "The SDSS-IV Extended Baryon Oscillation Spectroscopic Survey: Quasar Target Selection," *ApJS*, vol. 221, p. 27, Dec. 2015.

[99] D. Lang, D. W. Hogg, and D. J. Schlegel, "WISE photometry for 400 million SDSS sources," *ArXiv e-prints*, Oct. 2014.

[100] S. A. Smee, J. E. Gunn, A. Uomoto, N. Roe, D. Schlegel, C. M. Rockosi, M. A. Carr, F. Leger, K. S. Dawson, M. D. Olmstead, J. Brinkmann, R. Owen, R. H. Barkhouser, K. Honscheid, P. Harding, D. Long, R. H. Lupton, C. Loomis, L. Anderson, J. Annis, M. Bernardi, V. Bhardwaj, D. Bizyaev, A. S. Bolton, H. Brewington, J. W. Briggs, S. Burles, J. G. Burns, F. J. Castander, A. Connolly, J. R. A. Davenport, G. Ebelke, H. Epps, P. D. Feldman, S. D. Friedman, J. Frieman, T. Heckman, C. L. Hull, G. R. Knapp, D. M. Lawrence, J. Loveday, E. J. Mannery, E. Malanushenko, V. Malanushenko, A. J. Merrelli, D. Muna, P. R. Newman, R. C. Nichol, D. Oravetz, K. Pan, A. C. Pope, P. G. Ricketts, A. Shelden, D. Sandford, W. Siegmund, A. Simmons, D. S. Smith, S. Snedden, D. P. Schneider, M. SubbaRao, C. Tremonti, P. Waddell, and D. G. York, "The Multi-object, Fiber-fed Spectrographs for the Sloan Digital Sky Survey and the Baryon Oscillation Spectroscopic Survey," *AJ*, vol. 146, p. 32, Aug. 2013.

[101] P. C. Hewett and V. Wild, "Improved redshifts for SDSS quasar spectra," *MNRAS*, vol. 405, pp. 2302–2316, July 2010.

[102] P. Martini, S. Bailey, R. W. Besuner, D. Brooks, P. Doel, J. Edelstein, D. Eisenstein, B. Flaugher, G. Gutierrez, S. E. Harris, K. Honscheid, P. Jelinsky, R. Joyce, S. Kent, M. Levi, F. Prada, C. Poppett, D. Rabinowitz, C. Rockosi, L. Cardiel Sas, D. J. Schlegel, M. Schubnell, R. Sharples, J. H. Silber, D. Sprayberry, and R. Wechsler, "Overview of the Dark Energy Spectroscopic Instrument," in *Society of Photo-Optical Instrumentation Engineers (SPIE) Conference Series*, vol. 10702 of *Society of Photo-Optical Instrumentation Engineers (SPIE) Conference Series*, p. 107021F, July 2018.

[103] The Dark Energy Survey Collaboration, "The Dark Energy Survey," *ArXiv Astrophysics e-prints*, Oct. 2005.

[104] D. Bianchi, H. Gil-Marín, R. Ruggeri, and W. J. Percival, "Measuring line-of-sight-dependent Fourier-space clustering using FFTs," *MNRAS*, vol. 453, pp. L11–L15, Oct. 2015.

[105] A. S. Szalay, T. Matsubara, and S. D. Landy, "Redshift-Space Distortions of the Correlation Function in Wide-Angle Galaxy Surveys," *ApJL*, vol. 498, pp. L1–L4, May 1998.

[106] I. Szapudi, "Wide-Angle Redshift Distortions Revisited," *ApJ*, vol. 614, pp. 51–55, Oct. 2004.

[107] F. Beutler, C. Blake, M. Colless, D. H. Jones, L. Staveley-Smith, G. B. Poole, L. Campbell, Q. Parker, W. Saunders, and F. Watson, "The 6dF Galaxy Survey: z 0 measurements of the growth rate and σ_8," *MNRAS*, vol. 423, pp. 3430–3444, July 2012.

[108] L. Samushia, W. J. Percival, and A. Raccanelli, "Interpreting large-scale redshift-space distortion measurements," *MNRAS*, vol. 420, pp. 2102–2119, Mar. 2012.

[109] J. Yoo and U. Seljak, "Wide-angle effects in future galaxy surveys," *MNRAS*, vol. 447, pp. 1789–1805, Feb. 2015.

[110] S. D. Landy and A. S. Szalay, "Bias and variance of angular correlation functions," *ApJ*, vol. 412, pp. 64–71, July 1993.

[111] K. B. Fisher, C. A. Scharf, and O. Lahav, "A spherical harmonic approach to redshift distortion and a measurement of Omega(0) from the 1.2-Jy IRAS Redshift Survey," *MNRAS*, vol. 266, p. 219, Jan. 1994.

[112] A. F. Heavens and A. N. Taylor, "A spherical harmonic analysis of redshift space," *MNRAS*, vol. 275, pp. 483–497, July 1995.

[113] K. Yamamoto, M. Nakamichi, A. Kamino, B. A. Bassett, and H. Nishioka, "A Measurement of the Quadrupole Power Spectrum in the Clustering of the 2dF QSO Survey," *PASJ*, vol. 58, pp. 93–102, Feb. 2006.

[114] L. Samushia, E. Branchini, and W. J. Percival, "Geometric biases in power-spectrum measurements," *MNRAS*, vol. 452, pp. 3704–3709, Oct. 2015.

[115] L. Anderson, É. Aubourg, S. Bailey, F. Beutler, V. Bhardwaj, M. Blanton, A. S. Bolton, J. Brinkmann, J. R. Brownstein, A. Burden, C.-H. Chuang, A. J. Cuesta, K. S. Dawson, D. J. Eisenstein, S. Escoffier, J. E. Gunn, H. Guo, S. Ho, K. Honscheid, C. Howlett, D. Kirkby, R. H. Lupton, M. Manera, C. Maraston, C. K. McBride, O. Mena, F. Montesano, R. C. Nichol, S. E. Nuza, M. D. Olmstead, N. Padmanabhan, N. Palanque-Delabrouille, J. Parejko, W. J. Percival, P. Petitjean, F. Prada, A. M. Price-Whelan, B. Reid, N. A. Roe, A. J. Ross, N. P. Ross, C. G. Sabiu, S. Saito, L. Samushia, A. G. Sánchez, D. J. Schlegel, D. P. Schneider, C. G. Scoccola, H.-J. Seo, R. A. Skibba, M. A. Strauss, M. E. C. Swanson, D. Thomas, J. L. Tinker, R. Tojeiro, M. V. Magaña,

L. Verde, D. A. Wake, B. A. Weaver, D. H. Weinberg, M. White, X. Xu, C. Yèche, I. Zehavi, and G.-B. Zhao, "The clustering of galaxies in the SDSS-III Baryon Oscillation Spectroscopic Survey: baryon acoustic oscillations in the Data Releases 10 and 11 Galaxy samples," *MNRAS*, vol. 441, pp. 24–62, June 2014.

[116] K. S. Dawson, D. J. Schlegel, C. P. Ahn, S. F. Anderson, É. Aubourg, S. Bailey, R. H. Barkhouser, J. E. Bautista, A. Beifiori, A. A. Berlind, V. Bhardwaj, D. Bizyaev, C. H. Blake, M. R. Blanton, M. Blomqvist, A. S. Bolton, A. Borde, J. Bovy, W. N. Brandt, H. Brewington, J. Brinkmann, P. J. Brown, J. R. Brownstein, K. Bundy, N. G. Busca, W. Carithers, A. R. Carnero, M. A. Carr, Y. Chen, J. Comparat, N. Connolly, F. Cope, R. A. C. Croft, A. J. Cuesta, L. N. da Costa, J. R. A. Davenport, T. Delubac, R. de Putter, S. Dhital, A. Ealet, G. L. Ebelke, D. J. Eisenstein, S. Escoffier, X. Fan, N. Filiz Ak, H. Finley, A. Font-Ribera, R. Génova-Santos, J. E. Gunn, H. Guo, D. Haggard, P. B. Hall, J.-C. Hamilton, B. Harris, D. W. Harris, S. Ho, D. W. Hogg, D. Holder, K. Honscheid, J. Huehnerhoff, B. Jordan, W. P. Jordan, G. Kauffmann, E. A. Kazin, D. Kirkby, M. A. Klaene, J.-P. Kneib, J.-M. Le Goff, K.-G. Lee, D. C. Long, C. P. Loomis, B. Lundgren, R. H. Lupton, M. A. G. Maia, M. Makler, E. Malanushenko, V. Malanushenko, R. Mandelbaum, M. Manera, C. Maraston, D. Margala, K. L. Masters, C. K. McBride, P. McDonald, I. D. McGreer, R. G. McMahon, O. Mena, J. Miralda-Escudé, A. D. Montero-Dorta, F. Montesano, D. Muna, A. D. Myers, T. Naugle, R. C. Nichol, P. Noterdaeme, S. E. Nuza, M. D. Olmstead, A. Oravetz, D. J. Oravetz, R. Owen, N. Padmanabhan, N. Palanque-Delabrouille, K. Pan, J. K. Parejko, I. Pâris, W. J. Percival, I. Pérez-Fournon, I. Pérez-Ràfols, P. Petitjean, R. Pfaffenberger, J. Pforr, M. M. Pieri, F. Prada, A. M. Price-Whelan, M. J. Raddick, R. Rebolo, J. Rich, G. T. Richards, C. M. Rockosi, N. A. Roe, A. J. Ross, N. P. Ross, G. Rossi, J. A. Rubiño-Martin, L. Samushia, A. G. Sánchez, C. Sayres, S. J. Schmidt, D. P. Schneider, C. G. Scóccola, H.-J. Seo, A. Shelden, E. Sheldon, Y. Shen, Y. Shu, A. Slosar, S. A. Smee, S. A. Snedden, F. Stauffer, O. Steele, M. A. Strauss, A. Streblyanska, N. Suzuki, M. E. C. Swanson, T. Tal, M. Tanaka, D. Thomas, J. L. Tinker, R. Tojeiro, C. A. Tremonti, M. Vargas Magaña, L. Verde, M. Viel, D. A. Wake, M. Watson, B. A. Weaver, D. H. Weinberg, B. J. Weiner, A. A. West, M. White, W. M. Wood-Vasey, C. Yeche, I. Zehavi, G.-B. Zhao, and Z. Zheng, "The Baryon Oscillation Spectroscopic Survey of SDSS-III," *AJ*, vol. 145, p. 10, Jan. 2013.

[117] H. Gil-Marín, J. Noreña, L. Verde, W. J. Percival, C. Wagner, M. Manera, and D. P.

Schneider, "The power spectrum and bispectrum of SDSS DR11 BOSS galaxies - I. Bias and gravity," *MNRAS*, vol. 451, pp. 539–580, July 2015.

[118] D. J. Eisenstein, D. H. Weinberg, E. Agol, H. Aihara, C. Allende Prieto, S. F. Anderson, J. A. Arns, É. Aubourg, S. Bailey, E. Balbinot, and et al., "SDSS-III: Massive Spectroscopic Surveys of the Distant Universe, the Milky Way, and Extra-Solar Planetary Systems," *AJ*, vol. 142, p. 72, Sept. 2011.

[119] M. Manera, R. Scoccimarro, W. J. Percival, L. Samushia, C. K. McBride, A. J. Ross, R. K. Sheth, M. White, B. A. Reid, A. G. Sánchez, R. de Putter, X. Xu, A. A. Berlind, J. Brinkmann, C. Maraston, B. Nichol, F. Montesano, N. Padmanabhan, R. A. Skibba, R. Tojeiro, and B. A. Weaver, "The clustering of galaxies in the SDSS-III Baryon Oscillation Spectroscopic Survey: a large sample of mock galaxy catalogues," *MNRAS*, vol. 428, pp. 1036–1054, Jan. 2013.

[120] Y. P. Jing, "Correcting for the Alias Effect When Measuring the Power Spectrum Using a Fast Fourier Transform," *ApJ*, vol. 620, pp. 559–563, Feb. 2005.

[121] E. A. Kazin, A. G. Sánchez, and M. R. Blanton, "Improving measurements of H(z) and D_A (z) by analysing clustering anisotropies," *MNRAS*, vol. 419, pp. 3223–3243, Feb. 2012.

[122] M. Levi, C. Bebek, T. Beers, R. Blum, R. Cahn, D. Eisenstein, B. Flaugher, K. Honscheid, R. Kron, O. Lahav, P. McDonald, N. Roe, D. Schlegel, and representing the DESI collaboration, "The DESI Experiment, a whitepaper for Snowmass 2013," *ArXiv e-prints*, Aug. 2013.

[123] R. Ruggeri, W. J. Percival, H. Gil-Marín, F. Zhu, G.-B. Zhao, and Y. Wang, "Optimal redshift weighting for redshift-space distortions," *MNRAS*, vol. 464, pp. 2698–2707, Jan. 2017.

[124] H. Gil-Marín, W. J. Percival, A. J. Cuesta, J. R. Brownstein, C.-H. Chuang, S. Ho, F.-S. Kitaura, C. Maraston, F. Prada, S. Rodríguez-Torres, A. J. Ross, D. J. Schlegel, D. P. Schneider, D. Thomas, J. L. Tinker, R. Tojeiro, M. Vargas Magaña, and G.-B. Zhao, "The clustering of galaxies in the SDSS-III Baryon Oscillation Spectroscopic Survey: BAO measurement from the LOS-dependent power spectrum of DR12 BOSS galaxies," *MNRAS*, vol. 460, pp. 4210–4219, Aug. 2016.

[125] D. J. Eisenstein, H.-J. Seo, and M. White, "On the Robustness of the Acoustic Scale in the Low-Redshift Clustering of Matter," *ApJ*, vol. 664, pp. 660–674, Aug. 2007.

[126] R. Scoccimarro, "Fast estimators for redshift-space clustering," *Phys. Rev. D,* vol. 92, p. 083532, Oct. 2015.

[127] F. Zhu, N. Padmanabhan, and M. White, "Optimal redshift weighting for baryon acoustic oscillations," *MNRAS,* vol. 451, pp. 236–243, July 2015.

[128] M. Tegmark, A. N. Taylor, and A. F. Heavens, "Karhunen-Loève Eigenvalue Problems in Cosmology: How Should We Tackle Large Data Sets?," *ApJ,* vol. 480, pp. 22–35, May 1997.

[129] M. S. Vogeley and A. S. Szalay, "Eigenmode Analysis of Galaxy Redshift Surveys. I. Theory and Methods," *ApJ,* vol. 465, p. 34, July 1996.

[130] A. Pope, A. Szalay, T. Matsubara, M. R. Blanton, D. J. Eisenstein, J. Gray, and B. Jain, "Cosmological Parameters from Eigenmode Analysis of Sloan Digital Sky Survey Galaxy Redshifts," in *The New Cosmology: Conference on Strings and Cosmology* (R. E. Allen, D. V. Nanopoulos, and C. N. Pope, eds.), vol. 743 of *American Institute of Physics Conference Series,* pp. 120–128, Dec. 2004.

[131] B. Kalus, W. J. Percival, and L. Samushia, "Cosmological parameter inference from galaxy clustering: the effect of the posterior distribution of the power spectrum," *MNRAS,* vol. 455, pp. 2573–2581, Jan. 2016.

[132] A. Rassat, A. Amara, L. Amendola, F. J. Castander, T. Kitching, M. Kunz, A. Refregier, Y. Wang, and J. Weller, "Deconstructing Baryon Acoustic Oscillations: A Comparison of Methods," *ArXiv e-prints,* Oct. 2008.

[133] E.-M. Mueller, W. J. Percival, and R. Ruggeri, "Optimising primordial non-Gaussianity measurements from galaxy surveys," *ArXiv e-prints,* Feb. 2017.

[134] C. Carbone, L. Verde, and S. Matarrese, "Non-Gaussian Halo Bias and Future Galaxy Surveys," *ApJL,* vol. 684, p. L1, Sept. 2008.

[135] C. Fedeli, C. Carbone, L. Moscardini, and A. Cimatti, "The clustering of galaxies and galaxy clusters: constraints on primordial non-Gaussianity from future wide-field surveys," *MNRAS,* vol. 414, pp. 1545–1559, June 2011.

[136] T. Giannantonio, C. Porciani, J. Carron, A. Amara, and A. Pillepich, "Constraining primordial non-Gaussianity with future galaxy surveys," *MNRAS,* vol. 422, pp. 2854–2877, June 2012.

[137] R. de Putter and O. Doré, "Designing an inflation galaxy survey: How to measure σ (f_{NL})
1 using scale-dependent galaxy bias," *Phys. Rev. D*, vol. 95, p. 123513, June 2017.

[138] S. Camera, M. G. Santos, and R. Maartens, "Probing primordial non-Gaussianity with SKA galaxy redshift surveys: a fully relativistic analysis," *MNRAS*, vol. 448, pp. 1035–1043, Apr. 2015.

[139] S. Ferraro and K. M. Smith, "Using large scale structure to measure f_{NL}, g_{NL} and τ_{NL}," *Phys. Rev. D*, vol. 91, p. 043506, Feb. 2015.

[140] J. Byun and R. Bean, "Non-Gaussian shape discrimination with spectroscopic galaxy surveys," *JCAP*, vol. 3, p. 019, Mar. 2015.

[141] A. Becker, D. Huterer, and K. Kadota, "Constraining scale-dependent non-Gaussianity with future large-scale structure and the CMB," *JCAP*, vol. 12, p. 034, Dec. 2012.

[142] A. Raccanelli, O. Doré, and N. Dalal, "Optimization of spectroscopic surveys for testing non-Gaussianity," *JCAP*, vol. 8, p. 034, Aug. 2015.

[143] S. Matarrese and L. Verde, "The Effect of Primordial Non-Gaussianity on Halo Bias," *ApJL*, vol. 677, p. L77, Apr. 2008.

[144] V. Desjacques and U. Seljak, "Primordial non-Gaussianity from the large-scale structure," *Classical and Quantum Gravity*, vol. 27, p. 124011, June 2010.

[145] L. Amendola, S. Appleby, D. Bacon, T. Baker, M. Baldi, N. Bartolo, A. Blanchard, C. Bonvin, S. Borgani, E. Branchini, C. Burrage, S. Camera, C. Carbone, L. Casarini, M. Cropper, C. de Rham, C. Di Porto, A. Ealet, P. G. Ferreira, F. Finelli, J. García-Bellido, T. Giannantonio, L. Guzzo, A. Heavens, L. Heisenberg, C. Heymans, H. Hoekstra, L. Hollenstein, R. Holmes, O. Horst, K. Jahnke, T. D. Kitching, T. Koivisto, M. Kunz, G. La Vacca, M. March, E. Majerotto, K. Markovic, D. Marsh, F. Marulli, R. Massey, Y. Mellier, D. F. Mota, N. J. Nunes, W. Percival, V. Pettorino, C. Porciani, C. Quercellini, J. Read, M. Rinaldi, D. Sapone, R. Scaramella, C. Skordis, F. Simpson, A. Taylor, S. Thomas, R. Trotta, L. Verde, F. Vernizzi, A. Vollmer, Y. Wang, J. Weller, and T. Zlosnik, "Cosmology and Fundamental Physics with the Euclid Satellite," *Living Reviews in Relativity*, vol. 16, p. 6, Sept. 2013.

[146] A. Font-Ribera, P. McDonald, N. Mostek, B. A. Reid, H.-J. Seo, and A. Slosar, "DESI and other Dark Energy experiments in the era of neutrino mass measurements," *JCAP*, vol. 5, p. 023, May 2014.

[147] F. Zhu, N. Padmanabhan, M. White, A. J. Ross, and G. Zhao, "Redshift weights for baryon acoustic oscillations: application to mock galaxy catalogues," *MNRAS*, vol. 461, pp. 2867–2878, Sept. 2016.

[148] E. Komatsu and D. N. Spergel, "Acoustic signatures in the primary microwave background bispectrum," *Phys. Rev. D*, vol. 63, p. 063002, Mar. 2001.

[149] A. Gangui, F. Lucchin, S. Matarrese, and S. Mollerach, "The three-point correlation function of the cosmic microwave background in inflationary models," *ApJ*, vol. 430, pp. 447–457, Aug. 1994.

[150] P. Coles and B. Jones, "A lognormal model for the cosmological mass distribution," *MNRAS*, vol. 248, pp. 1–13, Jan. 1991.

[151] D. W. Pearson, L. Samushia, and P. Gagrani, "Optimal weights for measuring redshift space distortions in multitracer galaxy catalogues," *MNRAS*, vol. 463, pp. 2708–2715, Dec. 2016.

[152] O. Doré, J. Bock, M. Ashby, P. Capak, A. Cooray, R. de Putter, T. Eifler, N. Flagey, Y. Gong, S. Habib, K. Heitmann, C. Hirata, W.-S. Jeong, R. Katti, P. Korngut, E. Krause, D.-H. Lee, D. Masters, P. Mauskopf, G. Melnick, B. Mennesson, H. Nguyen, K. Öberg, A. Pullen, A. Raccanelli, R. Smith, Y.-S. Song, V. Tolls, S. Unwin, T. Venumadhav, M. Viero, M. Werner, and M. Zemcov, "Cosmology with the SPHEREX All-Sky Spectral Survey," *ArXiv e-prints*, Dec. 2014.

[153] R. Ruggeri, W. J. Percival, E.-M. Mueller, H. Gil-Marin, F. Zhu, N. Padmanabhan, and G.-B. Zhao, "The extended Baryon Oscillation Spectroscopic Survey (eBOSS): testing a new approach to measure the evolution of the structure growth," *ArXiv e-prints*, Dec. 2017.

[154] L. Anderson, E. Aubourg, S. Bailey, D. Bizyaev, M. Blanton, A. S. Bolton, J. Brinkmann, J. R. Brownstein, A. Burden, A. J. Cuesta, L. A. N. da Costa, K. S. Dawson, R. de Putter, D. J. Eisenstein, J. E. Gunn, H. Guo, J.-C. Hamilton, P. Harding, S. Ho, K. Honscheid, E. Kazin, D. Kirkby, J.-P. Kneib, A. Labatie, C. Loomis, R. H. Lupton, E. Malanushenko, V. Malanushenko, R. Mandelbaum, M. Manera, C. Maraston,

C. K. McBride, K. T. Mehta, O. Mena, F. Montesano, D. Muna, R. C. Nichol, S. E. Nuza, M. D. Olmstead, D. Oravetz, N. Padmanabhan, N. Palanque-Delabrouille, K. Pan, J. Parejko, I. Pâris, W. J. Percival, P. Petitjean, F. Prada, B. Reid, N. A. Roe, A. J. Ross, N. P. Ross, L. Samushia, A. G. Sánchez, D. J. Schlegel, D. P. Schneider, C. G. Scóccola, H.-J. Seo, E. S. Sheldon, A. Simmons, R. A. Skibba, M. A. Strauss, M. E. C. Swanson, D. Thomas, J. L. Tinker, R. Tojeiro, M. V. Magaña, L. Verde, C. Wagner, D. A. Wake, B. A. Weaver, D. H. Weinberg, M. White, X. Xu, C. Yèche, I. Zehavi, and G.-B. Zhao, "The clustering of galaxies in the SDSS-III Baryon Oscillation Spectroscopic Survey: baryon acoustic oscillations in the Data Release 9 spectroscopic galaxy sample," *MNRAS*, vol. 427, pp. 3435–3467, Dec. 2012.

[155] C.-H. Chuang, F.-S. Kitaura, F. Prada, C. Zhao, and G. Yepes, "EZmocks: extending the Zel'dovich approximation to generate mock galaxy catalogues with accurate clustering statistics," *MNRAS*, vol. 446, pp. 2621–2628, Jan. 2015.

[156] P. Laurent, S. Eftekharzadeh, J.-M. Le Goff, A. Myers, E. Burtin, M. White, A. J. Ross, J. Tinker, R. Tojeiro, J. Bautista, J. Brinkmann, J. Comparat, K. Dawson, H. du Mas des Bourboux, J.-P. Kneib, I. D. McGreer, N. Palanque-Delabrouille, W. J. Percival, F. Prada, G. Rossi, D. P. Schneider, D. Weinberg, C. Yèche, P. Zarrouk, and G.-B. Zhao, "Clustering of quasars in SDSS-IV eBOSS: study of potential systematics and bias determination," *JCAP*, vol. 7, p. 017, July 2017.

[157] A. Klypin, G. Yepes, S. Gottlöber, F. Prada, and S. Heß, "MultiDark simulations: the story of dark matter halo concentrations and density profiles," *MNRAS*, vol. 457, pp. 4340–4359, Apr. 2016.

[158] V. Springel, "The cosmological simulation code GADGET-2," *MNRAS*, vol. 364, pp. 1105–1134, Dec. 2005.

[159] Y.-S. Song and W. J. Percival, "Reconstructing the history of structure formation using redshift distortions," *JCAP*, vol. 10, p. 004, Oct. 2009.

[160] T. Baldauf, U. Seljak, V. Desjacques, and P. McDonald, "Evidence for quadratic tidal tensor bias from the halo bispectrum," *Phys. Rev. D*, vol. 86, p. 083540, Oct. 2012.

[161] A. Lewis and S. Bridle, "Cosmological parameters from CMB and other data: A Monte Carlo approach," *Phys. Rev.*, vol. D66, p. 103511, 2002.

[162] M. J. Wilson, J. A. Peacock, A. N. Taylor, and S. de la Torre, "Rapid modelling of the redshift-space power spectrum multipoles for a masked density field," *MNRAS*, vol. 464, pp. 3121–3130, Jan. 2017.

[163] J. Hartlap, P. Simon, and P. Schneider, "Why your model parameter confidences might be too optimistic. Unbiased estimation of the inverse covariance matrix," *A&A*, vol. 464, pp. 399–404, Mar. 2007.

[164] A. Gelman and D. Rubin, "Inference from iterative simulation using multiple sequences," *Statistical Science*, vol. 7, pp. 457–511, 1992.
http://www.stat.columbia.edu/~gelman/research/published/itsim.pdf.

[165] R. Ruggeri, W. J. Percival, H. Gil Marin, F. Beutler, E. M. Mueller, F. Zhu, N. Padmanabhan, G.-B. Zhao, P. Zarrouk, A. G. Sanchez, J. Bautista, J. Brinkmann, J. R. Brownstein, F. Baumgarten, C. H. Chuang, K. Dawson, H. Jong Seo, R. Tojeiro, and C. Zhao, "The clustering of the SDSS-IV extended Baryon Oscillation Spectroscopic Survey DR14 quasar sample: measuring the evolution of the growth rate using redshift space distortions between redshift 0.8 and 2.2," *ArXiv e-prints*, Jan. 2018.

[166] S. M. Croom, R. J. Smith, B. J. Boyle, T. Shanks, L. Miller, P. J. Outram, and N. S. Loaring, "The 2dF QSO Redshift Survey - XII. The spectroscopic catalogue and luminosity function," *MNRAS*, vol. 349, pp. 1397–1418, Apr. 2004.

[167] G.-B. Zhao, Y. Wang, S. Saito, H. Gil-Marín, W. J. Percival, D. Wang, C.-H. Chuang, R. Ruggeri, E.-M. Mueller, F. Zhu, A. J. Ross, R. Tojeiro, I. Pâris, A. D. Myers, J. L. Tinker, J. Li, E. Burtin, P. Zarrouk, F. Beutler, F. Baumgarten, J. E. Bautista, J. R. Brownstein, K. S. Dawson, J. Hou, A. de la Macorra, G. Rossi, J. A. Peacock, A. G. Sánchez, A. Shafieloo, D. P. Schneider, and C. Zhao, "The clustering of the SDSS-IV extended Baryon Oscillation Spectroscopic Survey DR14 quasar sample: a tomographic measurement of cosmic structure growth and expansion rate based on optimal redshift weights," *ArXiv e-prints*, Jan. 2018.

[168] D. Wang, G.-B. Zhao, Y. Wang, W. J. Percival, R. Ruggeri, F. Zhu, R. Tojeiro, A. D. Myers, C.-H. Chuang, F. Baumgarten, C. Zhao, H. Gil-Marín, A. J. Ross, E. Burtin, P. Zarrouk, J. Bautista, J. Brinkmann, K. Dawson, J. R. Brownstein, A. de la Macorra, D. P. Schneider, and A. Shafieloo, "The clustering of the SDSS-IV extended Baryon Oscillation Spectroscopic Survey DR14 quasar sample: anisotropic Baryon Acoustic Oscillations measurements in Fourier-space with optimal redshift weights," *MNRAS*, vol. 477, pp. 1528–1535, June 2018.

[169] H. Aihara, C. Allende Prieto, D. An, S. F. Anderson, É. Aubourg, E. Balbinot, T. C. Beers, A. A. Berlind, S. J. Bickerton, D. Bizyaev, M. R. Blanton, J. J. Bochanski, A. S. Bolton, J. Bovy, W. N. Brandt, J. Brinkmann, P. J. Brown, J. R. Brownstein, N. G. Busca, H. Campbell, M. A. Carr, Y. Chen, C. Chiappini, J. Comparat, N. Connolly, M. Cortes, R. A. C. Croft, A. J. Cuesta, L. N. da Costa, J. R. A. Davenport, K. Dawson, S. Dhital, A. Ealet, G. L. Ebelke, E. M. Edmondson, D. J. Eisenstein, S. Escoffier, M. Esposito, M. L. Evans, X. Fan, B. Femenía Castellá, A. Font-Ribera, P. M. Frinchaboy, J. Ge, B. A. Gillespie, G. Gilmore, J. I. González Hernández, J. R. Gott, A. Gould, E. K. Grebel, J. E. Gunn, J.-C. Hamilton, P. Harding, D. W. Harris, S. L. Hawley, F. R. Hearty, S. Ho, D. W. Hogg, J. A. Holtzman, K. Honscheid, N. Inada, I. I. Ivans, L. Jiang, J. A. Johnson, C. Jordan, W. P. Jordan, E. A. Kazin, D. Kirkby, M. A. Klaene, G. R. Knapp, J.-P. Kneib, C. S. Kochanek, L. Koesterke, J. A. Kollmeier, R. G. Kron, H. Lampeitl, D. Lang, J.-M. Le Goff, Y. S. Lee, Y.-T. Lin, D. C. Long, C. P. Loomis, S. Lucatello, B. Lundgren, R. H. Lupton, Z. Ma, N. MacDonald, S. Mahadevan, M. A. G. Maia, M. Makler, E. Malanushenko, V. Malanushenko, R. Mandelbaum, C. Maraston, D. Margala, K. L. Masters, C. K. McBride, P. M. McGehee, I. D. McGreer, B. Ménard, J. Miralda-Escudé, H. L. Morrison, F. Mullally, D. Muna, J. A. Munn, H. Murayama, A. D. Myers, T. Naugle, A. F. Neto, D. C. Nguyen, R. C. Nichol, R. W. O'Connell, R. L. C. Ogando, M. D. Olmstead, D. J. Oravetz, N. Padmanabhan, N. Palanque-Delabrouille, K. Pan, P. Pandey, I. Pâris, W. J. Percival, P. Petitjean, R. Pfaffenberger, J. Pforr, S. Phleps, C. Pichon, M. M. Pieri, F. Prada, A. M. Price-Whelan, M. J. Raddick, B. H. F. Ramos, C. Reylé, J. Rich, G. T. Richards, H.-W. Rix, A. C. Robin, H. J. Rocha-Pinto, C. M. Rockosi, N. A. Roe, E. Rollinde, A. J. Ross, N. P. Ross, B. M. Rossetto, A. G. Sánchez, C. Sayres, D. J. Schlegel, K. J. Schlesinger, S. J. Schmidt, D. P. Schneider, E. Sheldon, Y. Shu, J. Simmerer, A. E. Simmons, T. Sivarani, S. A. Snedden, J. S. Sobeck, M. Steinmetz, M. A. Strauss, A. S. Szalay, M. Tanaka, A. R. Thakar, D. Thomas, J. L. Tinker, B. M. Tofflemire, R. Tojeiro, C. A. Tremonti, J. Vandenberg, M. Vargas Magaña, L. Verde, N. P. Vogt, D. A. Wake, J. Wang, B. A. Weaver, D. H. Weinberg, M. White, S. D. M. White, B. Yanny, N. Yasuda, C. Yeche, and I. Zehavi, "The Eighth Data Release of the Sloan Digital Sky Survey: First Data from SDSS-III," *ApJS*, vol. 193, p. 29, Apr. 2011.

[170] E. L. Wright, P. R. M. Eisenhardt, A. K. Mainzer, M. E. Ressler, R. M. Cutri, T. Jarrett, J. D. Kirkpatrick, D. Padgett, R. S. McMillan, M. Skrutskie, S. A. Stanford, M. Cohen, R. G. Walker, J. C. Mather, D. Leisawitz, T. N. Gautier, III, I. McLean, D. Benford, C. J. Lonsdale, A. Blain, B. Mendez, W. R. Irace, V. Duval, F. Liu, D. Royer, I. Heinrichsen,

J. Howard, M. Shannon, M. Kendall, A. L. Walsh, M. Larsen, J. G. Cardon, S. Schick, M. Schwalm, M. Abid, B. Fabinsky, L. Naes, and C.-W. Tsai, "The Wide-field Infrared Survey Explorer (WISE): Mission Description and Initial On-orbit Performance," *AJ*, vol. 140, pp. 1868–1881, Dec. 2010.

[171] J. E. Gunn, W. A. Siegmund, E. J. Mannery, R. E. Owen, C. L. Hull, R. F. Leger, L. N. Carey, G. R. Knapp, D. G. York, W. N. Boroski, S. M. Kent, R. H. Lupton, C. M. Rockosi, M. L. Evans, P. Waddell, J. E. Anderson, J. Annis, J. C. Barentine, L. M. Bartoszek, S. Bastian, S. B. Bracker, H. J. Brewington, C. I. Briegel, J. Brinkmann, Y. J. Brown, M. A. Carr, P. C. Czarapata, C. C. Drennan, T. Dombeck, G. R. Federwitz, B. A. Gillespie, C. Gonzales, S. U. Hansen, M. Harvanek, J. Hayes, W. Jordan, E. Kinney, M. Klaene, S. J. Kleinman, R. G. Kron, J. Kresinski, G. Lee, S. Limmongkol, C. W. Lindenmeyer, D. C. Long, C. L. Loomis, P. M. McGehee, P. M. Mantsch, E. H. Neilsen, Jr., R. M. Neswold, P. R. Newman, A. Nitta, J. Peoples, Jr., J. R. Pier, P. S. Prieto, A. Prosapio, C. Rivetta, D. P. Schneider, S. Snedden, and S.-i. Wang, "The 2.5 m Telescope of the Sloan Digital Sky Survey," *AJ*, vol. 131, pp. 2332–2359, Apr. 2006.

[172] A. S. Bolton, D. J. Schlegel, É. Aubourg, S. Bailey, V. Bhardwaj, J. R. Brownstein, S. Burles, Y.-M. Chen, K. Dawson, D. J. Eisenstein, J. E. Gunn, G. R. Knapp, C. P. Loomis, R. H. Lupton, C. Maraston, D. Muna, A. D. Myers, M. D. Olmstead, N. Padmanabhan, I. Pâris, W. J. Percival, P. Petitjean, C. M. Rockosi, N. P. Ross, D. P. Schneider, Y. Shu, M. A. Strauss, D. Thomas, C. A. Tremonti, D. A. Wake, B. A. Weaver, and W. M. Wood-Vasey, "Spectral Classification and Redshift Measurement for the SDSS-III Baryon Oscillation Spectroscopic Survey," *AJ*, vol. 144, p. 144, Nov. 2012.

[173] P. Zarrouk, E. Burtin, H. Gil-Marín, A. J. Ross, R. Tojeiro, I. Pâris, K. S. Dawson, A. D. Myers, W. J. Percival, C.-H. Chuang, G.-B. Zhao, J. Bautista, J. Comparat, V. González-Pérez, S. Habib, K. Heitmann, J. Hou, P. Laurent, J.-M. Le Goff, F. Prada, S. A. Rodríguez-Torres, G. Rossi, R. Ruggeri, A. G. Sánchez, D. P. Schneider, J. L. Tinker, Y. Wang, C. Yèche, F. Baumgarten, J. R. Brownstein, S. de la Torre, H. du Mas des Bourboux, J.-P. Kneib, V. Mariappan, N. Palanque-Delabrouille, J. Peacock, P. Petitjean, H.-J. Seo, and C. Zhao, "The clustering of the SDSS-IV extended Baryon Oscillation Spectroscopic Survey DR14 quasar sample: measurement of the growth rate of structure from the anisotropic correlation function between redshift 0.8 and 2.2," *MNRAS*, vol. 477, pp. 1639–1663, June 2018.

[174] H. Gil-Marín, J. Guy, P. Zarrouk, E. Burtin, C.-H. Chuang, W. J. Percival, A. J. Ross,

R. Ruggeri, R. Tojerio, G.-B. Zhao, Y. Wang, J. Bautista, J. Hou, A. G. Sánchez, I. Pâris, F. Baumgarten, J. R. Brownstein, K. S. Dawson, S. Eftekharzadeh, V. González-Pérez, S. Habib, K. Heitmann, A. D. Myers, G. Rossi, D. P. Schneider, H.-J. Seo, J. L. Tinker, and C. Zhao, "The clustering of the SDSS-IV extended Baryon Oscillation Spectroscopic Survey DR14 quasar sample: structure growth rate measurement from the anisotropic quasar power spectrum in the redshift range 0.8 z 2.2," *MNRAS*, vol. 477, pp. 1604–1638, June 2018.

[175] S. Saito, T. Baldauf, Z. Vlah, U. Seljak, T. Okumura, and P. McDonald, "Understanding higher-order nonlocal halo bias at large scales by combining the power spectrum with the bispectrum," *Phys. Rev. D*, vol. 90, p. 123522, Dec. 2014.

[176] S. M. Croom, B. J. Boyle, T. Shanks, R. J. Smith, L. Miller, P. J. Outram, N. S. Loaring, F. Hoyle, and J. da Ângela, "The 2dF QSO Redshift Survey - XIV. Structure and evolution from the two-point correlation function," *MNRAS*, vol. 356, pp. 415–438, Jan. 2005.

[177] S. Habib, A. Pope, H. Finkel, N. Frontiere, K. Heitmann, D. Daniel, P. Fasel, V. Morozov, G. Zagaris, T. Peterka, V. Vishwanath, Z. Lukić, S. Sehrish, and W.-k. Liao, "HACC: Simulating sky surveys on state-of-the-art supercomputing architectures," , vol. 42, pp. 49–65, Jan. 2016.

[178] J. Hou, A. G. Sánchez, R. Scoccimarro, S. Salazar-Albornoz, E. Burtin, H. Gil-Marín, W. J. Percival, R. Ruggeri, P. Zarrouk, G.-B. Zhao, J. Bautista, J. Brinkmann, J. R. Brownstein, K. S. Dawson, N. C. Devi, A. D. Myers, S. Habib, K. Heitmann, R. Tojeiro, G. Rossi, D. P. Schneider, H.-J. Seo, and Y. Wang, "The clustering of the SDSS-IV extended Baryon Oscillation Spectroscopic Survey DR14 quasar sample: anisotropic clustering analysis in configuration space," *MNRAS*, vol. 480, pp. 2521–2534, Oct. 2018.

[179] S. Dodelson and M. D. Schneider, "The effect of covariance estimator error on cosmological parameter constraints," *Phys. Rev. D*, vol. 88, p. 063537, Sept. 2013.

[180] E. Sellentin and A. F. Heavens, "Parameter inference with estimated covariance matrices," *MNRAS*, vol. 456, pp. L132–L136, Feb. 2016.

[181] N. Padmanabhan and M. White, "Constraining anisotropic baryon oscillations," *Phys. Rev. D*, vol. 77, p. 123540, June 2008.

[182] C. Blake, T. Davis, G. B. Poole, D. Parkinson, S. Brough, M. Colless, C. Contreras, W. Couch, S. Croom, M. J. Drinkwater, K. Forster, D. Gilbank, M. Gladders, K. Glazebrook, B. Jelliffe, R. J. Jurek, I.-H. Li, B. Madore, D. C. Martin, K. Pimbblet, M. Pracy, R. Sharp, E. Wisnioski, D. Woods, T. K. Wyder, and H. K. C. Yee, "The WiggleZ Dark Energy Survey: testing the cosmological model with baryon acoustic oscillations at z= 0.6," *MNRAS*, vol. 415, pp. 2892–2909, Aug. 2011.

FORM UPR16

Research Ethics Review Checklist

Please include this completed form as an appendix to your thesis (see the Research Degrees Operational Handbook for more information

Postgraduate Research Student (PGRS) Information		Student ID:	754180
PGRS Name:	Rossana Ruggeri		
Department:	ICG	**First Supervisor:**	Will Percival
Start Date: (or progression date for Prof Doc students)	10/14		

Study Mode and Route:	Part-time	☐	MPhil	☐	MD	☐
	Full-time	☒	PhD	☒	Professional Doctorate	☐

Title of Thesis:	Using galaxy surveys to understand the cosmological evolution
Thesis Word Count: (excluding ancillary data)	60000

If you are unsure about any of the following, please contact the local representative on your Faculty Ethics Committee for advice. Please note that it is your responsibility to follow the University's Ethics Policy and any relevant University, academic or professional guidelines in the conduct of your study

Although the Ethics Committee may have given your study a favourable opinion, the final responsibility for the ethical conduct of this work lies with the researcher(s).

UKRIO Finished Research Checklist:
(If you would like to know more about the checklist, please see your Faculty or Departmental Ethics Committee rep or see the online version of the full checklist at: http://www.ukrio.org/what-we-do/code-of-practice-for-research/)

a)	Have all of your research and findings been reported accurately, honestly and within a reasonable time frame?	YES NO	☒ ☐
b)	Have all contributions to knowledge been acknowledged?	YES NO	☒ ☐
c)	Have you complied with all agreements relating to intellectual property, publication and authorship?	YES NO	☒ ☐
d)	Has your research data been retained in a secure and accessible form and will it remain so for the required duration?	YES NO	☒ ☐
e)	Does your research comply with all legal, ethical, and contractual requirements?	YES NO	☐ ☒

Candidate Statement:

I have considered the ethical dimensions of the above named research project, and have successfully obtained the necessary ethical approval(s)

Ethical review number(s) from Faculty Ethics Committee (or from NRES/SCREC):	Certificate Code: 97B2-F642-B172-6D7B-5E55-B52B-C06E-56E0

If you have *not* submitted your work for ethical review, and/or you have answered 'No' to one or more of questions a) to e), please explain below why this is so:

Signed *(PGRS)*:	*Rossana Ruggeri*	**Date:** 20/11/18